# Schlussbericht

zu dem IGF-Vorhaben

***Methan katalytisch 2***

der Forschungsstelle(n)

FS 1: Lehrstuhl Chemische Technik, Institut für Technische Chemie und Polymerchemie (ITCP), Karlsruher Institut für Technologie (KIT)

FS 2: Lehrstuhl Chemische Technik und Katalyse, Institut für Technische Chemie und Polymcherchemie (ITCP), Karlsruher Institut für Technologie (KIT)

Das IGF-Vorhaben 128 EN der Forschungsvereinigung Forschungsvereinigung Verbrennungskraftmaschinen (FVV) e.V. wurde über die

im Rahmen des Programms zur Förderung der Industriellen Gemeinschaftsforschung (IGF) vom


aufgrund eines Beschlusses des Deutschen Bundestages gefördert.

| | |
|---|---|
| Ort, Datum | Prof. O. Deutschmann Prof. J.-D. Grunwaldt<br>Name und Unterschrift des/der Projektleiter(s)<br>an der/den Forschungsstelle(n) |

# Methan katalytisch 2

**Methan-Oxidations-Katalysatoren: Einfluss von Katalysatorzusammensetzung, Druck und Gaszusammensetzung auf Aktivität, Alterung und Reaktivierung.**

## Abschlussbericht


**Kurzfassung:**

Im CORNET Projekt „ZEEM“ wurden an einer Forschungsstelle in den Niederlanden und zwei Forschungsstellen in Deutschland Untersuchungen zur Minimierung von Emissionen von Gasmotoren durchgeführt. Der deutsche Teil des Projektes mit der Bezeichnung „Methan katalytisch 2“ und der Projektnummer BMWi/IGF 128 EN (FVV Vorhaben 1177) wurde am Karlsruher Institut für Technologie (KIT) durchgeführt. Hier lag der Fokus auf experimentellen Arbeiten und Simulationen zur katalytischen Oxidation von Methan. Mit Hilfe der Synthese, Testung und Charakterisierung von Katalysatoren sowie der Modellierung des Umsatzverhaltens wurden wichtige Parameter zur Optimierung des Gesamtsystems aufgezeigt. Der entwickelte Mechanismus gibt Möglichkeiten für die Verbesserung der Katalysatoren und der deaktivierende Einfluss von Wasser im Abgasstrang konnte auf die Bildung schädlicher Oberflächenspezies an Pd-basierten Katalysatoren zurückgeführt werden. Ebenso konnte der negative Einfluss von kleinsten Mengen Schwefel im Abgas erklärt werden sowie Strategien zur effizienten Regenerierung gealterter Proben aufgezeigt werden. Weiterhin wurde der Einfluss der Positionierung von Katalysatoren vor dem Turbolader untersucht und zeigte besonders durch die dort vorherrschenden hohen Temperaturen großes Potential für zukünftige Anwendungen.

Die Ergebnisse wurden verglichen mit Ergebnissen am Gasmotor. Dieser holländische Teil des Projektes wurde an der Hogeschool van Arnhem en Nijmegen (HAN) durchgeführt. Unterstützt durch eine Literaturrecherche wurden die Entstehungsquellen von Emissionen im Motor aufgedeckt und Optimierungsmöglichkeiten aufgezeigt. Zudem wurde die internationale Emissionsgesetzgebung bzgl. neuer Grenzwerte untersucht. Experimentelle Untersuchungen und die Testung von Katalysatoren an einem Gasmotor rundeten die Arbeit ab.

Das Ziel des Forschungsvorhabens ist erreicht worden.



| | |
|---|---|
| Berichtsumfang: | 145 S., 113 Abb., 24 Tab., 119 Lit. |
| Beginn der Arbeiten: | 01.10.2014 |
| Ende der Arbeiten: | 30.09.2016 |
| Zuschussgeber: | BMWi / IGF-Nr. 128 EN |
| Forschungsstelle: | Institut für Technische Chemie und Polymerchemie (ITCP)<br>Karlsruher Institut für Technologie<br>Lehrstuhl Chemische Technik<br>Leiter: Prof. Dr. Olaf Deutschmann<br>Lehrstuhl Chemische Technik und Katalyse<br>Leiter: Prof Dr. Jan-Dierk Grunwaldt<br>Hogeschool van Arnhem en Nijmegen, HAN Automotive<br>Leiter: Dr. P.A. Bram Veenhuizen |
| Bearbeiter und Verfasser: | Dr. Alexey Boubnov (ITCP)<br>Dr. Maria Casapu (ITCP)<br>Dipl.-Chem. Andreas Gremminger (ITCP)<br>Dipl.-Ing. Bentolhoda Torkashvand (ITCP)<br>M.Eng. Menno Merts (HAN) |
| Obmann des Arbeitskreises: | Dr. Christian Breuer, Heraeus GmbH |
| Vorsitzender des Beirates: | Dr. T. Lösche-ter Horst, Volkswagen AG |
| Weitere Berichte zum Forschungsvorhaben: | - |

[Leerseite für doppelseitigen Druck]

## Table of content

# 1 Management Report

Lean burn gas engines enjoy growing popularity due to growing supply of natural gas (e.g. natural gas, biogas, power to gas) and high power with respect to $CO_2$ emissions. However, gas engines suffer from methane slip, i.e. the emission of unburned methane into the exhaust pipe. The strong greenhouse activity of methane and tightening legislation makes it necessary to lower the emissions. This project tackles this problem from two sides:

1. The catalytic converter with studies on the influence of noble metal state, support material, gas compositions and pre-turbo positioning. This part of the project, which includes a mechanistic view and simulations, was performed at Karlsruhe Institute of Technology in Germany (KIT).

2. The engine itself with studies on the cause of methane emission and tests on a gas engine equipped with a dedicated catalytic converter. This part of the project was done at the University of Applied Science of Arnhem and Nijmegen in the Netherlands (HAN).

The work at KIT focused on the catalytic total oxidation of methane with the principal focus on catalyst deactivation by water and sulfur. To understand what happens during this reaction and how it is influenced by other parameters, several palladium and platinum based systems were investigated. A set of 3 catalysts supported on alumina was synthesized: $Pd/Al_2O_3$, $Pt/Al_2O_3$ and bimetallic $Pd\text{-}Pt/Al_2O_3$. The catalysts were characterized by various *ex situ* and *in situ* techniques. It was found that the noble metal particles are nicely distributed on the alumina support. The noble metal particles have a diameter below 7 nm with fully oxidized PdO. Conversion tests revealed the unique high activity of palladium-based catalysts, exhibiting full methane conversion above 350°C under dry reaction conditions. In contrast, Pt-only catalysts do not show distinct conversion below 550°C. The Pd monometallic and Pd-Pt bimetallic samples however, are strongly influenced by the presence of water. The light-off temperature is shifted by 50 to 100 K depending on the concentration of external water. Furthermore, the catalysts deactivate over time. This process is faster for higher water concentrations and at lower temperatures. *Operando* characterization techniques were applied to reveal the processes taking place on the catalyst surface during water inhibition. X-ray Absorption Spectroscopy (XAS) combined with the concept of Modulation Excitation Spectroscopy (MES) was used to characterize the noble metals under transient conditions during periodic switches between dry and wet conditions. The fast response of the catalyst under these dynamic conditions by means of $CH_4$ conversion is accompanied by distinct structural changes. From the data we conclude that the negative effect is caused by the bonding of water molecules to the low-coordinated PdO sites or to already present palladium hydroxide via hydrogen bonds. However, during fast transients the changes observed are only caused by approximately 1% of the noble metals, which most probably correspond to Pd atoms on the nanoparticle surface or at the interface with $Al_2O_3$. In line with the observed decativation over time, this process might advance to the bulk phase during long-term exposure to the water-containing exhaust gas mixture. The same observations were made for the Pd-only as well as for the bimetallic $Pd\text{-}Pt/Al_2O_3$. Diffusive Reflectance Infrared Fourier Transformed Spectroscopy (DRIFTS) was used as complementary tool to look on the surface species during inhibition by water. It was observed that the formed hydroxyls hinder methane adsorption which would be necessary for its conversion.

Additional DRIFTS experiments aimed at a better understanding of the general methane oxidation mechanism on PdO. Comparing the surface species during oxidation of methane with oxidation of methanol and formic acid revealed the presence of formate species as intermediates during the reaction. No significant carbonate formation was observed.

Since water is always present in the exhaust-gas stream of an engine, different strategies for stabilization of the catalysts activity or its regeneration were investigated. It was found that $NO_x$ is able to stabilize the conversion in presence of $H_2O$ while it is inhibiting the activity under dry conditions. In both cases it does not matter whether NO or $NO_2$ is present. Besides $NO_x$ also reductive treatment was found to regenerate the catalyst. Rich conditions either caused by hydrogen or methane in the absence of oxygen are able to regenerate the Pd and $PdPt/Al_2O_3$ catalysts in very short time (5 minutes). Operando XAS tests have demonstrated that under

these conditions and at elevated temperature PdO will be completely reduced to metallic Pd. This process is accompanied by desorption of water from the surface. Under lean reaction conditions Pd is reoxidized to active PdO. However, the extent of reoxidation is depending on temperature being faster and more pronounced at higher temperatures. Therefore, also the efficiency of the regeneration depends on temperature.

The synthesis of bimetallic Pd-Pt catalysts on various porous materials ($SiO_2$, $CeO_2$, $CeZrO_x$) allowed us to study the influence of the support material. Especially when it comes to long-term stability under isothermal conditions in the presence of water, significant differences are observed for these catalysts. $Al_2O_3$ and $SiO_2$ based samples deactivate very fast, with a drop in conversion at 450°C down to 20 and 0%, respectively. However, Pd-Pt on $CeO_2$ demonstrate constant high conversion at 450°C and even at lower temperatures. Thermogravimetric experiments revealed that $CeO_2$ is not able to store water at temperatures higher than 200°C as $Al_2O_3$ can do. Furthermore, as uncovered by operando XAS, Ce-containing supports also influence the redox properties of Pd and consequently the deactivation/regeneration behavior.

Besides inhibition of the activity and deactivation due to water, sulfur plays a critical role in the behavior of Pd-based catalysts. Experiments on $Al_2O_3$ and $CeZrO_x$ supported catalysts showed that methane conversion rapidly drops in the presence of $SO_2$ in the low ppm range (2 -5). Severe poisoning was observed within short-term exposure. Regeneration of such poisoned catalysts is difficult, especially under lean conditions. However, when switching to reducing conditions, the regeneration is much more effective. At temperatures above 525°C partial regeneration was achieved. Even in the presence of $SO_2$, fuel rich conditions lead to an increasement in activity of a poisoned and completely deactivated Pd-Pt/$CeZrO_x$ catalyst at 550°C.

All methane oxidation catalysts require rather high temperatures. High temperatures are available closer to the engine which would mean positioning of the catalyst in front of the turbocharger. At this location higher temperature but also higher pressure is present while the mass flow stays the same. The tests revealed that higher pressure can have both negative and positive effects on the conversion. With higher pressure the residence time increases, which is beneficial for the conversion. However, higher pressure leads to higher concentration of the gaseous species influencing the kinetics of the reaction. In the case of fresh Pd based catalysts, it was found that these two factors almost outbalance each other with slightly lower conversion at higher pressure in the low temperature range. This can be explained by a negative reaction order of water gaining more importance with higher water concentration. Simulations were able to match the experimental data when an inhibiting term by water was adapted.

The knowledge gained during laboratory tests with numerous catalytic systems was used to design experiments on an gas engine at HAN Automotive. For this the engine at was equipped with a catalyst prepared by a consortium of partners of the working group. The engine used was a VW 1.4 TSi petrol engine, converted to MPi CNG, running lean burn. For the test an engine calibration was created which resulted in an methane emission off over 2000 ppm.

The first test performed was an endurance test, running in total 60 hours. The catalyst was tested at 450ºC and λ=1.68. After warming up a conversion grade of 78% was reached. During the test this percentage gradually went down, until 21% after 60 hours.

In a second test session, with a second sample catalyst, the regeneration behavior was tested. The same engine and same operating conditions were used for this test. In a first phase the catalyst was used under lean conditions, to initiate significant deterioration, which was seen after 12 hours. The conversion grade at that moment was 65%. To regenerate the catalyst a period of rich operation was used, for 30 minutes. This increased conversion grade by 10%. Further shorter regeneration attempts, of 1 and 5 minutes, each led to an increase between 5% and 10%. Although being the first preliminary results, it seems regeneration by rich operation has effect, but it reaching its initial performance is not achieved yet.

Subsequent analysis of the engine aged catalyst at KIT revealed the presence of sulfur species on the catalyst surface. This is in line with fuel gas analysis that demonstrated the presence of

a sulfur containing odorizer in the Dutch natural gas. The sulfur poisoning was found to be more pronounced at the inlet position and lead to pronounced shift of the light-off curve compared to a fresh catalyst. Activity was partly regained when the sample was heated to 925°C in $N_2$ leading to the decomposition of surface sulfates.

The experimental work was accompanied by literature research at both institutes.

HAN focused on the literature relevant for gas engines and the report describes the main causes and solutions to lower emissions coming out of the combustion engine. The main causes are scavenging of fuel through the engine, fuel not taking part of the combustion process, and misfires. Solutions can be found in the conceptual engine choice, valve timing, combustion chamber modifications and optimal fuel system/engine control.

Also the various legislations are reviewed. Combustion engines are applied in multiple working fields, each with its own regulations. The sectors are road transport, non-road, marine and stationary machinery. Two different approaches for methane emissions occur. It can be shared under general hydrocarbon emission, or specific as methane emissions. In the most recent version of each sector's legislation an allowable value of HC emissions is between 0.1 and 0.2 g/kWh, whereas methane emissions in stage V proposal for inland shipping are limited at 6 g/kWh. This is a typical value where methane emission is brake-even with $CO_2$ advantage, in terms of greenhouse gas production.

At KIT the literature relevant to catalytic total oxidation of methane was reviewed. Factors influencing the activity of noble metal based catalysts are described and compared with results found within this project.

# 2 Literature study

## 2.1 Literature study on causes of $CH_4$ emission and legislation (HAN)

### 2.1.1 Introduction

In the shipping sector there is an increasing focus on exhaust gas emissions. Combined with the worldwide concern about the future shortage of fossil oil, and a sound look on the commercial aspect of transport fuel, this leads to a strong interest in the usage of natural gas as engine fuel.

In general natural gas is known as a clean fuel. This is because of its relatively low $CO_2$ and particle matter emissions. Moreover, it is favored because of its origin. Although a fossil fuel, it seems there are currently larger reserves than crude oil, and often on favorable locations. In parallel a strong growth of the bio-gas sector is going on, which can make it a sustainable fuel.

Natural gas can be used either compressed (CNG), or liquefied (LNG). This document applies for both variants.

Besides the positive aspects of natural gas there is also a drawback: methane emissions (often called methane slip). The emission of unburned methane from an engine can be severe, and is considered as a strong greenhouse gas. In this document the causes for methane emissions are described. Also it will be explained which parameters are influencing methane emissions, and finally an overview of emission legislation is given.

The mentioned $CO_2$ reduction finds its cause in the nature of the fuel. A lower carbon to hydrogen ratio results in lower $CO_2$ emissions. This is advantage can be offset by a higher overall fuel consumption, which increases $CO_2$ emissions again. Although in traditional combustion engines $CO_2$ is the only greenhouse gas, for natural gas engines also the methane emissions are considered as greenhouse gas. Their environmental impact is significantly higher than that of $CO_2$. For comparison the Greenhouse-gas Warming Potential (GWP) is used, an indicator of how strongly a gas traps heat in the atmosphere. Looking at a period of 100 years, this factor is for methane 21 times higher than for $CO_2$. Figure 1 shows the greenhouse gas advantage of a gas engine compared to a diesel engine, dependent of methane slip and engine efficiency.

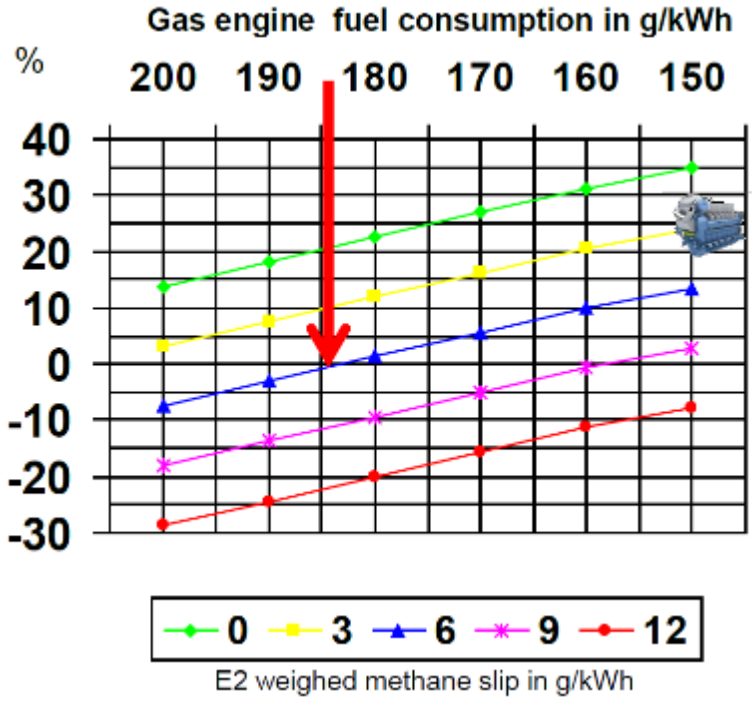


- For every level of methane slip a separate line is drawn.
- Each line shows the relation between fuel consumption and greenhouse gas improvement.
- The indicated point shows a 0% greenhouse gas advantage, for an engine with 184g/kWh fuel consumption and 6 g/kWh methane slip.

**Figure 1:** Greenhouse gas advantage for methane engines (Copyright, (Horgen)).

### 2.1.2 Methane emission causes

#### 2.1.2.1 Introduction: engine-concepts

Before going into detail about methane emission the different possible engine concepts for natural gas are listed. It can be used in a spark ignited (SI) engine, or a dual fuel engine.

The SI engine, well known from its application in passenger cars as “petrol-engine” uses an external ignition source (spark plug), the fuel and air is premixed, has a limited compression ratio, and the torque of the engine is quantity controlled. SI natural gas engines are available as lambda 1 engines, or as lean burn engines.

Dual fuel engines are in the base compression ignited (CI) engines, better known as diesel engines. The gas is usually metered into the intake manifold and as air gas mixture entering the combustion chamber. At the end of the compression stroke a small quantity of diesel is injected into the hot air/gas mixture and acts as an ignition source. These engines are characterized by a higher compression ratio and a quality controlled torque.

Each engine concept has its own pro’s and con’s considering methane emissions. An overview can be seen in Table 1.

**Table 1:** Overview of CNG engine concepts (CIMAC, 2014)

| Combustion System | scavenging process, valve overlap | quenching effects in lean mixture zones | quenching effects near walls | trapped Methane in fireland | delayed combustion/misfiring |
|---|---|---|---|---|---|
| same engine speed | | | | | |
| Rich burn combustion system (SI) | medium | low | low | medium | Low |
| Lean burn combustion system (SI/DF) | low | medium | medium | higher | medium |
| same $NO^x$ level, same gas admission system | | | | | |
| Lean combustion: small bore – high speed (SI/DF) | medium | low | low | higher | Low |
| Lean combustion: large bore – medium speed (SI/DF) | low | medium | medium | higher | medium |
| same $NO^x$ level | | | | | |
| Homogenous charge (SI/DF) | medium | low | low | higher | Low |
| Port injection (SI/DF) | medium | medium | low | higher | Low |
| Direct injection (SI/DF) | low | medium | low | low | medium |

#### 2.1.2.2 Scavenging

During the design of a 4-stroke engine there are various aspects taken into account when choosing valve timing. The theoretical expected timing of opening and closing of valves, exactly at the start/end of the intake respectively exhaust stroke, is almost never applied. Usually the exhaust valve closes after top dead center (TDC), while the intake valve already opens before TDC. The exact angles are optimized for a certain speed(-range) of the engine. This valve timing is chosen to get as much fresh air into the cylinder and thus maximizing performance. Another reason to use this so called overlap, is to spool fresh air through the cylinder into the exhaust system. On direct injected SI engines the resulting high scavenging rates are mainly used to improve turbocharger dynamics. But more common it is used on CI engines, to

cool the combustion chamber and exhaust valves. Cool air passes the components and the hot exhaust gas is diluted, reducing temperature.

This mechanism is only valid on direct injected engines, where fuel is injected after closing of the exhaust valve. In other configurations it is very likely not only fresh air, but an air/fuel mixture is scavenged. The fuel, methane, is directly spooled into the exhaust system and thus finally into the environment. This is one of the main causes of methane slip.

It is a problem on dual fuel engines, which have the high overlap valve timing of a CI engine, but also on SI CNG when they are converted SI engines and still use the same camshaft. On dedicated CNG engines the problem is smaller, but still present. Here often a more mild valve timing is chosen, but still some overlap is needed to assure appropriate engine performance.

The sensitivity of methane slip on valve overlap is also dependent on the pressure levels (boost-pressure and exhaust gas back-pressure) of a turbocharger. A larger positive pressure difference over the cylinder, increases scavenging and thus methane slip.

### 2.1.3 Quenching in lean mixture zones

For almost all fuels there is a limit on air-fuel ratio for which combustion can be guaranteed. For methane the combustion stability starts to decrease from lambda 1,6~1,8. The exact value is dependent on combustion chamber shape and temperature, and motion and homogeneity of the mixture.

When the air and fuel are not perfectly mixed, local lean zones can arise, where incomplete combustion takes place. Usually also the temperature in these zones is limited, further reducing the lean-burn limit. The flame-front is quenching in such zones and the unburned methane will be emitted with the exhaust gasses.

#### 2.1.3.1 Quenching effects near walls

For almost all fuels, a flame-front will not reach the walls of the cylinder. For this there are two reasons. Firstly a flame has a certain quenching distance; it is not able to propagate within infinite small dimensions. Secondly near cylinder walls the influence of temperature plays a role on quenching. The cylinder wall is cooled from the outside by engine coolant, which usually has a temperature around 90˚C. Although heated by the combustion the inside temperature of the wall has a typical temperature of 150~250˚C. This is far below the ignition temperature of methane of 580 ˚C and thus supports the quenching of the mixture in this zone. The unburned mixture generates methane emissions.

#### 2.1.3.2 Trapped methane in fire land

The quenching distance of an air fuel mixture plays a role around the piston. Just above the piston ring there is a cavity between the piston and cylinder wall, the fire-land. Usually the piston has a slightly decreased diameter on this position to allow for thermal expansion of the piston. The play between cylinder and piston can be easily more than 0.1 mm on this position. On the other hand the upper piston ring is not completely on top of the piston, but slightly lower to reduce the thermal stress on the piston ring. The distance can vary from a few millimeters on a small car engine with 60mm bore, up till centimeters on a large ship engine with a 450mm bore.

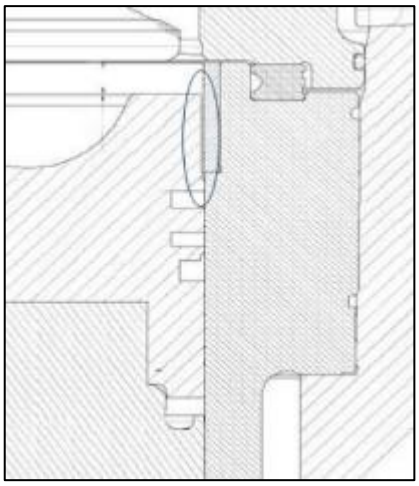

**Figure 2:** Area between piston and cylinder (CIMAC, 2014).

By these design aspects a volume is created in which mixture is entering during the induction and compression stroke. Although the flame front will reach this area, it is not able to fully enter this area and generate a completely combustion. The unburned mixture is a severe contribution on methane emissions.

#### 2.1.3.3 Delayed combustion/misfiring

An intermitting source of methane emission can be delayed combustion or misfiring. Although misfiring can't be continuously occurring on all cylinders (the engine won't be running), it can happen intermitting, partly, or on just one cylinder. When the mixture is not burned at all in a cylinder, this obviously gives a large methane emission.

Various reasons can cause these misfires. The most common ones are problems with the mixture composition or with the ignition systems on SI engines.

*Mixture*

The air fuel mixture can be too lean or rich, or not homogeneous enough. An incorrect lambda value is more prone to occur on open loop controlled fuel systems. The deviation on lambda is not noticed on such a system. But also on a closed loop system it is not guaranteed the required mixture is created. An error can occur in the lambda measurement loop, or the controller can run out of its control range.

Main causes for incorrect lambda values can be found both on the air and the fuel side of the engine. Most seen issues are on the air side of the engine:

- Incorrect boost pressure
- Contamination on intake trajectory
- Clogged air filter
- Wrong valve play
- Unexpected ambient conditions
- Clogged exhaust muffler or after-treatment components.
- Incorrect EGR flow
- Defective sensors

On the fuel side of the engine:

- Contamination or defects in fuel mixer or injectors
- Deviation in supply pressure
- Changed fuel composition.
- Defective sensors.

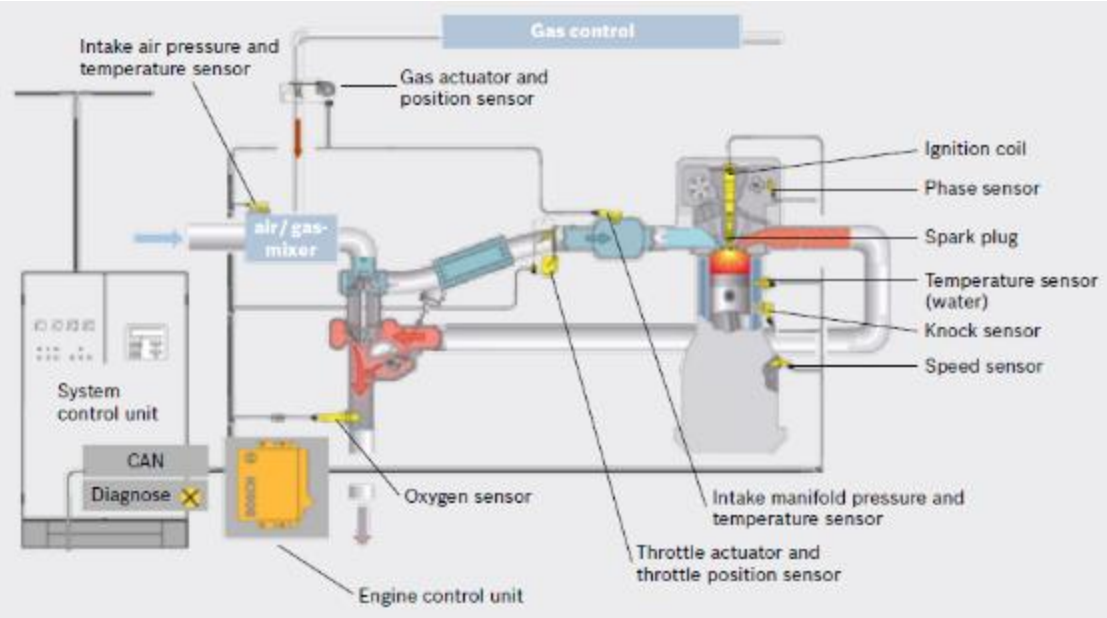


**Figure 3:** General system overview SI CNG engine (Copyright, Bosch).

*Ignition*
Especially methane puts a strong load on the ignition system. The required high voltage to ionize the mixture and create a spark is higher than for example on a petrol fueled engine. This makes the ignition system on a methane engine more sensitive. Reasons for failing ignition can be defects or lack of maintenance. Defective coils, damaged or bad connected wires and high tension leads can create misfire problems. Also worn spark plugs are a well-known cause for misfiring.

Intermitting ignition problems can not only be a cause for misfires and methane slip, but can also load to backfire and thus should be prevented carefully.

### 2.1.4 Parameters limiting methane emissions

#### 2.1.4.1 Introduction

Where in 2.1.2 the main causes for methane slip are explained, are in this chapter the parameters described that can be used to reduce methane slip. Most parameters are of interest while developing a methane engine or converting an engine to CNG or dual fuel. But also during the process of engine/fuel selection, it can be used as background-information.

#### 2.1.4.2 Valve timing

To reduce methane slip, valve timing with less valve overlap should be chosen. It is not possible to tell upfront which camshaft duration gives best result on a given engine.

On engines with separate camshafts for intake- and exhaust valves some result can be achieved by re-phasing the camshafts. Advancing the exhaust camshaft and retarding the intake camshaft reduces valve overlap and thus theoretically also reduces the methane slip. With the intended early closing of the exhaust valve also comes an early opening, and at the intake side the retarded opening also results in late closing of the intake valve.

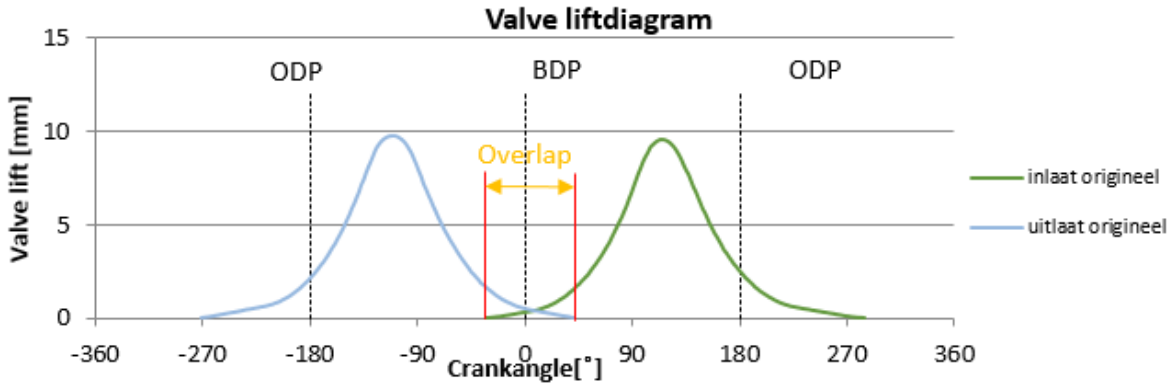


**Figure 4:** Valve timing, with overlap (Copyright, HAN).

The early opening of the exhaust valve improves turbocharger response but limits engine efficiency. Not all energy is taken from the combustion. Also incomplete combustion can be the result, and thus an increased methane emission. The late opening of the intake valve can reduces volumetric efficiency at low engine speeds. It is likely these drawbacks are so unacceptable that re-phasing the stock camshafts can't be used as a measure to reduce methane slip then.

A better approach would be the design of new cam-shaft(s) completely aimed at good engine performance, efficiency and emissions. The following aspects should be taken into account.

- Thermal efficiency
- Volumetric efficiency
- Exhaust gas temperature
- Turbo charger response
- Methane emissions
-

In most cases the chosen timing is a trade-off between listed aspects.

As most heavy duty engines are turbo-charged engines, this is an extra factor to take into account when optimizing valve timing. It is closely related to turbo-matching. Normally a sound turbo-matching on an engine should lead to a boost pressure which is higher than the pressure in the exhaust manifold. Although positive for engine performance and cylinder filling, this pressure difference can increase the amount of methane that is directly scavenged through the engine. When this can't be reduced enough by the chosen valve timing, this can be a reason to limit boost pressure, or choose a slightly smaller turbine. Again there are no discrete numbers predictable. This design process requires iterative testing, eventually combined with engine simulations.

#### 2.1.4.3 Injection timing

As explained a major reason of methane slip is the scavenging of air-methane mixture through the engine. On engines with a central fueling system, very early in the inlet trajectory, the intake manifold is always filled with mixture and thus scavenging is done with methane. When the fuel system uses sequential multi point injection, an optimized injection timing can be used to limit methane emission. With late injection during the intake stroke, the scavenging during valve overlap can be done with fresh air only. Just after closing of the exhaust valve the gas should be injected and can thus can enter the combustion chamber. To ensure the right amount of gas, the injection should be finished before the intake valve closes. This puts a requirement on the injection hardware. Where traditionally a complete engine cycle (two revolutions) is available for injection, now all gas should be injected in less than half a revolution. This requires large injectors combined with high enough supply pressure.

#### 2.1.4.4 Direct injection

Instead of letting the gas into the cylinder through the intake manifold, it can also be directly injected into the combustion chamber. For Diesel engines this is (almost) the only way, for petrol engines direct injection is applied more and more, but for gas engines it is not very common yet. Reason for this is the lack of available injection hardware.

To inject gas a much larger injector is needed, compared to injection of a liquid. Another requirement is the supply pressure of the fuel, which should be high enough to overcome the compression pressure of the engine. When using tank-pressure for this the tank can't be fully emptied during usage and thus autonomy is reduced. Another option is to use a pump or compressor, but this is not as easy as with a liquid fuel.

Quite new on the market are two injectors from Canadian company Westport. For dual fuel they have a combined injector available, which can inject the main amount of energy in gas form, and a small quantity of diesel to ignite the mixture. This injector aims at heavy duty engines. For SI engines a CNG-DI injector is or will be available from Westport. The company also announces a natural gas compressor module, to supply the DI injectors with enough gaseous fuel.

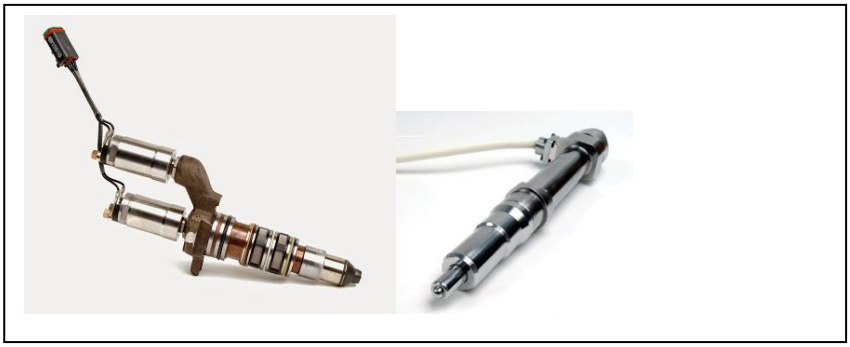

**Figure 5:** Direct injection hardware (Copyright, Westport).

Advantage of direct injection is the possibility to completely stop direct methane slip through the engine. When the fuel is injected while the valves are closed, there is no possibility for the gas to enter the exhaust system before combustion takes place.

When the injection is done during the compression stroke, it also compensates the loss of volumetric efficiency which normally occurs on gas-engines.

#### 2.1.4.5 Combustion chamber optimization

As already described in chapter 2 multiple causes of methane emissions find their basis in effects happening inside the combustion chamber. For this reason it makes sense to pay attention to the design of the combustion chamber. On an existing engine this usually means a design change of the piston crown. A new cylinder head is almost never developed.

Most important in the combustion chamber is the absence of dead volume; volume which is at certain crank position hardly connected with the center of the combustion chamber. This means a basic design with no special shapes, and the first piston ring placed relatively high in the piston. Another parameters that can be used is squish. By having outer areas of the piston approaching the cylinder head very close (< 1mm), turbulence is induced in the mixture, and it is positively pushed towards the burning center of the combustion chamber.

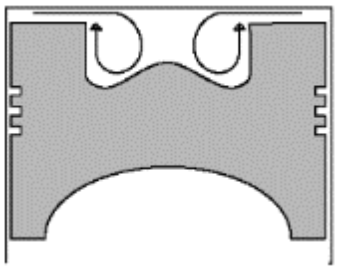

**Figure 6:** Squish motion (Copyright, Vegburner).

For dual fuel the characteristic diesel piston with its bowl in the center of the crown may not be always optimal. The diesel combustion is centered in this cavity, since the fuel-injection is pointed towards this location. Since the homogenous cng mixture is everywhere in the combustion chamber, an alternative shape might guarantee a better promotion of the flame-front.

#### 2.1.4.6 EGR

Both on SI and CI engines exhaust gas recirculation is often applied. The main goal is to reduce peak temperature of the combustion. This has a positive influence on emissions, since a lower peak temperature reduces the formation of $NO_x$. On quantity controlled engines the effect of adding exhaust gas to the fresh inlet charge is the addition of mass, which has to be heated by the combustion. When the same amount of energy from combustion is used to heat more mass, a lower end temperature will be the result. On quality controlled engines the amount of gas is not significantly changed when EGR is applied. The only difference is that he mixture contains more $CO_2$ and less $N_2$ and $O_2$. Since $CO_2$ has a higher specific heat capacity, it takes more energy from the combustion and again a lower end-temperature is the result.

Although peak temperature is reduced, adding hot exhaust gas to the fresh mixture increases the starting temperature of the combustion process. This can limit efficiency, and increase knock sensitivity. For this reason the recirculated exhaust gas is often cooled down, before entering the combustion chamber again.

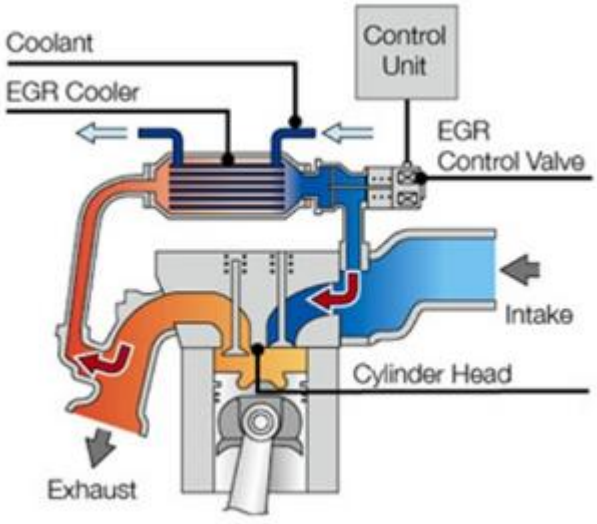


**Figure 7:** EGR system with cooling (Copyright, Ecusafe).

A second effect of EGR, specifically on natural gas engines, is the re-burning of methane. The exhaust gas which enters the combustion chamber again can contain 1000's of ppm's $CH_4$. Even if only a part of this methane is burned, it reduced the overall methane emissions. There is a limit on how much EGR can be applied. Adding to much inert gas to the mixture decreased the burning stability. A typical rate is 30% (volume).

On petrol and diesel fueled engines the hydrocarbon content in the exhaust gas is so low, that usually the effect of re-burning this emission in the end has a lower impact than the increase in hydrocarbon emissions which is caused by reduced burning stability when using EGR. So on these engines EGR has only benefits for $NO_x$ emissions.

#### 2.1.4.7 Fuel ratio's

Of great importance for lean burn SI engines is the chosen lambda value. Operating an engine on a lean mixture basically increases engine efficiency, but also can have its negative effect on methane emissions as described in chapter 2.3 and 2.6. This asks for a correct choice of target lambda value for each operation point of the engine: as lean as possible without a strong increase in methane emission. So the chosen lambda has to be richer than the misfire-limit. This has to be calibrated on an engine test bench for combination of load and rpm. Depending on the engine configuration this limit is at a Lambda value of 1.6~2.0. A trend which can be expected is that on higher loads and higher engine speeds a leaner mixture can be accepted, because of increased temperature and increased flame-front intensity. Typical behavior of methane emissions can be seen in the HC line in Figure 8.

During engine testing one can look at the engine efficiency in combination with methane emissions. Another good and easy indicator that shows the position of the misfire limit, is a sharp increase in Coefficient Of Variance (COV) of the delivered torque. It indicates that some combustions are failing or running way to slow, typical signs of too lean mixture.

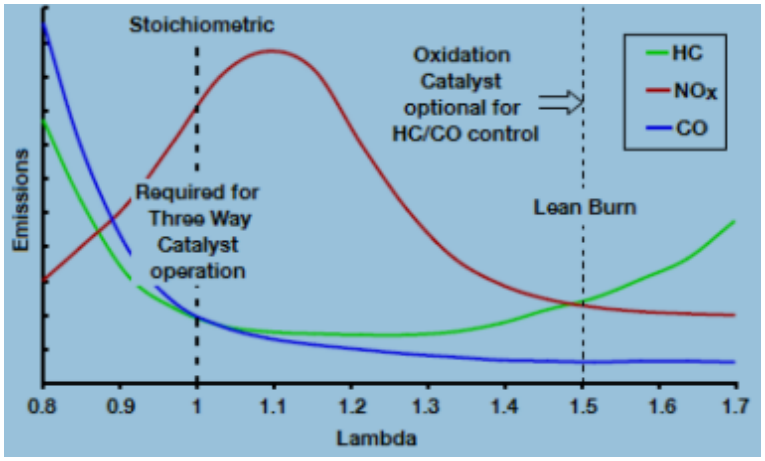


**Figure 8:** Emissions versus lambda (Copyright, Westport).

On dual fuel engines the load is quality controlled: there is no fixed setpoint for lambda, but it is a function of the required engine load. With increasing load the fuel amount is increased, resulting in a lower lambda value. On the rich side limitations can be formed by excessive smoke of the diesel combustion, or knocking of the gas part. On the lean side, at very low torque, another problem occurs.

The small amount of required torque asks for a minimal amount of fuel. This makes the homogenous CNG mixture extremely lean leading to high methane emissions, misfires, or even complete lack of methane combustion. The problem is worsened because of the required minimum size of the diesel injection. This decreases the CNG/diesel ratio even further, making the

homogenous CNG mixture even more lean. A common solution is to run very low loads completely on diesel, and start dual fuel operation from the point where the homogenous CNG part of the mixture is rich enough to burn. A typical implementation can be seen in Figure 9.

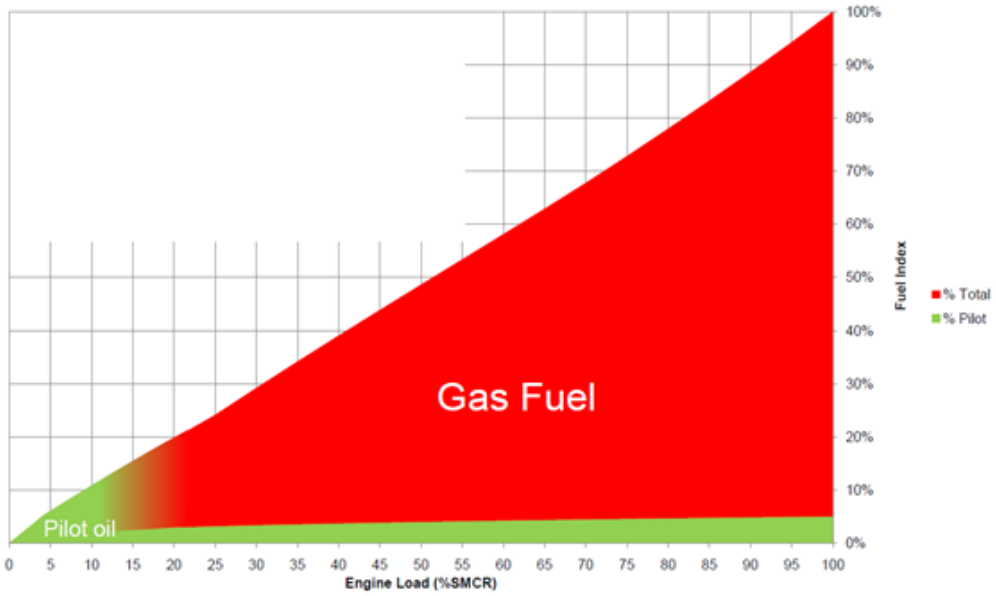


**Figure 9:** Diesel pilot versus Gaseous fuel ratio in Dual Fuel engine. (Copyright, (MAN, 2011)).

### 2.1.5 Regulations

Combustion engines are used in different working-fields, but in almost all cases exhaust gas emissions are relevant. The most dominant areas are:

- Road transport;
- Non road;
- Marine;
- Stationary machinery.

For each sector the applying rules and limits are listed. Only the regulations where vehicles/engines within Europe have to comply to will be discussed, due to the fact that these are the regulations that are relevant for this research.

#### 2.1.5.1 Road transport

The Netherlands are following the European exhaust gas emission regulations; the euro limits. The first limit, Euro 1, was introduced in 1993. Since 2013 Euro6 limits are active. There are separate limits for passenger cars and heavy duty vehicles. The limits for the heavy duty vehicles are divided into limits for CI (compressed ignition) engines and limits for PI (positive ignition) engines.

1. The limits for heavy duty vehicles with compressed ignition are as shown as in Table 2
2. The limits for heavy duty vehicles with positive ignition are as shown as in Table 3

**Table 2:** European heavy duty emission limits with CI (Dieselnet, sd)

| Stage | Date | Test | CO | HC | NOx | PM | PN | Smoke |
|---|---|---|---|---|---|---|---|---|
| | | | *g/kWh* | | | | *1/kWh* | *1/m* |
| Euro I | 1992, ≤ 85 kW | ECE R-49 | 4.5 | 1.1 | 8.0 | 0.612 | | |
| | 1992, > 85 kW | | 4.5 | 1.1 | 8.0 | 0.36 | | |
| Euro II | 1996.10 | | 4.0 | 1.1 | 7.0 | 0.25 | | |
| | 1998.10 | | 4.0 | 1.1 | 7.0 | 0.15 | | |
| Euro III | *1999.10 EEV only* | ESC & ELR | *1.5* | *0.25* | *2.0* | *0.02* | | *0.15* |
| | 2000.10 | | 2.1 | 0.66 | 5.0 | 0.10[a] | | 0.8 |
| Euro IV | 2005.10 | | 1.5 | 0.46 | 3.5 | 0.02 | | 0.5 |
| Euro V | 2008.10 | | 1.5 | 0.46 | 2.0 | 0.02 | | 0.5 |
| Euro VI | 2013.01 | WHSC | 1.5 | 0.13 | 0.40 | 0.01 | $8.0\times10^{11}$ | |

a - PM = 0.13 g/kWh for engines < 0.75 $dm^3$ swept volume per cylinder and a rated power speed > 3000 $min^{-1}$

In the future, the maximum allowed emissions will be further reduced. At this moment, it is not known when Euro VII will be adopted. It is expected that the focus will lie on reducing $CO_2$ emissions, because the maximum allowed amount of other pollutants are already very low, but they will be slightly further reduced (Hogg, 2014). Another reason for this expectation is the 2015 Paris Climate Conference (COP21). The goal of this conference is to keep the global warming at a maximum of 2°C. This requires a reduction of $CO_2$ emissions. Every participant has to use his available resources and techniques to achieve this goal (Klimaatconferentie Parijs 2015 COP21, 2015) Based on this information, assumptions are made concerning the expectation of the Euro VII emission standards for heavy duty vehicles. However, $CO_2$ emissions have to be limited in another way, because a liter of diesel will always generate the same amount of $CO_2$ due to the composition of the fuel. Therefore, the amount of $CO_2$ emitted/kWh will always be the same, unless another fuel like natural gas is chosen. The maximum amount of $CO_2$ emitted has to be linked to the efficiency of a whole vehicle, for instance fuel economy. For this reason, the $CO_2$ emission limits are not predicted in Table 4 and Table 5. The limits of the other pollutants are estimated values.

**Table 3:** European heavy duty emission limits with PI (Dieselnet, sd)

| Stage | Date | Test | CO | NMHC | $CH_4$[a] | NOx | PM[b] | PN[e] |
|---|---|---|---|---|---|---|---|---|
| | | | *g/kWh* | | | | | *1/kWh* |
| Euro III | *1999.10 EEV only* | ETC | *3.0* | *0.40* | *0.65* | *2.0* | *0.02* | |
| | 2000.10 | | 5.45 | 0.78 | 1.6 | 5.0 | 0.16[c] | |
| Euro IV | 2005.10 | | 4.0 | 0.55 | 1.1 | 3.5 | 0.03 | |
| Euro V | 2008.10 | | 4.0 | 0.55 | 1.1 | 2.0 | 0.03 | |
| Euro VI | 2013.01 | WHTC | 4.0 | 0.16[d] | 0.5 | 0.46 | 0.01 | $6.0\times10^{11}$ |

a – for gas engines only (Euro III–V: NG only; Euro VI: NG + LPG)
b – not applicable for gas fueled engines at the Euro III–IV stages
c – PM = 0.21 g/kWh for engines < 0.75 $dm^3$ swept volume per cylinder and a rated power speed > 3000 $min^{-1}$
d – THC for diesel engines
e – for diesel engines; PN limit for positive ignition engines TBD

**Table 4:** Expected Euro VII emission standards for heavy duty vehicles with CI (Dieselnet, sd)

| Stage | Date | Test | CO | HC | NOx | PM | PN | Smoke |
|---|---|---|---|---|---|---|---|---|
| | | | *g/kWh* | | | | *1/kWh* | *1/m* |
| Euro VII | 2020.01 | | 1.5 | 0.10 | 0.30 | 0.01 | $8.0\times10^{11}$ | |

a – PM = 0.13 g/kWh for engines < 0.75 $dm^3$ swept volume per cylinder and a rated power speed > 3000 $min^{-1}$

**Table 5:** Expected Euro VII emission standards for heavy duty vehicles with PI (Dieselnet, sd)

| Stage | Date | Test | CO | NMHC | $CH_4$[a] | NOx | PM[b] | PN[e] |
|---|---|---|---|---|---|---|---|---|
| | | | *g/kWh* | | | | | *1/kWh* |
| Euro VII | 2020.01 | | 4.0 | 0.16 | 0.025 | 0.36 | 0.01 | $6.0\times10^{11}$ |

a – for gas engines only (Euro III–V: NG only; Euro VI: NG + LPG)
b – not applicable for gas fueled engines at the Euro III–IV stages
c – PM = 0.21 g/kWh for engines < 0.75 $dm^3$ swept volume per cylinder and a rated power speed > 3000 $min^{-1}$
d – THC for diesel engines
e – for diesel engines; PN limit for positive ignition engines TBD

### 2.1.5.2 Non road

The non-road section consists of combustion engine driven machinery, not used on-highway. It applies to mobile equipment like used in agriculture, industry and construction. Airplanes are not included. In Europe the Stage regulations are used. From 2006 - 2013 the Stage IIIA and Stage IIIB limits were phased in (Table 6). The most recent version, stage IV, was adopted in 2014 (Table 7).

**Table 6:** Stage III A/B Emission standards for European non road diesel engines (Dieselnet, sd)

| Cat. | Net Power | Date† | CO | HC | HC+NOx | NOx | PM |
|---|---|---|---|---|---|---|---|
| | *kW* | | *g/kWh* | | | | |
| **Stage III A** | | | | | | | |
| H | 130 ≤ P ≤ 560 | 2006.01 | 3.5 | - | 4.0 | - | 0.2 |
| I | 75 ≤ P < 130 | 2007.01 | 5.0 | - | 4.0 | - | 0.3 |
| J | 37 ≤ P < 75 | 2008.01 | 5.0 | - | 4.7 | - | 0.4 |
| K | 19 ≤ P < 37 | 2007.01 | 5.5 | - | 7.5 | - | 0.6 |
| **Stage III B** | | | | | | | |
| L | 130 ≤ P ≤ 560 | 2011.01 | 3.5 | 0.19 | - | 2.0 | 0.025 |
| M | 75 ≤ P < 130 | 2012.01 | 5.0 | 0.19 | - | 3.3 | 0.025 |
| N | 56 ≤ P < 75 | 2012.01 | 5.0 | 0.19 | - | 3.3 | 0.025 |
| P | 37 ≤ P < 56 | 2013.01 | 5.0 | - | 4.7 | - | 0.025 |
| † Dates for constant speed engines are: 2011.01 for categories H, I and K; 2012.01 for category J. | | | | | | | |

The goal of adopting the Stage IIIB regulations was to force the use of Diesel Particulate Filters (DPF). Because of the technological development of engines, most new engines could comply with the new regulations without the utilization of a DPF.

**Table 7:** Stage IV Emission standards for European non road diesel engines (Dieselnet, sd)

| Cat. | Net Power | Date | CO | HC | NOx | PM |
|---|---|---|---|---|---|---|
| | *kW* | | *g/kWh* | | | |
| Q | 130 ≤ P ≤ 560 | 2014.01 | 3.5 | 0.19 | 0.4 | 0.025 |
| R | 56 ≤ P < 130 | 2014.10 | 5.0 | 0.19 | 0.4 | 0.025 |

The goal of the Stage IV emission standards was the reduction of $NO_x$ emissions. Complying with these new emission standards is mostly accomplished by using Urea-SCR. The Stage III/IV emissions standard are applicable to new equipment/engines.

### 2.1.5.3 Marine

The International Maritime Organization (IMO) is concerned with emission limits for ships. Their MARPOL Annex VI convention is the basis for most marine regulations worldwide. In Europe this is defined in the Stage limits. These limits are based on the Stage IIIA limits. There are no Stage IIIB or Stage IV limits for waterway vessels. The emission standards for inland waterway vessels are as shown as in Table 8. Testcycles are defined in ISO8178; (E2, E3 cycles for various types of propulsion engines, D2 for constant speed auxiliary engines, C1 for variable speed and load auxiliary engines).

At this moment, $CH_4$ emissions are not restricted directly. $CH_4$ emissions are indirectly restricted by the maximum allowed amount of HC emitted.

**Table 8:** Stage IIIA Emission Standards for Inland Waterway Vessels (Dieselnet, sd)

| Category | Displacement (D) | Date | CO | HC+NOx | PM |
|---|---|---|---|---|---|
| | *$dm^3$ per cylinder* | | *g/kWh* | | |
| V1:1 | D ≤ 0.9, P > 37 kW | 2007 | 5.0 | 7.5 | 0.40 |
| V1:2 | 0.9 < D ≤ 1.2 | | 5.0 | 7.2 | 0.30 |
| V1:3 | 1.2 < D ≤ 2.5 | | 5.0 | 7.2 | 0.20 |
| V1:4 | 2.5 < D ≤ 5 | 2009 | 5.0 | 7.2 | 0.20 |
| V2:1 | 5 < D ≤ 15 | | 5.0 | 7.8 | 0.27 |
| V2:2 | 15 < D ≤ 20, P ≤ 3300 kW | | 5.0 | 8.7 | 0.50 |
| V2:3 | 15 < D ≤ 20, P > 3300 kW | | 5.0 | 9.8 | 0.50 |
| V2:4 | 20 < D ≤ 25 | | 5.0 | 9.8 | 0.50 |
| V2:5 | 25 < D ≤ 30 | | 5.0 | 11.0 | 0.50 |

In Europe also the CCR (Centrale Commisie Rijnvaart) is active, which has as a goal to regulate emissions for European inland shipping. Limits are again based on (non-road) TIER (US regulation) values.

**Table 9:** CCR Regulations (Van der Burg, 2013)

| Vermogen (kW) | Uitstoot | CCR 1 2001-2007 | CCR 2 2007-2013 | CCR 3 2013-2016 | CCR 4 >2016 |
|---|---|---|---|---|---|
| 18-37 | PM (g/kWh) | | 0,8 | 0,45 | 0,025 |
| | NOx (g/kWh) | | 8 | 6 | 0,4 |
| | | | | | |
| 37-75 | PM (g/kWh) | 0,85 | 0,4 | 0,3 | 0,025 |
| | NOx (g/kWh) | 9,2 | 7 | 5 | 0,4 |
| | | | | | |
| 75-130 | PM (g/kWh) | 0,7 | 0,3 | 0,23 | 0,025 |
| | NOx (g/kWh) | 9,2 | 6 | 4 | 0,4 |
| | | | | | |
| >130 | PM (g/kWh) | 0,54 | 0,2 | 0,16 | 0,025 |
| | NOx (g/kWh) | 9,2 | 6 | 4 | 0,4 |

The most significant difference between Stage IIIA standards and CCR standards, is the distinction in categories. The Stage IIIA standards contains more categories to cover a wider spectrum of engines. Also, the categories from the Stage IIIA standards are based on the volume of the cylinder, while the categories from the CCR standards are based on power. It is noteworthy that the last category of the CCR standards contains every engine over 130kW, and that the focus lies completely on $NO_x$ and PM. CCR4 is postponed and will probably be adopted in 2020. At this moment, there are still a lot of CCR0 or CCR1 engines operating within inland shipping, because there are no adverse effects. There are rumors that, before 2025, it will not be allowed to operate CCR0 or CCR1 engine powered ships within the region of Rotterdam (Waarom zou ik investeren in een SCR-katalysator of roetfilter, 2014)

In 2014 the European Commission proposed a new set of standards for non-road engines, Stage V. The proposed limits are as shown as in Table 9. In this proposal, there has been made a distinction between propulsion engines and auxiliary engines. Also, the categories are defined based on the power of the engine, instead of the displacement per cylinder (current standards). Another important difference is the distinction between gas engines and diesel engines concerning HC emissions:

For engine categories where an A factor is defined, the HC limit for fully and partially gaseous-fueled engines indicated in the table is replaced by the one calculated from the formula:

HC = 0.19 + (1.5 × A × GER)

where GER is the average gas energy ratio over the appropriate cycle. Where both a steady-state and transient test cycle applies, the GER shall be determined from the hot-start transient test cycle. If the calculated limit for HC exceeds the value of 0.19 + A, the limit for HC should be set to 0.19 + A (Dieselnet, sd).

**Table 10:** Stage V proposal for Inland Water Vessels (Dieselnet, sd)

| Category | Net Power | Date | CO | HC[a] | NOx | PM | PN |
|---|---|---|---|---|---|---|---|
| | *kW* | | *g/kWh* | | | | *1/kWh* |
| Propulsion Engines—Category IWP | | | | | | | |
| IWP-v/c-1 | 37 ≤P < 75 | 2019 | 5.00 | 4.70[b] | | 0.30[b] | - |
| IWP-v/c-2 | 75 ≤ P < 130 | 2019 | 5.00 | 5.40[b] | | 0.14 | - |
| IWP-v/c-3 | 130 ≤ P < 300 | 2019 | 3.50 | 1.00 | 2.10 | 0.11 | - |
| IWP-v/c-4 | 300 ≤ P < 1000 | 2020 | 3.50 | 0.19 | 1.20 | 0.02 | $1\times10^{12}$ |
| IWP-v/c-5 | P ≥ 1000 | 2021 | 3.50 | 0.19 | 0.40 | 0.01 | $1\times10^{12}$ |
| Auxiliary Engines—Category IWA | | | | | | | |
| IWA-v/c-1 | 560 ≤ P < 1000 | 2020 | 3.50 | 0.19 | 1.20 | 0.02 | $1\times10^{12}$ |
| IWA-v/c-2 | P ≥ 1000 | 2021 | 3.50 | 0.19 | 0.40 | 0.01 | $1\times10^{12}$ |

[a] A = 6.00 for gas engines
[b] HC + NOx

There can be concluded that the maximum allowed amount of emitted pollutants is reduced over the years in every sector. Complying with these rules is done by developing engine improvements and developing after treatment systems. It is noteworthy that a vessel with an old engine can continue operating without complying with the new rules in Europe and this will not change within 10 years (The Blue World – Sustainable Inland Ships, 2015). In road transport, trucks with old engines can't enter some cities due to the amount of pollutants emitted, e.g. Amsterdam (Milieuzone vrachtauto's, 2016). The problem with ships is that an engine is used for more than 20 years. A sudden change in emission standards will not cause a quick improvement in the amount of emitted pollutants.

#### 2.1.5.4 Stationary machinery

In the Netherlands stationary machinery is regulated by the BEMS, “Besluit Emissie-eisen Middelgrote Stookinstallaties”. It aims at gas- and diesel-engines, turbines, and burners. For engines and turbines, it applies up till a thermal power of 50 MW.

**Table 11:** BEMS limits

| | $No_x$ | $SO_2$ | Dust (PM) | $C_xH_y$ (HC) |
|---|---|---|---|---|
| Power | [mg/Nm$^3$] | [mg/Nm$^3$] | [mg/Nm$^3$] | [mg/Nm$^3$] |
| >2.5MWth | 100 | 200 | | 1500 |
| Possible future limit 'rapport aanscherpingeisen' | | | | 1200 |
| <2.5MWth or >95% biomass | 340 | 200 | | |
| Possible future limit 'rapport aanscherpingeisen' | 140 | | | 1200 |
| Previous BEMS | $\frac{500 * \eta\_motor}{30}$ | | | |

Complication with BEMS limit values is the fact that they are given as maximum allowed mass of a component per volume of exhaust gas, mg/Nm$^3$. For other regulations the common unit is mass per energy delivery, g/kWh.

In Germany the TA-Luft (Technische Anleitung zur Reinhaltung der Luft) regulations apply. In the Netherlands it is sometimes advised by industry to apply this regulation instead of BEMS, to create more uniformity.

**Table 12:** TA Luft 2002 limits

| | $No_x$ | $SO_2$ | Dust (PM) | $C_xH_y$ (HC) | CO |
|---|---|---|---|---|---|
| | [mg/Nm$^3$] | [mg/Nm$^3$] | [mg/Nm$^3$] | [mg/Nm$^3$] | [mg/Nm$^3$] |
| SI biogas or SI lean burn | 500 | | no limit | | 650 |
| Other 4 stroke | 250 | | no limit | | 650 |

The European Union requires portable generator sets in the range from 18-560 KVA to meet Stage IIIA limits.

In the United States the emissions for stationary engines are regulated in National Standard for Hazardous Air Pollutants (NESHAP) and the New Source Performance Standards (NSPS). Gradually they are replaced by Tier limits, and since 2012 all engine categories should comply with non-road Tier limits.

#### 2.1.5.5 Overview of limit values

To get a clear overview of all regulations, the most important values are summarized.

For methane, multiple approaches can be recognized. Classically the HC emissions are regulated, as being a harmful gas. It consists of hydrocarbons in general, where in some rules

methane is explicitly excluded. For methane, two approaches can be recognized, either as harmful emission, or as greenhouse gas.

As greenhouse gas, methane's environmental impact is significantly higher than that of $CO_2$. For comparison the Greenhouse gas Warming Potential (GWP) is used, an indicator of how strongly a gas traps heat in the atmosphere. Looking at a period of 100 years, this factor is for methane 21 times higher than for $CO_2$. Figure 1 shows the greenhouse gas advantage of a gas engine compared to a diesel engine, dependent of methane slip and engine efficiency. Usually it is considered that a gas engine emitting 6g/kWh methane doesn't have a greenhouse gas advantage over a Diesel engine.

The actual regulations for methane emissions in various sectors can be found in Table 13.

**Table 13:** Overview methane emissions

| | Methane emissions | | |
|---|---|---|---|
| | g/kWh | Sector | Comment |
| Stage V proposal | 6,19 | Inland waterway vessels | Dual fuel @ 95% CNG |
| Euro 6 | 0,5 | On-road heavy duty | |
| BEMS | 5,41 | Stationary machinery | Currently only for >2,5MW th engines |
| BEMS | 4,33 | Stationary machinery | Expected future value |

In the graphs Figure 102 to Figure 106 in the appendix the limit values of NOx and Particle matter can be seen, including their historic development. A differentiation is made between engine output power below and above 560 kW, and cylinder volume between 1.2 and 2.5 liter, or between 2.5 and 5 liter. (most regulations differentiate on one of these aspects)

In general, it can be concluded that there are no big differences in values of the most stringent level for each legislation. The variation is mostly in the year of introduction.

For more details, the individual regulations, as already given in this chapter, should be consulted.

## 2.2 Literature study on catalytic methane oxidation (KIT)

### 2.2.1 Introduction

The total catalytic oxidation of methane to water and carbon dioxide is a long-studied topic and has been summarized in some review articles [1, 2]. Typically, a catalyst for exhaust-gas after-treatment consists of a support material providing a high surface area and a catalytically active component distributed thereon. Two different variants have been demonstrated as active systems. On the one hand, the combustion of methane can be catalyzed by noble metals, especially Pd and Pt. On the other hand, oxides of other transition metals such as nickel, cobalt, copper or manganese exhibit catalytic activity. However, non-noble metals exhibit a low specific catalytic activity. Especially under temperatures relevant for exhaust-gas after-treatment, insufficient $CH_4$ conversion is observed. Because of this, the literature study focuses on noble metal based catalysts.
Common to all active systems is a strong dependency on other parameters. In addition to the active metal itself, the activity of the catalyst is decisively influenced by the support material, the oxidation state of active species, the promoters, the catalysts synthesis, temperature, pressure and the gas composition.

### 2.2.2 Noble metal based catalysts

Besides studies on the catalytic combustion of methane on gold [3], which is however not stable enough, and rhodium as an active species, research is focused on platinum and especially palladium-containing catalysts. Methane is the most difficult molecule to oxidze in the exhaust gas and it has been generally confirmed that Pd-based catalysts exhibit the highest activity at low temperatures. Pd based systems have been intensively investigated in recent years which is illustrated in some review articles [4, 5]. Despite the many studies with palladium-based catalysts, many phenomena remain unexplained. When comparing experimental data from different publications, it is aggravating that the reaction conditions have a great impact on the results of the investigations. Substrate, gas composition, pretreatment, particle size, precursors in synthesis, etc. influence the activity of the system and make direct comparisons more difficult.

In general, it could be confirmed that the active form consists of oxidized palladium and the oxidation state of the palladium is the reason for a hysteresis behavior of the methane conversion during heating and cooling in the high temperature range. *Farrauto et al.* [6] showed by thermogravimetric measurements with a PdO/γ-$Al_2O_3$ catalyst already 1992 that PdO is reduced (in air) to thermodynamically more stable, metallic Pd at ~ 800°C. At the same time the methane conversion drops. During cooling, the reoxidation is only observed at about 600°C, which is accompanied by an increase in methane conversion. *Grunwaldt et al.* [7] reported similar behavior for a Pd/$ZrO_2$ catalyst synthesized by flame spray pyrolysis. Using different *in-operando* characterization methods (XAS, X-ray Absorption Spectroscopy and XRD, X-ray Diffraction), the change of Pd oxidation state simultaneously to the activity was monitored. It was found that the initially oxidized catalyst loses its activity at about 720°C while at the same time the PdO gets reduced to metallic Pd. In addition, sintering of the particles occurs during the reduction. During cooling, the reoxidation of the Pd shifts to lower temperatures (< 600°C) and the methane conversion increases again. *Datye et al.* [8] concluded from transmission electron microscopy (TEM), x-ray diffraction (XRD) and x-ray photo electron spectroscopy (XPS) measurements during reduction and reoxidation of a Pd/θ-$Al_2O_3$ catalyst the formation of an amorphous PdO layer during the cooling phase. This is responsible for the shift of reoxidation temperature. Furthermore, a dependence of the reduction temperature and reoxidation temperature on the carrier material could be found [9]. *Colussi et al.* [10] showed that the addition of 10% $CeO_2$ to a Pd/γ-$Al_2O_3$ catalyst promotes reoxidation of the Pd at high temperatures. This applies to particles which are in contact with the $CeO_2$.

Despite the many studies which report to a higher activity of PdO compared to metallic $Pd^0$, *Ciuparu et al.* [11] proposed that a slightly reduced catalyst has higher activity than a fully oxidized one. This was investigated by pulse experiments on Pd/$Al_2O_3$. It was also found [12, 13] that previously reduced catalysts based on palladium show a higher activity under lean reaction conditions depending on the reduction temperature. However, this is supposed to not be caused by the presence of metallic palladium, but by altered properties of the palladium oxide phase after reoxidation under reaction conditions.

As reaction mechanism for total oxidation of methane on PdO, at least in part, a Mars van-Krevelen mechanism [14] is assumed. *Ciuparu et al.* and *Au-Yeung et al.* [15, 16] showed by means experiments with isotopically labeled gases on a PdO/$ZrO_2$ catalysts that $CO_2$ is mainly formed from lattice oxygen of the catalyst. This corresponds to a redox mechanism which the Mars van Krevelen mechanism is [14]. *Müller et al.* [12] investigated the distribution of the oxidation products by mass spectrometry using a PdO/$ZrO_2$ catalyst pre-oxidized by isotopically labeled oxygen ($^{18}O$). They were less clear about the presence of a redox mechanism than *Ciuparu et al.* and *Au-Yeung et al.*. In pulse experiments with 1% $CH_4$. 4% $^{16}O_2$ in helium, 20% of labeled $CO_2$ were found in the gas stream as well as small amounts of labeled $H_2O$. It was concluded that the formation of water can be explained by a normal surface reaction with

oxygen from the gas phase. Furthermore, they discuss that the formation of isotopically labeled $CO_2$ could also have arisen from exchange processes between $CO_2$ already formed by normal surface reactions (Langmuir-Hinshelwood or Eley-Rideal) and the $^{18}O$ of the catalyst. For low temperatures, this exchange is less likely than for higher temperatures. Therefore, *Müller et al.* concluded that the redox mechanism must play a major part during methane oxidation on Pd.

In connection with the reactivity of the lattice oxygen, there is also a postulated particle size dependence of the reaction. Müller et al. [12] showed that the reaction rate per specific palladium site (turnover frequency, TOF) increases for larger particles. However, as the particle size increases, the specific PdO surface (dispersion) decreases. $PdO/ZrO_2$ catalysts were investigated, where reduction steps at different temperatures lead to PdO particles differing in size. Activity measurements with 1% $CH_4$ and 4% $O_2$ in He revealed that large particles of PdO (~ 13 nm) are more active than small particles (~ 5 nm). This was attributed to a smaller influence of the support for large particles. *Stakheev et al.* [17] reported similar results on a $Pd/Al_2O_3$ catalyst. Furthermore, for a $Pt/Al_2O_3$ catalyst, only a small improvement of the TOF with growth of particles from 1 nm to 3 nm was observed. Further increase in particle size does not lead to a change in activity, which corresponds to a structural insensitivity on Pt. For PdO particles, however, the TOF was improved by an order of magnitude as the particle diameter increased from 1 to 20 nm. This effect is attributed to a minimized Pd-O bond strength in larger particles, since there is relatively little interaction with the support. The reduced Pd-O binding strength favors the catalytic activity of the PdO by increased oxygen mobility in the Mars-van-Krevelen mechanism. *Castellazzi et al.* [18] were able to make similar observations on a $Pd/Al_2O_3$ catalyst. They correlated the lower TOF on small particles to a higher resistance towards reduction by performing Temperature-Programmed-Reduction (TPR) experiments and Raman spectroscopy. However, considering the overall activity of the system, the dispersion of the noble metals also plays a significant role. Even more small particles with lower specific activity can still achieve a higher overall conversion.

The catalytic oxidation of methane to carbon dioxide and water is also dependent on the gas composition. Particularly of interest are gases, which are typically contained in the exhaust-gas of combustion engines. Water vapor for example has a big influence on Pd based catalysts. Numerous studies have shown that water has a negative effect on the activity and at the same time causes deactivation. Since the catalytic combustion itself produces water as a reaction product, an inhibitory effect can also be seen in a dry gas stream.

In literature it is discussed, that the formation of hydroxyls is responsible for the inhibition. Based on thermodynamic calculation *Cullis et al.* [19] suggested in the formation of $Pd(OH)_2$ in presence of water leading to a blockage of the active sites. Ciuparu et al. [20] were able to detect adsorbed hydroxyls by means of DRIFTS measurements (diffuse reflectance infrared fourier transform spectroscopy) on a $PdO/Al_2O_3$ catalyst. These block the active sites and make a reoxidation to PdO difficult. It has also been found that hydroxyls formed by the reaction of methane are much more likely to stick on the surface than hydroxyls formed by the adsorption of water vapor from the gas phase. Furthermore, the extent of the inhibiting effect of water on the support material could be determined. The greater the oxygen mobility on the surface of the carrier material, the more resistant the catalyst is to the influence of water. This suggests that hydroxides on the surface are responsible for a lower oxygen exchange between noble metal and carrier and thus the activity is adversely affected. Experiments done by *Schwartz et al.* [21] support this theory. *Escandon et al.* [22] found a partial reversibility of the inhibitory effect of water on a $Pd/CeO_2$-$ZrO_2$ catalyst. Catalysts were tested both in the presence of external water and under dry reaction conditions at 550°C over longer time. Both catalysts lost activity, the decrease being enhanced in the presence of water. After 15h, the water was removed or added respectively. An improvement in the activity of the catalyst, which had previously been used under a water containing atmosphere, to a value corresponding to that in a dry atmosphere, was found. The catalyst, to which water was added, showed a stronger activity decrease than before. An improvement in activity could thus be achieved by removing the water in the reaction stream, but the initially high conversion rate was never achieved.

Surprisingly, the presence of nitric oxides was found to improve the long-term activity of Pd based catalysts recently [23]. The decomposition of inhibiting OH-groups on the surface by formation of HNO in presence of $NO_x$ were discussed to provoke this positive effect [24].

In addition to water, other gaseous components may also influence the activity of the catalyst. Sulfur compounds, some of which can occur to a considerable extent in natural gas, lead to the poisoning of the catalyst and drastically reduce its activity. The reason is, among other things, the formation of sulfates and/or sulfites with the catalytically active component. PdO as well as Pt is capable of oxidizing $SO_2$ to $SO_3$ under lean conditions [25]. $SO_3$ adsorbs strongly on the PdO surface and formation of $Pd(SO_4)$ occurs. *Mowery et al.* were able to confirm this by XPS measurements [26]. Carrier materials, which themselves can form sulfates, for example $Al_2O_3$, influence the poisoning process. This support acts as a scavenger, in which it itself forms sulfates. They therefore retard to a certain degree the deactivation of the catalyst. *Yu and Shaw* [27] found a reduction of the specific surface area on a $Pd/\gamma\text{-}Al_2O_3$ catalyst in addition to the direct poisoning of the active Pd centers. This has been attributed to the formation of aluminum sulfates hindering the diffusion processes inside the porous washcoat. In the presence of sulfur (in form as $SO_2$, $SO_3$, or $H_2S$) in the exhaust-gas stream, the long-term activity of Pd based catalysts is completely dominated by this. Fast deactivation occurs at relevant temperatures of 350°C to 450°C [23]. Attempts were made to improve the sulfur tolerance. *Guliaeff et al.* [28] showed that Pd and Pt, which were fixed in a zeolite structure using an unspecified method, showed a markedly resistance to sulfur poisoning. Even after 125 hours under 100ppm of $SO_2$, 250 ppm $C_3H_8$ and 5% $H_2O$ in air (500°C.), the catalyst showed only a conversion drop of 30%. However,

From these studies on the basic properties and mechanisms of methane oxidation on Pd catalysts, one can see how complex and sensitive the reaction is. Many publications deal with the attempt to influence the catalysts behavior by addition of promotors such as lanthanides (La, Ce) and transition metals (V, Cr, Mn), by choice or modification of the support material (zeolites, ZrO2, TiO2 etc.) or by specific preparation methods (flame spray, sol-gel, etc.) For example, *Cargnello et al.* [29] synthesized nanostructured $Pd\text{-}CeO_2$ particles, which were deposited on $Al_2O_3$. The active particles form a core-shell structure. Small Pd particles (about 2 nm) are surrounded by a shell of crystalline $CeO_2$. This catalyst exhibited extremely high activity at low temperatures and could maintain a high conversion up to very high temperature ranges of 850°C. Several factors are given as an explanation for the outstanding positive effects of the $CeO_2$ shell. Because of their small size, it is likely that the $CeO_2$ is under mechanical stress, which could increase oxygen mobility. Furthermore, it is speculated that the small crystal size of the $CeO_2$ causes some defects and thus a higher degree of reduction is possible. It is thus shown that the active species palladium can be influenced in its properties by selective interaction with further constituents. Open in this publication remains the resistance towards factors such as presence of water or sulfur and how long the catalyst can maintain its high activity.

Although the former discussed core-shell bimetallic catalysts shows interesting properties, further work needs to be done to understand and apply such systems. Under realistic conditions, bimetallic Pd-Pt system have proven to be the best choice for methane oxidation. By the addition of platinum, palladium catalysts can have a higher activity at low temperatures on the one hand [30] and on the other hand, the resistance towards aging is strengthened. *Narui et al.* [31] showed on a $PtPd/\alpha\text{-}Al_2O_3$ catalyst with a molar ratio of Pt to Pd of 0.2 and a $Pd/\alpha Al_2O_3$ catalyst that the bimetallic catalyst provides a higher methane conversion at 350°C. The activity was also maintained over longer time than on the Pd only sample. TEM measurements have shown that the addition of Pt leads to a considerably lower sintering of noble metal particles under reaction conditions. *Strobel et al.* [32] also observed this positive effect of small amounts of Pt (4% by weight) on sintering phenomena at high temperatures. Furthermore, thermogravimetric measurements have shown that Pt additions lead to an increased readiness to reduce the PdO to metallic $Pd^0$ at a lower temperature. *Ersson et al.* [33] confirmed this behavior by Temperature-Programmed-Oxidation (TPO) measurements.

To summarize, the total oxidation of methane on PGM based catalysts is a multi-faceted reaction. Although investigated for long time, fundamental steps of the reaction are still under debate. During application under gas engine conditions the influencing parameter even increase. The presence of inhibiting and poisoning species have a strong impact on the catalyst activity and stability. Knowledge-based optimization of the catalyst is needed to face the challenges in real application and to ensure the fulfilment of legislative standards.

# 3 Overview and Principles on Characterization Techniques and Modeling (KIT)

## 3.1 $N_2$ Physisorption

$N_2$ physisorption is a frequently used standard technique to obtain the specific surface and pore volume of materials. The gas, called the adsorptive, is thereby adsorbed on the surface of a solid material (adsorbent) via the rather weak van-der-Waals interaction. As the size ratio of a single gas is known, the specific surface area of the adsorbent can be calculated by taking the amount of adsorbed gas of one monolayer into account.

Experimentally, nitrogen is dosed into an evacuated test tube at a temperature of about -196 °C (which is close to the boiling point of nitrogen) and the resulting pressure is monitored. By plotting the volume of gas added versus relative pressure and short reductions of the pressure, so-called adsorption-desorption-isotherms are obtained. Their curve progression allows furthermore conclusions on the materials pores, mesoporous substances (2 - 50 mm diameter), for instance, show a clear hysteresis due to multilayer adsorption in the pores.

Usually not only mono- but also multilayer adsorption occurs which can be taken into account using the so-called BET-model, named after its developers Brunauer, Emmet and Teller, the specific surface can be calculated from adsorption-desorption-isotherm [34].

$$\frac{\frac{p}{p_0}}{n_{ads}\frac{1-p}{p_0}} = \frac{1}{n_m C} + \frac{C-1}{n_m C}\cdot\frac{p}{p_0} \qquad 3.1$$

- $p$ equilibrium pressure of adsorbate
- $p_0$ saturation pressure of adsorbate
- $n_{ads}$ adsorbed gas quantity
- $n_m$ monolayer adsorbed gas quantity
- $C$ BET constant

Assuming cylindrical pores the average pore volume can be described by the Barrett-Joyner-Halenda model (BJH), which uses the effect of pore condensation to obtain the pore volume from the desorption-isotherm.

## 3.2 CO Chemisorption

Chemisorption measurements are applied to obtain the catalytic surface of a catalyst by directly measuring the number of surface atoms by means of adsorbed gas. In the exhaust gas oxidation catalysis the active sites are mostly metal atoms, forming small particles on a support material. Knowing the dispersion (D), given by formula (3.2) and defined as the ratio of the number of metal atoms present on the particles surface ($N_{surface}$) and the total number of metal atoms on the surface and in the bulk ($N_{total}$), offers valuable clues to the distribution of catalytic active metal on the support material.

$$D = \frac{N_{surface}}{N_{total}} \qquad 3.2$$

To determine the dispersion, the sample is exposed to molecules that can chemisorb selectively on the active metal sites, which saturate the metal surface by forming a single layer. Typical probe molecules used for determining the dispersion of noble metal based catalysts are for example carbon monoxide (CO) hydrogen ($H_2$),. If the stoichiometry of adsorption is known, the catalytically active surface can be calculated from the amount of molecules adsorbed. Different stoichiometry

is possible due to various adsorption geometries, e.g. linear (1:1), or bridged (2:1). This is influenced by the noble metal itself as well as by particle size, temperature or pressure [35]

Substances like $CeO_2$, for instance, can adsorb/react with probe molecules like CO as well, resulting in a higher number of adsorbed probe molecules and therefore an overestimation of dispersion values. This effect can be suppressed by either masking the support with $CO_2$ [36] or by performing CO-adsorption at very low temperature (- 78 °C) [37], leading to a selective adsorption of CO only on the (noble) metal surface.

## 3.3 X-Ray Diffraction

X-ray diffraction is used to identify and characterize crystalline phases, which cause X-rays to scatter into various directions. As the distances in a crystal lattice have the same range ($10^{-10}$ m) like the wavelength of X-rays, a three-dimensional lattice acts as a diffraction grating. The angles and intensities of the diffracted beams can be measured, resulting in a diffraction pattern characteristic for a substance. Therefore, the composition of a material can be analyzed by means of XRD-measurements.

Monochromatic X-rays striking the atomic lattice are diffracted and depending whether the waves are in phase there is constructive interference or destructive interference. Bragg's law connects the scattering angle $\Theta$ and the interplanar distance $d$ between two planes with the condition for constructive interference: Only if the wavelength of the X-rays is an integer multiple of the path difference between two waves there is constructive interference.

$$n \cdot \lambda = 2d \sin \Theta \tag{3.3}$$

| | |
|---|---|
| n | integer |
| λ | wavelength of X-rays |
| d | interplanar distance |
| Θ | scattering angle |

Position, intensity and shape of the detected reflexes contain further valuable information. Line broadening, for instance, can be used to determine crystallite sizes. In general, the broader the reflex, the smaller the crystallite size. Thereby the average grain size can be estimated by means of the Scherrer equation (3.4).

$$L = \frac{K\lambda}{B(2\Theta)\cos\Theta} \tag{3.4}$$

| | |
|---|---|
| L | average grain size |
| K | Scherrer constant |
| λ | wavelength of X-rays |
| B(2Θ) | full width at half maximum (FWHM) |
| Θ | scattering angle |

## 3.4 Electron Microscopy

Both, electron microscopy and light microscopy, focus on visualizing the catalyst, however the resolution by using electrons instead of photons is increased significantly as electrons have a much shorter wavelength. By means of electron microscopy investigations on a catalyst's morphology are possible, even resolving samples on an atomic scale, allowing an evaluation of the distribution

of noble metals on the support material, for instance. This complements chemisorption measurements by adding extensive knowledge on the size, shape and distribution of particles. Using electrons that are absorbed in case of collision with gas molecules makes it imperative to perform measurements under vacuum conditions.

In an electron microscope, electrons emitted by a cathode are accelerated by an anode and focused by several magnetic lenses. Wavelength can be tuned by modulation of acceleration voltage, as the kinetic energy of an electron is connected to its wavelength by the De-Broglie-equation (3.5).

$$\lambda = \frac{h}{m \cdot v} \tag{3.5}$$

λ wavelength

h Planck constant

m particle mass

v velocity

The electrons are then detected e.g. with a phosphor screen or CCDs (charge-coupled device). In case of using transmission electron microscopy (TEM), the samples have to be very thin, usually less than 100 nm, to allow the electrons to pass. The most common operational mode is bright field (BF) imaging, where thick areas appear dark in the obtained picture due to electron absorption whereas thin areas appear bright. Besides operation is possible in the dark-field mode, where the main beam is avoided and only scattered electrons are detected. A special form of electron microscopy is the scanning transmission electron microscopy (STEM), using a strongly focused electron beam to scan the sample. In this process, every pixel correlates to one point on the sample.

Furthermore, elemental analysis is possible by using the electron beam for energy dispersive X-ray spectroscopy (EDX). This technique uses the interaction between an electron beam of well-defined energy and atoms of the sample leading to the emission of characteristic X-ray radiation specific for an element. Detection of the X-rays allows the analysis of bimetallic catalyst samples, for instance, to investigate possible alloy formation.

## 3.5 X-Ray Absorption Spectroscopy

X-ray absorption spectroscopy (XAS) is based on the fact that electromagnetic radiation and matter can interact. Accelerated charged particles emit electromagnetic radiation radially, the so-called synchrotron radiation, covering the spectrum from microwaves to hard X-rays. Depending on the experiment, the wavelength can be tuned. To determine the local geometry and structure of a sample X-rays are used, which can excite core electrons due to absorption. Besides *ex situ* measurements, *in situ* investigation of catalysts under reaction conditions is possible as well, as X-rays penetrate gases in contrast to electrons. Several essential structural information can be extracted by collecting an X-Ray absorption spectra (XAS): (i) by analyzing the X-ray Absorption Near Edge Structure (XANES) the coordination environment and valence state of an atom can be obtained, e.g. determining its oxidation state by applying linear combination analysis; (ii) the Extended X-ray Absorption Fine Structure (EXAFS) of the spectra is used to derive bond distances in chemical compounds and number of neighboring atoms, which are useful to approximate the size of supported noble metal particles. XAS spectra are typically collected by detecting the transmitted X-ray intensity ($I_{transmitted}$) in relation to the incident ($I_0$), using Lambert Beer's law. Taking the absorption coefficient μ and the thickness of the sample d into account, this process can be described by equation (3.6).

$$I_{transmitted} = I_0 \cdot e^{-\mu d} \tag{3.6}$$

$I_{transmitted}$ transmitted X-ray intensity

$I_0$ incident X-ray intensity

μ absorption constant

d sample thickness

Alternatively, the characteristic fluorescent X-rays can be recorded which result due to refilling of core hole created by X-ray absorption. In this case solid state detectors (silicon or germanium) usually placed perpendicularly (to prevent detection of the elastic scattered photons) to the incoming beam are employed. This detection mode is especially applied for samples containing highly absorbing components and for a low concentration of a specific element.

## 3.6 Infrared Spectroscopy

Not only X-rays can interact with materials, radiation in the wavelength range of 800 nm to 1 mm does it as well. If the so-called infrared radiation hits a gas molecule or lattice bonds, a certain amount of radiation is absorbed due to excited vibrational and rotational transitions of the molecule. As the absorbed frequencies are characteristic for a specific molecule, qualitative analysis is possible. Furthermore, a precise quantification of species can be achieved by detecting the decrease of radiations intensity, especially if the measurement is done by transmission. Lambert-Beer's-law, given by formula (3.7), describes the absorption, for instance.

$$E_\lambda = \log\left(\frac{I_0}{I_1}\right) = \epsilon_\lambda \cdot c \cdot d \tag{3.7}$$

$E_\lambda$ Absorbance

$I_0$ incident intensity

$I_1$ transmitted intensity

$\varepsilon_\lambda$ molar attenuation coefficient

c concentration

d sample thickness

In case of strongly scattering or absorbing samples, the diffusive reflectance of the investigated material can be measured, which is called Diffusive Reflectance Infrared Fourier Transform Spectroscopy (DRIFTS). While a part of the infrared radiation is reflected on the surface, a certain amount of radiation enters the sample and leaves again after several times of scattering. Detection of the intensity and measurement of the spectral reflectance of the scattered infrared beam gives information on nature and also amount of surface species.

## 3.7 Raman Spectroscopy

Again, the interaction between light and matter is utilized for material characterization. For Raman spectroscopy usually a high intensity laser with the wavelength of visible light is used to irradiate the sample. This leads to molecular vibrations or rotations resulting in a scattering of the laser radiation, which can be scattered either elastic (Rayleigh-scattering) or inelastic (Raman-scattering, named after its discoverer C.V. Raman). While the elastically scattered photons have the same energy as the incident ones, a very small amount of scattered photons changes its frequency due to excitation of molecules as mentioned above. Thereby a change of the molecular polarizability is imperative. Then, the vibrational modes of the molecule can be excited. If the emitted photon has a higher energy than the absorbed one, the material released energy resulting in so-called anti-

Stokes Raman scattering. The other way round, the material absorbing energy and emitting a photon with lower energy than the initial one, the process is called Stokes scattering. By plotting the "intensity of the scattered light as a function of its frequency difference to the incident photons, a Raman spectrum is obtained in which Rayleigh-, Stokes- and anti-Stokes scattering is visible in terms of absorption bands.

## 3.8 Thermogravimetric Analysis

Changes of physical and chemical properties of materials (e.g. mass, structure, composition) induced by a controlled change of temperature are relevant in heterogeneous catalysis since often the catalytic process involves temperature variations. Thus, phenomena such as phase transitions, decomposition, chemisorption of gaseous molecules or solid state reactions might occur during the catalytic process. In our days, monitoring of mass variation, temperature or heat flow (reaction exothermicity / endothermicity) and evolved gases is carried out by using several coupled methods (thermogravimetry, differential scanning calorimetry, mass spectrometry etc.) within a simultaneous thermal analysis (STA) setup. Typically a sample is heated continuously while weighting its mass. With increasing temperature the sample can change which can be followed by detecting the mass loss/increase or heat flow variations. This procedure can be coupled with analysis of evolved gases by means of a mass spectrometer or FTIR, which makes it even clearer what kind of species are formed during the experiment. By varying the gas composition during a heating/cooling cycle, e.g. reductive or oxidative treatment, valuable information about the behavior of catalysts under different reaction conditions can be are obtained.

## 3.9 Fundamentals of Modeling

A profound understanding and optimization of systems based on heterogeneous catalysts requires the knowledge of the physical and chemical processes on a molecular level. In particular, at short contact times and high temperatures, at which reactions occur on the catalyst and in the gas-phase, the interactions between transport and chemistry become important.

The transport of momentum, energy, and chemical species inside a channel of a monolith can occur not only in axial but also in radial direction and have to be distinguished and evaluated individually. While the reactive mixture diffuses to the inner channel wall and the porous washcoat layer, gaseous species adsorb and react on the catalytic surface. The products desorb and diffuse back into the bulk flux. Diffusion processes in the washcoat layer, limiting the overall catalytic activity of the surface, superimpose transport of mass in the fluid phase. Furthermore, when temperature is high, chemical species can react homogeneously in the gas-phase [38].

Monolithic honeycomb reactors exhibit a number of advantageous properties and have therefore become particularly attractive for exhaust-gas after-treatment. Some of the advantages are low pressure drop under high fluid throughputs leading to an energy-efficient operation, short diffusion path in the catalyst and high external surface area [39].

## 3.10 Reaction kinetics

A global chemical reaction (for example $CH_4 + O_2 \rightarrow CO_2 + H_2O$) can be described by a series of elementary steps that lead to transformations of one species to another by re-arrangement or exchange of individual atoms. In contrast to global reactions, an elementary reaction describes the process how it occurs on a molecular level. In many catalytic reactors, the reactions do not exclusively occur on the catalyst surface but also in the fluid flow, depending on the operation temperature and pressure. Therefore, reactor simulations often need to include an appropriate model for

the homogeneous kinetics along with the heterogeneous reaction models [40]. A chemical reaction can be generally written as:

$$\sum_i \nu'_{ik} A_i \rightarrow \sum_i \nu''_{ik} A_i \qquad 3.1$$

with $\nu'_{ik}$,$\nu''_{ik}$ being the stoichiometric coefficients for species of reactant or product $A_i$. The rate of formation or consumption of a species in a chemical reaction is called reaction rate. For the species, the rate equation can be expressed as

$$\frac{dc_i}{dt} = (\nu''_{ik} - \nu'_{ik})k \prod_i c_i^{a'_{ik}} \qquad 3.2$$

In this equation, $c_i$ is the concentration (mol/m³) of species $i$, $k$ is the reaction rate coefficient and $a'_{ik}$ is the reaction order with respect to species $i$ .
The rate coefficient of reactions can be expressed by the Arrhenius equation:

$$k = A_k T^{\beta_k} exp\left[\frac{-E_a}{RT}\right] \qquad 3.3$$

Here, $A_k$ is the pre-exponential factor, $\beta_k$ is the temperature exponent and $-\mathrm{E_a}$ is the activation energy. For surface reactions, pressure has no direct effect on the rate coefficients, whereas for gas phase reactions, a pressure dependency of the rate coefficient can occur for dissociation and recombination reactions [40].

### 3.11 Reactive flow field

Mathematical modeling of chemically reacting flow in a tubular channel can be performed in 2D at steady-steady conditions based on the solution of Navier-Stokes equations in cylindrical coordinates for axisymmetric flow field in radial and axial coordinates. For the general description of a single monolithic channel, the Navier-Stokes equations are given as [41]:

Conservation of total mass:

$$\frac{\partial(\rho u)}{\partial z} + \frac{1}{r}\frac{\partial(r\rho v)}{\partial r} = 0 \qquad 3.4$$

Conservation of axial momentum:

$$\rho\left(u\frac{\partial u}{\partial z} + v\frac{\partial u}{\partial r}\right) = -\frac{\partial p}{\partial z} + \frac{\partial}{\partial z}\left[2\mu\frac{\partial u}{\partial z} - \frac{2}{3}\mu\left(\frac{\partial u}{\partial z} + \frac{1}{r}\frac{\partial rv}{\partial r}\right)\right] + \frac{1}{r}\frac{\partial}{\partial r}\left[\mu r\left(\frac{\partial v}{\partial z} + \frac{\partial u}{\partial r}\right)\right] \qquad 3.5$$

Conservation of radial momentum:

$$\rho\left(u\frac{\partial v}{\partial z}+v\frac{\partial v}{\partial r}\right) = -\frac{\partial p}{\partial r}+\frac{\partial}{\partial z}\left[\mu\left(\frac{\partial v}{\partial z}+\frac{\partial u}{\partial r}\right)\right]+\frac{\partial}{\partial z}\left[2\mu\frac{\partial v}{\partial r}-\frac{2}{3}\mu\left(\frac{\partial u}{\partial z}+\frac{1}{r}\frac{\partial rv}{\partial r}\right)\right] + \frac{2\mu}{r}\left[\left(\frac{\partial v}{\partial r}-\frac{v}{r}\right)\right] \quad 3.6$$

Conservation of species:

$$\rho u\frac{\partial Y_i}{\partial z}+\rho v\frac{\partial Y_i}{\partial r}=-\frac{\partial j_{i,z}}{\partial z}+\frac{1}{r}\frac{\partial(rj_{i,r})}{\partial r}+R_i \quad 3.7$$

Conservation of energy:

$$\rho\rho c_p\left(u\frac{\partial T}{\partial z}+v\frac{\partial T}{\partial r}\right) = u\left(\frac{\partial p}{\partial z}+v\frac{\partial p}{\partial r}\right)+\frac{\partial}{\partial z}\left(\lambda\frac{\partial T}{\partial z}\right)+\frac{\partial}{\partial r}\left(r\lambda\frac{\partial T}{\partial r}\right) - \sum_{i=1}^{K}c_{pi}\left(j_{i,z}\frac{\partial T}{\partial z}+j_{i,r}\frac{\partial T}{\partial r}\right)-\sum_{i=1}^{K}h_iR_i \quad 3.8$$

In these equations, $r$ and $z$ are the independent variables in radial and axial coordinates respectively. The dependent variables are, $u$ axial velocity , $v$ radial velocity , $Y_i$ species mass fractions , $T$ temperature and$pp$ pressure . The other variables are, $\rho$ density, $\mu$ viscosity, $\lambda$ thermal conductivity, $h_i$ species enthalpy and $c_p$ specific heat . In species continuity thermal energy equations, the diffusive mass flux term appears as $j_i$. The term $R_i$ represents the mass of *i* produced by the gas phase reactions. The equations are expressed in steady-state conditions, while gravitational forces and mass sources are neglected.

### 3.11.1 Coupling of Chemical Reactions with the Flow-field

The chemical processes at the surface are coupled with the surrounding flow-field by balance equations at the gas-surface interface. Surface reactions are now considered as a boundary condition in the conservation of species mass equation. Since the production rates of species on the catalytic surface are dependent on adsorption and desorption rates and, therefore, dependent on the gaseous fluid phase, the mass transport of these has to be considered. In dependence of boundary conditions, such as temperature, pressure, and species concentrations, the net reaction rates of homogeneous gas-phase and heterogeneous surface reactions become dependent on the mass transport of species *i* and are, therefore, determined by mass balances, considering diffusive and convective mass transport terms. To get a detailed description of the reactor with axial resolution in species concentration, the equations for flow field description are coupled with the reaction rates of the occurring chemical reactions on an elementary level. In most catalysts, washcoats are

applied on the catalyst support to enlarge the available surface area. The washcoat thickness varies from 10 to 200 µm and can exhibit a non-uniform distribution on the support, for instance in small channels, where the edges of a channel have thicker washcoat layers than the center of a channel wall for reasons of cohesiveness. Mass transport limitation in a porous structure lead to concentration profiles in the structure and, hence, to reaction rates which vary with position. For a description of the washcoat´s properties the detailed washcoat model is introduced. The detailed washcoat model solves the reaction-diffusion equations in radial direction for every species *i* within the washcoat. The species gradients in the washcoat affect the local surface reaction rates $s_i$. Assuming that the axial concentration gradients are considerably lower compared to the radial gradients leads to the one-dimensional discretization of the washcoat model. Therefore, the reaction–diffusion equation can be calculated with the following expression [42]:

$$\frac{\partial j}{\partial r} - \gamma \dot{s} = 0 \tag{3.9}$$

where the radial diffusion flux of species *i* is calculated by

$$j_i = -D_{\mathrm{eff},i} \frac{\partial c_i}{\partial r} \tag{3.10}$$

Here $D_{eff,i}$ is the effective diffusion coefficient of species *i*, for which the definition depends on the pore size distribution of the washcoat.

The effective diffusion coefficient ($D_{\mathrm{eff},i}$ ) can be calculated by taking into account the Knudsen diffusion coefficient ($D_{\mathrm{knud},i}$ ) and the molecular diffusion coefficient ($D_{\mathrm{mol},i}$ ) of the Species *i* in the mixture (Eq. 3.11).

$$\frac{1}{D_{\mathrm{eff},i}} = \frac{\tau}{\varepsilon}\left(\frac{1}{D_{\mathrm{mol},i}} + \frac{1}{D_{\mathrm{Knud},i}}\right) \tag{3.11}$$

The empirical variable tortuosity $\tau$ represents the deviation of the washcoat pores from the ideal cylinder. The Knudsen diffusion coefficient for the *i*th species is given by Eq. 3.12:

$$D_{K\mathrm{nud},i} = \frac{d_p}{3}\sqrt{\frac{8RT}{\pi M_i}} \tag{3.12}$$

### 3.12 DETCHEM Code

DETCHEM (DETailed CHEMistry) is a software package written in Fortran used to calculate detailed descriptions of physical and chemical processes of a reactive systems by coupling transport and chemistry.. DETCHEM core library provides subroutines for the calculation of reaction rates and transport coefficients, i.e., binary diffusion coefficients, thermal conductivity, viscosity for each species and bulk phase. In addition to the library, many DETCHEM applications are available that implement specific reactor and flow configurations. The names of the applications refer to the flow configuration or the reactor type modeled, such as DETCHEM$^{\mathrm{PLUG}}$ for the 1D solution of continuous-flow reactor applications and DETCHEM$^{\mathrm{CHANNEL}}$ for 2D solution of reactive flows in a single channel of the monolithic catalyst. Furthermore entire monolith can be modeled in 2D or 3D by using

DETCHEM$^{MONOLITH}$ (Figure 10). Detailed information about the entire DETCHEM package is given in the manual [43].
Among various computational tools of DETCHEM software package, DETCHEM$^{BATCH}$, DETCHEM$^{PLUG}$ and DETCHEM$^{CHANNEL}$ are used in this work.

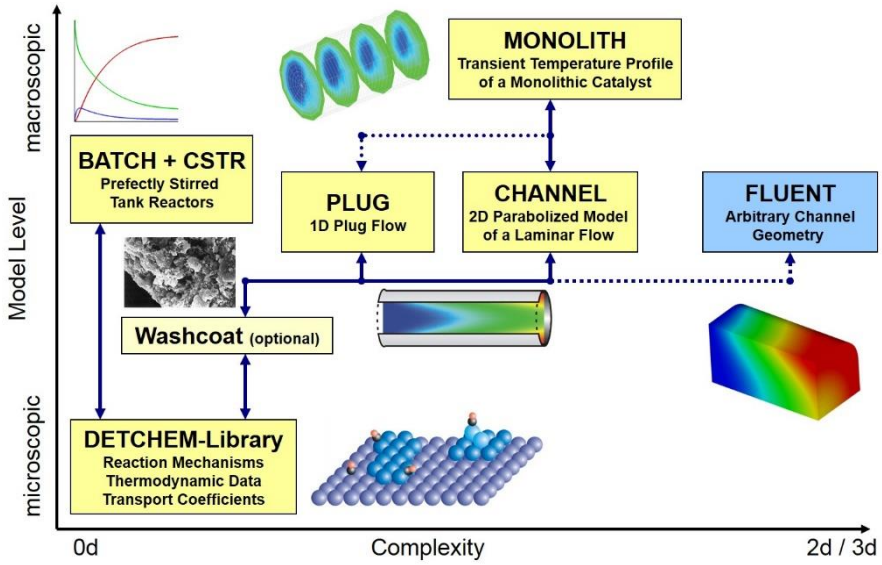


**Figure 10:** Structure of the DETCHEM software package [43].

### 3.12.1 DETCHEM$^{BATCH}$

The batch code simulates homogeneous gas phase and heterogeneous surface reactions in a batch reactor. The simulation of gas phase reactions relevant to pre-turbo placement were calculated using DETCHM$^{BATCH}$ code. The governing equations for description of a batch reactor are as follows:

Mass conservation:

$$\frac{dn_i}{dt} = VR_i + A\dot{s}_i \qquad 3.13$$

$$\frac{dn_i}{dt} = \alpha A\dot{s}_i \qquad 3.14$$

Equation of state:

$$PV = nRT \qquad 3.15$$

In the above equations $R_i$, $\dot{s}_i$, $A$, $V$, $\alpha$ represent the gas phase reaction rate, surface reaction rate, catalytic surface area, reactor volume, and surface relaxation factor respectively. The amount of species i $n_i$ are expressed in terms of mole numbers.

### 3.12.2 DETCHEM$^{PLUG}$

The plug code simulates the behavior of plug flow chemical reactors. The code is designed for the nondispersive one dimensional flow of chemically reacting ideal gas mixture. All the axial diffusive terms are neglected by assuming that, convective transport is dominant in the axial direction. All the radial variations are neglected by assuming that diffusive transport (mixing) is fast in the radial direction. With these assumptions, mass and continuity equations can be written in one dimension (Eq. 3.17). For setting up the governing equations it is assumed that firstly there is no variation in the transverse direction, and secondly axial diffusion of any quantity is negligible relative to the corresponding convective term.

Total continuity:

$$\frac{d(\rho u A_c)}{dz} = A_s \sum_{i=1}^{k} \dot{s}_i M_i \qquad 3.16$$

Species continuity:

$$\rho u A_c \frac{dY_i}{dz} + Y_i A_s \sum_{i=1}^{k} \dot{s}_i M_i = M_i (A_s \dot{s}_i + A_c R_i) \qquad 3.17$$

Energy continuity:

$$\rho u A_c \frac{d(C_p T)}{dz} + \sum_{i=1}^{k} \dot{\omega}_i h_i M_i A_c + \sum_{i=1}^{k} s_i h_i M_i A_s = U A_s (T_w - T) \qquad 3.18$$

Equation of state:

$$PM = \rho R T \qquad 3.19$$

For a tubular flow with a diameter of $r_0$ as shown in Figure 11 the cross sectional areas $A_c$ and the circumference $A_s$ can be derived as follows:

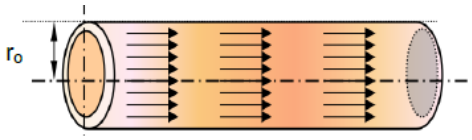


**Figure 11:** Plug-flow model.

$$A_c = \pi r_0^2 \quad \text{and} \quad A_s = 2\pi r_0 \qquad 3.20$$

### 3.12.3 DETCHEM$^{CHANNEL}$

DETCHEM$^{CHANNEL}$ enables the simulation of steady state parabolic two-dimensional reacting flows in straight channels using the boundary-layer approach to reduce the complexity of the system. The channel of the catalyst is approximated by a cylindrical geometry. This is a reasonable assumption due to the washcoat layer, being thicker in the corners of the channel. The assumption of a cylindrical channel leads to a two-dimensional flow, for which axial and radial positions are independent variables. The boundary-layer method produces accurate results with much lower computational cost compared to solving the complete Navier-Stokes equations. For a chemically reacting flow, it is assumed that, axial diffusive transport is diminished in comparison to radial diffusion and convective transport. This assumption is applicable for systems in which the velocity in flow direction is sufficiently high or the channel diameter is small enough that the diffusive transport along the axial direction is negligible compared to the convective flow [41, 42]. This assumption leads to all derivatives in the axial dimension being eliminated. They are neglected because they are small compared to others, although they do not truly vanish. Boundary-layer equations retain a full two-dimensional representation of all the field variables. The boundary-layer approach leads to the following governing equations for a single channel simulation.

Conservation of total mass:

$$\frac{\partial(\rho u)}{\partial z}+\frac{1}{r}\frac{\partial(r\rho v)}{\partial r}=0 \qquad 3.21$$

Conservation of axial momentum:

$$\rho u\frac{\partial u}{\partial z}+\rho v\frac{\partial u}{\partial r}=-\frac{\partial p}{\partial z}+\frac{1}{r}\frac{\partial}{\partial r}\left(\mu r\frac{\partial u}{\partial r}\right). \qquad 3.22$$

Conservation of radial momentum:

$$\frac{\partial p}{\partial r}=0 \qquad 3.23$$

Conservation of species:

$$\rho u\frac{\partial Y_i}{\partial z}+\rho v\frac{\partial Y_i}{\partial r}=-\frac{1}{r}\frac{\partial\left(rj_{i,r}\right)}{\partial r} \qquad 3.24$$

Conservation of energy:

$$\rho u\frac{\partial h}{\partial z}+\rho v\frac{\partial h}{\partial r}=u\frac{\partial p}{\partial z}-\frac{1}{r}\frac{\partial(rq_r)}{\partial r} \qquad 3.25$$

The effect of elevated pressure as a result of pre-turbo catalyst placement, on catalyst activity was investigated with DETCHEM$^{CHANNEL}$.

## 3.13 Kinetic model

### 3.13.1 Gas phase mechanism

The detailed reaction mechanism released by *A.A. Konnov* was used for simulation of reactions in the gas phase. The mechanism accurately describes pyrolysis, ignition, oxidation and detonation of many small hydrocarbon and nitrogen-containing fuels reacting with different oxidizers over a wide range of conditions typical for combustion processes. The mechanism consists of 1200 reactions among 127 species [44].

### 3.13.2 Catalytic oxidation of methane over Pd-Pt catalyst

The complexity of the kinetics of the catalytic oxidation of methane over bimetallic Pd-Pt catalyst is well-known through several studies [45-47]. Since the catalyst activity is a function of various parameters viz. operation conditions, composition of gas mixture, support material of washcoat, preparation method of catalyst, particle size of the noble metals and even oxidation state of palladium [12, 23, 48, 49], finding a detailed reaction mechanism including all mentioned parameters is not straightforward. It is therefore common to describe the kinetic of methane oxidation over Pd-Pt catalysts with global power law reaction rate expressions [50-53].

The order of the reaction rate with respect to methane is mainly found to be one. The impact of oxygen, water and carbon dioxide concentrations present in the gas mixture on the kinetic of methane oxidation are commonly known. The reaction mechanism is assumed as a Mars-Van Krevelen mechanism which leads to the expression:

$$\left(-r_{CH_4}\right) = \frac{k_2\, c_{CH_4}}{1 + (k_2/k_1)\left(c_{CH_4}/c_{O_2}\right)} \qquad 3.26$$

In lean burn operation and excess of oxygen and with $k_1 >> k_2$, indicating a rapid re-oxidation of the surface, the expression is simplified to a first order in methane and zero order to oxygen. The catalyst activity is affected by adsorbed water on the catalyst surface at low to moderate temperatures. Water inhibition is often explained by formation of hydroxyl species at low to moderate temperatures and even at high temperature, depending on the support type [51, 54], which covers the catalyst surface and forms palladium hydroxide from palladium oxide which is the main active site for methane oxidation. This process causes a reversible deactivation during long-term usage [22, 55]. It has been shown that only the palladium oxides present in the catalysts are responsible for the lowering of conversion since no water inhibition originates from the interaction with platinum sites [56]. No self-inhibition by addition of water is given by the Pt sites present in the bimetallic catalyst, also at a high concentration of water in the feed. Assuming a negative influence of water, the order of reaction with respect to water is often suggested to be -1 or slightly more. The inhibition effect of carbon dioxide in comparison with those of water is negligible [51]. The Expression in Eq. 3.26 can be extended as follows:

$$\left(-r_{CH_4}\right) = \frac{k_2\, c_{CH_4}}{1 + k_{H_2O} c_{H_2O} + (k_2/k_1)\left(c_{CH_4}/c_{O_2}\right)} \qquad 3.27$$

Under the same assumptions stated before, it can be written as:

$$\left(-r_{\mathrm{CH_4}}\right) = \frac{k_2\, c_{CH_4}}{1 + k_{H_2O} c_{H_2O}} \qquad 3.28$$

where $k_{H_2O}$ is the water adsorption constant.

### 3.13.3 Evaluation of kinetic data

In case of a global mechanism, kinetic parameters are required to define the reaction rate of the catalytic system.

Although kinetic parameters are usually evaluated through Arrhenius analysis using data obtained at differential conditions, light-off curves can provide all the necessary kinetic information viz. order of reaction, activation energy, and pre-exponential factor with reasonable accuracy [57].

The procedure to evaluate these terms consists in analyzing the light-off curves and drawing the Arrhenius plot which provides the necessary kinetic parameters.

An experiment dedicated to determining activation energies using Arrhenius plots (Figure 12) was conducted for methane oxidation. In this experiment, the catalyst was exposed to 1000 ppm $CH_4$, 10% $O_2$ diluted with $N_2$ and the temperature was stepwise increased by 5 K intervals in ambient pressure.

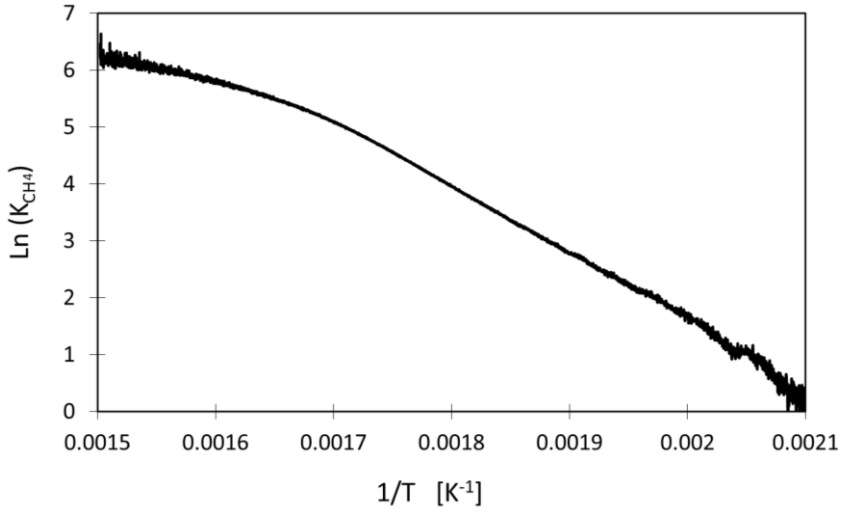


**Figure 12:** Arrhenius plot of oxidation of methane at 1bar with 1000ppm $CH_4$ and 10% $O_2$.

The slope and the y-axis intercept provide the kinetic data needed for methane oxidation. The resulting Arrhenius plot from 205 to 235 °C (inlet temperature), corresponding to conversions of between 2.0 and 10.0 %, is shown in Figure 13. The resulting activation energy and pre-exponential factor are 114 kJ/mol and $1\times10^9$ m/s respectively. The value of pre-exponential factor was tuned after addition of water inhibition term.

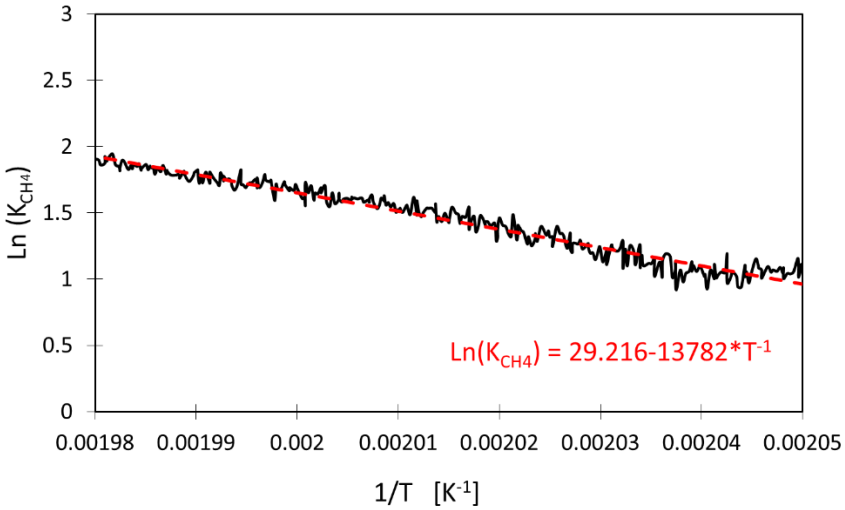


**Figure 13:** Estimation of intercept and slop of Arrhenius graph over kinetic regime.

The parameters of inhibition term of water were tuned for the best fit to the experimental results. The procedure is explained in chapter 8.3.

# 4 Experimental (KIT)

## 4.1 Catalyst Synthesis

Besides several catalysts provided by members of the working groups, monometallic and bimetallic catalysts as model catalysts were prepared at KIT. All samples were synthesized by Incipient Wetness Impregnation (IWI).

All prepared catalysts contain a total noble metal loading of 2.4 wt.%. For the bimetallic catalyst, a weight ratio of Pd:Pt = 5:1 was kept. Aqueous precursor solutions of tetraamminepalladium(II) nitrate (Chempur) and tetraammineplatinum(II) nitrate (Strem Chemicals) as well as their mixture for the bimetallic catalyst were prepared ready-to-use for the IWI.

For the $Al_2O_3$ based samples 10 grams of alumina (Puraflox, BET surface area = 180 $m^2/g$, calcined at 700°C for 5 hours, pore volume 0.85 $cm^3/g$ determined with water) was impregnated with 8.5 mL of the respective precursor solution. The samples were dried overnight at room temperature, followed by 1 hour at 70°C to remove all moisture and calcined at 500°C in air for 5 hours. For calcination, the powder was homogenized and spread in a thin layer (1-2 mm) in large crucibles to ensure air access to all powder. A sieve fraction of 125-250 µm was prepared by pressing the powder into a pellet at 10 tons, crushing and sieving. This sieve fraction was used for the catalytic tests.

Analogous bimetallic catalyst samples supported on $SiO_2$ (Aldrich, BET surface area 250 $m^2/g$, pore volume 1.05 $cm^3/g$), $CeO_2$ (BET surface area 60$m^2/g$, pore volume 1.05 $cm^3/g$) and $CeO_2$-$ZrO_2$-$Y_2O_3$-$La_2O_3$ mixed oxide (Interkat, metal weight ratios 30:60:5:5, in following referred to as CZ, BET surface area 75 $m^2/g$, calcined at 700°C for 5 hours, pore volume 0.39 $cm^3/g$) were prepared by IWI with the same PGM loading as the $Al_2O_3$-supported ones. The impregnation of $CeO_2$ and CZ was carried out in three respectively five subsequent steps with drying at room temperature and 70°C in between. An additional batch of 12% Pd-Pt/CZYL was synthesized for the XAS studies (*infra vide*) for an optimal signal from both noble metals. Calcination at 500°C for 5 hours concluded the synthesis.

The following list gives an overview of catalysts synthesized by Incipient Wetness Impregnation at KIT for this project:

Table 14: Overview of powder catalysts prepared at KIT.

| Monometallic samples | Bimetallic samples |
|---|---|
| 2.4 wt.% $Pd/Al_2O_3$ | 2 wt.% Pd-0.4 wt.% $Pt/Al_2O_3$ |
| 2.4 wt.% $Pt/Al_2O_3$ | 2 wt.% Pd-0.4 wt.% $Pt/CeO_2$ |
| | 2 wt.% Pd-0.4 wt.% $Pt/CeO_2$-$ZrO_2$-$Y_2O_3$-$La_2O_3$ |
| | 2 wt.% Pd-0.4 wt.% Pt $SiO_2$ |

## 4.2 Catalysts supplied by working group

Besides catalysts prepared at KIT, samples were also provided by companies from the working group.

A Pd-$Pt/Al_3O_3$ model catalyst was supplied by Heraeus, Hanau. The catalyst was already used in the FVV project “methane catalytic” [58]. The sample will be called “Pd-Pt Model catalyst” in the course of the report.

A $PdPt/Al_2O_3$ catalyst was provided by Johnson Matthey. The sample will be called “JM catalyst” in the report.

A PdPt/$CeO_2$-$ZrO_2$-$Y_2O_3$-$La_2O_3$ catalyst was provided by a joint group of different companies. The support material was supplied by Interkat. Clariant was responsible for the catalyst synthesis according to a recipe from KIT (analogous to the above mentioned procedure) and for washcoating on metallic substrates from Emitec. Two big bricks for engine tests (120mm diameter, 130mm length) and two smaller cores for laboratory tests (25mm diameter 25mm length) were supplied.

## 4.3 Physical and Chemical Characterization

### 4.3.1 $N_2$-Physisorption

The specific surface area was determined using $N_2$-physisorption at 77 K on a Rubotherm Belsorp-mini II instrument using the Brunauer-Emmet-Teller (BET) [34] method. Prior to the measurements, all samples were degassed at 300°C for 2 hours under vacuum.

### 4.3.2 CO-Chemisorption

#### 4.3.2.1 Standard procedure for $Al_2O_3$ based samples

The overall noble metal dispersion was determined using temperature programmed desorption of CO (CO-TPD) under continuous flow of 500 mL/min on an in-house built setup [59]. The samples were placed in a tubular quartz glass reactor. Prior to the measurements, the catalysts were pretreated in air for 15 min at 400°C, followed by a reduction in 4% $H_2/N_2$ at 400°C for 30 minutes. Subsequently, the reactor was rapidly cooled down to room temperature under $N_2$ flow. After saturating the catalyst with 1% $CO/N_2$ for 1 hour, weakly adsorbed CO was removed by purging the reactor with pure $N_2$ for 45 minutes. TPD in a $N_2$ flow was performed by linearly ramping the temperature at 20 K/min up to 400°C. Gas concentrations of CO and $CO_2$ evolved during TPD were monitored by an NDIR detector (BINOS1000). For determining the noble metal dispersion (D), an adsorption stoichiometry of CO:(Pd,Pt) = 1:1 was assumed [60-62]. Assuming a hemispherical geometry of the supported noble metal particles, average surface-based particle diameters ($d_s$) were calculated using the relation $d_s = 11.1/D$, using structural parameters of the noble metals listed in [63].

#### 4.3.2.2 Cooling method for $CeO_2$ based samples

Since CO also adsorbs on the surface of the ceria as storage component [36], a more advanced experimental procedure has to be applied. In this case, the samples were pretreated with 5 % $O_2$ in $N_2$ and subsequently with 4 % $H_2$ in $N_2$ at 400 °C for 15 min, respectively. Finally, the catalysts were saturated with 100 ppm CO in $N_2$ at -78°C [37]. The noble metal dispersion was calculated based on the amount of CO adsorbed on the sample during saturation at -78°C.

### 4.3.3 X-ray Diffraction (XRD)

X-ray diffraction patterns were acquired using a Bruker D8 Advance diffractometer using Cu Kα radiation (λ = 1.54 Å) generated by accelerating electrons over 40 kV at an anode current of 35 mA. The intensity of scattered X-rays was measured in a 2θ-range of 20-90°. The PdO (112) reflection at 55° and the Pt (311) reflection at 80.1° were analyzed using the Scherrer equation to determine the average crystallite size.

### 4.3.4 Electron microscopy

The morphology of the catalyst was studied by HAADF-STEM on an aberration-corrected FEI Titan380-300 transmission electron microscope at 300 kV acceleration tension. The chemical composition of single nanoparticles was investigated by energy-dispersive X-ray spectroscopy (EDXS) performed with the FEI Titan380-300microscope at 300 kV by using an EDAX Si(Li) detector. EDX spec-tra are quantified with the FEI software package “TEM imaging and analysis” (TIA) version 3.2. Using TIA, element concentrations were calculated on the basis of a refined Kramer’s law model, which includes corrections for detector absorption and background subtraction. EDX spectra obtained during scanning of a rectangular-lar area within single nanoparticles are used to determine their average chemical composition. The concentration profiles of different chemical elements within a nanoparticle were determined from EDX spectra measured along a line-scan that passes through its center. EDX profile analysis and determination of complex nanoparticle compositions was performed as described in detail in reference [64]. In case of Pd-Pt nanoparticles the quantification of EDX spectra (area or line-scans) is performed on the basis of the characteristic X-ray lines. Samples for HAADF-STEM were prepared by deposition of particles on an amorphous carbon (Lacey–) film copper grid.

### 4.3.5 Diffuse Reflectance Infrared Fourier Transform Spectroscopy (DRIFTS)

DRIFTS spectra were recorded on a Bruker VERTEX 70 spectrometer equipped with diffuse-reflectance optics (Praying Mantis, Harrick) and an *in situ* cell (Harrick) for heating in a gas flow (**Figure 14**). The sample powder in a sieve fraction 125-250 µm was placed in the sample cup (6 mm diameter and 3 mm depth) and the cell was closed with a dome cover with KBr windows. The gas passed the sample from the top of the cup and exited through a wire mesh at the bottom.

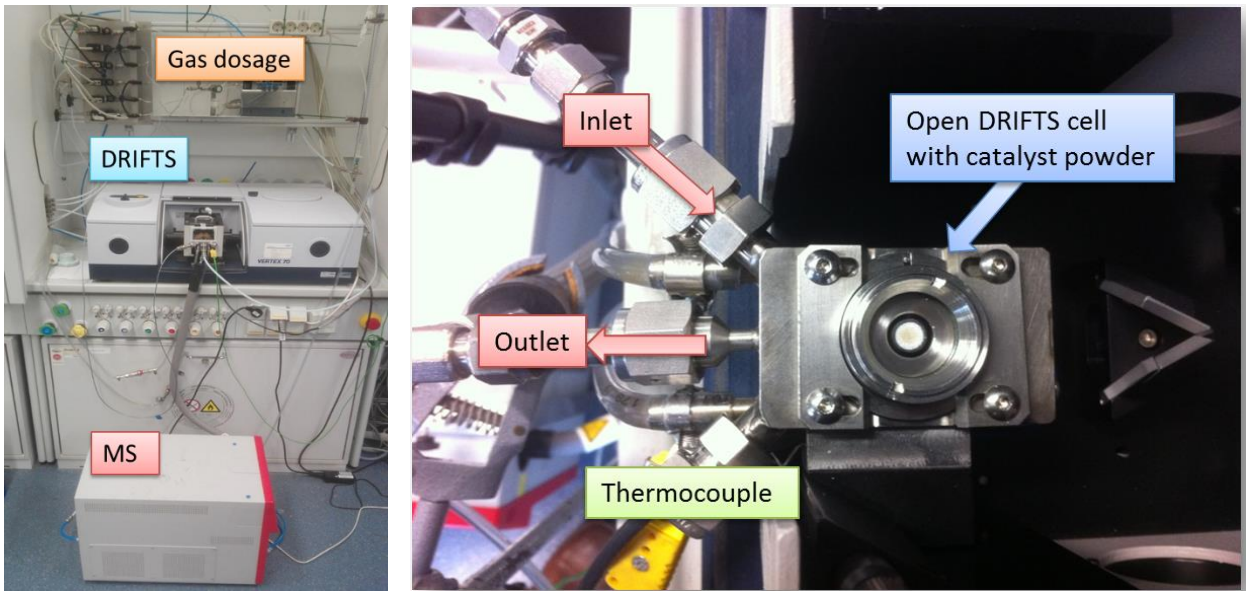


**Figure 14:** Operando DRIFTS setup with gas dosage system, analytics for evolved gas analysis (MS) and Praying Mantis cell (Copyright, KIT).

Gases (Air Liquide, purity 5.0) were dosed using mass flow controllers and mixed before being directed to the cell (Figure 14).The gas composition at the exit of the cell was analyzed by mass spectrometry. The spectra were acquired in reflectance mode ($R = I_r/I_0$) and converted to the Kubelka-Munk function $KM(R) = ½(1-R)^2/R$, where $I_r$ is the reflected intensity and $I_0$ the “incident intensity” measured in diffuse reflectance mode of monocrystalline $CaF_2$ (sieve fraction 125-250 µm). The measurements of $CaF_2$ were conducted at temperatures of the catalyst measurements to take the significant contribution of blackbody radiation into account.

### 4.3.6 X-ray absorption spectroscopy

X-ray absorption spectroscopy measurements were performed at SOLEIL synchrotron (Saint-Aubin, France) at the ROCK (Rocking Optics for Chemical Kinetics) beamline. The storage ring was operated at 2.75 GeV with a ring current of 450 mA in top-up mode. ROCK is a bending-magnet beamline equipped with a horizontally focusing toroidal mirror inside the shield wall of the storage ring in order collect the maximum number of photons. Quick-scanning EXAFS (QEXAFS) monochromators equipped with Si(111) and Si(220) channel-cut crystals were operated at 2 Hz for data acquisition at the Pt L3,2,1-edges (11564 eV, 13273 eV and 13880 eV) in one sweep and the Pd K-edge (24350 eV) respectively. Incident and transmitted beam intensity was measured by ionization chambers (OKEN). Pt and Pd foils were placed between the 2nd and 3rd ionization chambers for checking the energy calibration.

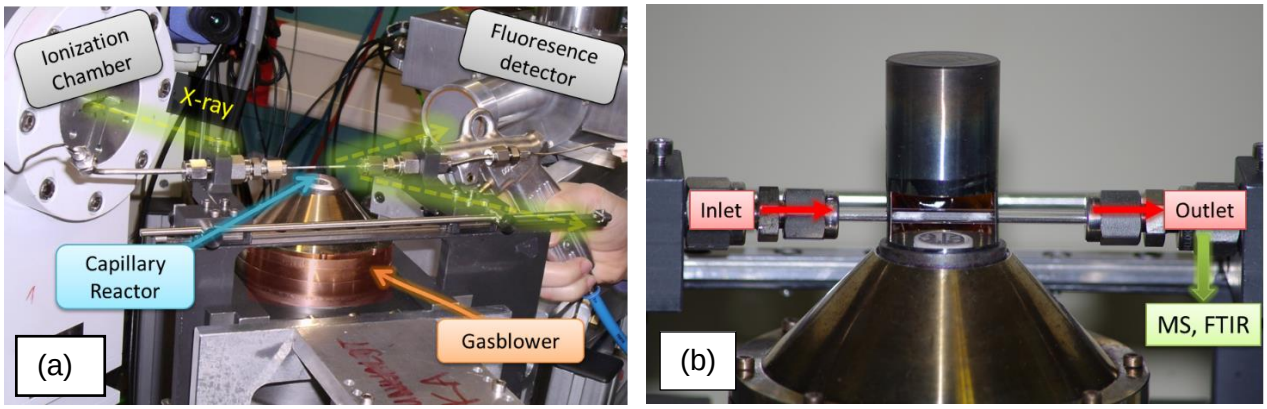


**Figure 15:** Operando capillary reactor [7] for XAS investigations: (a) Capillary reactor heated by a hot gas blower with ionization chambers and Ge fluorescence detector for detecting the transmitted X-ray and the fluorescence, respectively; (b) capillary microreactor with catalyst bed (Copyright, KIT).

As illustrated in Figure 15, the catalytic experiments at the beamline were conducted using the quartz capillary reactor setup heated by a hot gas blower (FMB Oxford) and connected to analytics for evolved gas analysis (MS or FTIR instruments). Gas dosage was done via MFCs and water by using a saturator at room temperature.

## 4.4 Activity tests

### 4.4.1 Experimental setups

#### 4.4.1.1 High-Pressure Setup

All tests related to pre-turbo positioning of the catalyst were performed at the so-called “High pressure setup” (Figure 16).

**Figure 16.** “High-Pressure Setup” at Abgaszentrum Karlsruhe (Copyright, KIT).

The setup allows the simultaneous dosage of gases, like air, $N_2$, $H_2O$, CO, $CO_2$, HC, NO, $NO_2$, $NH_3$, $SO_2$. The single gas dosages are measured and controlled by mass flow controllers (EL-FLOW®, Bronkhorst). Gaseous water is provided by controlled evaporation of liquid water (Liqui Flow and Controlled Evaporation Mixer (CEM), Bronkhorst). The different gases are collected and flow in preheated stainless steel pipes. The lines as well as the stainless steel reactor are coated with a Silicon based inert layer (Silco Tek). Heating of the reactor is realized by an electrical furnace surrounding the reactor controlled by a Eurotherm 2402 controller. The catalyst samples are introduced in the stainless steel reactor and fixed with quartz glass wool in order to keep it tight to the walls and prevent any movement also at high gas flows on the one hand, and to limit bypass on the other hand. 5mm upstream and downstream of the monolithic sample, temperature is measured by two type K thermocouples (diameter = 3 mm) referred to as temperature inlet and outlet. For the investigated conditions the temperature gradient along the catalyst in inert gas mixture is always smaller than 8 K. The pressure in the reactor is regulated by a pressure regulator (Hermann Ehlers GmbH) that adjusts the flow leaving the reactor. Pressures up to 5 bar can be realized. Gaseous inlet concentrations and reaction products are analyzed at ambient pressure using a Fourier transform infrared spectrometer (FTIR) from MKS (MG2030) via a bypass line or via a route through the reactor.

#### 4.4.1.2 NSC setup

Tests performed with powdered catalysts and tests with the JM catalyst were done at the so-called NSC setup. The setup itself is similar to the High pressure setup described in 4.4.1.1 and uses the same devices for gas dosage and analysis. However, tests can only be run at ambient pressure and the reactor consists of quartz glass. For powdered catalysts the reactor has an inner diameter of 8mm and the catalyst is fixed in a bed by quartz glass wool (Figure 17). The catalyst (sieve fraction 125 – 250µm) is diluted with quartz (sieve fraction 125 – 250µm) in a wt. ratio of 3:7 (catalyst:quartz). Temperature is measured by 2 Type N thermocouples (diameter 3mm) placed 5 mm upstream and downstream of the catalyst bed.

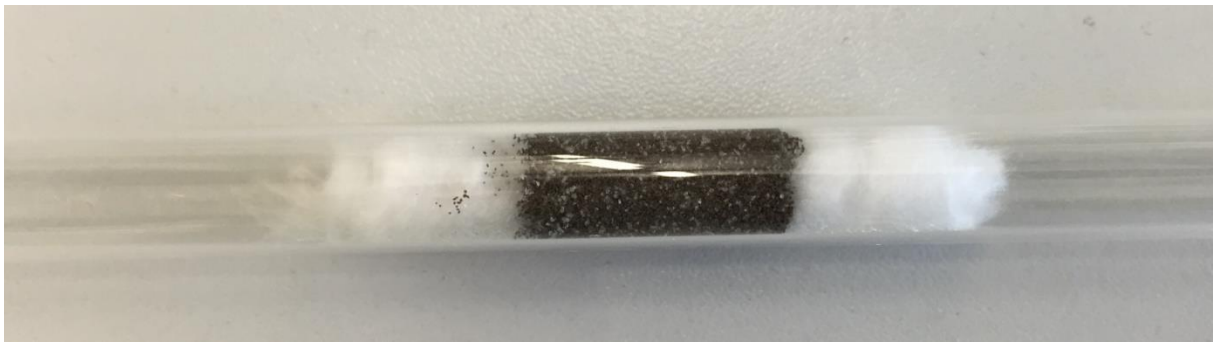

**Figure 17:** Catalyst diluted with quartz (125 – 250 µm sieve fraction) in a quartz glass reactor used for catalytic tests at the NSC setup. The catalyst bed is fixed by quartz glass wool.

#### 4.4.1.3 High Flow setup

Parts of the tests were performed at the so-called High flow setup. The setup itself is similar to the High-pressure setup described in 4.4.1.1 and enables to measure structured catalysts. The setup is described more in detail in the final report of FVV project “Methane Catalytic” [58].

### 4.4.2 Experimental procedures

The experimental procedures are described in detail in the relevant chapter together with the results. To sum up, different packages of measurements were conducted to answer the questions in focus (cf. proposal).

# 5 Catalyst Synthesis and Characterization (KIT)

## 5.1 Pd-Pt/$Al_2O_3$, Pd/$Al_2O_3$, Pt/$Al_2O_3$, Pd-Pt Model catalyst

In the as-prepared state, thePd-Pt/$Al_2O_3$ and the Pd/$Al_2O_3$ KIT catalysts contain on average 5 nm PdO particles as evidenced by TEM (Figure 18). They are X-ray amorphous as they exhibit a practically undetectable fingerprint in the X-ray diffraction pattern shown in Figure 19.

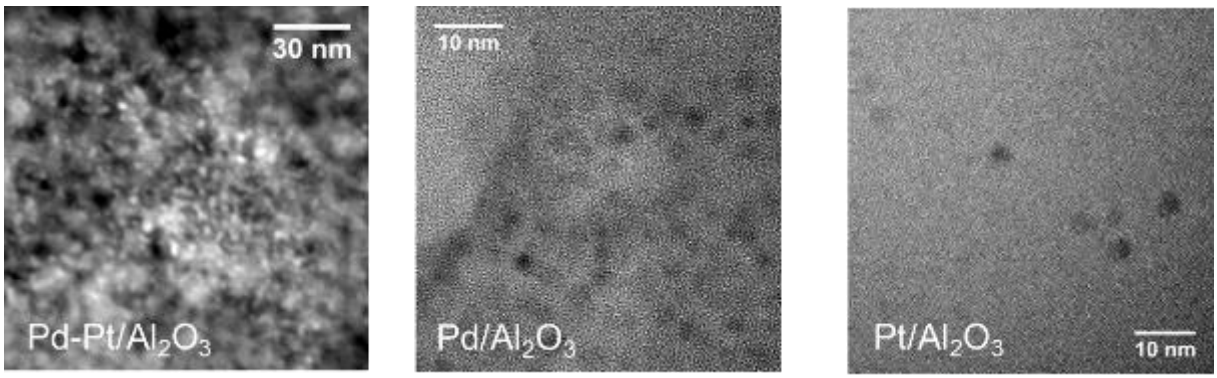


**Figure 18:** HAADF-STEM images of Pd-Pt/$Al_3O_3$, Pd/$Al_2O_3$ and Pt/$Al_2O_3$ that were synthesized at KIT.

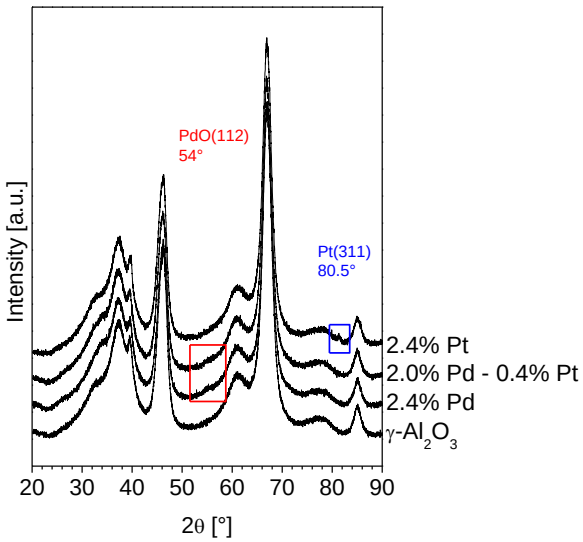


**Figure 19:** X-ray diffraction pattern of Pd-Pt/$Al_3O_3$, Pd/$Al_2O_3$ and Pt/$Al_2O_3$ that were synthesized at KIT and pure alumina for comparison.

Visual comparison of the Pd K-edge XANES spectra obtained for the KIT catalysts with the XANES of Pd and PdO reference materials (Figure 20) indicate that in the fresh and used state, the Pd component in both the Pd-Pt/$Al_2O_3$ and the Pd/$Al_2O_3$ catalysts is completely oxidized, i.e. in PdO stoichiometry. This also applies to the Pd-Pt/$Al_2O_3$ Model catalyst (supplied by Heraeus). The corresponding FT- EXAFS data, which displays the pseudo-radial distribution of the neighboring atoms around the Pd center, confirm that the Pd component is present in a PdO-like phase (Figure 21 (a-b) and Table 15). Relative to PdO reference, the monometallic and bimetallic catalysts are characterized by identical back-scattering paths for the nearest-neighbor Pd-O shell (2.02 Å) and the further Pd-Pd shells (3.06-3.07 Å and 3.41-3.46 Å). The Pd-Pd shells are weak in intensity for the fresh catalysts and gain amplitude in the used samples, indicating a slightly larger particle size for the latter.

Linear combination analysis of the Pt L3 XANES region uncovered that the Pt component is present as completely oxidized $Pt^{4+}$-species in the fresh state, but is slightly reduced in the used state, reducing to O/Pt = 0.8 in the reference catalyst (model catalyst provided by Heraeus) Indeed, the

FT-EXAFS data shown in Figure 21 and fitting results in Table 15 for the bimetallic catalysts identify Pt-Pt and Pt-Pd distances at 2.75 Å, which suggest Pd-Pt alloy. The further coordination shells are Pt-O typical for $PtO_2$, as well as further Pt-Pd shells, clearly indicating that the Pt atoms are incorporated into the PdO matrix at lattice positions of Pd atoms which is in line with .

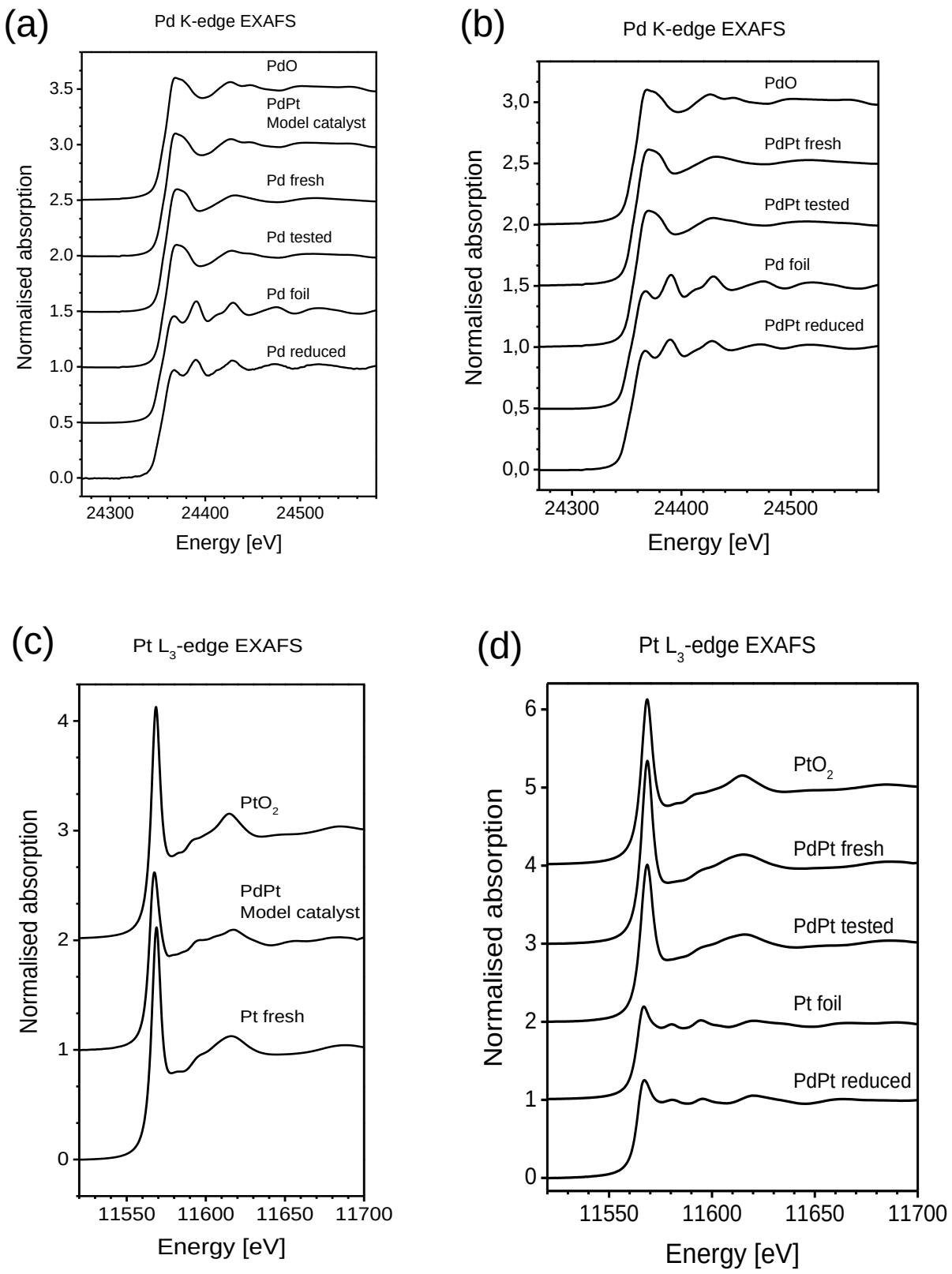


**Figure 20:** XANES spectra of the monometallic and bimetallic KIT made catalysts on $Al_2O_3$, of the PdPt Model catalyst supplied by Heraeus and reference oxides and metal foils at the Pd K-edge (a-b) and the Pt $L_3$-edge (c-d).

The low coordination numbers observed in the catalysts relative to the bulk structures of PdO and $PtO_2$ show that crystalline order is low and extends on the range of maximum a only few nanometers.

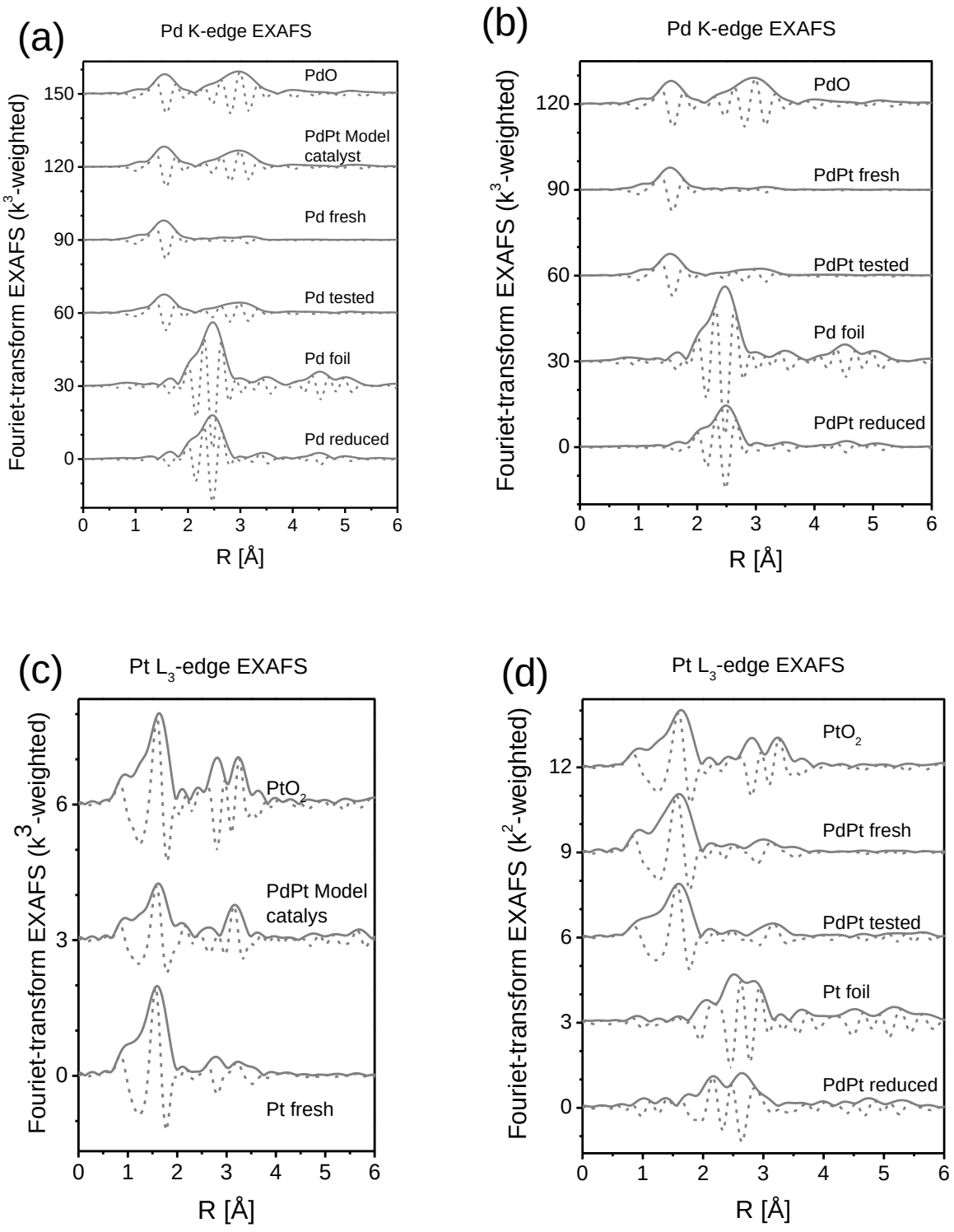


**Figure 21:** EXAFS spectra of the the monometallic and bimetallic KIT made catalysts on $Al_2O_3$, of the PdPt Model catalyst supplied by Heraeus, reference oxides and metal foils at the Pd K-edge (a-b) and the Pt $L_3$-edge (c-d).

In the reduced state (after exposure to $CH_4$/He at 400°C), the EXAFS data obtained for Pd and Pd-Pt catalysts on $Al_2O_3$ confirm the presence of small metallic nanoparticles. The total metal-metal coordination number of ca. 11 (Pd-Pd-distance 2.72-2.75 Å) points towards an average 3 nm metallic particle size [65]. Distinct Pd-Pt and Pt-Pd shells prove Pt-Pd alloying.

**Table 15:** EXAFS analysis results of the catalysts on $Al_2O_3$ and reference oxides and metal foils at the Pd K-edge (Pd-x paths) and the Pt $L_3$-edge (Pt-x paths). Distances (d) and mean thermal displacements ($\sigma^2$) marked with an asterisk (*) were fixed during the fit.

| Sample | Path | d [Å] | CN | $\sigma^2$ [Å$^2$] | $\Delta E_0$ [eV] | R-factor [%] |
|---|---|---|---|---|---|---|
| PdO | Pd-O | 2.02 | 3.9 | 0.0013 | -1.4 | 1.5 |
| O/Pd = 1 | Pd-Pd | 3.06 | 3.9 | 0.0034 | | |
| | Pd-Pd | 3.46 | 7.8 | 0.0057 | | |
| Pd/$Al_2O_3$ (used) | Pd-O | 2.02 | 4.0 | 0.0021 | -2.4 | 1.0 |
| O/Pd = 1 | Pd-Pd | 3.06 | 2.9 | 0.0063 | | |
| | Pd-Pd | 3.44 | 5.9 | 0.0092 | | |
| Pd/$Al_2O_3$ (fresh) | Pd-O | 2.01 | 4.2 | 0.0020 | -2.2 | 1.4 |
| O/Pd = 1 | Pd-Pd | 3.07 | 2.5 | 0.0114 | | |
| | Pd-Pd | 3.41 | 10.2 | 0.0233 | | |
| Pd-Pt/$Al_2O_3$ (Model catalyst Heraeus) | Pd-O | 2.02 | 4.2 | 0.0016 | -2.0 | 1.1 |
| O/Pd = 1 | Pd-Pd | 3.06 | 3.3 | 0.0041 | | |
| O/Pt = 0.8 | Pd-Pd | 3.46 | 5.4 | 0.0054 | | |
| | Pt-O | 2.02 | 2.9 | 0.0016 | 6.6 | 6.1 |
| | Pt-Pd | 3.11 | 12.5 | 0.0137 | | |
| | Pt-Pd | 3.11 | 8.9 | 0.0137 | | |
| | Pt-Pt | 2.75* | 8.5 | 0.0137 | | |
| | Pt-Pd | 2.75* | 4.5 | 0.0137 | | |
| Pd-Pt/$Al_2O_3$ (used) | Pd-O | 2.01 | 4.0 | 0.0022 | -1.8 | 1.2 |
| O/Pd= 1 | Pd-Pd | 3.08 | 2.7 | 0.0091 | | |
| O/Pt = 1.8 | Pd-Pd | 3.44 | 6.8 | 0.0144 | | |
| | Pt-O | 1.97 | 4.7 | 0.003* | 6.3 | 8.7 |
| | Pt-Pd | 3.02 | 7.7 | 0.01* | | |
| | Pt-Pd | 3.49 | 2.5 | 0. 01* | | |
| | Pt-Pt | 2.75* | 5.2 | 0. 01* | | |
| | Pt-Pd | 2.75* | 2.0 | 0. 01* | | |
| Pd-Pt/$Al_2O_3$ (fresh) | Pd-O | 2.01 | 4.1 | 0.0021 | -1.9 | 1.3 |
| O/Pd = 1 | Pd-Pd | 3.06 | 1.8 | 0.0120 | | |
| O/Pt = 2.1 | | | | | | |
| | Pt-O | 1.99 | 5.3 | 0.003* | 7.7 | 11.1 |
| | Pt-Pd | 3.01 | 3.5 | 0.01* | | |
| | Pt-Pd | 3.70 | 2.8 | 0.01* | | |
| Pd foil | Pd-Pd | 2.75 | 12.6 | 0.0053 | -5.4 | 0.5 |
| Pd/$Al_2O_3$ (reduced) | Pd-Pd | 2.75 | 10.8 | 0.0064 | -5.5 | 0.8 |
| Pd-Pt/$Al_2O_3$ (reduced) | Pd-Pd | 2.75 | 9.2 | 0.0068 | -5.7 | 0.4 |
| | Pd-Pt | 2.72 | 2.1 | 0.0071 | | |
| | Pt-Pd | 2.73 | 6.3 | 0.0053 | 5.8 | 4.7 |
| | Pt-Pt | 2.73 | 4.9 | 0.0070 | | |
| $PtO_2$ | Pt-O | 2.02 | 5.2 | 0.0012 | 9.4 | 5.2 |
| O/Pt = 2 | Pt-Pt | 3.11 | 14.2 | 0.0075 | | |
| Pt/$Al_2O_3$ (fresh) | Pt-O | 1.99 | 5.0 | 0.0013 | 8.1 | 6.1 |
| O/Pt = 2 | | | | | | |
| Pt foil | Pt-Pt | 2.77 | 12.0 | 0.0043 | 7.5 | 0.9 |

The results from CO chemisorption confirm the presence of small noble metal particles in the samples prepared at KIT. This is reflected by the high dispersion values, which are 40% for the Pd-

containing samples and 60% for $Pt/Al_2O_3$. The BET surface area for all three $Al_2O_3$ supported KIT samples is of about 195 m²/g. In contrast, the model catalyst provided by Heraeus has a noble metal dispersion of only 9% and a BET surface area of 140 m²/g

## 5.2 Pd-Pt/$CeO_2$ catalyst

The Pd-Pt catalyst on $CeO_2$ that was prepared for work package 4 was also characterized by several techniques. Figure 22 shows the XRD patterns of the catalyst and of the pure $CeO_2$ support. At 2Θ of 54° where PdO should appear, only a very small shoulder can be observed. This indicates the presence of very small crystalline PdO particles. This is also supported by electron microscopy (TEM) where very small nanoparticles < 5nm were observed.

CO chemisorption at -78°C revealed a noble metal dispersion of 15 % with the assumption of a 1:1: adsorption stoichiometry for CO on Pd and Pt. The BET surface area of the Pd-Pt/$CeO_2$ sample is clearly lower than for the $Al_2O_3$ based samples namely 30 m²/g

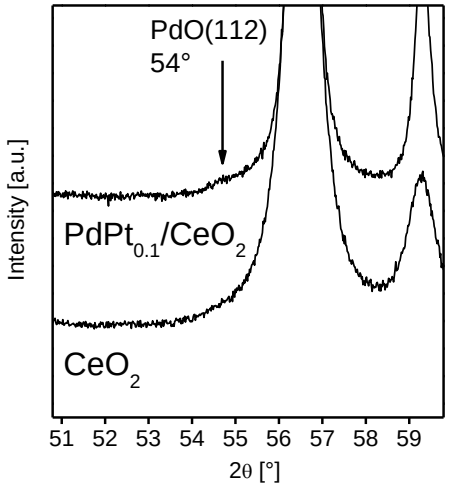


**Figure 22:** XRD patterns of PdPt/$CeO_2$ and pure $CeO_2$.

## 5.3 Pd-Pt/$SiO_2$ catalyst

Another support material which was investigated within this project is $SiO_2$. PdPt catalyst on $SiO_2$ shows a BET surface area of 220 m²/g. The PGM particles are homogenously distributed on the support and the mean particle diameter is around 2.5 nm (Figure 23). EDX mapping revealed the presence of small bimetallic particles with different Pd:Pt ratios between 8:2 to 9.5:0.5 which is in accordance with the expected value of 9:1.

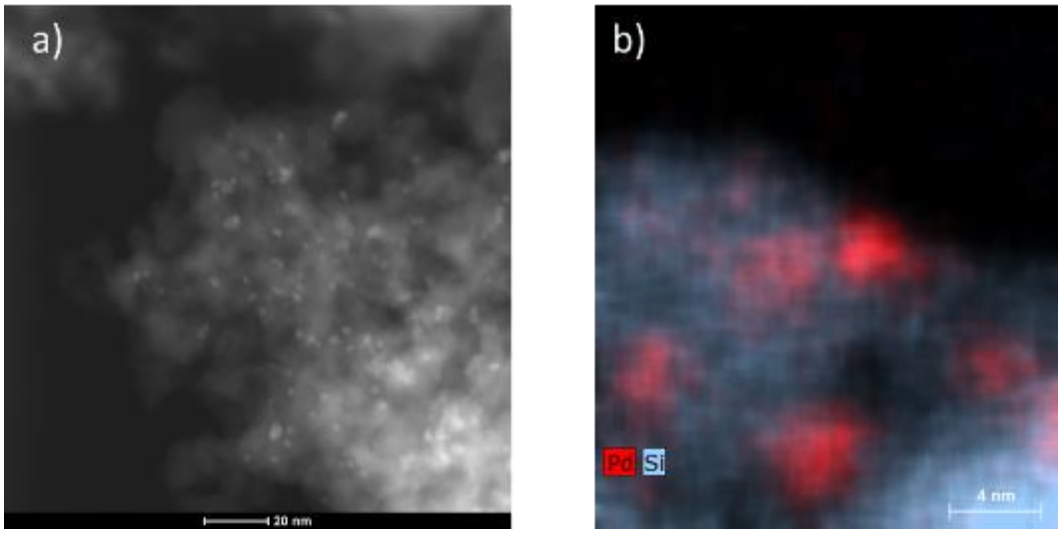


**Figure 23:** a) HAADF-STEM images of Pd-Pt/$SiO_2$. Bright spots represent PGM particles. b) HAADF-STEM images with color code for Si and Pd derived from EDX mapping.

## 5.4 Pd-Pt/CZ catalyst

Due to the high molar mass of the $CeZrO_x$ support a clear observation of the noble metals with TEM is difficult. A combination with EDX mapping reveals the distribution of Pd on the surface (Figure 24). Small Pd particles can be observed besides bigger agglomerates of $CeZrO_x$. The presence of highly dispersed non crystalline noble metal particles is also confirmed by X-ray diffraction.

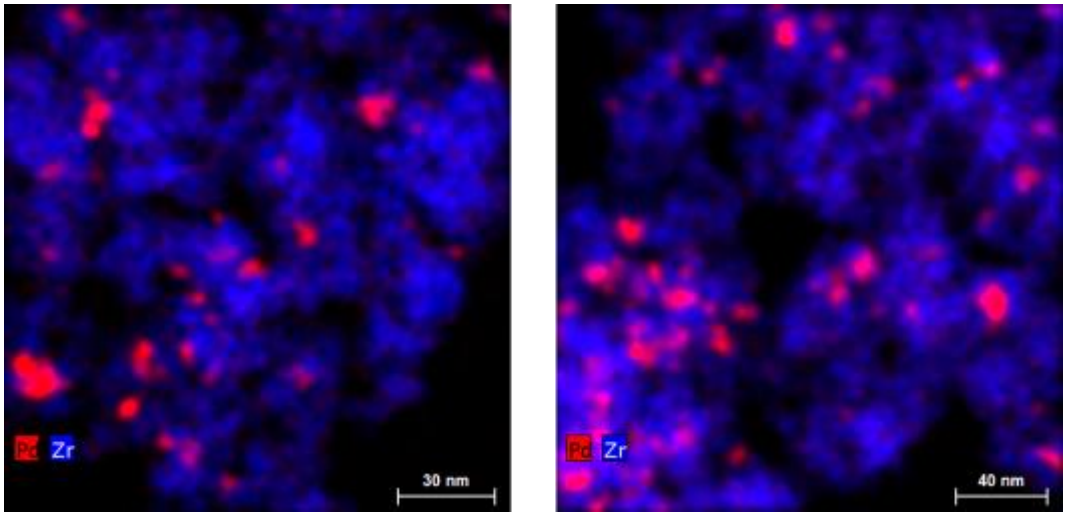


**Figure 24:** HAADF-STEM images of PdPt/CZ with color code for Zr and Pd derived from EDX scans.

## 5.5 Overview on investigated catalysts

Table 16 summarizes the information derived from electron microscopy, CO-chemisorption and BET surface area measurements for all catalyst samples within this project. In addition to the KIT samples and the model catalyst from Heraeus, several coated catalysts have been analyzed.

**Table 16.** Overview of investigated catalysts.

| Catalyst | Catalyst abbrevation | Particle size [nm] derived by TEM | Noble metal dispersion [%] | BET surface area [m²/g] | Cell density [cpsi] |
|---|---|---|---|---|---|
| 2.4 wt.% Pd on $Al_2O_3$ | $Pd/Al_2O_3$ | 3 - 5 | 40 | 195 | powder |
| 2.0 wt.% Pd 0.4wt.% Pt on $Al_2O_3$ | $Pd\text{-}Pt/Al_2O_3$ | 4 – 6 | 40 | 195 | powder |
| 2.4 wt.% Pt on $Al_2O_3$ | $Pt/Al_2O_3$ | 3 – 5 | 60 | 200 | powder |
| 20 g/ft³ Pt on $Al_2O_3$ | $Pt/Al_2O_3$ KIT 2 | - | - | - | 400 |
| 100 g/ft³ Pd-Pt on $Al_2O_3$ (Pd:Pt 5:1) provided by Heraeus | $Pd\text{-}Pt/Al_2O_3$ model catalyst | - | 9 | 140 | 400 and as powder with 2.4wt.% loading |
| 2.0 wt.% Pd 0.4 wt.% Pt on $CeO_2$ | $Pd\text{-}Pt/CeO_2$ | 3 - 6 | 15 | 30 | powder |
| 2.0 wt.% Pd 0.4 wt.% Pt on $SiO_2$ | $Pd\text{-}Pt/SiO_2$ | 2 - 5 | - | 220 | powder |
| 2.0 wt.% Pd 0.4 wt.% Pt on $CeO_2$-$ZrO_2$-$Y_2O_3$-$La_2O_3$ | Pd-Pt/CZ | 3 – 5 | - | 75 | powder |
| 10 wt.% Pd 2 wt.% Pt on $CeO_2$-$ZrO_2$-$Y_2O_3$-$La_2O_3$ | Pd-Pt/CZ high | - | - | - | powder |
| 100 g/ft³ Pd-Pt on $CeO_2$-$ZrO_2$-$Y_2O_3$-$La_2O_3$ on metal substrate from working group | Pd-Pt/CZ honeycomb | - | - | - | 400 |
| 120 g/ft³ Pd-Pt on $Al_2O_3$ (Pd:Pt 5:1) from Johnson Matthey | “JM catalyst” | - | - | - | 230 |

# 6 Results of catalytic activity tests under dry and wet conditions and regeneration (KIT)

## 6.1 Catalytic activity in fresh state

The synthesized samples described in chapter 5 were investigated by means of light-off experiments in dry reaction mixture (3200ppm $CH_4$, 10% $O_2$ in $N_2$). The procedure consisted of a pretreatment at 550°C (650°C for Pt) for 1h in 3200ppm $CH_4$, 10% $O_2$ in $N_2$ and a subsequent heating and cooling cycle between 225°C and 525°C in 3200ppm $CH_4$, 10% $O_2$ in $N_2$. Figure 25 a) shows the first light-off for the alumina based samples. It can clearly be seen that the Pt based catalyst shows very poor activity under these model conditions. 25% of $CH_4$ conversion is achieved around 540°C which is far away from temperatures present in the exhaust of a lean burn gas engine. However, the Pd based samples show high activity with 100% conversion above 350°C. Although the support is the same and the amount of Pd is even lower in the bimetallic sample (PGM loading is identical for all samples), higher activity can be observed for the Pd-Pt/$Al_2O_3$ catalyst. The addition of small amounts of Pt to a Pd catalyst can increase its low temperature activity [30] and stability [31, 66].

The activity of PdPt deposited on different supports is shown in Figure 25 b). Although the noble metal loading and Pd:Pt ratio is the same for all 4 samples, larger variations can be seen in the first light-off under dry conditions. The $Al_2O_3$ based sample provides the highest activity under these conditions while PdPt/CZ is the least active. A difference in $T_{50}$ of > 50K is between these two catalysts. Particle sizes derived from electron microscopy for the four catalysts do not differ too much. However, metal support interactions might play a major role for the activity of the bimetallic catalysts.

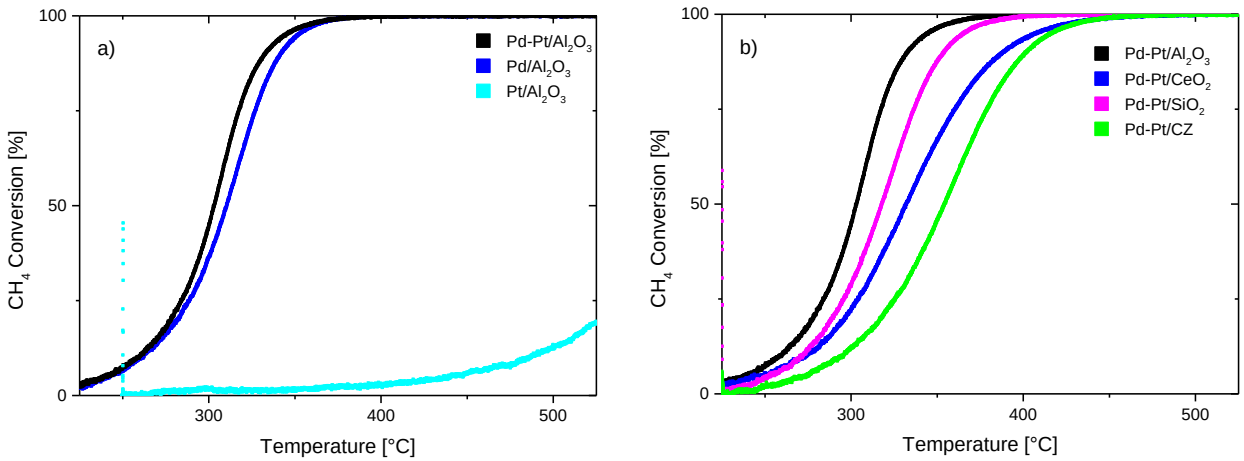


**Figure 25:** a) Methane conversion on $Al_2O_3$ based samples during first heating after 1h pretreatment at 550°C. b) Methane conversion on bimetallic samples deposited on different supports during first heating after 1h pretreatment at 550°C. Gas composition for all cases: 3200ppm $CH_4$, 10% $O_2$ balance $H_2$. Flow: 1L/min. amount of catalyst: 300mg.

The difference in conversion between the heating and cooling ramp is called hysteresis (or inverse hysteresis if the extinction temperature is at higher temperature than the ignition temperature [67]). Figure 26 a) shows the hysteresis for Pd/$Al_3O_3$. During the heating the activity is higher than during cooling. The same behavior is observed for Pd-Pt/$Al_2O_3$ and Pd-Pt/$SiO_2$. For CO oxidation on Pt based catalysts this phenomenon is widely discussed in literature and ascribed to different oxidation sates of Pt [67]. For $CH_4$ oxidation the effect is most probably caused by deactivation of the sample by water produced during the reaction [23]. However, the ceria-containing samples show the opposite trend. An increase in activity can be observed between heating and cooling. This effect is clearly caused by a strong metal support interaction. On explanation could be a redispersion of noble metal particles during lean operation at higher temperature as reported by *Wan et al.* [68]. Furthermore, changes in the PdPt particle morphology and electronic state could be influenced by the $CeO_2$ at higher temperature leading to a higher activity.

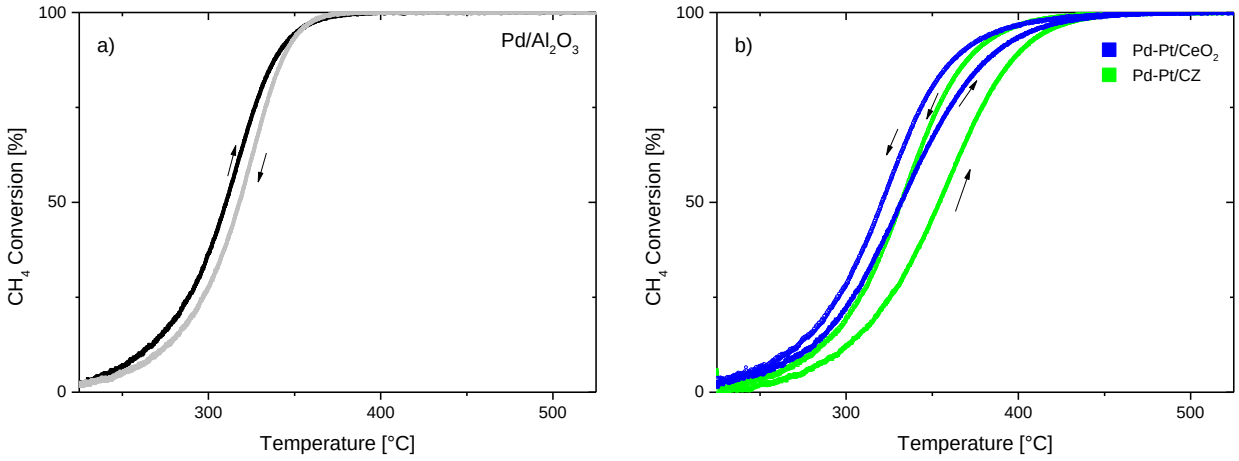


**Figure 26:** a) Methane conversion on $Pd/Al_2O_3$ during heating and cooling b) Methane conversion on PdPt/CZ and $PdPt/CeO_2$ during heating and cooling. Gas composition for all cases: 3200ppm $CH_4$, 10% $O_2$ balance $N_2$. Flow: 1L/min. amount of catalyst: 300mg.

The Pt on Alumina catalyst did not show any differences between heating and cooling.

## 6.2 Influence of water on methane oxidation

Water plays a critical role during methane oxidation on PGM based catalysts. In literature the reaction order with respect to water on Pd based catalysts is reported to be -1 [51]. Since water is always present in the exhaust stream of gas engines, its effect on the catalytic behavior is important to understand.

A pronounced negative effect of water can be seen in Figure 27 a). The conversion of $CH_4$ in the presence of water is shifted to higher temperature. Full conversion in presence of 12% water is only achieved at temperatures > 450°C. However, the extent of the inhibiting effect on activity is different on the different supported bimetallic catalysts. The alumina supported sample showed good activity in dry mixture but suffers enormously from water inhibition. $T_{50}$ increases more than 50K. Also the $SiO_2$ sample is strongly influenced by the presence of water showing the poorest activity under wet conditions. The ceria containing samples and especially pure $CeO_2$ demonstrate the highest $CH_4$ conversion activity under wet conditions.

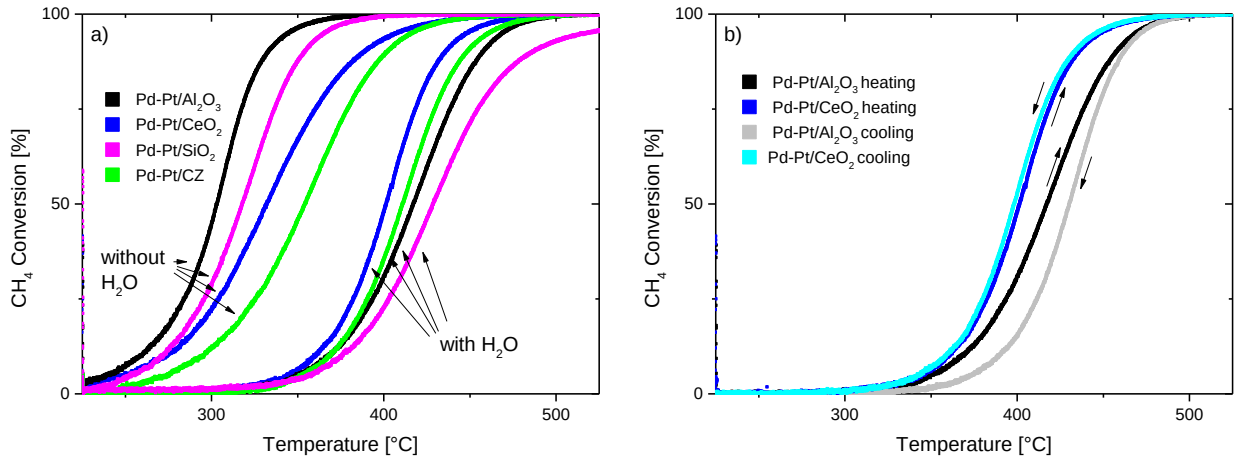


**Figure 27:** a) Comparison of $CH_4$ conversion during heating in presence and absence of 12% $H_2O$ for Pd-Pt on various supports. Gas composition: 3200ppm $CH_4$, 10% $O_2$, +/- 12%$H_2O$ balance N2. b) $CH_4$ conversion on $Pd\text{-}Pt/Al_2O_3$ and $Pd\text{-}Pt/CeO_2$ during heating and cooling. Gas composition: 3200ppm $CH_4$, 10% $O_2$, 12% $H_2O$ balance $N_2$.

On $CeO_2$ and ceria-zirconia the negative influence is the lowest. Furthermore, the samples still improve under these conditions. Figure 27 b) shows the heating and cooling curve of Pd-Pt/$Al_2O_3$ and Pd-Pt/$CeO_2$. The activity during cooling of the $CeO_2$ based catalyst is higher than during heating. A consecutive second light-off/down cycle was even better. Same behavior is observed for Pd-Pt/CZ. On the other hand, the $Al_2O_3$ and $SiO_2$ based samples suffer from constant deactivation under wet conditions meaning that consecutive light-off/down curves constantly shift to higher temperatures.

Pd on alumina is also strongly influenced by water and even more than the bimetallic $Al_2O_3$ based sample. Also under wet conditions the addition of small amounts of Pt seem to increase the activity and to stabilize the active sites in the bimetallic catalyst.

In contrast to the Pd-containing catalysts, Pt/$Al_2O_3$ does not suffer at all from $H_2O$ inhibition. $T_{50}$ in the presence and absence of 12% $H_2O$ only differs by 2-3 K.

The inhibiting effect of water on Pd based sample is also depending on the water concentration. As can be seen in Figure 28 the inhibiting effect increases with water concentration. However, the gap between 0 to 6% water and 6 to 12% water in light-off curves is bigger. This allows the presumption, that on small water level, the inhibiting effect is quite high and with increasing water concentration, the inhibiting effect becomes smaller.

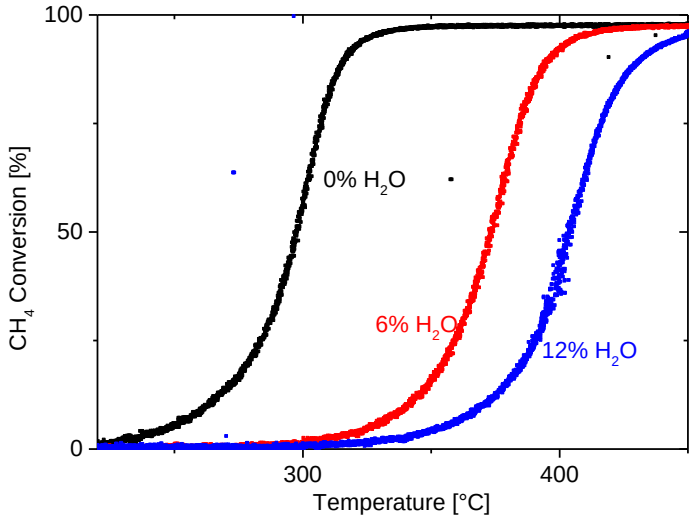


**Figure 28:** $CH_4$ conversion on Pd-Pt/$Al_2O_3$ model catalyst in presence of varying water concentration. Gas composition: 3200ppm $CH_4$, 0/6/12% $H_2O$, 10% $O_2$ in $N_2$. GHSV = 30000$h^{-1}$.

### 6.3 Influence of NO on methane oxidation

In the FVV project “methane catalytic” [58] a stabilizing effect of $NO_x$ on the long-term activity of Pd-Pt/$Al_2O_3$ model catalyst was found. In this chapter the effect of NO or $NO_2$ on the activity is described. Therefore experiments with dynamic changes in gas composition at constant temperature were performed. NO or $NO_2$ is added/removed from the gas stream while the space velocity is kept constant. A rapid reply of the catalyst by means of changing $CH_4$ conversion can be observed.

The result of such an experiment is plotted in Figure 29 for Pd-Pt/$Al_2O_3$ catalyst at ~$T_{50}$. The effect of NO addition (left) and $NO_2$ addition (right) is investigated. In both cases the presence of NO or $NO_2$ strongly inhibits the $CH_4$ conversion. One has to note that these tests were done in the absence of H2O. The effect of NO and $NO_2$ on catalyst performance are the same. Even the outlet concentrations of NO are almost the same in both experiments meaning that $NO_2$ gets decomposed to NO under these conditions. The experiments were repeated at higher (340°C) and lower (280°C) temperature and under all conditions an inhibiting effect by NO or $NO_2$ was observed.

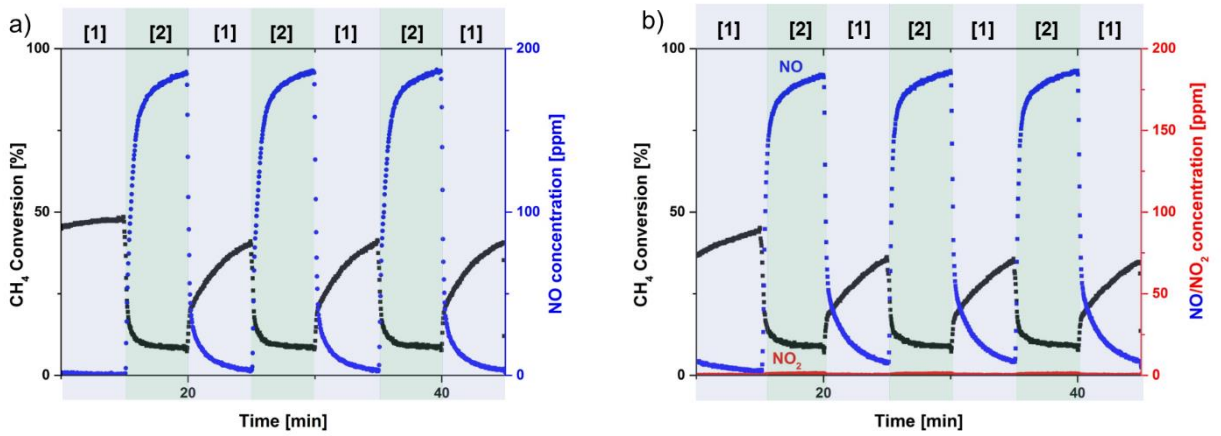


**Figure 29:** a): $CH_4$ conversion and NO concentration over time at 310°C with varying gas composition on Pd-Pt/$Al_2O_3$ [1]: 3200ppm $CH_4$, 10% $O_2$ in $N_2$ [2]: 200ppm NO, 3200ppm $CH_4$, 10% $O_2$ in $N_2$. b): $CH_4$ conversion, NO and $NO_2$ concentration over time at 310°C with varying gas composition on Pd-Pt/$Al_2O_3$ [1]: 3200ppm $CH_4$, 10% $O_2$ in $N_2$ [2]: 200ppm $NO_2$, 3200ppm $CH_4$, 10% $O_2$ in $N_2$.

Since $NO_x$ is supposed to have a positive effect on the $CH_4$ conversion when water is present, the previously described experiments were performed in the presence of 12% $H_2O$.

Figure 30 shows the results of the same tests in the presence of 12% $H_2O$ conducted over Pd/$Al_2O_3$ and Pd-Pt/$Al_2O_3$. Unlike in the absence of $H_2O$ the effect of NO addition is much smaller. Only a small inhibiting effect can be seen when NO is added at 400°C (same at 450°C). This might be due to the pronounced negative effect of external water covering the effect of NO. However, during periods where NO is present, the trend in $CH_4$ conversion is rising or at least stable in comparison to slowly decreasing activity when NO is not present. The same behavior as shown in Figure 30 with addition of NO, is also observed when $NO_2$ is added instead. As already found in “Methane catalytic 1” the presence of NO or $NO_2$ is able to stabilize the $CH_4$ conversion on Pd based catalysts. *Sadokhina et al.* [24] proposed the formation of HNO on the catalyst surface from reaction with OH groups and NO. The reported reaction order of -1 with respect to water has thus to be modified.

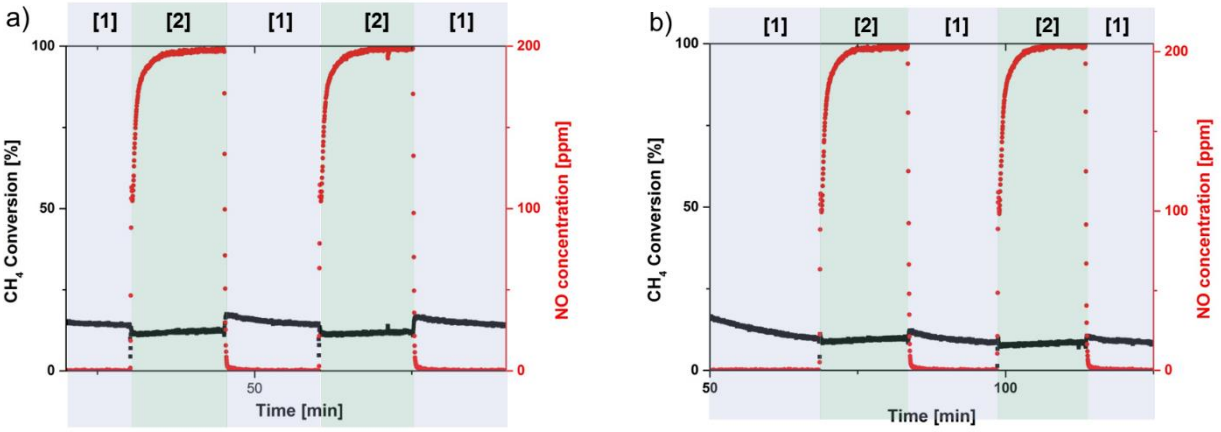


**Figure 30:** $CH_4$ conversion and NO concentration over time at 400°C with varying gas composition on a) Pd-Pt/$Al_2O_3$ and b) Pd/$Al_2O_3$. Gas composition [1]: 3200ppm $CH_4$, 10% $O_2$ in $N_2$ [2]: 200ppm NO, 3200ppm $CH_4$, 10% $O_2$ in $N_2$.

The same experiment as discussed in the former paragraph was conducted with Pd-Pt/$Al_2O_3$. Unlike for the $Al_2O_3$ based samples the inhibiting effect of NO in presence of 12% $H_2O$ was quite high leading to a shift of conversion from 50% to 35%. It seems that the $CeO_2$ sample is less inhibited

by water as already discussed in chapter 6.2 and more active sites are present to be inhibited/blocked by $NO_x$ species.

## 6.4 Long-term activity

As already observed in chapter 6.2 and discussed in several publications [19, 22, 23, 69] Pd based catalysts tend to deactivate over time under reaction conditions. This deactivation is not caused by sulfur poisoning or other harmful components but is even present when $CH_4$, $O_2$ in $N_2$ is fed to the catalyst.

Figure 31 shows the methane concentration downstream of the catalyst at different temperature over time. At 450°C a constant increase in $CH_4$ concentration is observed caused by decreasing activity of the Pd-Pt/$Al_2O_3$ model catalyst. Short temperature raises while keeping the gas flow constant leads to regeneration. At lower temperature (400°C) the initial activity is lower but also the rate of deactivation is higher. The methane concentration rises from 1000 ppm to 2500ppm within eight hours, which corresponds to a conversion drop of almost 50%.

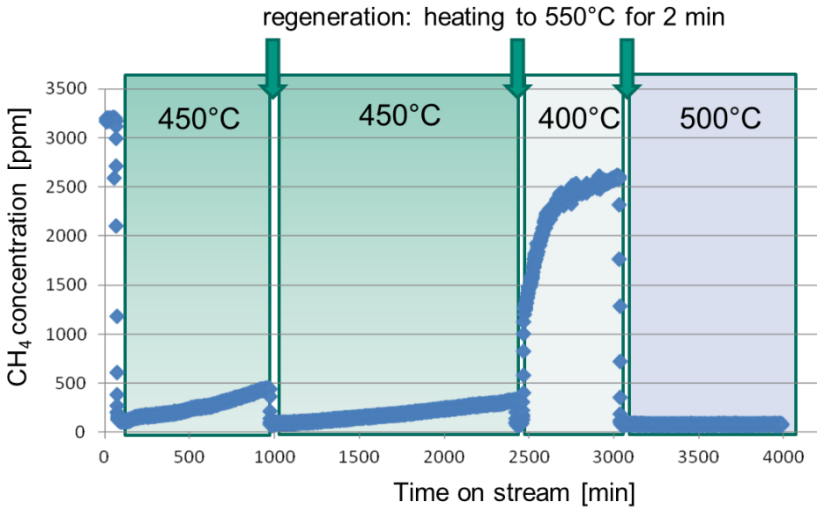


**Figure 31:** $CH_4$ concentration downstream Pd-Pt/$Al_2O_3$ model catalyst over time at different temperatures. Gas composition: 3200ppm $CH_4$, 10% $O_2$, 12% $H_2O$ in $N_2$. GHSV = 30000$h^{-1}$.

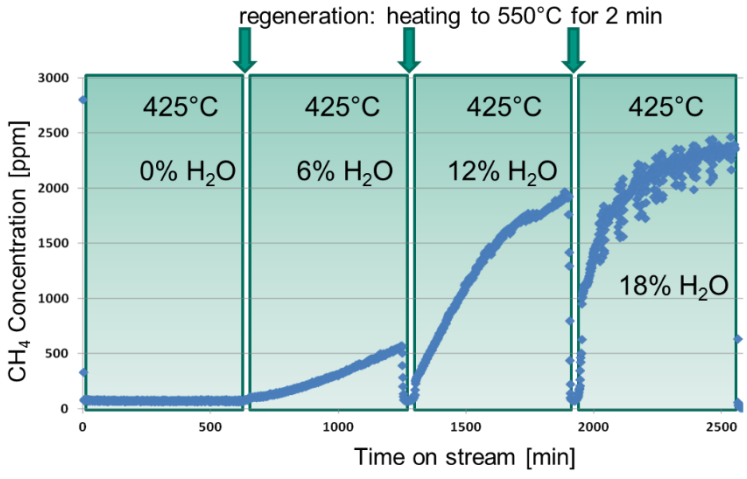


**Figure 32:** $CH_4$ concentration downstream Pd-Pt/$Al_2O_3$ model catalyst over time at constant temperature. Water concentration is varied while keeping GHSV constant. Gas composition: 3200ppm $CH_4$, 10% $O_2$, 0/6/12/18% $H_2O$ in $N_2$. GHSV = 30000$h^{-1}$.

Besides a temperature dependency of methane conversion and catalyst deactivation, also the water concentration plays a critical role. The higher the water concentration the lower the initial activity at constant temperature. Furthermore, deactivation proceeds faster when higher external water

concentration is present (Figure 32). The formation of hydroxyls on the catalyst surface is supposed to cause deactivation. Blockage of active sites by formation of Pd-OH is discussed [19, 20, 70] as well as hindering of O-transport from the carrier to the active sites [20, 21].

As seen from the light-off tests, deactivation due to water is further influenced by the support material. Therefore, the bimetallic KIT made samples were investigated in more detail by long-term tests.

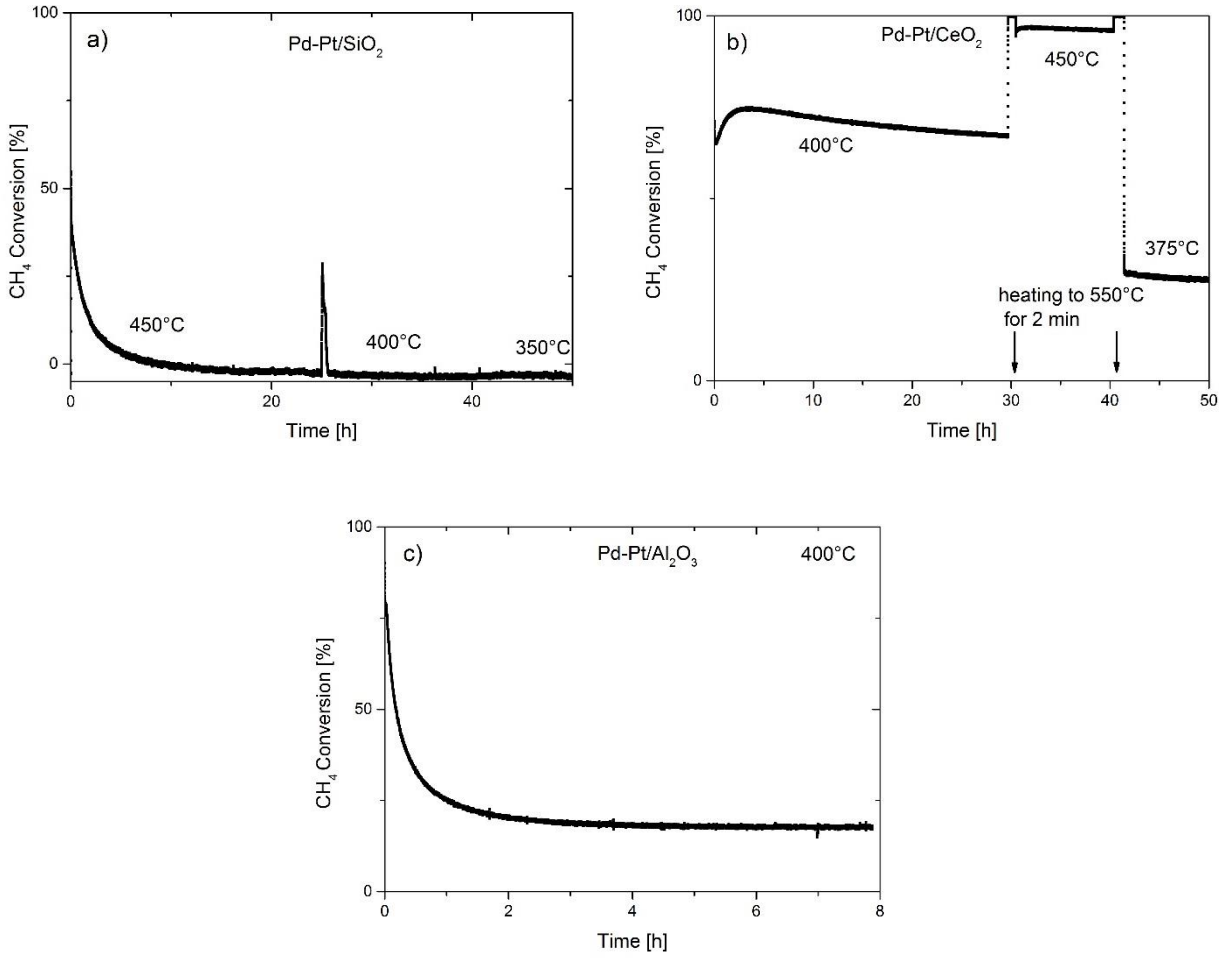


**Figure 33:** $CH_4$ conversion over time at different temperatures. Gas composition in all cases: 3200ppm $CH_4$, 10% $O_2$, 12% $H_2O$ in $N_2$. GHSV = 30000$h^{-1}$. a) Pd-Pt/$SiO_2$ b) Pd-Pt/$CeO_2$ c) Pd-Pt/$Al_2O_3$.

Pronounced differences in long-term stability can be observed for the different supported samples. Except Pd-Pt/$SiO_2$ all samples were in a fresh state after catalyst synthesis. The silica based sample was kept at 550°C in lean reaction mixture for one hour which could explain its bad initial activity. However, within a time shorter than 10h almost no methane gets converted anymore on Pd-Pt/$SiO_2$. A different behavior is observed for the ceria supported catalyst. An initial activation step as already demonstrated during light-off tests is followed by a slight deactivation over 25h. However, conversion stabilizes and even at 375°C at which deactivation should be quite pronounced constant conversion of ~30% is observed. The $Al_2O_3$ based sample is more resistant toward aging than $SiO_2$ based, but also loses activity very rapidly and only exhibits 20% $CH_4$ conversion after 2h at 450°C. Although dispersion values might differ for the samples, strong metal support interaction are addressed for the different deactivation trends. *Schwartz et al.* [21] proposed that the reason for deactivation is to some extent that hydroxyls on the support material slow down the process of O-transport to the active sites. Such species have been observed also during this study (chapter 7) Taking this into consideration, a more durable $CeO_2$ based catalyst could be explained by higher oxygen mobility on the surface and therefore stable conversion. In that case especially the sites on the intercept of PGM particles and support material play an important role in the catalyst activity

and stability. Thermogravimetric analyses were conducted to get a better insight into the properties of the support material. The Pd-Pt/$Al_2O_3$ and Pd-Pt/$CeO_2$ catalysts were heated in 10% $O_2$ in nitrogen from room temperature up to 700°C while the mass change of the sample and gaseous species were monitored. The results of these tests are shown in Figure 34. While the alumina based catalyst stores water up to 500°C Pd-Pt/$CeO_2$ hardly stores any water. This property seems to play an important role in the stabilization of high and constant methane conversion during operation.

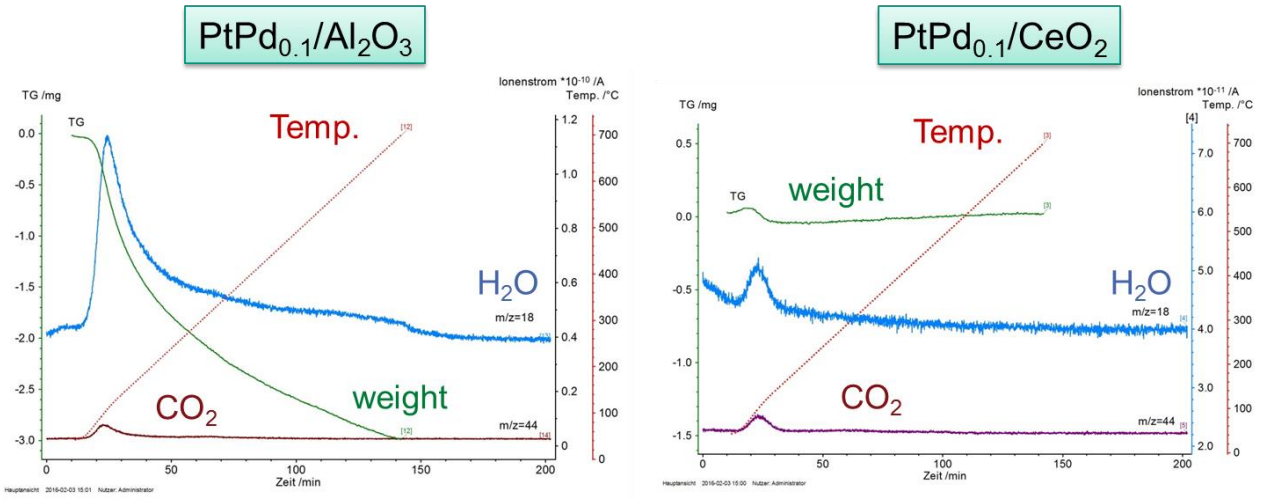


**Figure 34:** Thermogravimetric anylsis of Pd-Pt/$Al_2O_3$ and Pd-Pt/$CeO_2$. Samples were heated from room temperature to 700°C in 10% $O_2$ in $N_2$. Flow: 100 mL/min.

### 6.5 Regeneration of the catalysts after long term methane oxidation tests

The deactivation in $H_2O$ presence is reversible and can be slowed down as seen in Figure 31 and Figure 32 and Figure 30. Regeneration processes are divided into two parts in this report: oxidative and reductive treatments. In Figure 35 the successful regeneration under lean conditions is shown. After 25h the methane dosage was stopped and after 13 hours activity slightly regained. Although water was present all the time at constant temperature, a small increase in $CH_4$ oxidation is observed. This leads to the assumption, that water produced by the reaction plays a critical role during deactivation. Furthermore, also the addition of $NO_x$ leads to an increase in activity during operation. In that case the same effect was achieved by either adding NO or $NO_2$ or both at the same time.

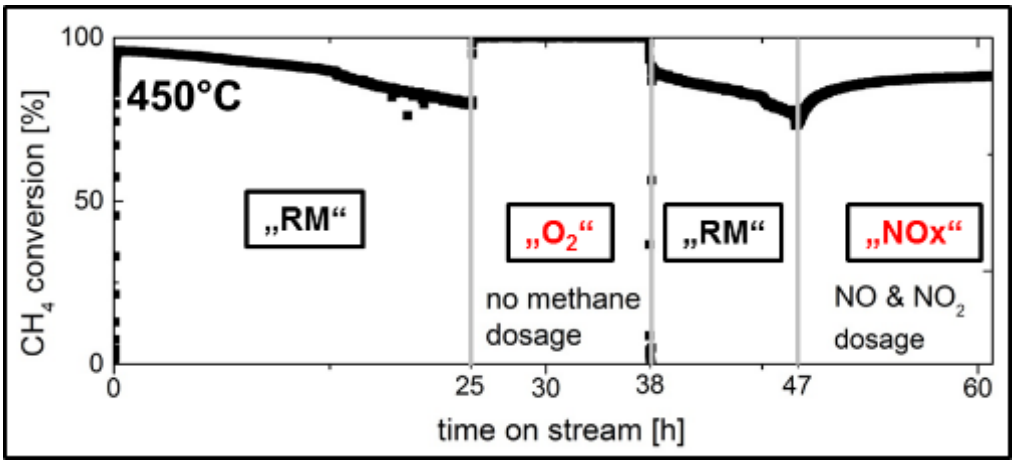


**Figure 35:** Oxidative treatments for catalyst regeneration with $CH_4$ conversion at 450°C under varying gas compositions on Pd-Pt model catalyst. “RM”: 3200ppm $CH_4$, 10% $O_2$, 12% $H_2O$ in $N_2$, “$O_2$”: 10%$O_2$, 12% $H_2O$ in $N_2$, “NOx”: 30ppm $NO_2$, 120ppm NO, 3200ppm $CH_4$, 10% $O_2$, 12% $H_2O$ in $N_2$.

Additionally, reductive conditions were found to be very effective for regeneration i.e. the time of reductive treatment is very short and the temperature does not have to be too high. From this

experiment no difference between rich atmosphere consisting primarily of $H_2$ or $CH_4$ was found. Switching to completely rich conditions ($H_2$) can recover the catalyst completely. Consecutive deactivation in wet reaction mixture was observed and shutting of $O_2$ (only $CH_4$, $H_2O$ and $N_2$) present lead also to complete regeneration. During rich operation under "$CH_4$" conditions methane still gets converted. However, partial oxidation as well as steam reforming occurs. The CO concentration behind the catalyst rises immediately and the temperature along the catalyst decreases since endothermic reactions take place.

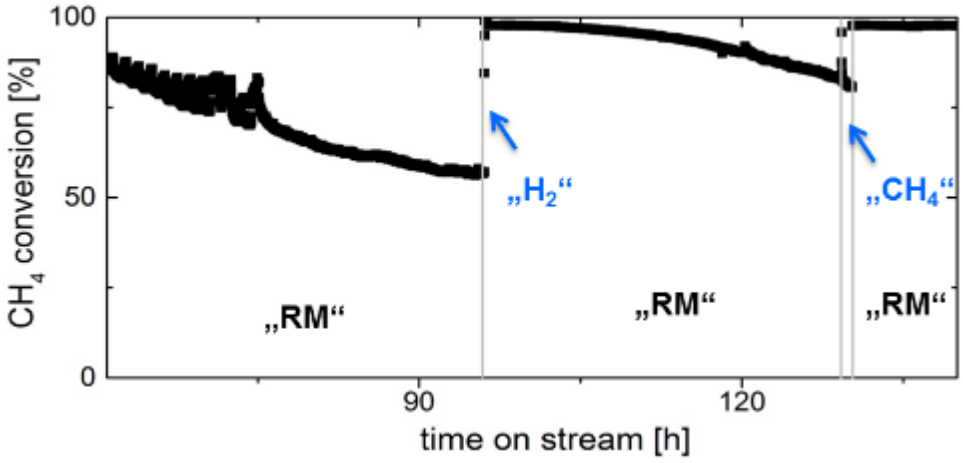


**Figure 36:** Reductive treatments for catalyst regeneration. $CH_4$ Conversion at 450°C under varying gas compositions on Pd-Pt model catalyst. "RM": 3200ppm $CH_4$, 10% $O_2$, 12% $H_2O$ in $N_2$, "$H_2$": 5%$H_2$ in $N_2$ for 5 min, "$CH_4$": 3200ppm $CH_4$, 12% $H_2O$ in $N_2$

## 6.6 Summary of the catalytic activity tests with and without water, NOx and influence of reactivation procedures

Testing of different catalysts revealed several interesting features. Water leads to pronounced inhibition of $CH_4$ oxidation on Pd based samples and not only to a negative reaction order. However, with a ceria based support this effect occurs to a smaller extent. The same behavior is observed for long-term activity. Pd-Pt/$CeO_2$ provided the best long-term activity while Pd-Pt/$Al_2O_3$ and Pd-Pt/$SiO_2$ almost deactivated completely at 450°C. A higher oxygen mobility on $CeO_2$ and the fact that adsorbed water is not as stable as on alumina can explain this effect. Regarding the different PGMs, Palladium is by far the most active metal for $CH_4$ oxidation. However, Pt shows no negative behavior in the presence of $H_2O$.

Due to the constant deactivation under lean burn reaction conditions, regeneration procedures were investigated. Almost every event that deviates from standard operation helps to partly regenerate the catalyst:

- heating in a reactive gas stream
- presence of NO or $NO_2$ or both
- absence of $CH_4$
- Rich conditions (hydrogen or only methane)

Based on these experiments, regeneration strategies can be derived, optimized and performed to ensure longer operating hours for methane oxidation catalysts.

# 7 *In operando* Characterization and Mechanism (KIT)

## 7.1 Introduction

The purpose of the operando XAS and DRIFTS studies was to uncover the structural variations of the catalysts which lead to the deactivation induced by water and NOx at low temperatures. Modulation-excitation XAS [71-73] results reported here are the first investigation of this type applied to study catalyst deactivation/reactivation during total methane oxidation. The obtained knowledge allowed us to better understand the impact of water on the noble metal sites during short or long exposure to a wet $CH_4$-oxidation atmosphere. Combined with complementary results on surface species acquired by DRIFTS, the negative effect of NOx on the low temperature catalyst conversion has also been clarified. As some of the experimental parameters are specific to these studies they are reported solely in this chapter.

## 7.2 Experimental

### 7.2.1 X-ray absorption spectroscopy (XAS)

X-ray absorption spectroscopy measurements were performed at SOLEIL synchrotron (Saint-Aubin, France) at the ROCK (Rocking Optics for Chemical Kinetics) beamline. The storage ring was operated at 2.75 GeV with a ring current of 450 mA in top-up mode. ROCK is a bending-magnet beamline equipped with a horizontally focusing toroidal mirror inside the shield wall of the storage ring in order collect the maximum number of photons. Quick-scanning EXAFS (QEXAFS) monochromators equipped with Si(111) and Si(220) channel-cut crystals were operated at 2 Hz for data acquisition at the Pt $L_{3,2,1}$-edges (11564 eV, 13273 eV and 13880 eV) in one sweep and the Pd K-edge (24350 eV) respectively. Incident and transmitted beam intensity was measured by ionization chambers (OKEN). Pt and Pd foils were placed between the 2$^{nd}$ and 3$^{rd}$ ionization chambers for checking the energy calibration similar to the experiments described in chapter 3.

### 7.2.2 *Operando* XAS experiment

The catalytic experiment at the beamline was conducted using the quartz capillary reactor setup used previously for synchrotron-based *operando* spectroscopy studies [74-76]. Ca. 30 mg of the Pd-Pt/$Al_2O_3$, Pd/$Al_2O_3$ and Pd-Pt/$SiO_2$ catalysts were loaded into 3 mm quartz capillaries (Hilgenberg) and the 12% Pd-Pt/CZYL in the 100-200 µm sieve fraction was loaded into a 0.5 mm diameter capillary (ca. 2 mg). The catalyst bed of ca. 9 mm length was fixed between plugs of quartz wool. Heating was provided by a hot air stream using the Gas Blower system (FMB Oxford) as done previously [23]. The temperature was controlled by a Eurotherm 2408 controller with a K-type thermocouple inside the Gas Blower.

Pure and mixed gases from gas cylinders (Air Liquide, purity >4.5) were dosed by mass flow controllers (MFCs, EL-flow, Bronkhorst). Gas mixtures in balance helium were composed of 4000 ppm $CH_4$, 10% $O_2$ and additionally 200 ppm NO and ca. 2% $H_2O$ added via a saturator at room temperature. In the following, gas compositions will be referred to only by the components, present in concentrations stated above. Total gas flows of 50 mL/min in the 3 mm capillary and 10 mL/min in the 0.5 mm capillary were applied, corresponding to space velocities between 50000 and 360000 $h^{-1}$ respectively. The higher space velocity applied to Pd-Pt/SZYL is justified by its high PGM loading, to maintain the same flow/mg PGM. Reaction products were analyzed by a quadrupole mass spectrometer (Thermostar, Pfeiffer Vacuum).

Light-off and light-out measurements were carried out during heating up from 100°C to 600°C at 5 K/min and cooling down at the same rate in the dry reaction mixture ($CH_4$ + $O_2$ in balance He) or using the wet reaction mixture with $H_2O$ from the saturator. Isothermal experiments were conducted at several temperatures to observe the long-term deactivation (1-1.5 hours). Reactivation by reduction in 4000 ppm $CH_4$ or 5% $H_2$, oxidative pre-treatment ($O_2$ on He only after $CH_4$ cut-off) and

temperature increase for a short time were conducted in between the long-term deactivation steps to monitor the effect on the noble metals' structure.

Operando QEXAFS measurements were performed to identify the optimal temperature for catalyst reactivation upon water long-term deactivation. For these test purpose, the catalyst were accommodated in the previously described capillary microreactor using 2 mm (catalyst supported on $Al_2O_3$) or 0.5 mm (for $CeO_2$-$ZrO_2$ catalysts) quartz capillaries and a main gas mixture containing 4000 ppm $CH_4$, 10%$O_2$ and He as balance. The Pd-sites were periodically reduced and reoxidized at selected temperatures by turning off/on the $O_2$ dosage.

### 7.2.3 X-ray absorption near-edge structure (XANES) and extended X-ray absorption fine-structure (EXAFS) data analysis

The raw data were processed using the Athena interface of the IFEFFIT software package [77]. The spectra were merged and normalized. The oxygen-to-noble-metal ratio (O/Pd and O/Pt) was estimated by linear combination analysis of the X-ray absorption near-edge structure (XANES) spectra of the catalysts with those of PdO, $PtO_2$ and the respective metal foils.

The extended X-ray absorption fine structure (EXAFS) was extracted in k-space and Fourier-transformation (FT) was conducted on the $k^3$-weighted EXAFS function (k = 2.0–12.5 $Å^{-1}$ for both Pd K and Pt $L_3$-edge spectra) to amplify the oscillations at high k-values. Phase shifts and amplitudes for relevant back-scattering paths were calculated using FEFF6. EXAFS refinement was carried out in R-space using the Artemis interface of the IFEFFIT software [77]. An R-range of 1.0-3.0 Å was used to analyze spectra of reduced Pt and 1.3-3.5 Å for all the other spectra. According to the Nyquist criterion, a maximum of 13 and 16 parameters can be extracted from the EXAFS data in these ranges respectively.

A fixed amplitude reduction factor ($S_0^2$= 0.75) determined from EXAFS refinement of PdO and $PtO_2$ and mean square thermal displacement ($\sigma^2$) values shared among the same back-scattering atoms in different shells were applied. In other cases, $\sigma^2$ was allowed to float unless stated otherwise.

### 7.2.4 Modulation excitation XAS

Modulation excitation XAS (MES) was conducted in order to amplify weak changes in the electronic structure of Pd and Pt while changing from high-conversion to low-conversion reaction conditions. The experiments were conducted isothermally at temperatures $T_{50}$, where approximately 50% methane conversion was achieved in the dry reaction mixture ($CH_4$ + $O_2$). Using a remotely-controlled four-way valve, periodic gas switches were conducted, so that dry mixture was dosed for 3 minutes, followed by a modified gas mixture for 3 minutes, which sums up to a full period of 6 minutes. The modified gas mixtures were (a) $O_2$ in He, (b) $CH_4$ + $O_2$ + $H_2O$, (c) $CH_4$ + $O_2$ + NO and (d) $CH_4$ in He. In order to obtain significant statistics, a total of 10-15 periods were carried out while measuring either at the Pd K or the Pt $L_3$-edge.

MES data analysis was carried out using a home-built script in MATLAB. The QEXAFS spectra corresponding to an integral number of periods were first selected by correlating the time stamp of the QEXAFS data with the online gas analysis data. On the order of 10000 spectra were normalized and averaged into one period of 36 spectra. The resulting time-resolved spectra were demodulated by multiplying each point by a sine function of 6 minutes period, taking into account phase-shifts in time and normalizing by the period duration. The demodulated spectrum with phase-shift zero thus corresponds to a difference spectrum between the active catalyst under the dry reaction mixture and that under the modified reaction mixture. The results were qualitatively and quantitatively evaluated by comparison to difference spectra of between PdO – Pd foil and $Pd(OH)_2$ – PdO for Pd K-edge spectra and $PtO_2$ – Pt foil and $H_2Pt(OH)_6$ – $PtO_2$ for Pt $L_3$-edge data.

### 7.2.5 Operando DRIFTS studies during pre-treatment and methane oxidation

DRIFTS (Diffuse Reflectance Infrared Fourier Transform Spectroscopy) spectra were recorded on a Bruker VERTEX 70 spectrometer equipped with diffuse-reflectance optics (Praying Mantis, Harrick) and an *in situ* cell (Harrick) for heating in a gas flow. The sample powder in a sieve fraction 125-250 µm was placed in the sample cup (6 mm diameter and 3 mm depth) and the cell was closed with a dome cover with KBr windows. The gas passed the sample from the top of the cup and exited through a wire mesh at the bottom.

Gases (Air Liquide, purity 5.0) were dosed using mass flow controllers and mixed before being directed to the cell. Liquid components (methanol and formic acid) were dosed via saturators in a He flow taking into account the vapor pressure at room temperature. The gas composition contained 4000 ppm fuel (methane, methanol or formic acid), 10% oxygen and balance helium. The total flow was 200 mL per minute. 200 ppm NO and 2% $H_2O$ were dosed as in XAS experiments. The gas composition at the exit of the cell was analyzed by mass spectrometry.

DRIFTS spectra were acquired in reflectance mode ($R = I_r/I_0$) and converted to the Kubelka-Munk function $KM(R) = ½(1-R)^2/R$, where $I_r$ is the reflected intensity and $I_0$ the "incident intensity" measured in diffuse reflectance mode of monocrystalline $CaF_2$ (sieve fraction 125-250 µm). The measurements of $CaF_2$ were conducted at temperatures of the catalyst measurements to take the significant contribution of blackbody radiation into account.

Each catalyst was baked out in a flow of $O_2$ in He at 600°C and background spectra at 550°C, 450°C, 350°C and 250°C, starting from the highest temperature and cooling in between. The background spectra correspond to the surface chemistry of a clean catalyst surface. Subsequently the catalyst was heated to 550°C, the first reaction mixture (methane and oxygen) was dosed and spectra were acquired at the same four temperatures in the same order, followed by a bake-out. The procedure was repeated with the other two reaction mixtures (methanol and oxygen, formic acid and oxygen). Results are reported as difference spectra between the catalyst under reaction conditions and the baked-out state at the relevant temperature.

In another experiment, light-off and light-out experiments were carried out by exposing a pretreated catalyst (bakeout in $O_2$/He at 600°C or reduction in $CH_4$/He at 400°C) to the reaction mixture (methane and oxygen) at 250°C, 350°C, 450°C and 550°C while heating, followed by measurements at the same temperatures in reverse order while cooling. Data are presented after subtracting spectra of the baked-out catalyst at corresponding temperatures.

Isothermal experiments at different temperatures were conducted under transient reaction conditions to study reversible and irreversible adsorption of molecules. For example, a sequence of reaction conditions $O_2 \rightarrow CH_4 + O_2 \rightarrow CH_4 + O_2 + NO \rightarrow CH_4 + O_2 \rightarrow O_2$ is designed to probe whether $CH_4$ and NO generate irreversibly adsorbed species on the catalyst. The results are reported as difference spectra relative to the baked-out state or the preceding state of the catalyst, as stated for each experiment. To investigate long-term effects under reaction conditions after various pre-treatments, difference spectra between the start and end of the exposure to the reaction conditions is presented.

## 7.3 Results and discussion

#### Inhibition by $H_2O$ and NO: effect on the noble metal

The addition of water (2% $H_2O$) and nitric oxide (200 ppm NO) to the gas flow has a pronounced negative effect, as shown in Figure 37. The isothermal study was conducted close to $T_{50}$, the temperature of 50% methane conversion where changes can be well-detected. Important is to note that the inhibition is reversible, as the conversion immediately increases once the inhibiting molecule is removed.

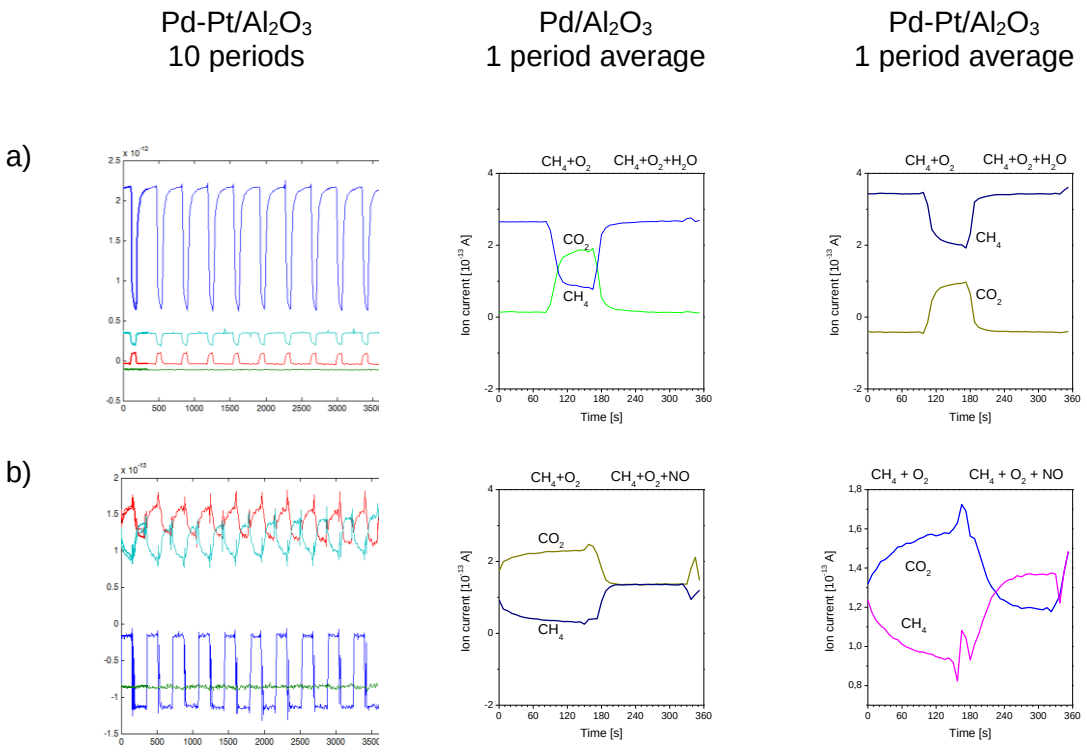


**Figure 37:** Mass spectrometer signals over 10 periods, and averaged to 1 period, of gas modulation (a) $CH_4 + O_2 \leftrightarrow CH_4 + O_2 + H_2O$ and (b) $CH_4 + O_2 \leftrightarrow CH_4 + O_2 + NO$.

Under periodic transient conditions, modulation excitation XAS studies on the Pd and Pd-Pt catalysts on $Al_2O_3$ are expected to reveal the effect on the noble metal of the inhibiting molecules. Figure 38 shows XANES spectra of the Pd and Pd-Pt catalysts under reaction conditions while switching $H_2O$ dosage on and off. The XANES spectra in Figure 38 (a) show completely oxidized Pd and Pt under dry and wet conditions. Demodulated spectra (Figure 38 (b)) reveal changes at the white line position (maximum after the edge) on the order of $10^{-3}$ in units of the normalized XANES spectrum. The in-phase demodulated spectra ($\Delta\phi = 0°$) exhibit the largest variation, showing that the structural changes are synchronous with the gas modulation. The demodulated spectra closely resemble the difference spectra between the hydroxide and the oxide (both in the same oxidation state, Figure 38(c)). The first interpretation of this is that switching from a dry to a wet reaction mixture induces the switch from a hydroxide to an oxide, which is counter-intuitive. XAS has merely shown that the electronic density at Pd and Pt decreased while turning to the wet mixture, which opens the possibility for other interpretations of the molecular interactions. The second, most likely, interpretation is that during switching to the wet mixture, the already present hydroxide groups on Pd and Pt bind via intermolecular hydrogen-bonds to the oxygen atom of the water molecules, thus also inducing a decrease of the electronic density at the metal atom. Quantitatively, the electronic effect seen in the demodulated spectra in Figure 38 (b) is only about 1% of the effect observed on the difference spectra in Figure 38 (c). This means that only 1% of available Pd-OH and Pt-OH groups interact with the water molecules. Since the noble metal dispersion is 40%, this small fraction corresponds to noble metal atoms at specific locations, such as at the periphery of the particles, in contact with the catalyst support.

In the Pd-Pt catalyst, the Pt atoms show the same response to the water switching as the Pd, indicating that both metals in the oxidized state occupy equivalent lattice positions and participate in the reaction. No segregation of Pt towards the core of the particles is observed here, as in the case where Pt is reduced to the metallic state [23].

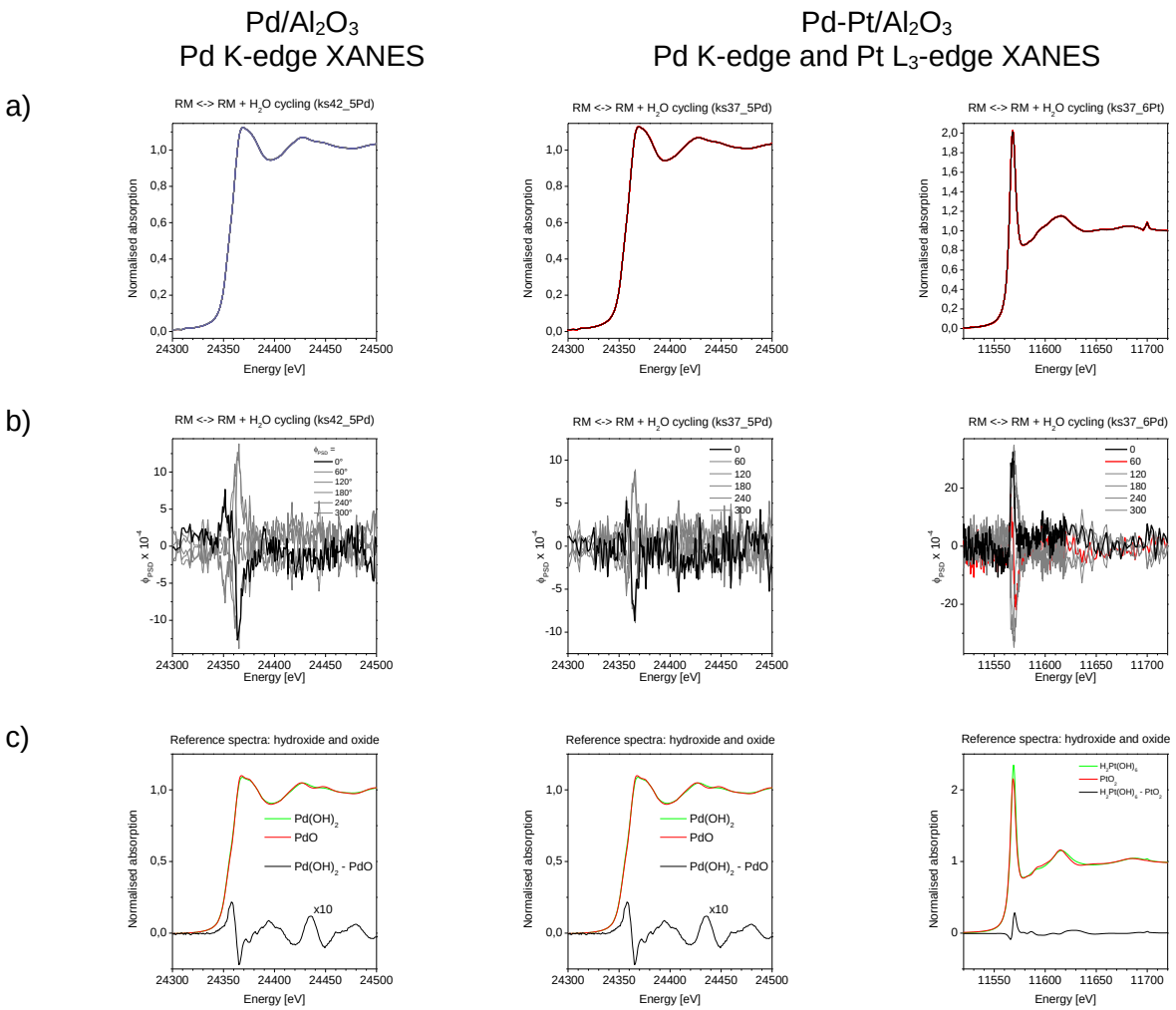


**Figure 38:** (a) Time-resolved and (b) phase-resolved XANES spectra during modulation excitation experiments without and with $H_2O$. (c) Reference spectra of respectively palladium and platinum hydroxide and oxide with difference for comparison to the phase-resolved spectra.

The response of the noble metal components towards nitric oxide is also weakly detectable and the modulation excitation method has successfully elucidated these effects. Figure 39 (a and b) shows the fully oxidized Pd and Pt during switching NO on and off and the demodulated spectra reflect the structural difference between the catalyst under the standard reaction mixture and the mixture with NO. The shape of the demodulated spectra is distinct from that in the dry-wet modulation and is similar to the difference spectra between PdO and Pd foil as well as $PtO_2$ and Pt foil in Figure 39 (c). As in the dry-wet modulation experiment, the extent of the changes is only 1% of the oxide – metal difference and the overall state of the noble metal is fully oxidised. Thus, the NO molecules donate electronic density to the Pd and Pt atoms, slightly increasing their electronic density. The binding of NO is known to be weak on Pd and strong on Pt [78], but due to the strong interaction of the two noble metals in the bimetallic catalyst, the effect is similar on both.

The inhibition of methane oxidation by water and NO are thus caused by electronic interaction with the Pd and Pt surface atoms and not by bulk changes such as reduction of the oxide to metal.

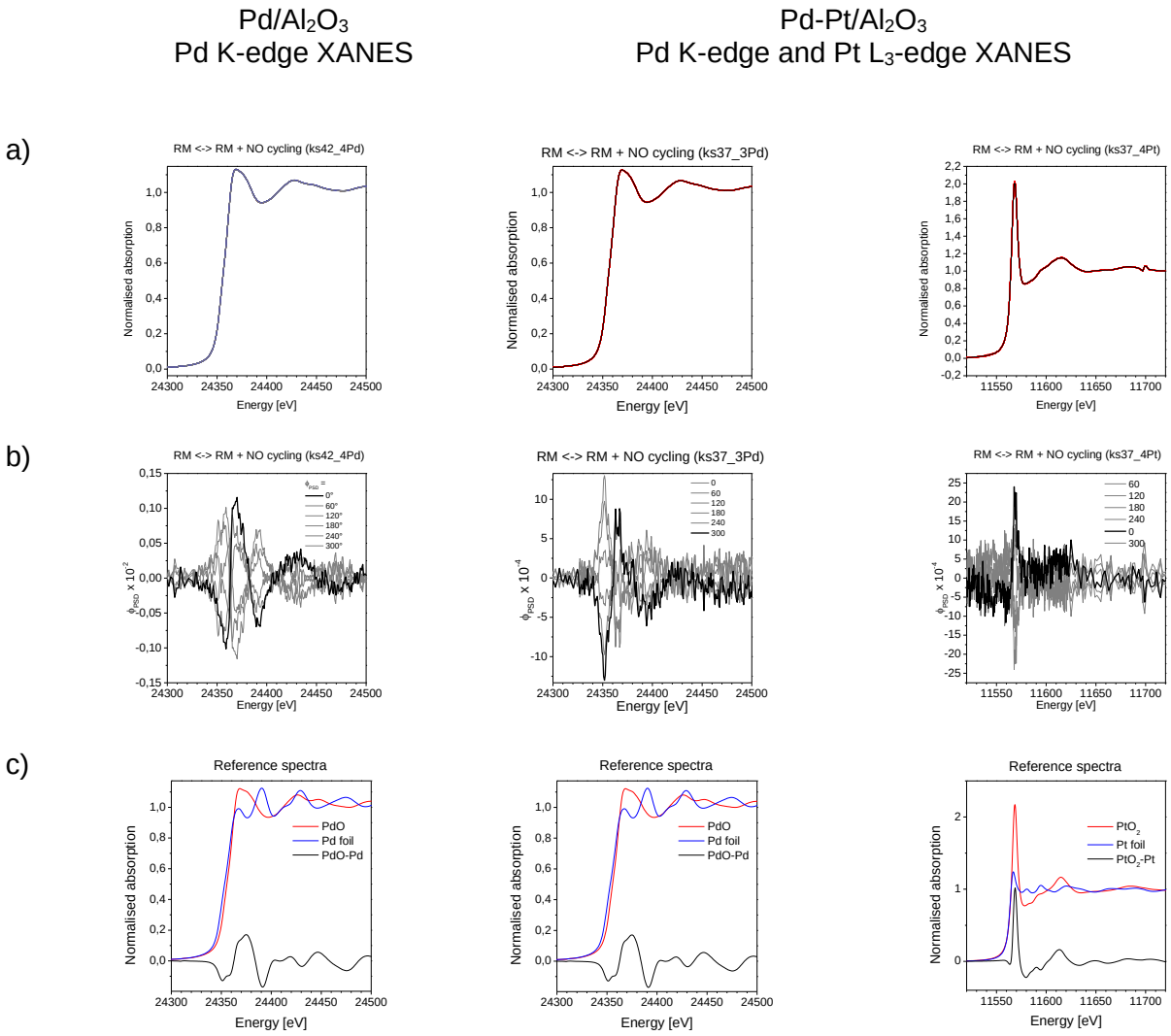


**Figure 39:** (a) Time-resolved and (b) phase-resolved XANES spectra during modulation excitation experiments without and with NO. (c) Reference spectra of respectively palladium and platinum oxide and metal with difference for comparison to the phase-resolved spectra.

### Surface species during methane oxidation

Using infrared spectroscopy (DRIFTS), long-lived educts, intermediates and products on the catalyst surface were identified. The monometallic $Pd/Al_2O_3$ catalyst was used for this set of experiments. Under dry reaction mixture (4000 ppm $CH_4$ + 10% $O_2$ in balance He), the narrow bands at 3000 and 1300 $cm^{-1}$ (marked orange in Figure 40 (a)) are due to gas-phase methane [79]. Broadened bands at 3000, 2900 [79], as well as 1600, 1400 and 1390 $cm^{-1}$ (marked green) are due to surface species formed as a result of adsorption and activation of methane. At 550°C the coverage by these molecules is low but at lower temperatures they are stable on the surface. The formation of these species is positively correlated with the methane conversion. These species are stable at low temperatures, also under dry air and humid conditions, see Figure 40 (d). Methane conversion was 100% at 550°C, 80% at 450°C, 25% at 350°C and 0% at 250°C.

Some of the water produced in the reaction adsorbed on the alumina surface hydroxyls, giving rise to a broad band between 3500-3600 $cm^{-1}$ (O-H stretch of the water molecule, marked blue) and a small negative band at 3770 $cm^{-1}$ (O-H stretch of the occupied surface hydroxyl of the alumina) [20].

When oxidizing methanol and formic acid in analogous experiments, conversion of both fuels was 100% in the reported temperature range. At 550°C and 450°C, the same broadened bands marked

green in Figure 40 (b and c) are observed as those when oxidizing methane. The intermediates common for oxidation of all three fuels thus contains carbon in an oxidation state of at least +2, as in formic acid, and are most probably formates. The pyrolytic decomposition route for methane [80] can thus be ruled out, although infrared signals of $CH_x$-metal complexes can be expected in the range <1000-1800 $cm^{-1}$ [81, 82]. The oxidized species are not carbonates, since characteristic bands for carbonates formed during dosage of $CO_2$ [82] were not observed.

Additional bands arising at 350°C and 250°C (2880, 1640, 1660 and 1315 $cm^{-1}$, marked red) are most probably due to weakly adsorbed formates, as these form during oxidation of both methanol and formic acid. No unique adsorbed species during oxidation of methanol were observed, indicating that methanol is rapidly oxidized via the formate route.

Water is likewise formed and adsorbed on the surface hydroxyl of the alumina. The weakly adsorbed formate groups are also likely associated with surface hydroxyls, since the appearance of their bands is correlated to a growth of the negative band at 3770 $cm^{-1}$ (marked red).

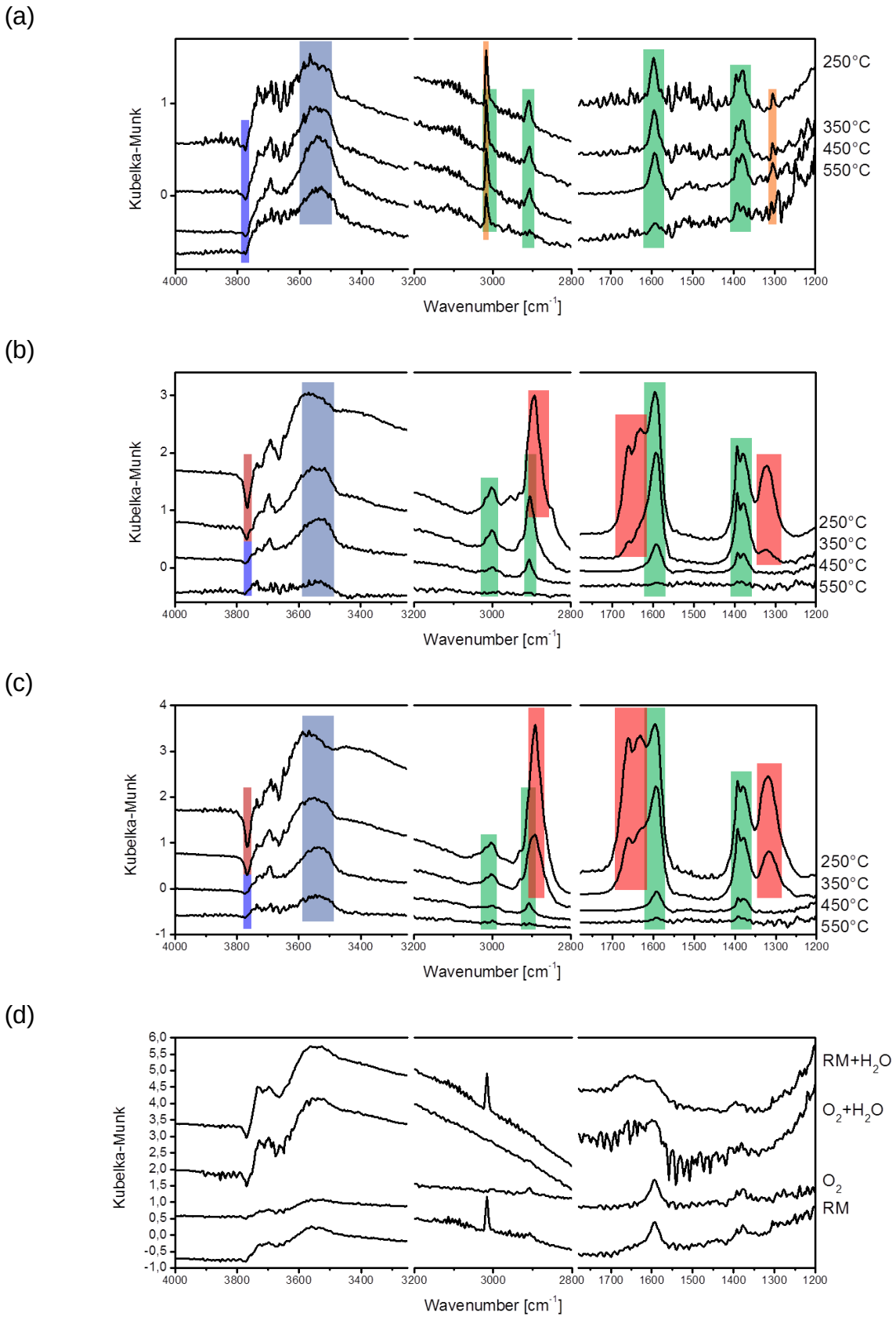


**Figure 40:** In situ DRIFT spectra of 2.4wt.-% $Pd/Al_2O_3$ catalyst exposed to (a) methane + oxygen, (b) methanol + oxygen and (c) formic acid + oxygen at indicated temperatures. (d) The same catalyst exposed to methane + oxygen, flushed with oxygen, exposed to water vapour and wet methane + oxygen at 350°C. The gas composition contained 4000 ppm fuel (methane, methanol or formic acid), 10% oxygen and balance helium. The total flow was 200 mL per minute.

The appearance of abovementioned methane and formate surface species depends strongly on temperature and methane conversion. Running methane oxidation in a dry mixture over a baked-out 2.4% $Pd/Al_2O_3$ catalyst will generate these surface species at 550°C (100% conversion), but not at 350°C (25% conversion), as seen in Figure 41 (a). The DRIFT spectra are shown as difference spectra relative to the baked-out catalyst in $O_2$/He before admitting methane. Water produced in the reaction is likewise adsorbed on the catalyst at 550°C. Interestingly, in the absence of Pd ($Al_2O_3$ only), none of the adsorbed species are formed and only gas-phase methane is detected.

Whether the methane and formate surface species are located on the PdO or $Al_2O_3$ sites is not clarified. The exposure of crystalline PdO and Pd mixed with $CaF_2$ to the reaction mixture has neither produced detectable surface species nor shown any methane conversion. From this it is clear that both the noble metal and the support are essential in the composition of the methane oxidation catalyst.

The effect of adding water (2% $H_2O$ via saturator) is shown in Figure 41 (b). The DRIFT spectra here are shown as differences to the spectra under dry conditions prior to adding water. Hydrogen-bond associated water occupies the surface of $Al_2O_3$, as the band at 3550 $cm^{-1}$ is observed both for the catalyst and bare $Al_2O_3$. Also at 350°C, weakly adsorbed water is observed as an HOH-scissors band at 1650 cm-1 [83]. Especially at 550°C, negative bands corresponding to methane and formate surface species appear, indicating that their adsorption is in competition with water. To some extent, the adsorption of methane but not of formates is inhibited at 350°C. The inhibition of these species' adsorption by the strongly competing water is likely to be linked to the inhibition of methane oxidation, even at high temperatures (550°C). On bare $Al_2O_3$, this competitive behaviour is not observed, as $Al_2O_3$ does not adsorb methane or formates under these conditions.

(a)

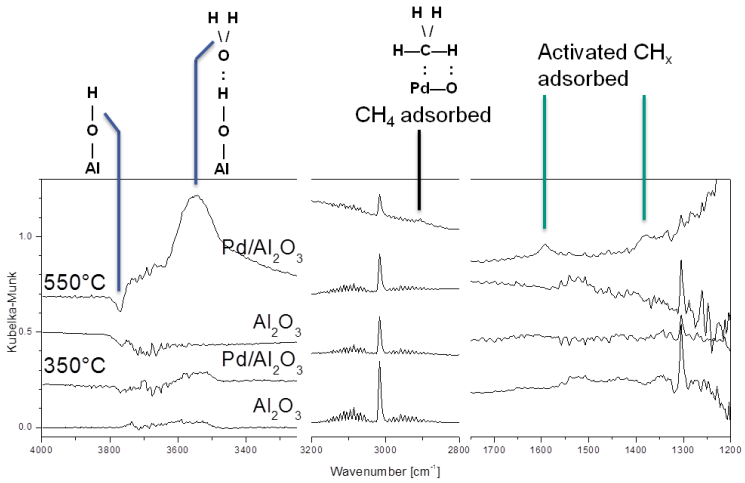


(b)

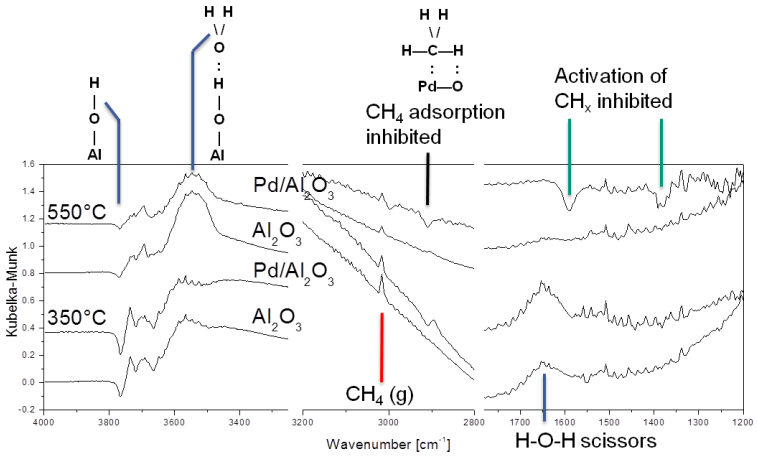

(c)

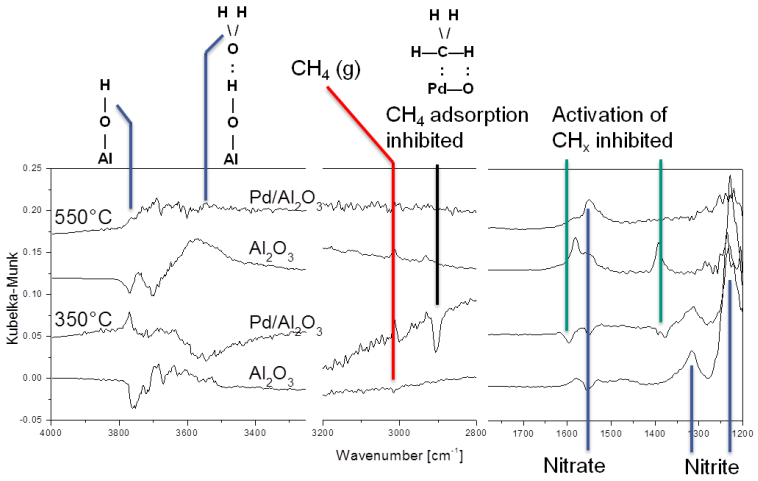


**Figure 41:** DRIFT spectra of $Pd/Al_2O_3$ expressed as difference spectra between (a) standard reaction conditions ($CH_4 + O_2$) and oxygen, (b) wet and dry reaction conditions and (c) reaction conditions with and without NO.

The effect of NO on the observed surface species was studied in an analogous manner. The DRIFT spectra shown in Figure 41 (c) are differences between spectra under reaction conditions with NO and without NO. At 350°C, surface nitrite groups are generated (1250 and 1320 $cm^{-1}$) [84] and the surface coverage of methane and formates is strongly decreased, as seen in the corresponding negative bands. The water production in the course of reaction is also inhibited; the bands in the range 3500-3800 $cm^{-1}$ are inverted. The effect on bare $Al_2O_3$ is insignificant. At 550°C, instead of the nitrite bands, nitrate species at 1550 $cm^{-1}$ [84] are observed both for the catalyst and bare $Al_2O_3$, indicating the thermodynamically favoured NO oxidation to $NO_2$. Under these conditions, no inhibition takes place over the catalyst, as no negative bands are observed. On the other hand, positive bands corresponding to methane and formate species as well as H-bond associated water are seen on the bare $Al_2O_3$. This is an indication of a gas-phase reaction of methane with $NO_2$ to $CO_2$ and NO, which has also been reported previously [85, 86] and which can explain the positive effect of $NO_x$ on methane oxidation above 450°C.

In order to study the adsorption reversibility of the methane, formate and nitrate species, DRIFT spectra were taken before and after exposure of the $Pd\text{-}Pt/Al_2O_3$ model catalyst (supplied by Heraeus) to the respective gas components Figure 42 (a and c) shows a sequence of spectra taken following bake-out, under the dry reaction mixture (RM, $CH_4 + O_2$ in He), after adding NO to RM, after turning off NO and after turning off $CH_4$ ($O_2$ only in He) at 430°C and 550°C respectively, starting from the uppermost plots. Long-term changes in surface coverage while steady-state conditions are reached under RM, RM with NO and subsequent exposure to RM at 430°C and 550°C are shown as time-differential plots in Figure 42 (b and d) respectively, starting from the uppermost plots.

At 430°C in the reaction mixture (50% methane conversion), bands characteristic for adsorbed methane and formates as well as H-bonded water are observed and continuously evolve. At 550°C (100% conversion) the same surface species appear, but much more rapidly. On inclusion of NO, nitrate species build up at both temperatures, replacing a part of methane and formate adsorbates. When NO is turned off, the nitrate species stay at 430°C but are removed at 550°C, demonstrating temperature-dependence of their coverage. At both temperatures, the methane and formate coverage decrease irreversibly during and after NO exposure. When methane is turned off, methane and formate adsorbates are removed at both temperatures. In summary it is noteworthy that NO has an inhibitory effect on methane adsorption and formate formation, even at high enough temperatures that the generated nitrates are desorbed.

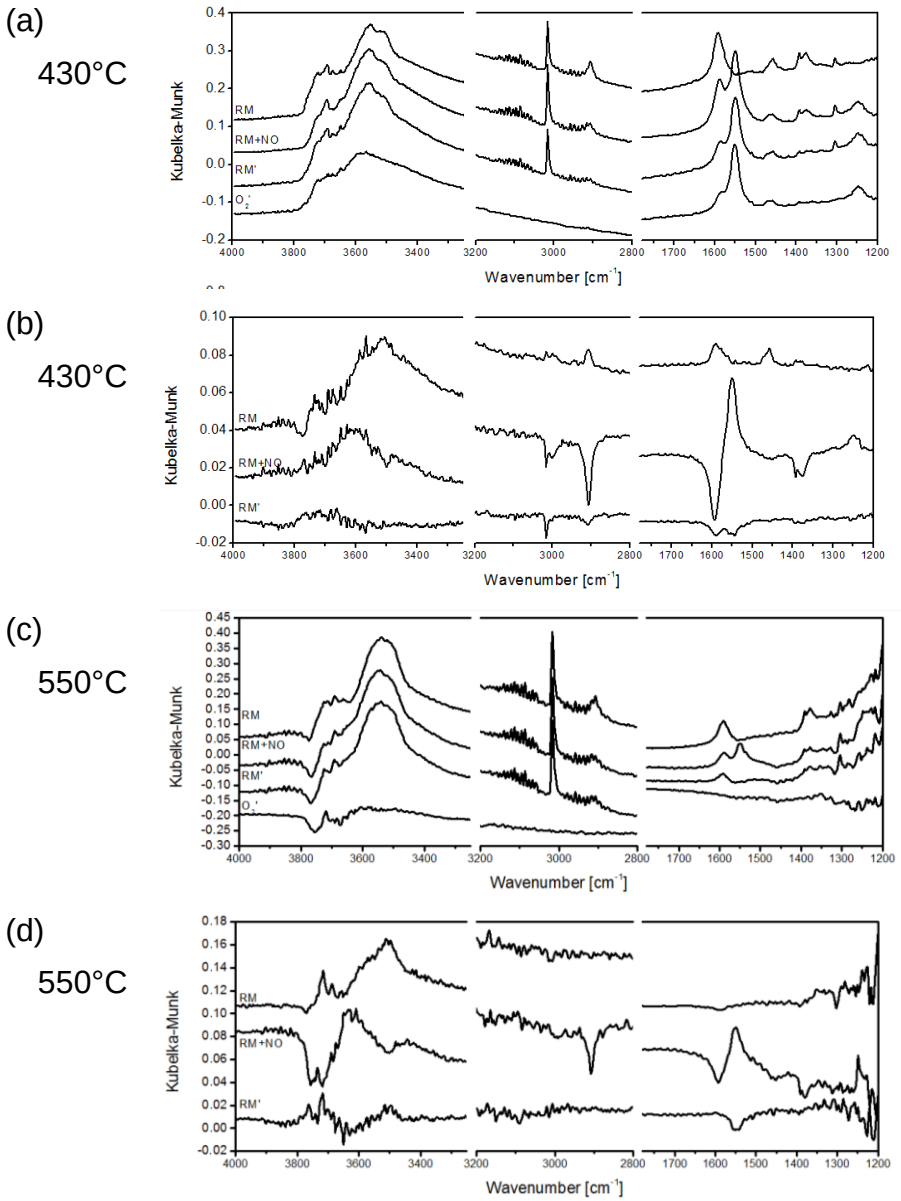


**Figure 42:** 2.4% Pd-Pt/$Al_2O_3$ model catalyst) exposed to a sequence of conditions: $CH_4$ + $O_2$ (RM) → $CH_4$ + $O_2$ + NO (RM + NO) → $CH_4$ + $O_2$ (RM) → $O_2$. (a and c) The experiment conducted at 430°C (50% methane conversion) and 550°C (100% methane conversion) respectively, starting from upper plots. (b and d) Long-term changes while steady-state conditions in (a and c) respectively are reached.

### DRIFTS studies of regeneration procedures

It has been shown that a deactivated catalyst can be regenerated by increasing its temperature. A DRIFTS study of this regeneration strategy of the 2.4wt.% Pd-Pt/$Al_2O_3$ KIT catalyst is shown in Figure 43(a). During this experiment the dry reaction mixture was dosed and the testing and measuring temperature was 410°C. After an initial run for 15 minutes, the methane conversion fell from 80% to 65%. The catalyst was subsequently baked out at 620°C for 5 minutes in the reaction mixture and returned to 410°C, where the conversion stabilized between 65-70%. The lower plot in Figure 43 (a, “baking”) shows the effect of baking as a difference spectrum between the state after baking and the state before. The upper plot (“RM baked”) shows the difference spectrum between the state after a further 15 minute run in the reaction mixture and the state immediately after baking-out. Increasing the temperature to 620°C causes adsorbed methane and formate species as well as water to desorb, seen as negative bands in the plot. A further run under reaction conditions generates all the adsorbates again. Especially the removal of water as a reaction inhibitor is an important regeneration step.

An analogous experiment has been conducted with 200 ppm NO in the reaction mixture used in the long-term deactivation, which brought the methane conversion down to 45% at 410°C. The bake-out and following run was carried out without NO and the resulting conversion at 410°C was 35%. DRIFT spectra shown in Figure 43 (b) show the negative bands of the desorbed nitrates, methane, formates and water as temperature was increased to 620°C ("baking after RM+NO"). After the following run at 410°C ("RM baked") the bands of adsorbed methane, formates and water re-appeared, but the formate bands were significantly weaker. The low methane conversion can thus be correlated to the low coverage of formate intermediates. The permanent loss of catalytic activity and formate intermediate formation by the presence of NO is once more demonstrated.

Further regeneration strategies are the pre-oxidation (methane cut-off) and the pre-reduction (oxygen cut-off) at isothermal conditions. DRIFTS spectra of the 2.4wt.-% Pd-Pt/$Al_2O_3$ catalyst recorded during the two types of regeneration steps as well as methane oxidation following the regeneration steps, all at 450°C, are shown in Figure 43 (c) as differences relative to the baked-out state. During methane oxidation over a pre-oxidized catalyst (plot "RM ox."), a stable methane conversion of 65% and the usual methane, formate and water adsorbates were observed. The same conversion and species were observed during methane oxidation over a pre-reduced catalyst (plot "RM red."). During the pre-reduction (plot "$CH_4$"), the spectral background increased due to the higher infrared absorption by metallic Pd, the coverage by methane and formates has slightly decreased and adsorbed water was completely removed. During the pre-oxidation (plot "$O_2$"), the water adsorbates also significantly decreased, but the methane and formates only slightly.

The various regeneration steps investigated here have in common the removal of adsorbed water, which takes place during bake-out as well as stopping the reaction by cut-off of fuel or oxygen. Methane and formate adsorbates are always generated on the catalyst surface and are an indication of the methane oxidation reaction. In the presence of NO, however, the catalyst suffers a permanent deactivation to some extent, even if the nitrate species have been removed at high temperatures.

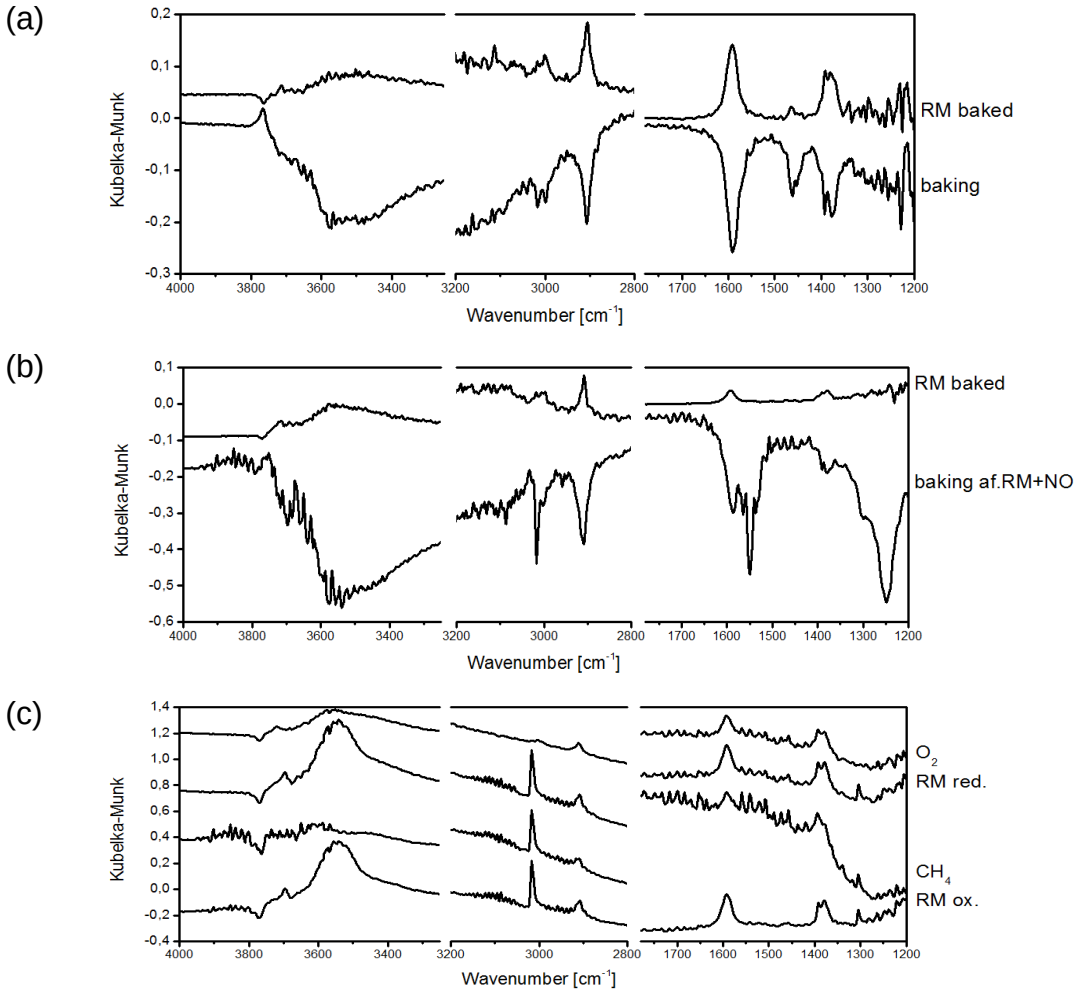


**Figure 43:** DRIFTS spectra of 2.4% Pd-Pt/$Al_2O_3$ during methane oxidation following catalyst regeneration and during the regeneration steps. (a) Short bake-out at 620°C in reaction mixture ($CH_4$ + $O_2$ in He) and returning to reaction temperature of 410°C. (b) Short bake-out at 620°C in reaction mixture ($CH_4$ + $O_2$ in He) after reaction in presence of 200 ppm NO and returning to reaction temperature of 410°C. Spectra in (a) and (b) show differences between after and before the bake-out ("baking") and between several minutes into the following reaction run and immediately after bake-out ("RM baked"). (c) Methane oxidation over a pre-oxidised catalyst ("RM ox."), pre-reduction by oxygen cut-off ("$CH_4$"), methane oxidation over a pre-reduced catalyst ("RM red.") and pre-oxidation by methane cut-off ("$O_2$"). The experiment was conducted at 450°C and the spectra are differences relative to the freshly baked-out catalyst.

### Temperature-dependent hysteresis of methane oxidation on Pd/CZ

The effect of pre-oxidation and pre-reduction was likewise studied on the 2.4% Pd/CZ by *in situ* DRIFTS. Pre-oxidation was done under a flow of 10% $O_2$ in He at 620°C and the pre-reduction under 4000 ppm $CH_4$ in He at 400°C. The pre-treated catalyst was exposed to the dry reaction mixture ($CH_4$ + $O_2$ in He) and spectra were acquired under steady-state conditions stabilized at 250°C, 350°C, 450°C and 550°C while heating up and at the same temperatures while cooling down. Figure 44 shows the methane conversion to $CO_2$ in both experiments. In both cases the methane conversion was lower during cooling down than heating up. The pre-oxidation and pre-reduction thus activate the catalyst, while reaction conditions deactivate it.

Figure 44 (b and c) show temperature-dependent DRIFT spectra during the heating and cooling cycles, advancing from lower to upper plots. The spectral features are slightly different to the ones observed on $Al_2O_3$-supported catalysts. The adsorbed methane band is at slightly lower wave numbers at 2850 $cm^{-1}$ and is observed at 250°C and 350°C, while at higher temperatures methane is not adsorbed. The presumably formate adsorbates exhibit a broad band between 1300-1600 $cm^{-1}$ and their presence remains largely unchanged at the different temperatures. Also remarkable is

that the intensity of the band of the H-bond-associated water practically is independent of temperature, suggesting that the CZ support is insensitive to the presence of water. In spectra at 350°C and 250°C in the cool-down cycle, a negative band at 1520 $cm^{-1}$ is observed in both experiments. The identification of surface species giving rise to this band is still to be investigated, but it cannot be excluded that this species is responsible for the increased activity of the freshly pre-treated catalyst and is removed during reaction at 550°C.

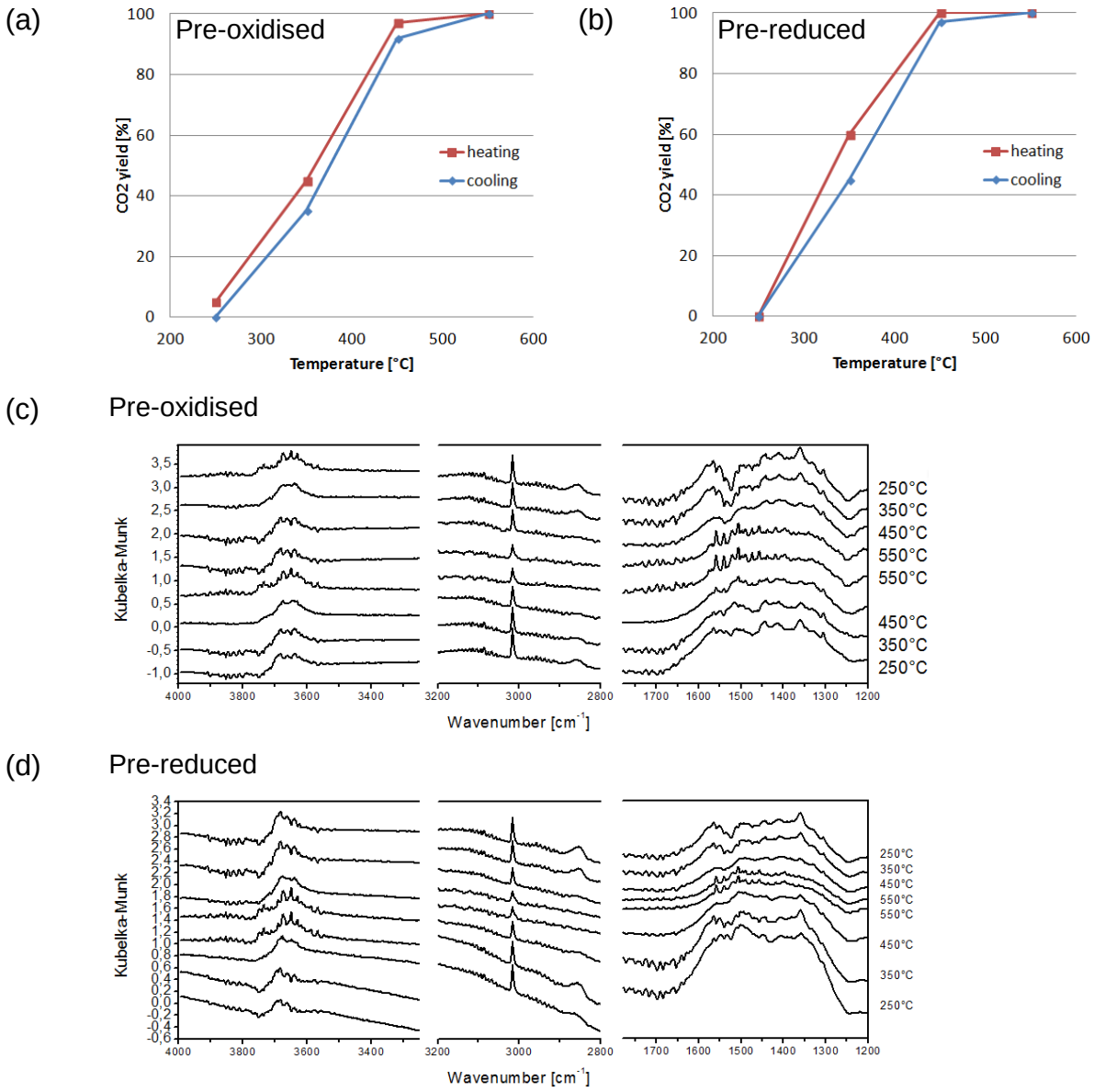


**Figure 44:** Temperature-dependent methane conversion over 2.4% Pd/CZ after pre-oxidation in $O_2$ in He at 620°C (a) and pre-reduction in $CH_4$ in He at 400°C (b). Heating and cooling took place in steps of 100°C, stabilising the reaction conditions at each temperature. DRIFT spectra recorded under corresponding reaction conditions (c) and (d) respectively. The DRIFT spectra are presented relative to $CaF_2$ measured at the same temperatures. The spectra in chronological order of the heating-cooling cycle advance from the lower to the upper plots.

The effect of external water and fuel cut-off during methane oxidation on the surface species of Pd/CZ was studies at 350°C. Additionally, pure CZ support was exposed to the same conditions to elucidate the role of the noble metal. DRIFT spectra in Figure 45 show methane and presumably formate adsorbates as well as water during exposure of Pd/CZ to the dry reaction mixture, while only some formates were observed over pure CZ. These formates are most probably spectator species formed during the interaction of methane and CZ. Fuel cut-off after reaction led to the

complete desorption of methane and water, leaving the abovementioned CZ-bonded formates. Addition of external 2% $H_2O$ has inhibited the adsorption of methane and led to generation of another surface adsorbate, exhibiting a broad band at 1630 $cm^{-1}$.

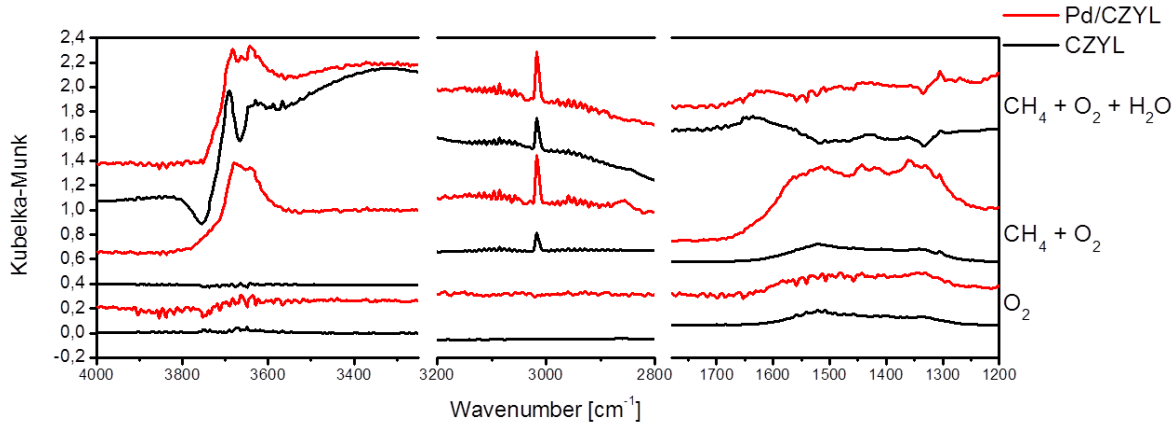


**Figure 45:** DRIFT spectra recorded at 350°C on 2.4% Pd/CZ and pure CZ during exposure to dry reaction conditions ($CH_4$ + $O_2$), subsequent fuel cut-off ($O_2$) and with 2% external water ($CH_4$ + $O_2$ + $H_2O$). Spectra are shown as differences relative to the baked-out state of the respective material.

### Long-term water deactivation and regeneration parameters

The long-term deactivation in wet reaction conditions ($CH_4$ + $O_2$ + $H_2O$ in He) and reductive regeneration with hydrogen was studied on 2.4% Pd-Pt/$Al_2O_3$ using *in situ* XAS at 335°C at both the Pd K-edge and the Pt $L_3$-edge. The oxidation state of Pd and Pt is expressed in terms of the O/Pd and O/Pt atomic ratio, determined by linear combination analysis of the reference oxide and foil XANES spectra (Figure 46 (a)). Prior to this experiment, the catalyst was exposed to reductive conditions, resulting is its partially reduced state. Starting with a peak methane conversion of 90%, it rapidly dropped to a final 35% after 90 minutes (Figure 46 (b)). The oxidation state of both noble metals remained constant. As previously explained, catalyst deactivation by water adsorption and formation of surface/bulk $Pd(OH)_2$ leads only to minor changes in the XANES spectra which could be uncovered only by operando modulation-excitation XAS. After a reductive treatment for 10 minutes in 5% $H_2$ in He, the noble metal were completely reduced. In a next step the $CH_4$ oxidation gas mixture was introduced over the catalyst bed at the same temperature of 335°C. The recorded MS signal (Figure 46 (b)) indicates only partial recovery of the catalyst activity with a slightly higher initial methane conversion. Nevertheless, this is immediately dropping due to water exposure. Such a behaviour seems to correlate with the evolution of Pd oxidation state. Thus, completely oxidized sites are present in the fresh catalyst and also during deactivation. To regenerate the catalyst reducing steps have been demonstrated as very efficient (chapter 6.5). At 335°C the complete reduction of Pd sites is achieved (Figure 46 (a)), which should remove the inhibiting hydroxyl groups from the noble metal sites. However, when switching back to the reaction mixture only a partial reoxidation or formation of a less effective amorphous PdOx phase was observed, relative to the oxidation state in the fresh catalyst. According to *Datye et al.* the transition from bulk metallic Pd to bulk PdO is a kinetically limited process [8] due to initial formation of an amorphous surface oxide which acts as a passivating layer.

Since the short reductive steps at 450°C (chapter 6.5) lead to integral recovery of activity, a higher temperature seems to be necessary for complete regeneration. To confirm this hypothesis, further measurements were done at selected temperatures along the light-off of methane oxidation (temperature of 30%, 50% and above 100% $CH_4$ conversion, as indicated in Table 16. The experiments were done for Pd-only and Pd-Pt/$Al_2O_3$ samples and also for the high loaded Pd-Pt/CZ catalysts, which has been found to not show such pronounced long-term deactivation (Figure 33).

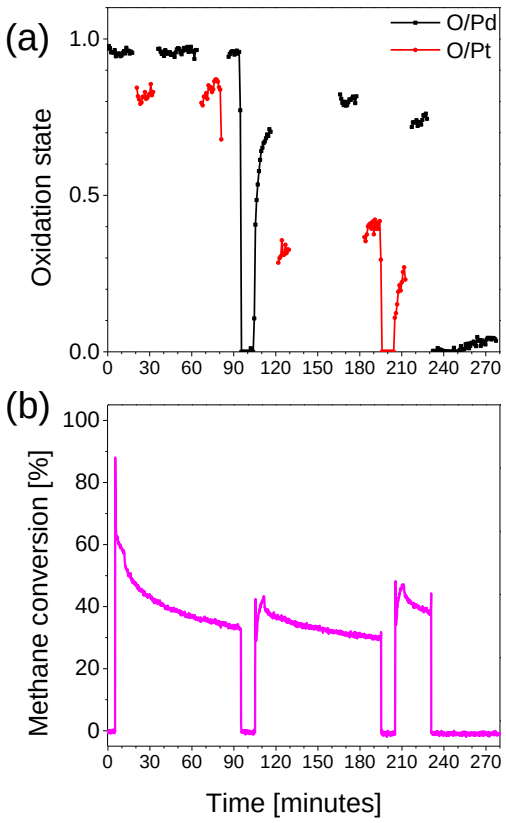


**Figure 46:** XAS study of long-term deactivation of 2.4wt.-% Pd-Pt/$Al_2O_3$ in a wet reaction mixture ($CH_4$ + $O_2$ + $H_2O$ in He) at 335°C for 90 minutes, followed by a treatment in 5% $H_2$/He for 10 minutes, repeated twice. (a) Oxidation state of the noble metals in terms of the O/Pd and O/Pt atomic ratios calculated from XANES of references PdO, Pd foil, $PtO_2$ and Pt foil. (b) Methane conversion measured online during the experiment.

**Table 17:** Overview of the investigated samples and applied conditions (temperatures of 30%, 50% and above 100% $CH_4$ conversion).

| catalyst | $T_{30}$ [°C] | $T_{50}$ [°C] | $T_{100}$ [°C] |
|---|---|---|---|
| PdPt/$Al_2O_3$ | 250 | 350 | 500 |
| Pd/$Al_2O_3$ | 280 | 335 | 500 |
| PdPt/CZ high | 280 | 315 | * |

As illustrated in Figure 47 (a) for Pd/$Al_2O_3$, the reduction of Pd sites by $CH_4$ is a very slow process at low temperatures on the light-off. Similarly, a relatively slow and incomplete reoxidation was observed when switching back to the reaction mixture. In contrast, at 500°C a fast and complete conversion to metallic Pd was recorded. However, even at this temperature, the formation of PdO requires a very long time. The addition of Pt does not improve the redox response of Pd sites. On contrary, the extent of reoxidation is lower at intermediate temperature (335°C). At full $CH_4$ conversion PdO forms but after about 15 min exposure to the reaction atmosphere.

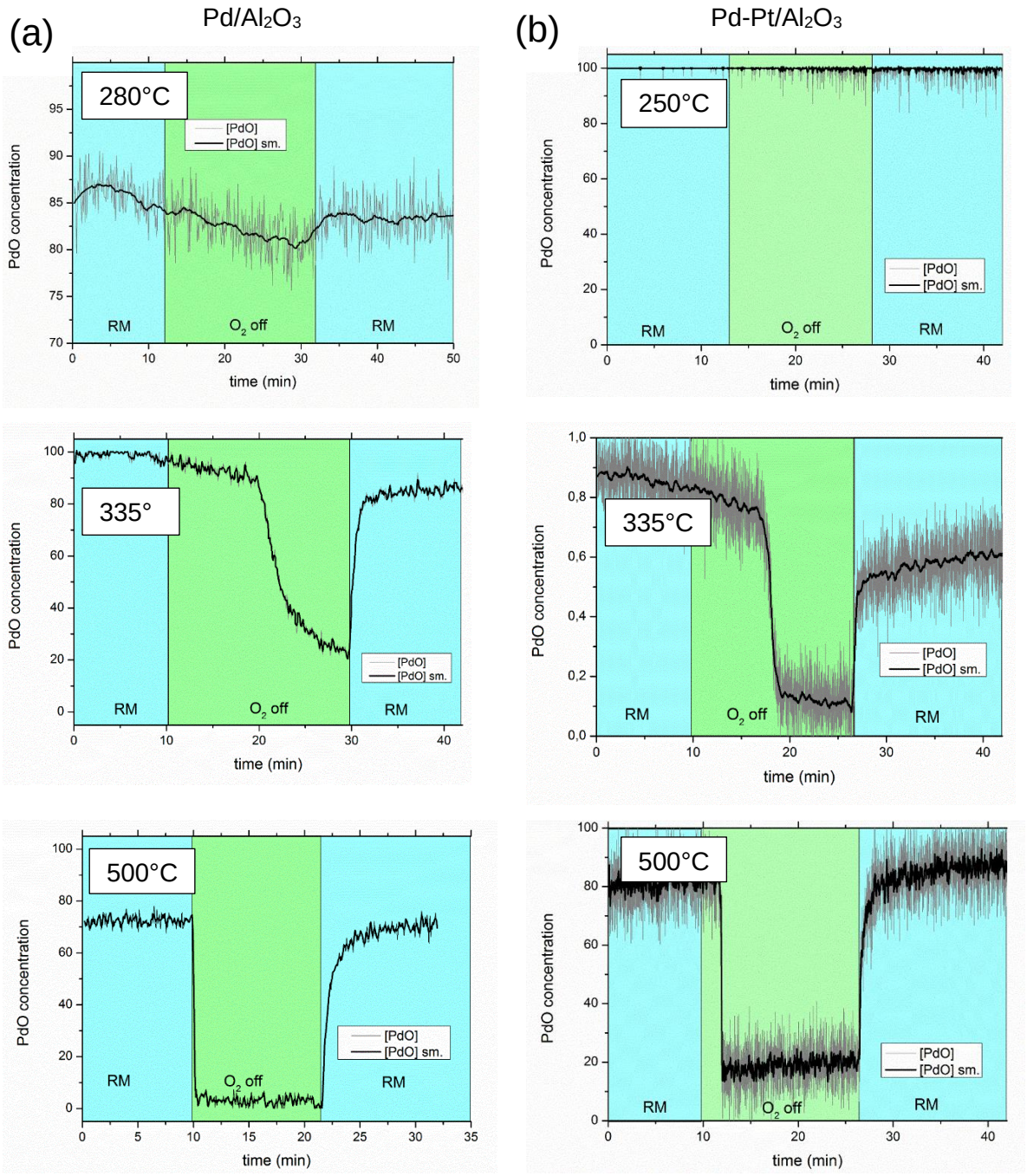


**Figure 47:** Results of the linear combination fit analysis of the XANES region for Pd K edge at selected temperatures during turning off/on the $O_2$ dosage; gas mixture 4000 ppm $CH_4$, 10% $O_2$ in He.

For a $CeO_2$-$ZrO_2$ supported Pd-Pt catalyst the reduction of Pd sites is an even slower process, probably due to the oxygen storage capacity of the ceria carrier. Furthermore, after 20 minutes in $CH_4$-He at 315°C only 50% of PdO was converted to metallic Pd. For similar intermediate temperatures (T50) on the light-off a more pronounced reduction occurs for the catalyst supported on $Al_2O_3$ (close to 100% conversion). The reoxidation of the sites seems to be additionally delayed in comparison with Pd-Pt/$Al_2O_3$, probably due to simultaneous carrier reoxidation. For a final unambiguous interpretation some further studies would be required.

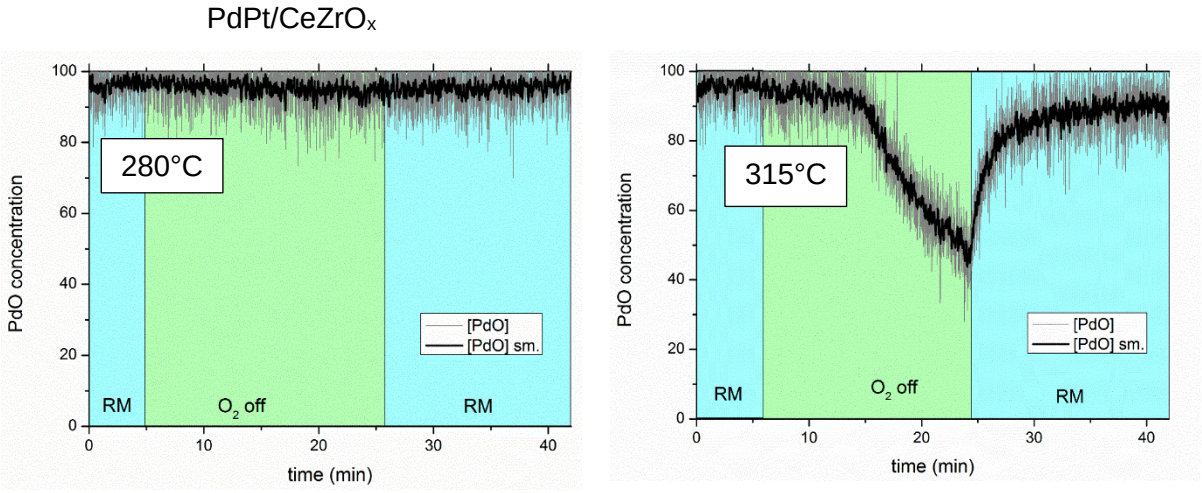


**Figure 48:** Results of the linear combination fit analysis of the XANES region for Pd K edge at selected temperatures during turning off/on the $O_2$ dosage; gas mixture 4000 ppm $CH_4$, 10% $O_2$ in He.

In summary, it appears that not only the reduction of the deactivated catalyst is important but also bulk reoxidation of Pd particles should be considered. Thus, for an effective regeneration, catalyst composition, reaction atmosphere and reactivation temperature are central parameters and can be taken as guidelines for improvement of the catalysts.

## 7.4 Summary *in operando* Characterization and Mechanism

*Operando* characterization has demonstrated to be a powerful tool to investigate the processes taking place during operation or deactivation of Pd-based catalysts. The strong inhibiting effect by water only causes small changes in the catalyst structure. This is most probably related to water bond on a Pd-OH species in close contact to the support. Using a surface sensitive characterization technique confirmed the presence of surface hydroxyls. Their presence leads to a blockage of sites and lowers the the possibility for methane to adsorb on the catalyst and to be oxidized. Once methane is adsorbed on an active site and the first C-H-bond is split is the rate determining step. For this, oxidized Pd is needed and then the reaction proceeds via the formation of formates to finally produce $CO_2$ and $H_2O$. Based on literature data and results presented in this chapter, a schematic mechanism for the oxidation of methane on PdO is suggested. Figure 49 clearly demonstrates the different steps during $CH_4$ oxidation, i.e. adsorption of $CH_4$ on the surface, 1$^{st}$ C-H bond break, water desorption, formation of surface formate, desorption of $CO_2$ and reoxidation of partly reduced Pd by oxygen from the gas phase (or by oxygen adsorbed on the support material).

As discussed before, highly active PdO transforms in the presence of water to PdO surrounded by water molecules. To regenerate the catalyst reductive treatment was found to be very powerful. Pd gets reduced easily by hydrogen and also by methane at temperatures above 300°C. The reduction to metallic Pd is accompanied by desorption of $H_2O$ from the surface. To regain the initial activity however, elevated temperatures are needed that lead to full reoxidation of Pd to PdO. This explains why the reductive regeneration has to be performed at high temperature to be most effective.

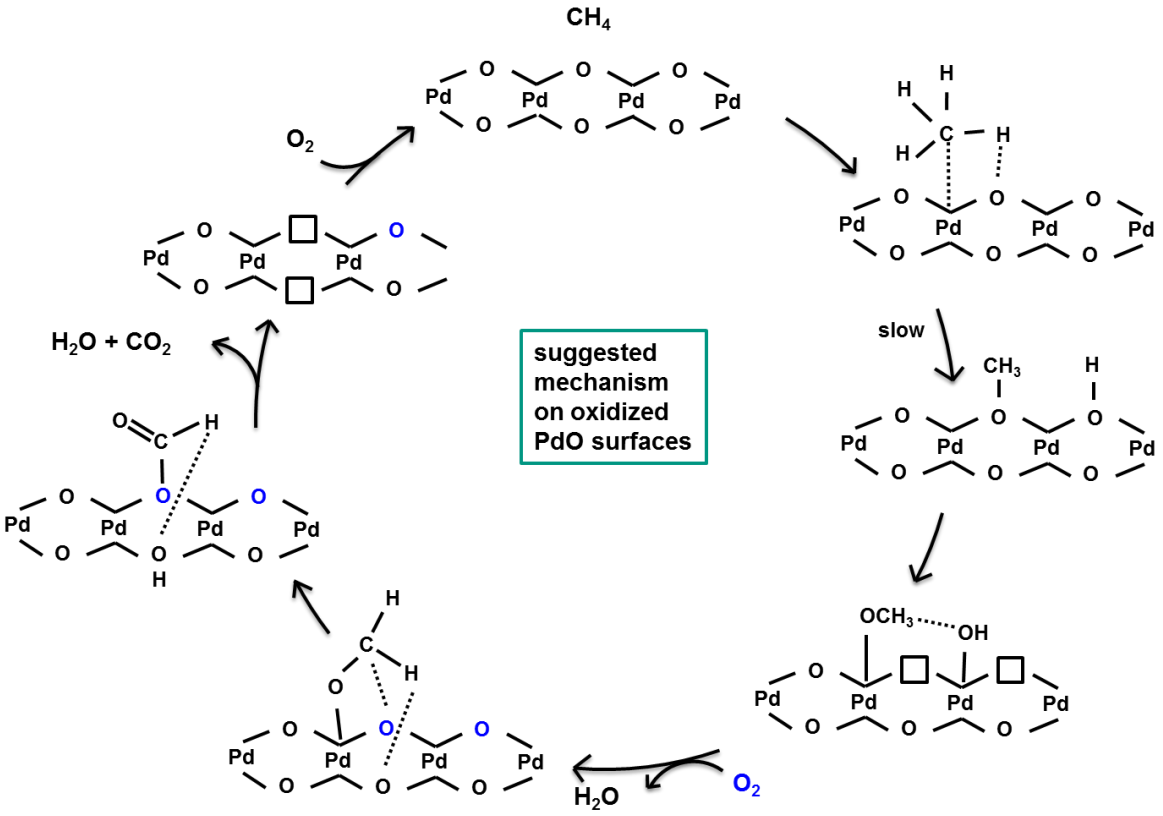


**Figure 49:** Suggested mechanism for the total oxidation of methane.

# 8 Results of High Pressure Tests and Simulations (KIT)

To evaluate the catalyst behavior under pre turbo positioning conditions, tests were performed at different pressures and temperatures. Two different catalytic systems were tested, namely:

- **Pd-Pt Model catalyst** (5:1: Pd:Pt) corresponding to the catalyst from FVV project “Methane Catalytic 1”
    - 100g/ft³
    - 400 cpsi
    - $Al_2O_3$ based washcoat

- **Pt/$Al_2O_3$ KIT2** synthesized at KIT
    - 20 g/ft³
    - 400 cpsi
    - $Al_2O_3$ based washcoat

In both cases cylindrical honeycomb samples with 3 cm length and a diameter of 2.5 cm were used.

Furthermore, tests with the catalyst provided from Johnson Matthey were performed at higher pressures. However, the results are incorporated in 9.1.3 since the tests were conducted to investigate the influence of sulfur species under pre turbo conditions.

Before the catalytic test possible gas phase reactions were identified in an empty reactor. The experimental results are complemented by modeling studies.

In all experiments, the total mass flow is kept constant while the pressure inside the reactor is varied.

## 8.1 Gas phase tests

### 8.1.1 Result of simulation with DETCHEM$^{BATCH}$ using simulated exhaust gas

The effect of pressure on the reaction in the gas phase was studied using DETCHEM$^{BATCH}$, which gives the concentration profile of reactants and products over reaction time. The reaction time corresponds to the residence time inside a batch reactor. However, inside a Plug-flow-reactor this residence time is linked to the reactor length. The time dependent profiles can then be used for better understanding of effect of residence time and consequently the length of reactor on the progress of gas phase reactions.

The simulations were carried out for a gas mixture consisting of 3200 ppm $CH_4$, 150 ppm $C_2H_6$, 25 ppm $C_2H_4$, 25 ppm $C_3H_6$, 120 ppm NO, 30 ppm $NO_2$, 10% $O_2$ and 12 % $H_2O$ diluted with $N_2$ (Table 18) at 650 °C at 3 and 5 bar. The composition of the gas mixture refers to common emission values of lean burn gas engines.

**Table 18**: Composition of feed gas mixtures used for gas phase reactions

| | **$CH_4$** | **$C_2H_6$** | **$C_2H_4$** | **$C_3H_6$** | **NO** | **$NO_2$** | **$O_2$** | **$H_2O$** |
|---|---|---|---|---|---|---|---|---|
| | ppm | ppm | ppm | ppm | ppm | ppm | % | % |
| **Simulated exhaust gas** | 3200 | 150 | 25 | 25 | 120 | - | 10 | 12 |
| **Model gas** | 800 | - | - | - | - | - | 10 | 12 |

Concentration profiles obtained from simulation of gas phase reactions at 650°C and 3 bar are plotted in Figure 51 and Figure 50. The simulation results reveal that 10 seconds are needed to

get completely rid of hydrocarbons and reach the equilibrium at which $CO_2$ and water are the ultimate products. However, from the profiles one can see that after almost 2 seconds the complete conversion of all hydrocarbons, both dosed or produced one, is gained.

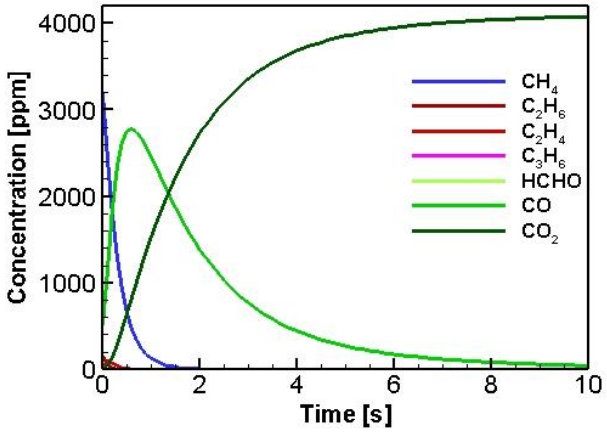


**Figure 50:** Simulated results of concentration of hydrocarbons, CO and $CO_2$ in gas phase within10 sec. using DETCHEM$^{BATCH}$. Feed gas: simulated exhaust gas (Table 18) at 650 °C and 3 bar.

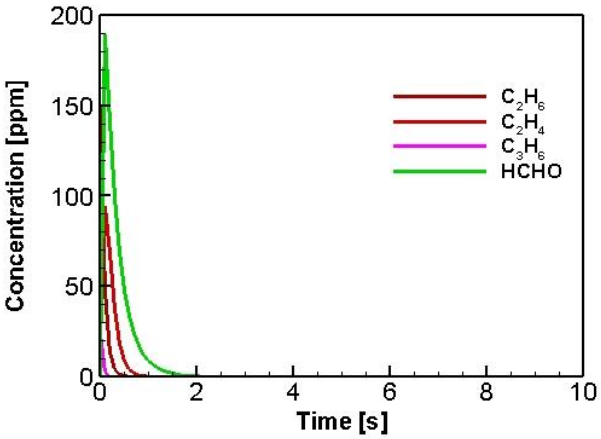


**Figure 51:** Simulated results of concentration of hydrocarbons in gas phase within10 sec. using DETCHEM$^{BATCH}$. Feed gas: simulated exhaust gas (Table 18) at 650 °C and 3 bar.

Methane is first converted to CO and formaldehyde. Within 10 seconds all CO disappeared and converted to $CO_2$, which is expected at equilibrium conditions. Moreover, ethylene seems to be firstly produced and complete conversion is achieved within first second.

In case of nitrogen oxides, (Figure 52 and Figure 53), a spike in the $NO_2$ to $NO_x$ ratio is observed initially after which the ratio reached the equilibrium (after 100 seconds).

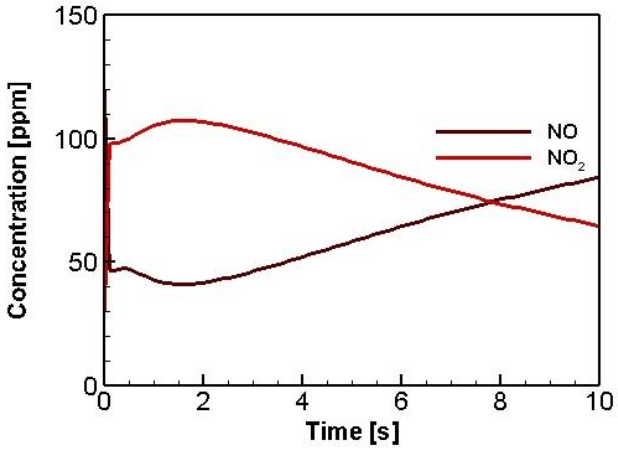


**Figure 52:** Simulated results of concentration of NO and $NO_2$ in gas phase within 10 sec. using DETCHEM$^{BATCH}$. Feed gas: simulated exhaust gas (Table 18) at 650 °C and 3 bar.

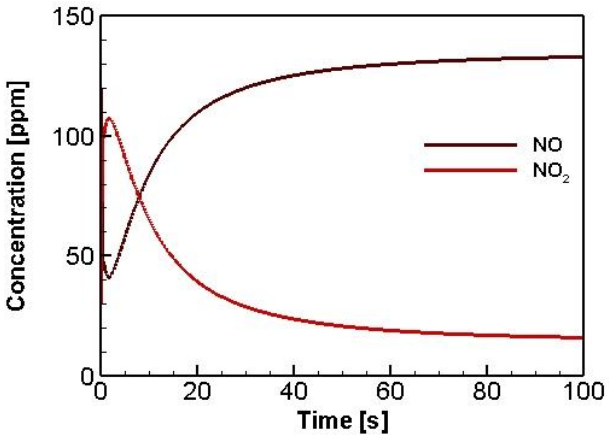


**Figure 53:** Simulated result of concentration of NO and $NO_2$ in gas phase within 100 sec. using DETCHEM$^{BATCH}$. Feed gas: simulated exhaust gas (Table 18) at 650 °C and 3 bar.

The results of simulation with simulated exhaust gas mixture (Table 18) at 5 bar are depicted in Figure 54 and Figure 55. Here the conversion of hydrocarbons to water and $CO_2$ is faster and equilibrium products are completely formed after 3.5 seconds. Methane is vanishing within almost 0.6 second and the other hydrocarbons need less than 0.4 second to be converted. Similar to results of gas phase reaction at three bar an initial peak due to formation of ethylene is present in its concentration profile.

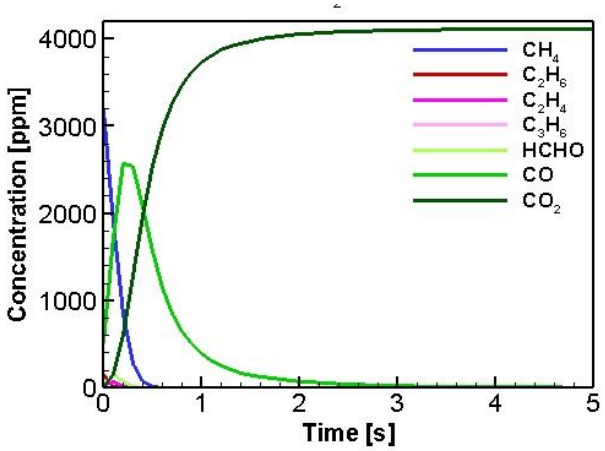


**Figure 54:** Simulated results of concentration of hydrocarbons, CO and $CO_2$ in gas phase within 5 sec. using DETCHEM$^{BATCH}$. Feed gas: simulated exhaust gas (Table 18) at 650 °C and 5 bar.

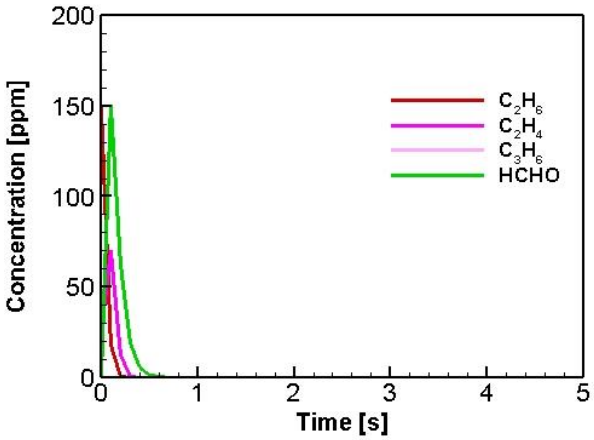


**Figure 55:** Simulated results of concentration of hydrocarbons, in gas phase within 5 sec. using DETCHEM$^{BATCH}$. Feed gas: simulated exhaust gas (Table 18) at 650 °C and 5 bar.

The $NO_2$ to $NO_x$ ratio started here also with an initial rise and the ratio attained equilibrium after 50 sec.

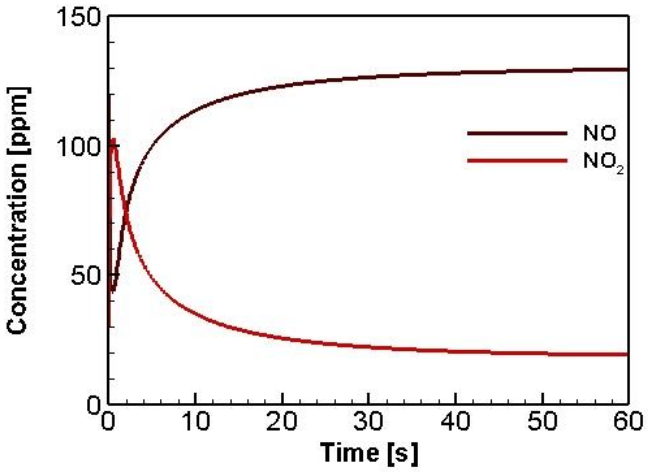


**Figure 56:** Simulated result of concentration of hydrocarbons, NO and $NO_2$ in gas phase within 60 sec. using DETCHEM$^{BATCH}$ Feed gas: simulated exhaust gas (Table 18) at 650 °C and 5 bar.

Based on the simulation results of gas phase reactions with DETCHEM$^{BATCH}$ it is found that depending on residence time of gas mixture and also operation pressure different products with different ratios are expected and higher pressure leads to an earlier equilibrium.

### 8.1.2 Plug reactor: experiment and simulation using simulated exhaust gas

The gas phase reactions were also investigated both experimentally and numerically in an empty reactor with simulated exhaust gas (Table 18) at 3 and 5 bar. Simulation were executed by DETCHEM$^{PLUG}$. The experiments were performed at the High-Pressure Setup (4.4.1.1)

The experimental procedure consisted of feeding the gas mixture from Table 18 (3200ppm $CH_4$,150 ppm $C_2H_6$, 25ppm $C_2H_4$, 25ppm $C_3H_6$, 120 ppm NO, 30 ppm $NO_2$, 10% $O_2$ and 12% $H_2O$, balance $N_2$) to the empty reactor. Temperature was increased with 5K/min up to 650°C while the pressure was kept constant at 1 bar. After reaching 650°C, pressure was increased to 3 and 5 bar while the total mass flow was kept constant and consecutively lowered to 1 bar again followed by cooling to 225°C.

From Figure 57 it can be seen that already under atmospheric conditions methane gets converted above 600°C under these conditions reaching ~10% conversion at 650°C. With increasing pressure the conversion also increases to ~20% at 3 bar and ~40% at 5bar at 650°C. The trend of methane is also observed for the other hydrocarbons present but to a more distinctive extent. Propylene for example is completely converted at 5bar at 650°C in the empty reactor. Under all conditions > 600°C CO and $CH_2O$ as products of partial are detected besides $CO_2$ as complete combustion product.

It can be seen that with higher pressure gas phase reactions are favored. This can be explained by a higher residence time in the reactor with increasing pressure and also with higher concentration due to a denser gas at higher pressure.

It has to be mentioned that the conversion of methane in the gas phase up to 650°C only occurs in the presence of nitric oxides (NO or $NO_2$). Tests performed without $NO_x$ (not shown) revealed changes in methane conversion <1% at 650°C and 5bar. $NO_x$ is needed as a radical starter to promote the gas phase reaction behaving like a homogenous catalyst [87, 88].

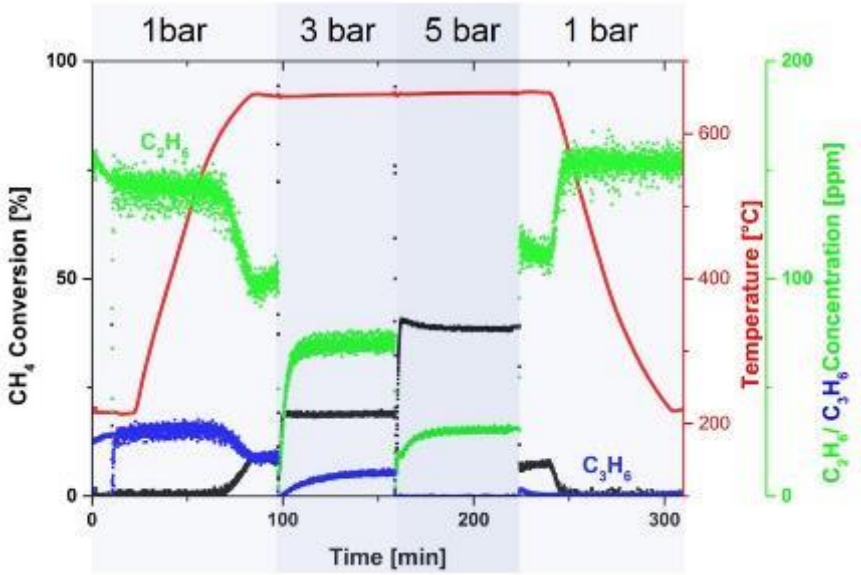


**Figure 57:** Course of $CH_4$ conversion as well as $C_3H_6$ and $C_2H_6$ concentration during gas phase experiment. Gas composition: 3200ppm $CH_4$, 150ppm $C_2H_6$, 25ppm $C_2H_4$, 25ppm $C_3H_6$, 120ppm NO, 30ppm $NO_2$, 10% $O_2$ and 12 % $H_2O$, balance $N_2$. Temperature is increased by 5K/min and pressure inside reactor is increased at 650°C from 1 to 3 to 5 bar. Flow: 20 L/min (standard conditions).

The 1D concentration profiles of hydrocarbons, CO and $CO_2$, simulated with DETCHEM$^{PLUG}$ at 5 bar are presented in Figure 58 and Figure 59. The results show methane is mainly converted to CO along the reactor. Small amount of formaldehyde is also formed from methane, which is at most 6% of methane in the reactor inlet. This maximum value of formaldehyde is reached at 0.06 m of the reactor length and decreases to 130ppm (4% of methane in the feed) at reactor outlet. Formation of CO and formaldehyde is in line with result of Batch model. Due to very short residence time of feed gas in the reactor the main products of methane conversion are then CO and formaldehyde and total conversion of methane cannot be reached.

The concentration of ethane and propylene decreases also along the reactor. Propylene is totally converted at 0.05 m and 96% of ethane is converted at reactor outlet. The course of concentration profile of ethylene is the same as formaldehyde as it was in case of batch model. It reaches to the maximum value of 92ppm at 0.06 m and decreases to 48ppm at reactor outlet, which is almost twice as much as ethylene dosed in the feed gas. The $CO_2$ concentration is increasing along the reactor and reaches 230ppm at reactor outlet.

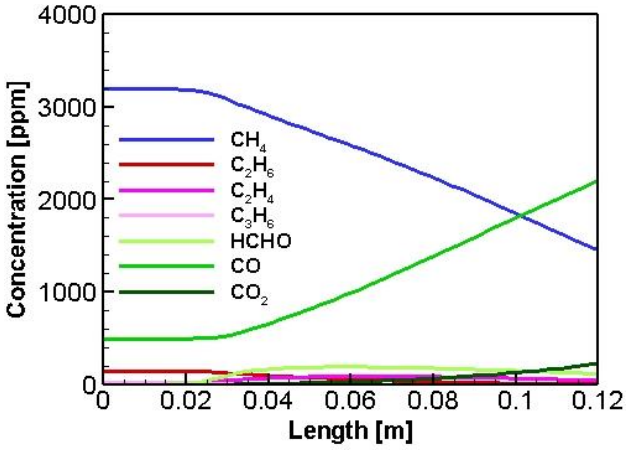


**Figure 58:** Simulated results of concentration of hydrocarbons, CO and $CO_2$ in gas phase along the reactor, using DETCHEM$^{PLUG}$.
Feed gas: simulated exhaust gas (Table 18) at 650°C and 5 bar.

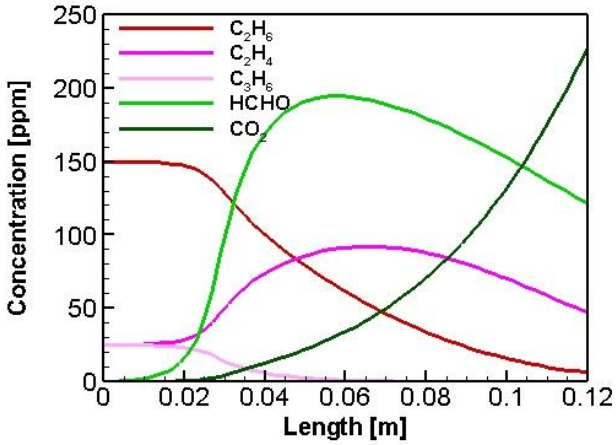


**Figure 59:** simulated result of concentration of hydrocarbons and $CO_2$ in gas phase along the reactor, using DETCHEM$^{PLUG}$.
Feed gas: simulated exhaust gas (Table 18) at 650°C and 5 bar.

The concentration profile of NO and $NO_2$, simulated with DETCHEM$^{PLUG}$, are displayed in Figure 60.

NO concentration reduces from 120ppm to 36ppm at 0.06 m and plateaus. $NO_2$ is accordingly produced and with a concentration of 84ppm leaves the reactor at outlet.

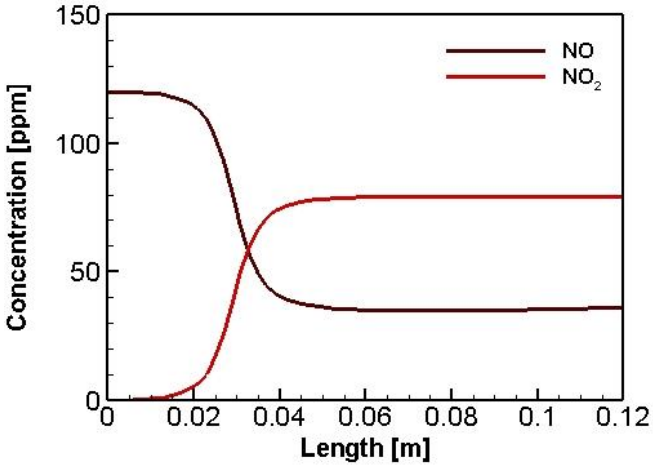


**Figure 60:** Simulated result of concentration of hydrocarbons, NO and $NO_2$ in gas phase along the reactor, using DETCHEM$^{CHANNEL}$. Feed gas: simulated exhaust gas (Table 18) at 650°C and 5 bar.

The comparison of 1D concentration profiles of 5 and 3 bar (not shown here), exhibits that higher pressure leads to faster progress of gas phase reactions which results in higher conversion of methane, propylene and ethane whereas produced formaldehyde and ethylene are more favorable at lower pressure. This conclusion is in agreement with experimental result plotted in Figure 61 and Figure 62.

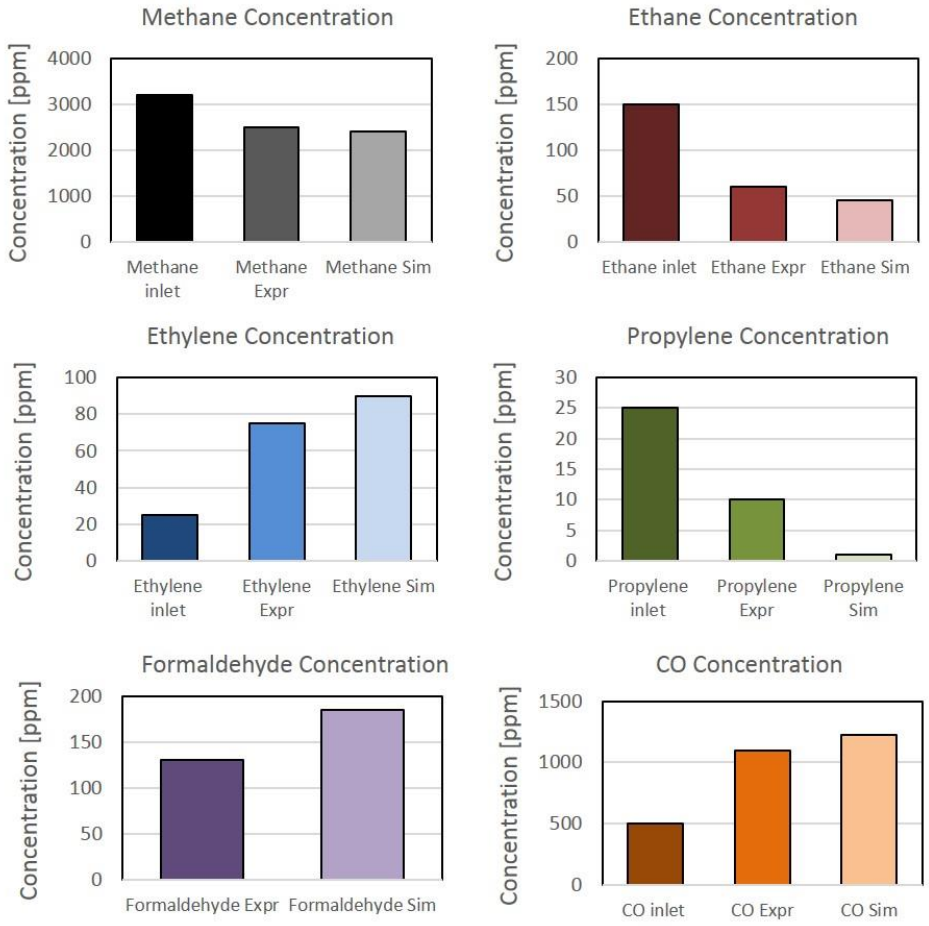


**Figure 61:** Inlet concentration (first column), experimentally measured outlet concentration (second column) and simulated concentration (third column) of hydrocarbons, CO and $CO_2$. Feed gas: simulated exhaust gas (Table 18) at 650°C and 3 bar.

In Figure 61 and Figure 62, the first bars from left show the inlet concentration of each gas component. The second bars are outlet concentrations measured experimentally and the third bars are the simulated outlet concentration, for each species. In case of formaldehyde, first bar is experimentally measured concentration and second bar is simulated one as no formaldehyde was dosed in the feed gas.

Simulated concentration values of hydrocarbons particularly at 5 bar are in good agreement with experimental one. In case of 3 bar the production of ethylene and formaldehyde and also conversion of propylene are overestimated in the model. Comparison of experimental result of 3 and 5 bar with each other, assures that the higher is the pressure the higher is the conversion of methane, ethane and propylene. Formation of ethylene and formaldehyde is less and CO production is favorable at higher pressure. The effect of pressure on production and consumption of different hydrocarbons and CO could be modeled with acceptable accuracy.

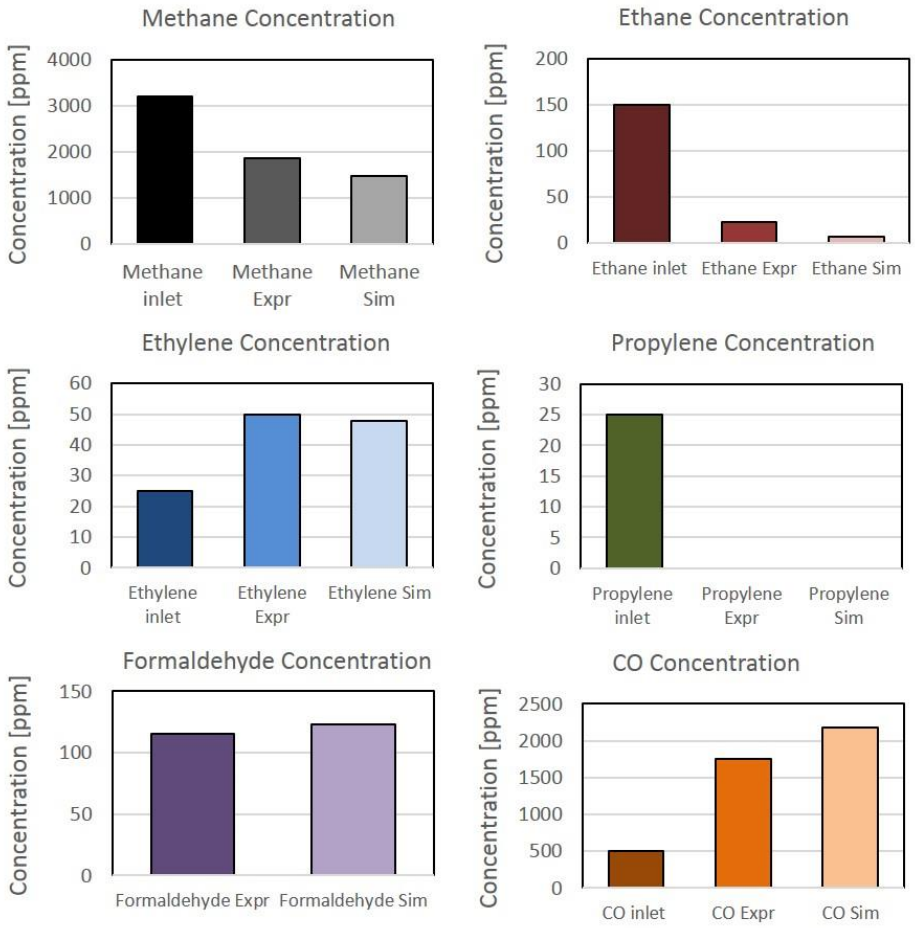


**Figure 62:** Inlet concentration (first column), experimentally measured outlet concentration (second column) and simulated concentration (third column) of hydrocarbons, CO and $CO_2$. Feed gas: simulated exhaust gas (Table 18) at 650°C and 5 bar.

### 8.1.3 Gas phase reaction using model gas

Additional gas phase experiments were performed to check if pronounced gas phase reactions could occur and interfere with the catalytic tests described in 8.2 and 8.3. This analysis was carried out using an inert cordierite monolith in place of the coated one. For this test, a model gas (Table 18) consisting of 800ppm $CH_4$, 10% $O_2$ and 12% $H_2O$ diluted with $N_2$ at 10sL/m (standard liters per minute) was fed into the reactor. Temperature was ramped up with 5K/min at 1 bar up to 700°C at which the pressure was increased to 2 and 4 bar, consecutively. Cooling was realized under the same conditions at 4 bar pressure.

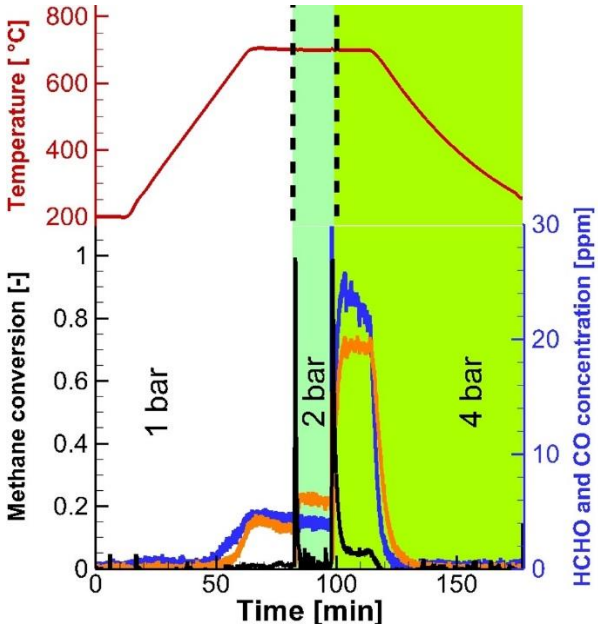


**Figure 63:** Reactor temperature, methane conversion, CO and HCHO concentration of gas phase reaction at 1, 2 and 4 bar. Gas mixture: 800ppm $CH_4$, 10% $O_2$ and 12% $H_2O$ diluted with $N_2$ at 10sL/min.

The result of the gas phase experiment is presented in Figure 63. Temperature, methane conversion, CO concentration and HCHO concentration are represented by red, black, blue and orange lines, respectively. Products of partial oxidation of methane, namely CO and formaldehyde, were observed starting above 650°C at 1 bar. However, due to a low extent of total and partial oxidation only approximately 1% of methane are converted at 700°C and 1 bar. Rising pressure from 1 to 2 and 4 bar leads to an increase in $CH_4$ conversion and in the concentrations of CO and HCHO. Highest methane conversion (5%) is found at highest elevated temperature and pressure. This can be explained by a higher residence time within the reactor due to an increase in pressure while keeping a constant mass flow. The cooling curve at 4 bar shows that the products of partial oxidation can already be observed above 600°C compared to 650°C at 1 bar. In Figure 63, one can see that gas phase reactions have a bearing on total methane oxidation only at T > 600°C. As the catalytic tests were conducted up to a temperature of 600°C, the outcome does not suffer from any interference caused by reactions in the gas phase. Hence, the methane conversion detected in catalytic tests can be attributed only to the catalyst activity.

## 8.2 $Pt/Al_2O_3$ KIT2

The catalyst was investigated by light-off experiments. These experiments were performed at different pressures while keeping the mass flow constant to investigate the effect of pressure on the catalyst activity.

The catalysts are subjected to the following gas flow, corresponding to GSV=60000 $h^{-1}$, and composition:

**Table 19:** Flow and gas composition for Light off tests on $Pt/Al_2O_3$.

| Flow (sL/min) | $CH_4$ (ppm) | $O_2$ (%) | $N_2$ |
|---|---|---|---|
| 10 | 800 | 10 | balance |

For every single LO the catalyst is heated up from 250°C with a ramp rate of 5K/min up to 700°C which is held for 15 minutes. Then the catalyst is cooled down to 250°C with the same ramp rate of 5K/min. Thus, analogous cycle is run with the same parameters to obtain a second LO. This second LO cycle is necessary in order to understand whether the catalyst is already experiencing deactivation.

This procedure is repeated identically for three pressure levels (1, 2, 4 bar) while keeping the mass flow constant. The execution procedure of the LO tests, including pretreatment, are better clarified in Figure 64.

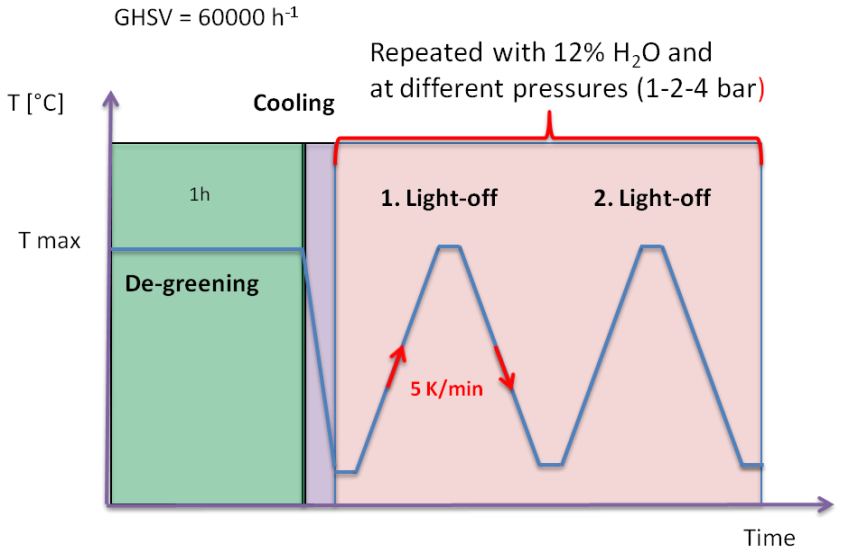


**Figure 64:** Procedure for LO test.

At 1 bar the LO curves without (a) and with additional water (b) are plotted in Figure 65. Methane starts to be converted at around 600°C and $T_{50}$ is not reached during the test done up to 700°C. The low activity can be explained on the one hand by the low activity of Pt for $CH_4$ oxidation that was already shown before (Figure 25). On the other hand by the low loading of 20 g/ft³ and high space velocity of 60000 $h^{-1}$.

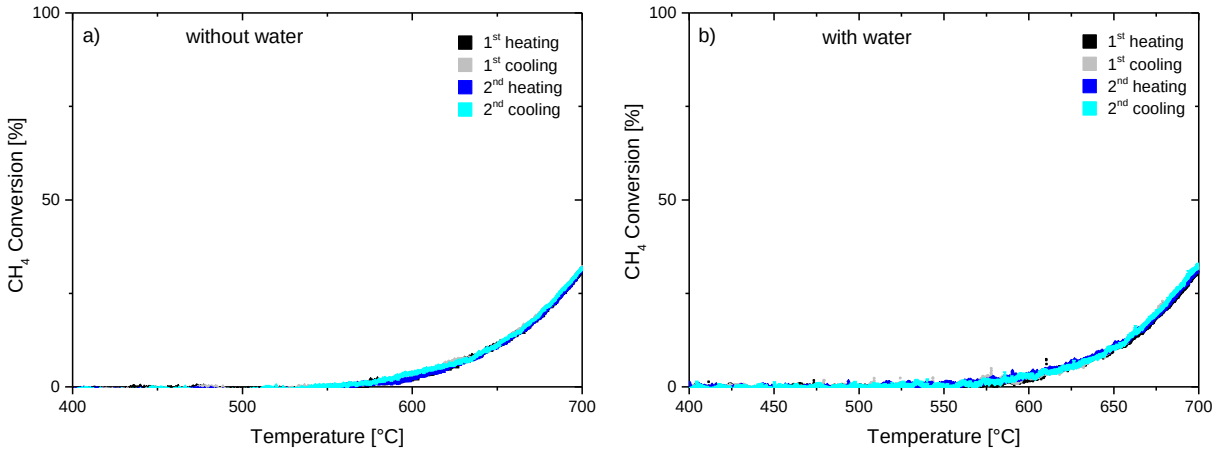


**Figure 65:** Methane conversion depending on temperature over $Pt/Al_2O_3$ KIT 2. Gas composition: 800ppm $CH_4$, 10% $O_2$, 0% $H_2O$ (a) and 12% $H_2O$ (b), balance $N_2$. GHSV = 60000 $h^{-1}$. Pressure = 1bar.

In Figure 65 a) and b) it can be seen that there is no deactivation between the first and second LO cycle and the heating and corresponding cooling curves are coincident. All the curves plotted superimpose and show no activity differences. This is in line with results from chapter 6.2. Moreover,

the addition of 12% water does not lead to any drop in activity. The dry feed curves and wet feed curves overlap perfectly. Water, even at high concentration, does not inhibit the catalyst in this high temperature range. The same behavior regarding heating and cooling is found also at 2 bar and 4 bar (not shown)

Concerning the pressure effect on activity, the heating curve of the second cycle is plotted for different pressures in Figure 66 for the dry and wet case.

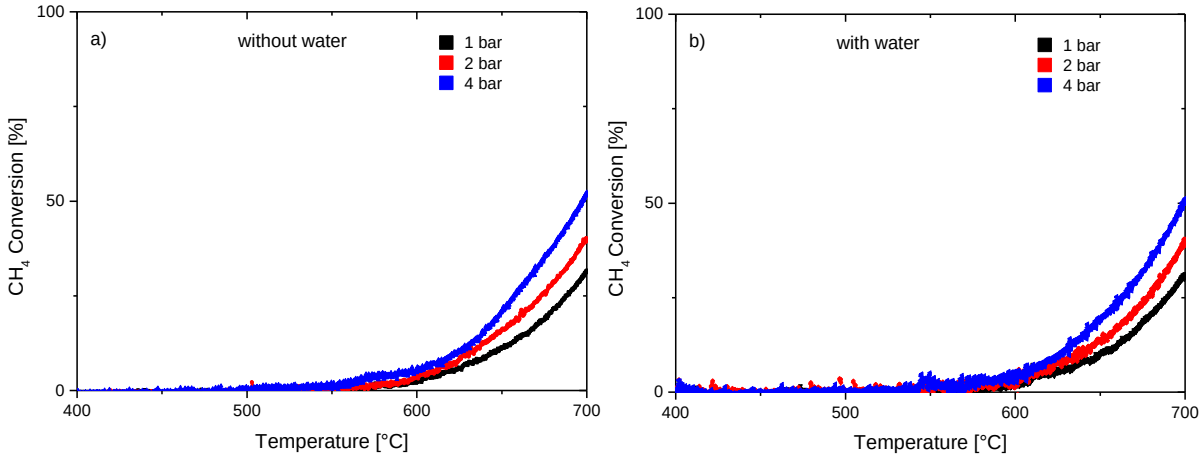


**Figure 66:** Methane conversion depending on temperature over $Pt/Al_2O_3$ KIT 2 during 2nd heating. Gas composition: 800ppm $CH_4$, 10% $O_2$, 0% $H_2O$ (a) and 12% $H_2O$ (b), balance $N_2$. GHSV = 60000 $h^{-1}$. Pressure = 1, 2 and 4 bar.

In both cases activity increases with pressure. Water inhibition plays no role in this trend, regardless of its content in the feed. The unique contributions to the activity-pressure dependence come from the higher residence time caused by higher pressure (constant mass flow).

## 8.3 Pd-Pt Model catalyst

Light-off experiments were performed with two different gas compositions (Table 20) maintaining a constant mass flow and a gas hourly space velocity (GHSV) of 60,000 h-1. To investigate the effect of pressure, two consecutive heating and cooling cycles ranging from 200 to 450°C (up to 600°C in the case 12% water are present) with 3 K/min were conducted at 1, 2 and 4 bar. Prior to each run of light-offs at certain pressure, the sample was pretreated to preserve a defined state of the catalyst and prevent wrong results due to deactivation effects. The pretreatment consisted of reduction with 2% $H_2$ in $N_2$ at 600°C, reoxidation in 10% $O_2$ in $N_2$ at 600°C and consecutive cooling to 200°C in 10% $O_2$ in $N_2$. This pretreatment was found to provide reproducible light-off curves.

**Table 20:** Composition of wet and dry gas mixture for light-off tests.

| Gas Mixture | $CH_4$ [ppm] | $O_2$ [%] | $H_2O$ [%] | Balance |
|---|---|---|---|---|
| 1 | 800 | 10 | - | $N_2$ |
| 2 | 800 | 10 | 12 | $N_2$ |

The experimental results of a second run of light-off tests with gas mixture 1 and 2 are depicted in Figure 67 a and Figure 67 b, respectively. In these cases, the experiments were conducted at three different pressures between 200-600°C.

The conversion-temperature profile shows the typical S-shape of light-off curves for methane oxidation for both dry and wet feeds. The results show a dramatic drop in catalyst activity in wet conditions (Figure 67 b) which leads to a shift of the light-off curve towards a higher temperature in comparison to the light-off curves obtained in a dry feed. In the case of wet feed, methane starts to react at 370°C, where the conversion in the dry feed has already achieved its maximum and has plateaued for all pressure levels. The considerable loss of activity due to the presence of additional water in the feed is thoroughly in line with former, previously discussed, studies [20-22, 54, 89].

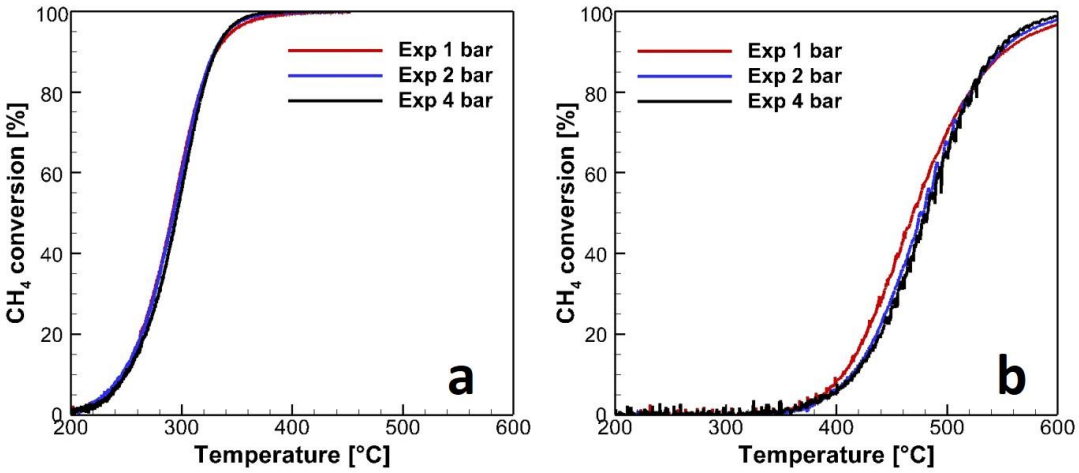


**Figure 67:** Methane conversion during 2nd heating as a function of temperature at 1, 2 and 4 bar with gas mixture 1 (a) and gas mixture 2 (b).

Considering the effect of pressure on the catalyst activity for dry feed, there is no significant change in the conversion of methane during light-off, which is in contrast to the beneficial effect of longer residence time on catalyst activity caused by higher pressure, as shown in the following equations

$$\frac{d\tau}{dz} = \frac{1}{u}, \tag{8.1}$$

$$u = \frac{T}{T_0}.\frac{u_0(GHSV)}{p}.P_0\,, \tag{8.2}$$

$$\tau = \frac{V_R.P.T_0}{A_R.P_0.T.u_0(GHSV)}. \tag{8.3}$$

Assuming a first order reaction in a plug-flow reactor, an increase in residence time shifts the conversion curve to lower temperatures. For example, at 260°C, the doubling of the residence time increases the conversion from 17% to 31% (see Figure 69). Taking the effect of pressure on mass transport and the diffusion coefficient of species into account, the obtained results might be an evidence of transport-controlled kinetic caused by the limitation in radial diffusion of species into the catalytic surface. The reduction of radial diffusion at higher pressure can be explained by the reverse pressure dependency of the binary diffusion coefficient of gas species (Eq. 8.4), which is used for the calculation of flux $j_{i,r}$ in Eq. 3.24 [90].

$$D_{ij} = \frac{3}{16}\frac{\sqrt{2\pi N_A k_B^3 T^3 / M_{ij}}}{p\pi\sigma_{ij}^2 \Omega_{ij}^{(1,1)*}(T_{ij}^*)} \qquad 8.4$$

Another possible explanation for the performed catalyst activity at higher pressures can also be the inverse reaction rate dependency to the water concentration as pointed out in the literature. Concerning this matter, simulations were done for better analysis of the experimental results.

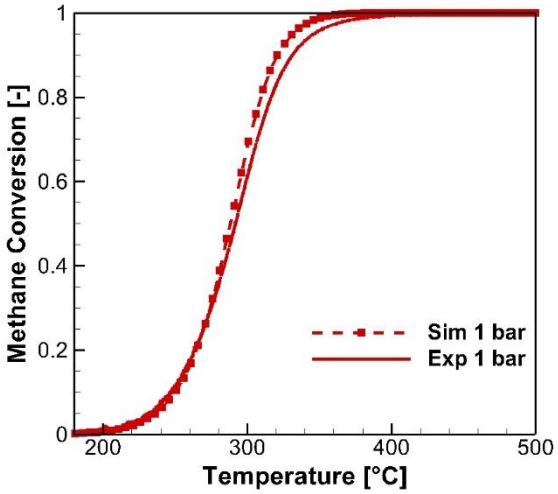


**Figure 68:** Comparison of experimental (solid line) and simulated results (dashed line) at 1 bar with gas mixture 1. For the 2-D model, the first order reaction rate with respect to methane without inhibition factor (Eq. 8.5) is applied.

Figure 68 shows the experimental and simulated results of the light-off curve for dry feed at 1 bar using the reaction rate expression in 3.3. The Arrhenius parameters required for the reaction constant were calculated from experimental results of tests under the same condition. An activation energy of 114 kJ/mol and a pre-exponential factor of $3.01\times10^8$ m/s are obtained under a kinetically controlled regime (from 205 to 235 °C).

$$-r_{CH_4} = k_1 c_{CH_4} \qquad 8.5$$

In Figure 68 one can see that simulated light-off curves match the experimental one perfectly for a temperature below 300°C, where the light-off point is not yet reached. For temperatures higher than 300°C, the model shows higher methane conversion. Applying the same reaction rate expression for 2 and 4 bar results in an overestimation of catalyst activity. In these cases, the simulated results are the same as expected with longer residence time (Figure 69). The higher performance obtained from Eq. 8.5 is not reproducing the real catalyst performance. Nevertheless, it is an indication of a kinetically controlled reaction since higher pressure leads to higher simulated conversion over the whole temperature ranges.

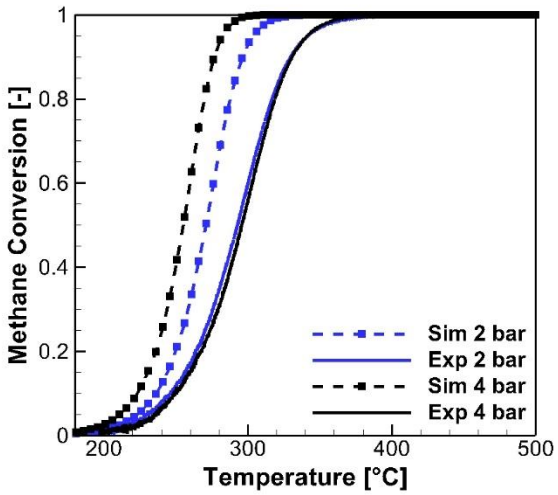


**Figure 69:** Comparison of experimental (solid line) and simulated results (dashed line) at 2 bar (blue lines) and 4 bar (black lines) with gas mixture 1. For the 2-D model, the first order reaction rate with respect to methane without inhibition factor is applied.

To explain the conversion-pressure trend for the case of dry feed, it is necessary to consider the possibility of an inhibiting effect of the water produced by total oxidation of methane. Thus, an inhibition term leading to 8.7 was added to the reaction rate expression and the corresponding parameters have been tuned. The activation energy and the pre-exponential factor were not changed.

$$I = \frac{1}{\left(1 + k_{H_2O,0} Exp\left(\frac{-\Delta H_{ads}}{RT}\right) c_{H_2O}^{\beta}\right)}. \qquad 8.6$$

The order of the inhibition term with respect to the water was set to 1.15, which is higher than the order suggested in the literature [47, 51, 91]. However, this assumption is consistent with the experimental results. After modifying (Eq. 8.7), the rate constant is decreased for all temperatures depending on the water concentration presence in the gas mixture, as expected.

$$-r_{CH_4} = \frac{k_1 cCH_4}{1 + k_2\, c_{H_2O}^{1.15}} \qquad 8.7$$

The related simulation results are depicted in Figure 70. As shown here, the obtained curves with the implemented model match the experimental data. The inhibition factor added to the reaction rate reduces the catalyst activity at higher temperatures while water concentration produced by methane oxidation increases, especially after reaching the light-off temperature.

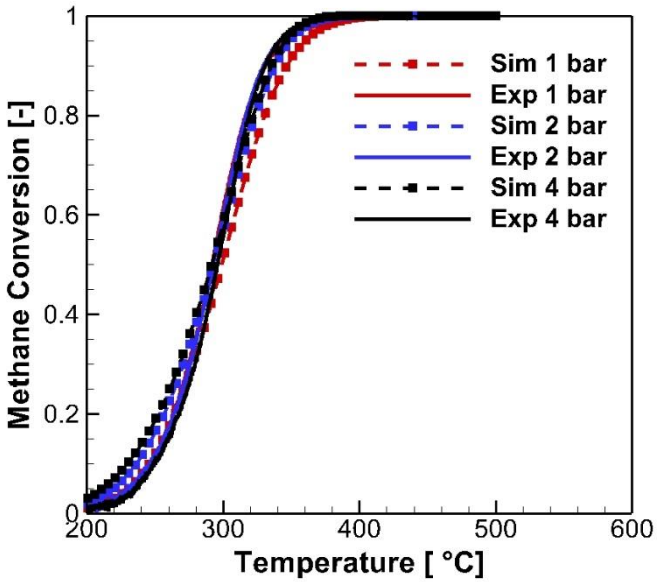


**Figure 70:** Comparison of experimental (solid line) and simulated results (dashed line) at 1 bar (red lines), 2 bar (blue lines) and 4 bar (black lines) with gas mixture 1. For the 2-D model, the first order reaction rate with respect to methane including inhibition factor (8.7) is applied.

In case of the wet feed, the activity-pressure relation changes in comparison to the dry feed. Figure 67 b exhibits an inversion in the conversion-pressure trend around 525°C. At lower temperatures than 525°C, higher pressure leads to lower activity and at temperatures higher than this, an increase in pressure causes an increase in catalyst activity. As mentioned previously, higher pressure determines higher water inhibition, lowering in turn the level of conversion at the same temperature. It must be highlighted that this water inhibition effect is not constant with temperature: At higher temperature, the potentially less active palladium hydroxyl sites are less stable [47, 51, 52]. Hence, the conversion-pressure trend in the light-off curve could be explained by considering this contribution and weighing the main effects determined by pressure changes. At lower temperatures, the water inhibition prevails over the increasing residence time when pressure increases. Thus, activity becomes lower with the pressure. At higher temperatures, the water inhibition becomes minor and the residence time has the main contribution, bringing about an increase of activity with pressure. To sum up, this change in trend over the temperature range analyzed can be attributed directly to the water effect, getting slightly weaker with temperature increase.

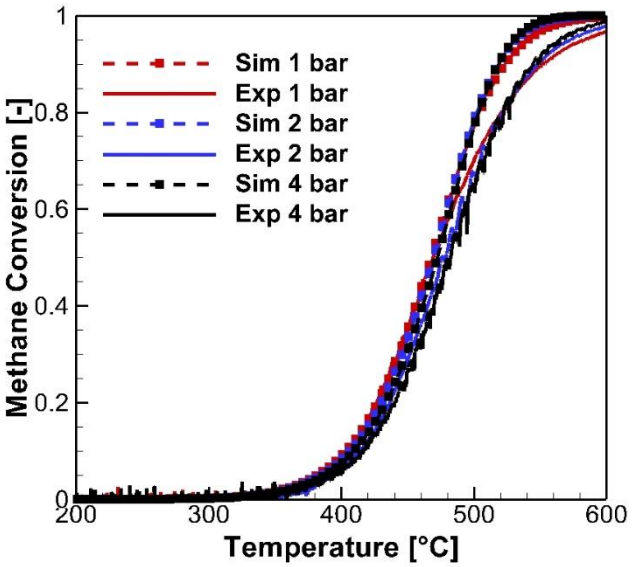


**Figure 71:** Comparison of experimental (solid line) and simulated results (dashed line) at 1 bar (red lines), 2 bar (blue lines) and 4 bar (black lines) with gas mixture 2. For the 2-D model, the first order reaction rate with respect to methane including inhibition factor (8.7) is applied.

Applying a modified reaction rate Eq. 8.7 in the case of wet feed gives the simulation results depicted in Figure 71. The model is able to simulate the catalyst performance with a reasonable accuracy up to light-off temperature for each investigated pressure. The lower catalyst activity after this point in the experimental results can be attributed to deactivation of the catalyst in the presence of water, which becomes faster with a higher concentration of water. This suggestion is in line with literature [22, 53]. It should be pointed out that using one as order of water concentration in the inhibition term, leads to an over estimation of catalyst activity since the negative effect of water can be totally compensated by the effect of longer residence time. Hence, the value of 1.15 enables us to have a better prediction of pressure effects on methane conversion over temperature in both cases of with and without additional water.

The Light-off experiments shown before were performed after full regeneration of the catalyst under reducing conditions (2% $H_2$ in $N_2$) and consecutive reoxidation (10% $O_2$ in $N_2$) at 600°C. This pretreatment leads to a completely regenerated catalyst in highly active state. However, this fresh state is also very sensitive to water inhibition both from externally added water and water produced by catalytic oxidation of $CH_4$. As discussed before, higher pressure leads to higher water concentration and therefore stronger inhibition on the kinetics. For samples that are already in a more stable state (after initial deactivation) the inhibiting effect of water concentration and therefore of pressure might decrease.

Figure 72 shows the results of an experiment that was designed to address the former discussed issue. At constant temperature of 300°C, 1000ppm $CH_4$ and 10% $O_2$ in $N_2$ are dosed to the freshly regenerated $PdPt/Al_2O_3$ catalyst. In the beginning and after 2.5h pressure was increased from 1 to 2 to 4 bar.

It can be seen that the catalyst deactivates fast in the beginning losing almost 25% of conversion within 10 minutes at 1bar. Changing the pressure to 2 bar and 4 bar does not change the conversion markedly and the deactivation goes on. In that case the higher residence time caused by higher pressure is counterbalanced by the negative effect of higher pressure on water that is produced by the catalytic reaction. However, after 2.5 hours when the deactivation slows down and the catalyst is in a more stable state, the increase in pressure leads to an increase in $CH_4$ conversion. Methane conversion rises from 57% to 59% to 61% while pressure is increased from 1 to 2 to 4bar. In a more deactivated state the sensitivity towards water inhibition from reaction slightly decreases and the positive effect of residence time predominates when pressure is increased.

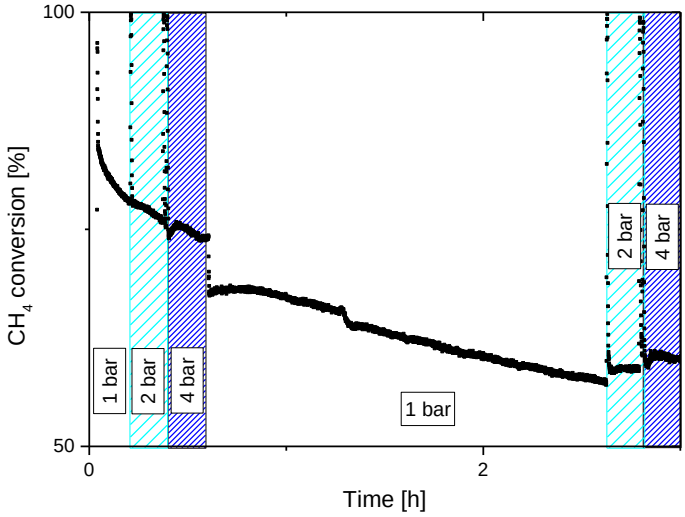


**Figure 72:** Methane conversion over time on Pd-Pt/$Al_2O_3$ Model catalyst at 300°C after reductive/oxidative regeneration. Gas composition: 1000ppm $CH_4$, 10% $O_2$ in $N_2$. GHSV = 60000$h^{-1}$. Pressure is increased from 1 to 3 to 5 bar while mass flow is kept constant.

Other tests at constant temperature in presence and absence of $H_2O$ were performed to also have a look on temperature effects. For this test a catalyst was used that already went through several light-off tests. Pretreatment before the tests only consisted of oxidative treatment with 10% $O_2$ in $N_2$ at 500°C for 0.5h. No reductive regeneration was performed. Therefore, it can be assumed that the catalyst is in a conditioned state and sensitivity towards water effects is decreased.

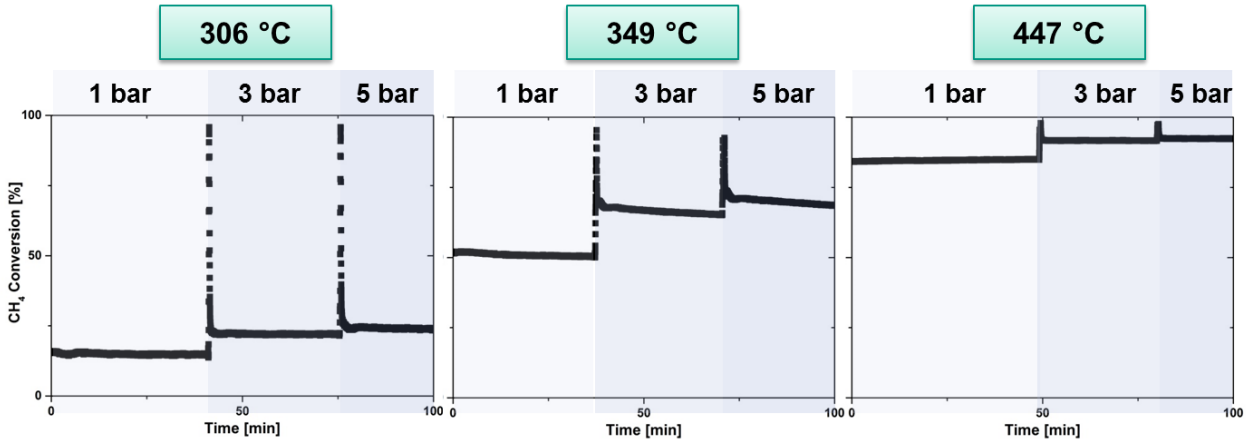


**Figure 73:** $CH_4$ conversion on already used Pd-Pt/$Al_2O_3$ model catalyst over time at different temperatures and pressures. Gas composition: 3200ppm $CH_4$, 10% $O_2$ in $N_2$. GHSV = 115000$h^{-1}$.

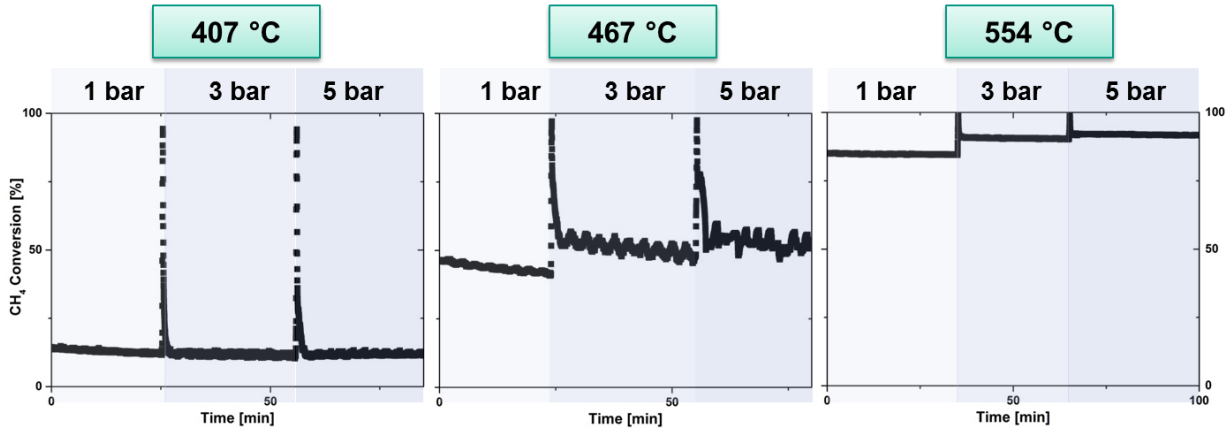


**Figure 74:** $CH_4$ conversion on already used Pd-Pt/$Al_2O_3$ model catalyst over time at different temperatures and pressures. Gas composition: 3200ppm $CH_4$, 10% $O_2$, 12% $H_2O$ in $N_2$. GHSV = 115000$h^{-1}$.

Figure 73 and Figure 74 shows the $CH_4$ conversion at different temperatures and pressures without additional water and with additional water respectively. Although space velocity and methane concentration is different to previously discussed tests, the trends in $CH_4$ conversion are as expected. In the case no additional water is present (Figure 73), conversion increases with increasing pressure. In the presence of 12% $H_2O$ in the gas stream, this trend is confirmed at temperatures > 450°C on the used catalyst. At 407°C, at which $CH_4$ conversion is around 12%, a positive influence of pressure cannot be observed. At this temperature, the negative effect of higher partial pressure of the external water might still counterbalance the positive effect of higher residence time.

## 8.4 Summary High Pressure Tests

Placing the catalytic converter in front of the turbocharger changes the operating conditions for the catalyst in a quite pronounced manner. Besides higher temperature – which is beneficial for catalytic methane oxidation – the pressure upstream of the turbine is also higher. Typically, the pressure is in the range of 3 – 5 bar for lean burn gas engines. Increasing pressure affects the catalyst in three ways:

1. The residence time increases
2. The diffusion coefficient of gaseous species decreases
3. The concentrations of species increase

Depending on the catalytic system, these three parameters have a different effect on the catalyst activity. On the one hand higher residence time leads to better conversion, since more time is available for the reaction. On the other hand, lower diffusion coefficients reduce the mass transport reducing the conversion. The influence of changing concentrations depends on the reaction kinetics and therefore is different on different catalyst systems.

Considering gas phase reactions, the tests showed that increasing the pressure leads to higher conversion of methane and other hydrocarbons. Especially at temperatures > 600°C and in the presence of $NO_x$ methane gets converted to a remarkable extent. Higher pressure favors this reaction.

Regarding the influence on catalysts, the tests revealed a pronounced difference between Pt based and Pd based catalysts. Platinum-based catalysts are influenced in positive way by higher pressure because higher residence time plays the major role. For 400 cpsi catalysts the slower diffusion does not contribute too much [92] and the kinetics of $CH_4$ oxidation are not negatively influenced by changing the concentrations that are typically present. However, Pt based catalysts are not very active for methane oxidation and need high operating temperatures. Pd based catalysts have a significantly higher intrinsic activity for methane oxidation. Besides the positive effect of residence

time however, the catalysts performance is also influenced by higher partial pressure of water. At high temperature this inhibiting effect of water decreases and the positive influence of higher pressure dominates. In addition, for a catalyst that is not in a fresh state, water deactivation should have proceeded quite far and the positive influence of higher residence time caused by higher pressure leads to better conversion of $CH_4$.

# 9 Results of Catalytic Tests in the Presence of $SO_2$ (KIT)

The influence of small amounts of sulfur containing compounds in the exhaust stream was investigated. Therefore, activity tests and long-term tests were performed as well as characterization of the fresh and sulfur poisoned samples. For these experiments two different catalyst were used which have already been described in chapter 5:

1. JM catalyst:

- Pd and Pt as active species
- 120 g/ft³ noble metal loading
- $Al_2O_3$ based washcoat
- 230 cpsi

2. PdPt/CZ
   a. PdPt/CZ KIT:

      2.4 wt.% PdPt on CeZrOx (Pd:Pt = 5:1)
      125 – 250 µm sieve fraction

   b. PdPt/CZ joneycomb

   - 100g/ft³ PdPt on CeZrOx (Pd:Pt = 5:1)
   - 200 cpsi honeycomb

## 9.1 JM catalyst

### 9.1.1 Deactivation with $SO_2$

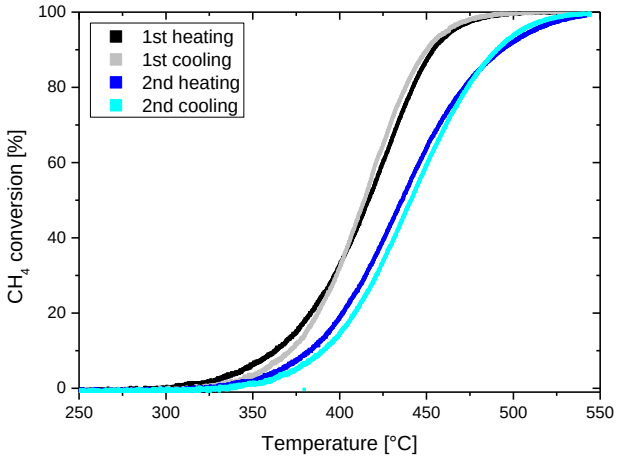


**Figure 75:** $CH_4$ conversion profiles for two consecutive reaction runs on "JM catalyst" from 225°C to 550°C with 3 K/min. Gas composition: 2.5ppm $SO_2$, 3200ppm $CH_4$, 10% $O_2$, 12% $H_2O$ in $N_2$. GHSV = 30000$h^{-1}$.

In Figure **75** the activity of the catalyst in presence of 2.5 ppm is shown. While during the 1st heating and cooling cycle 50% of methane is converted at 417°C (without 2.5ppm $SO_2$ $T_{50}$ = 410 °C) the catalyst shows a lower activity in the 2nd consecutive run with a $T_{50}$ of 436°C (without $SO_2$ $T_{50}$ in

second run is at 412°C). The presence of small amounts of $SO_2$ shows already drastic effects during Light off experiments. This trend was already observed during the first methane catalytic project on a $PdPt/Al_2O_3$ catalyst [23, 58]. To further investigate the poisoning effect of $SO_2$, long-term experiments were performed. Figure 76 demonstrates the experimental procedure in a graphical way. For every experiment a fresh sample with 2 cm diameter and 3 cm length was used.

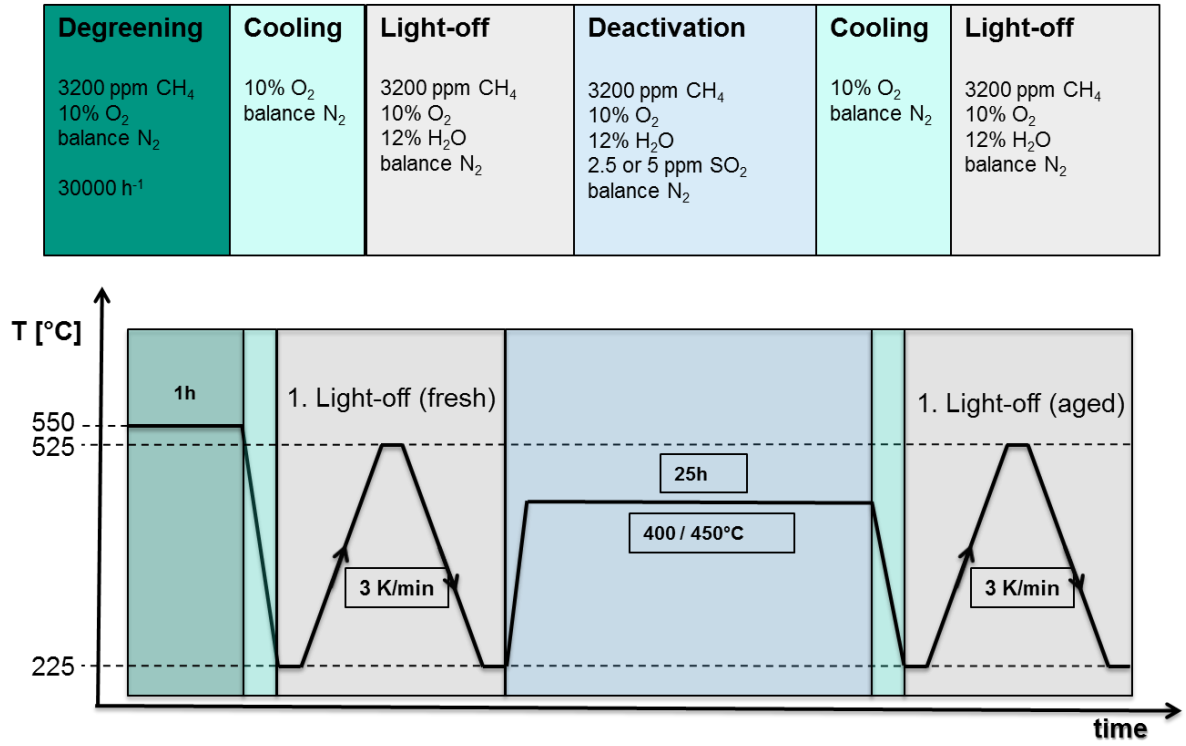


**Figure 76:** Experimental procedure for long-term testing of "JM catalyst" under $SO_2$ containing atmosphere. For the deactivation two Temperatures (400°C and 450°C) and two $SO_2$ concentrations (2.5 and 5ppm) are investigated.

Four sets of experiments were run to investigate the influence of temperature (400°C and 450°C) and the influence of $SO_2$ concentration (2.5ppm and 5ppm) on the long-term activity of the catalyst during constant temperature runs of 25h. The results are summarized in Figure 77. In all cases a drastic drop in $CH_4$ conversion can be observed over time. The rate of deactivation is depending on the $SO_2$ concentration when the temperature is kept constant. In the experiment performed at 450°C, the $CH_4$ conversion decreases from initially 100% to 17% when 5 ppm $SO_2$ are present. In this case a constant low conversion of 17% can already be observed after 15h on stream. In the case 2.5ppm $SO_2$ are present (450°C), the $CH_4$ conversion after 25h on stream stands at 21% with a still negative trend. It seems that a steady state is not reached yet and that the deactivation curve might end up in the range of 17% conversion as in the case of 5ppm $SO_2$. In comparison to the experiments performed at 450°C, the catalysts tested at 400°C show a lower initial activity at the beginning of the long-term experiment. $CH_4$ conversion of roughly 60% at 400°C is in line with light-off experiments in the fresh state. However, the activity rapidly drops as also observed in the experiments at 450°C. The rate of deactivation is depending on $SO_2$ concentration. The higher the $SO_2$ concentration the faster steady state of conversion is reached. In the case of 400°C the conversion ends up just slightly above 0% of conversion. Figure 78 proves that the rate of deactivation is depending on the $SO_2$ concentration. Based on the amount of $SO_2$ entering the catalyst, the two deactivation curves for tests with 2.5ppm and 5ppm $SO_2$ at 400°C nicely overlap. In the range of up to 5ppm $SO_2$ a linear dependency is given. This fact has to be considered when constructing an after-treatment system or employing regeneration strategies. Even very low amounts of sulfur-containing species (even odorizers) lead to a deactivation in the typical exhaust-gas temperature range of 400°C – 450°C. Since typical sulfur-containing species in the fuel (for example Tetrahydrothiophen, THT) are oxidized easily to $SO_2$ the source of sulfur should not affect the poisoning

process distinctly. For example, $H_2S$ gets oxidized easily to $SO_2$ by PdO or Pt in lean exhaust-gas mixture [93].

However, the time for deactivation is depending on the absolute sulfur content, i.e. on the fuel quality. Lower sulfur content leads to longer lifetime of the catalyst. The reason for deactivation in presence of $SO_2$ is the deposition of different sulfur-containing species on the surface of the catalyst [25, 94-96]. Especially in the presence of Pt $SO_2$ gets oxidized to $SO_3$ and $H_2SO_4$ (sulfuric acid). These gaseous compounds can react with the $Al_2O_3$ [97] as well as with the noble metals especially with Palladium. Depending on the conditions (Temperature, gas composition) stable species like $Al_2(SO_4)_3$ and $PdSO_4$ can be formed [93]. Furthermore, also chemisorbed $SO_2$, $SO_3$ and sulfite species are present on the surface and lead to a blockage of the active sites, which is responsible for the drastic drop in $CH_4$ conversion.

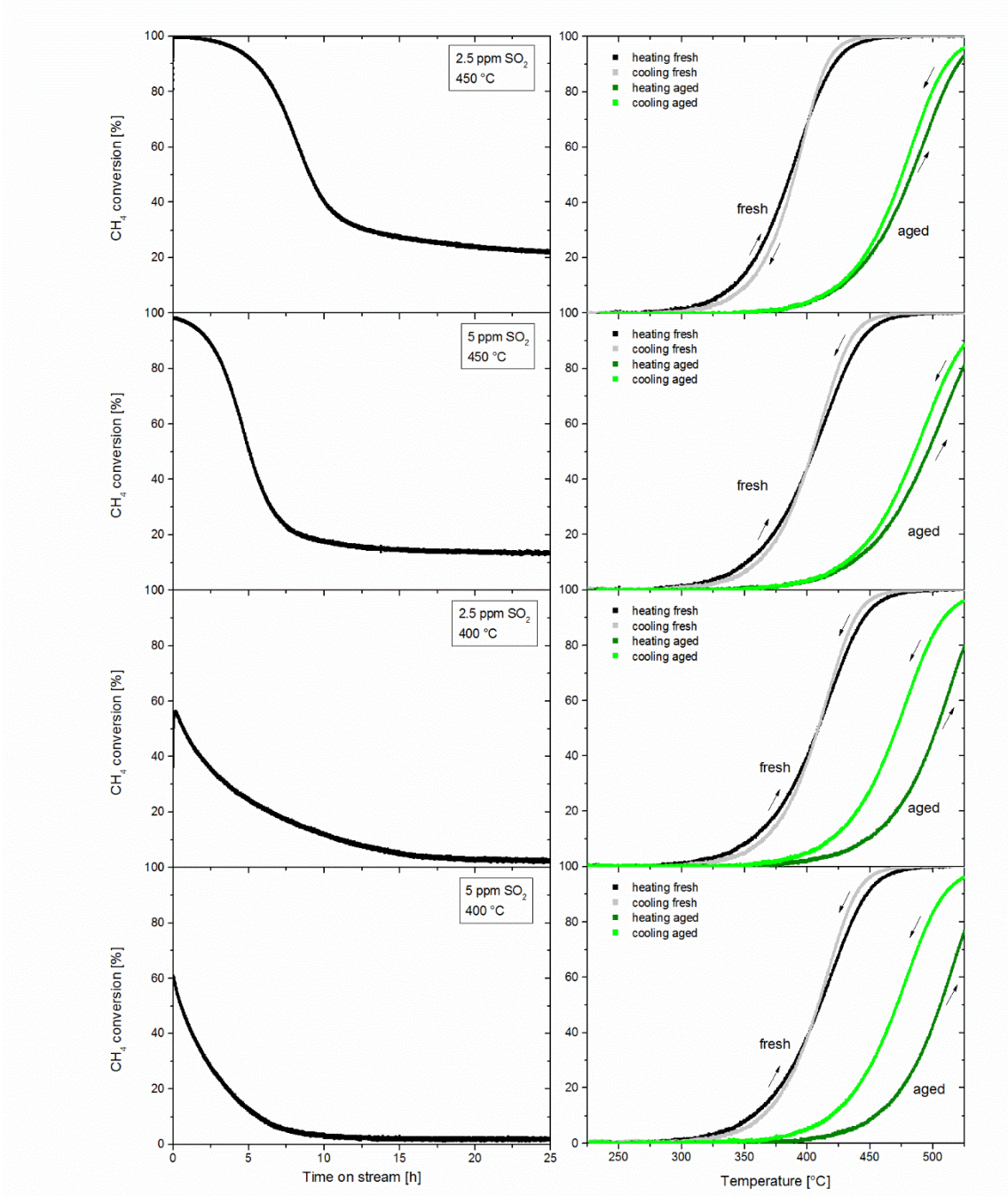


**Figure 77:** Left: $CH_4$ conversion depending on time on stream over "JM catalyst" at two different temperatures (400°C and 450°C) and two $SO_2$ concentrations (2.5ppm and 5ppm). Right: $CH_4$ conversion profiles before (fresh) and after 25h time on stream (aged). Gas composition for Light-offs: 3200ppm $CH_4$, 10% $O_2$, 12% $H_2O$ in $N_2$. For the long-term tests 2.5ppm or 5ppm $SO_2$ are added. GHSV = 30000$h^{-1}$.

The poisoning effect of $SO_2$ during the 25h long-term experiment can also be seen when comparing light-off profiles in fresh and aged state of the catalyst. In all four cases the Light off temperature is increased for the aged sample. While in the fresh state $T_{50}$ is at ~385°C, the $T_{50}$ during heating in the aged state is shifted by > 100K to higher temperature for all samples with the biggest change observed for samples aged at 400°C ($T_{50}$ aged: 505°C). Samples deactivated at 450 °C show a difference in the consecutive Light off test of 12 K ($T_{50}$ (450°C/5ppm) = 496°C; $T_{50}$ (450°C/2.5ppm) = 484°C). This stronger deactivation for the case of 5 ppm $SO_2$ can be explained by a not completely poisoned state of the catalyst.

Interestingly, the light-off profiles of the aged samples show a more or less pronounced inverse hysteresis i.e. a higher activity during cooling than during heating. This phenomenon is very distinct in case of poisoning at 400°C. In this case, the sample recovers and $T_{50}$ improves by 30 K. A reason for this is the regeneration and desorption of sulfur-species from the catalyst during the light-off itself. Since the light-off experiment was performed up to a temperature of 525°C, unstable adsorbates like $SO_2$ or $SO_3$ or less stable sulfites could be decomposed and desorbed leading to more accessible active sites and therefore higher activity. The difference between the behavior of samples poisoned at 400°C and 450°C could be explained by the stability of sulfur-species formed during the long-term run. Oxidation from $SO_2$ to $SO_3$ and from $SO_3$ to stable surface sulfates is favored at higher temperature leading to a more stable poisoned state. Following the amount of $SO_2$ released during the Light-off experiment of the aged samples (no $SO_2$ dosed) a clear difference between samples deactivated 400°C and 450°C can be observed which confirms the theory of stronger bound species in the case of 450°C. The amount of $SO_2$ released from the samples deactivated at 400°C is much higher compared to the 450°C aged samples starting at ~425°C during ramping up the temperature.

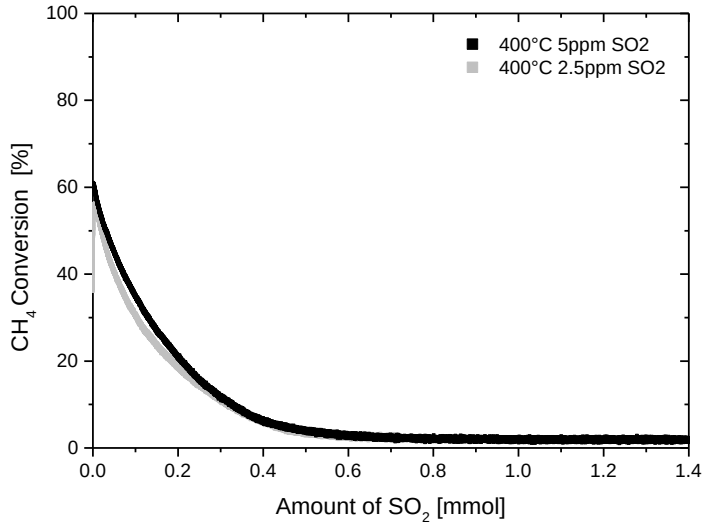


**Figure 78:** $CH_4$ conversion on "JM catalyst" plotted as function of absolute $SO_2$ amount entering the catalyst during long-term tests of 25h with two different $SO_2$ concentrations at 400°C. Gas composition for Light-offs: 2.5 or 5ppm $SO_2$, 3200ppm $CH_4$, 10% $O_2$, 12% $H_2O$ in $N_2$. GHSV = 30000$h^{-1}$.

### 9.1.2 Regeneration Tests

The results reported in 9.1.1 disclosed the strong sensitivity of the catalyst towards $SO_2$ and the fast poisoning. Because of this, different conditions were investigated to get a better understanding of how to regenerate poisoned samples efficiently. In general, the regeneration aims at the desorption of sulfur based species from the catalyst surface.

Based on the results above, a deactivation experiment followed by different regeneration in different gas compositions were developed. The procedure is described in Figure 79. A time on stream

of 15 hours at 450°C and 5ppm $SO_2$ were chosen as conditions for the poisoning. Under these conditions a strong and as far as possible complete deactivation is expected. In contrast to the tests shown in Figure 76 small amounts of $NO_x$ are added to the reaction mixture. This is due to the fact that $NO_x$ was found to have a stabilizing effect during $CH_4$ oxidation as also shown in 6.3(compare also FVV project “Methane Catalytic ” [23, 58]). In this case, the deactivation can solely be attributed to the presence of $SO_2$.

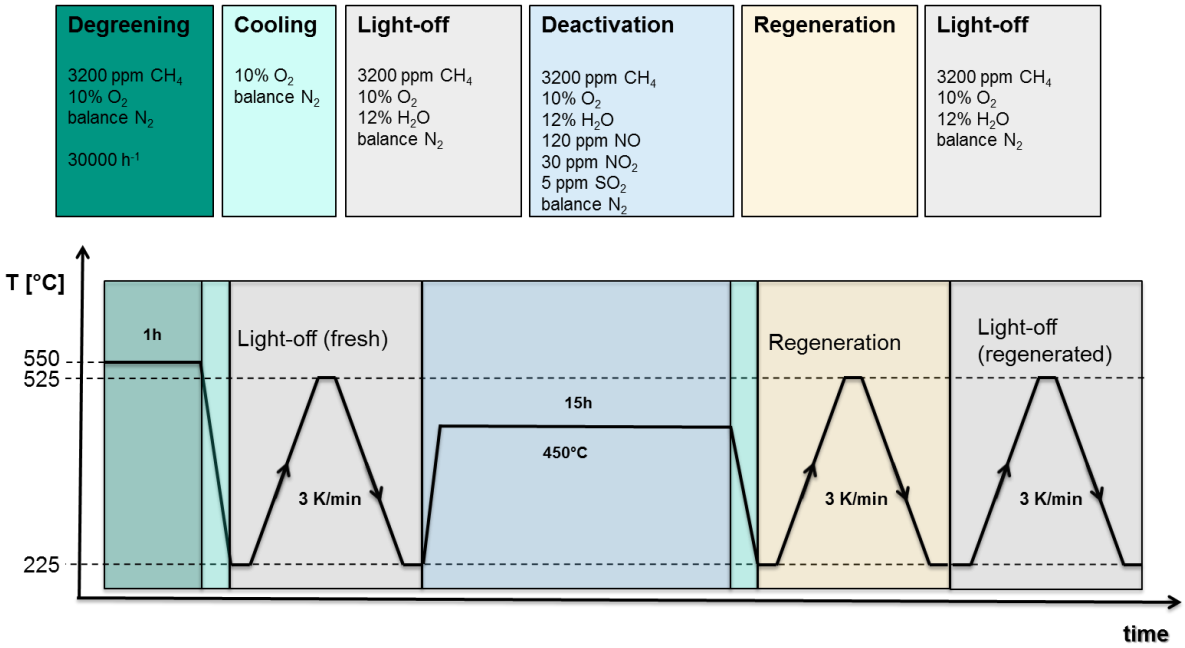


**Figure 79:** Experimental procedure for investigating three different reactivation strategies for $SO_2$-poisoned samples. For every procedure a fresh sample was used.

After 15 hours on stream, the samples were regenerated by means of heating to 550°C and subsequent cooling to 225°C in different gas compositions. The three different gas compositions for regeneration are:

a) “RM”: 3200ppm $CH_4$, 10% $O_2$, 12% $H_2O$ in $N_2$

b) “lean” 10% $O_2$, 12% $H_2O$ in $N_2$

c) “rich” 3200ppm $CH_4$, 12% $H_2O$ in $N_2$

Conditions a) correlate to two consecutive light-offs in reaction mixture while the first light-off is considered as a regeneration procedure. However, this gives the opportunity to get a light-off temperature for the poisoned sample.

The deactivation during 15 hours in $SO_2$ containing atmosphere at 450°C is shown in Figure 80 and is representative for all three investigated samples. As already discussed in 9.1.1 the catalyst activity rapidly drops from initial high methane conversion of 98% to only 19% after 15h. A consecutive light-off revealed a shift of $T_{50}$ from 400°C to 500°C after the deactivation period. This can also be seen in Figure 81 where $T_{50}$ is plotted as bars for the three regeneration experiments (fresh state, aged state from sample a) “RM” for comparison and in the regenerated state after procedures a), b) and c)).

Cases a) and b) only differ in the presence of methane in case a) during regeneration. In both cases the regeneration procedure leads to a lower $T_{50}$ in the consecutive light-off. However, regeneration in the presence of $CH_4$ is more successful ($T_{50}$ of 483°C vs. 498°C in regenerated state). Conditions a) lead to a 21K lower $T_{50}$ while procedure b) leads to only 6 K lower $T_{50}$. The positive effect of the presence of methane can be explained by a higher temperature of the catalyst. Since the exothermic methane oxidation takes place in case a) a higher temperature along the catalyst is present. Comparing the outlet temperatures (downstream of the catalyst) a ΔT of 20 K is observed between case a) and b).

Regeneration under rich conditions (conditions c) was found to be most effective of all investigated conditions. After rich regeneration, the light-off temperature is found to be 400°C, which is even slightly lower than in the fresh state. The sulfur species formed during 15h of poisoning must have been decomposed during the regeneration step.

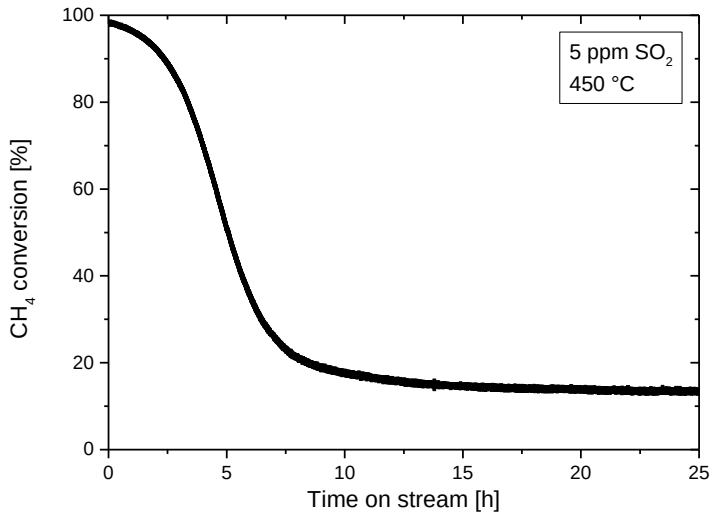


**Figure 80:** Methane conversion during 15 hours on stream for "JM catalyst". Gas composition: 5ppm $SO_2$, 30ppm $NO_2$, 120ppm NO, 3200ppm $CH_4$, 10% $O_2$, 12% $H_2O$ in $N_2$. GHSV = 30000 $h^{-1}$.

Regeneration of sulfur-poisoned catalysts is also discussed in literature [98-101]. The reductive conditions lead to a reduction of surface sulfates to gaseous $H_2S$ and $SO_2$ which leave the catalyst. However, for this process a critical temperature is needed depending on support material and gas components concentration. For example, *Xi et al.* [98] compared 2 different rich gas compositions and found a better reactivation of an engine aged (sulfur poisoned) sample for a mixture containing $CH_4$, CO and $H_2$ in comparison to only $CH_4$ in 10 vol.% $H_2O$, 7 vol.% $CO_2$ and 5000 ppm $O_2$ in Ar. While under oxidizing conditions the formed sulfates are quite stable and start to decompose at around 400°C – 450°C [102], under reducing conditions this process already starts at around 250°C – 350°C. *Luo et al.* investigated the $O_2$ concentration during regeneration of a poisoned $Pt/Al_2O_3$ catalyst. They found that with higher $O_2$ content the desorption of $SO_2$ is shifted to higher temperature i.e. decomposition of surface sulfates needs higher temperature the higher the oxygen content in the stream.

The light-off temperature during cooling of the regenerated catalyst under conditions c) is almost 20K higher than during heating up (Figure 81). This phenomenon can be explained by a transition of sulfur species still present on the support material ($Al_2O_3$) back to the freshly regenerated Pd or Pt sites during the preceding heating. This so-called "spill over" leads to lower activity after the initial regeneration which was also proved by a second light off (not shown) revealing a constant decrease of activity.

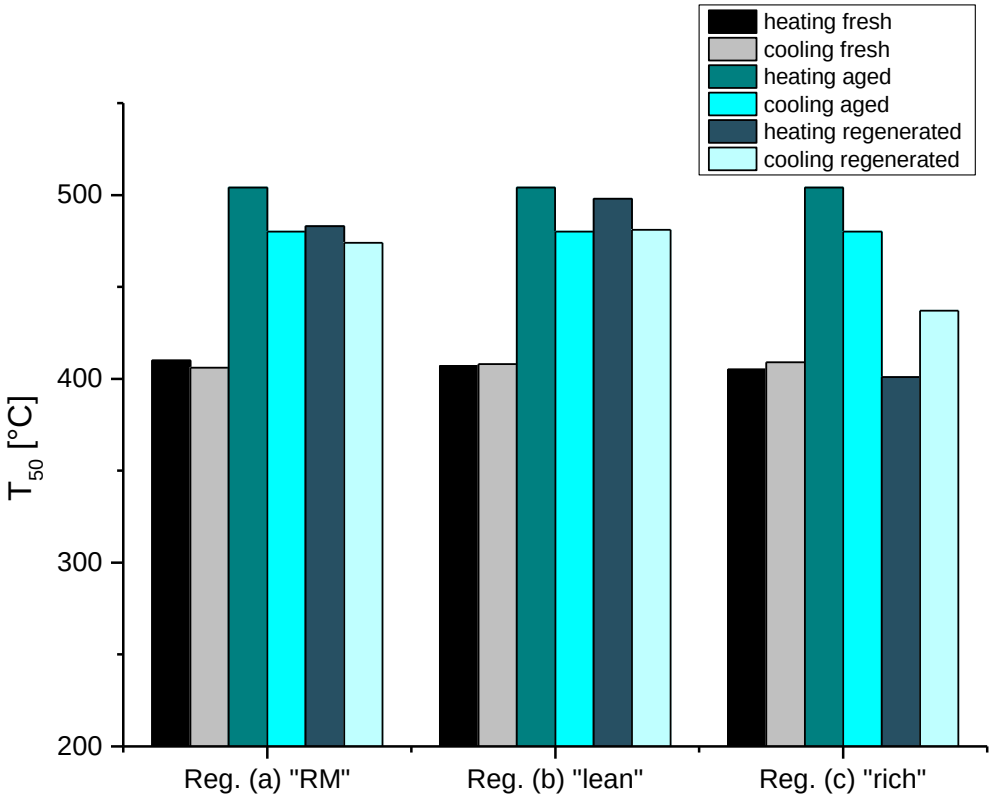


**Figure 81:** Temperature at which 50% methane conversion occurs ($T_{50}$) in fresh, aged and regenerated state (bars from left to right) for three different regeneration experiments on “JM catalyst”. Values for aged state are taken from procedure “RM”.

### 9.1.3 Influence of $SO_2$ at higher pressure

A potential positioning of the catalyst in front of the turbocharger changes the operating conditions for the catalytic converter. While temperatures are generally higher in pre turbo position, the pressure is higher as well, typically in ranges of 3 – 5 bar. While the effect of pressure under sulfur free conditions was already discussed in chapter 0, this chapter presents the results of tests performed with $SO_2$ containing atmosphere.

The experiments consisted of long-term tests for 20h at different temperatures (450°C and 600°C) and 2 different pressures (1bar and 4bar) in $SO_2$ containing atmosphere (5ppm $SO_2$, 30ppm $NO_2$, 120ppm NO, 1000ppm $CH_4$, 10% $O_2$, 12% $H_2O$ in $N_2$) with a GHSV of 60000 $h^{-1}$. For every test, a fresh sample was used. Additionally, light-off measurements in fresh state and after 20h time on stream were performed. The light-off experiments consisted of two consecutive heating and cooling cycles between 225°C and 525°C in 3200ppm $CH_4$, 10% $O_2$ in $N_2$ with a GHSV of 30000 $h^{-1}$.

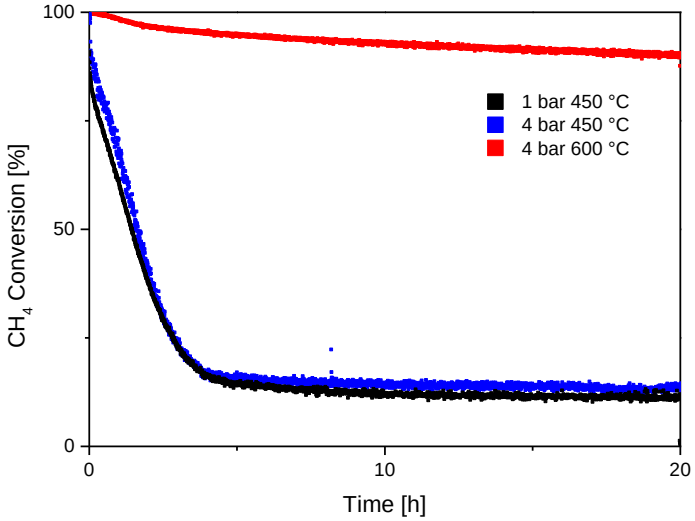


**Figure 82:** Methane conversion of "JM catalyst" during 20h time on stream at 1bar and 4bar at 450°C and 600°C. Gas composition: 5ppm $SO_2$, 30ppm $NO_2$, 120ppm NO, 1000ppm $CH_4$, 10% $O_2$, 12% $H_2O$ in $N_2$. GHSV = 60000 $h^{-1}$.

Figure 82 shows the methane conversion over time. The $CH_4$ conversion curves at 450°C are quite similar and show a fast deactivation leading to only 11% of conversion after 20 h. Considering a space velocity that is twice as high as in chapter 9.1.2 the rate of deactivation is comparable to previously discussed results and can be explained by formation of sulfates leading to blockage of the noble metals. Analogous to the trend of $CH_4$ conversion, the concentration of $NO_2$ is also decreasing rapidly in the first 2 h. While at 4 bar within the first 1h on stream NO is oxidized to $NO_2$, this trend changes after advancing poisoning which leads to a decomposition of $NO_2$ to NO (Appendix Figure 106).

Comparing the two different pressures at 450°C it can be seen that at 4 bar the $CH_4$ conversion is slightly higher in the beginning and also about 2% higher after 20 h on stream than at 1 bar. This can be explained by a higher residence time in the 4bar case. The higher partial pressure of $SO_2$ in the 4bar case and therefore a higher concentration of $SO_2$ (while the amount of $SO_2$ fed to reactor is constant in both cases) does not lead to a stronger inhibiting and deactivating effect.

The test conducted at 600°C and 4bar, which represents typical pre turbo conditions, shows a different $CH_4$ conversion trend. The higher temperature and therefore higher catalyst activity results in $CH_4$ conversion > 90°C during the 20h on stream. However, also at 600°C a decrease of activity can be observed leading to the hypothesis that $SO_2$ poisoning plays a role at higher temperature as well. *Mateo et al.* [103] also observed a deactivation of a $Pd/SiO_2$-$Al_2O_3$ catalyst in $SO_2$ containing atmosphere at 600°C. They also detected sulfate formation during deactivation at 600°C. However, also sintering of the noble metals might have led to a slight decrease in $CH_4$ conversion at 600°C.

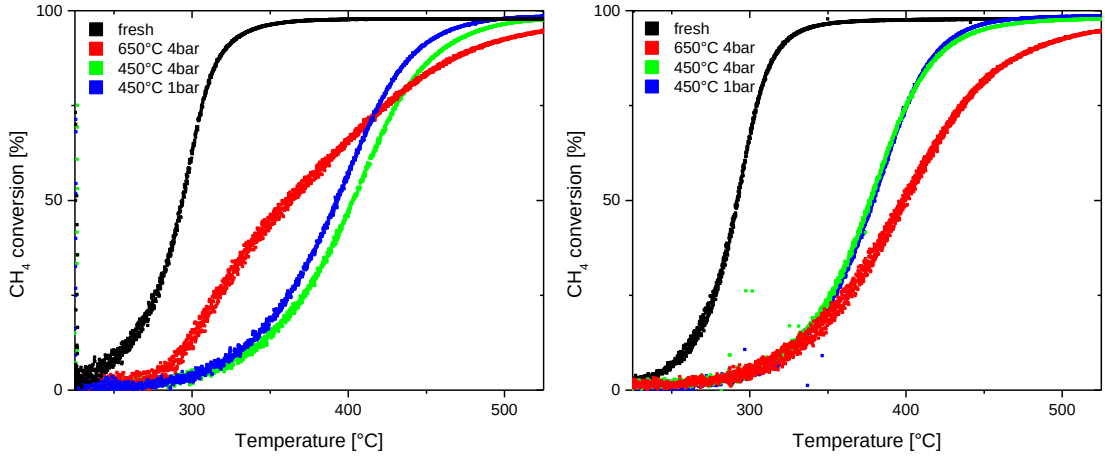


**Figure 83:** $CH_4$ conversion profiles of fresh and deactivated "JM catalyst" samples. Gas composition: 3200ppm $CH_4$, 10% $O_2$ in $N_2$. GHSV =f 30000 $h^{-1}$. Left: heating. Right: cooling

When comparing the fresh sample with the samples after 20 h on stream, a clear shift in light-off temperature can be observed. While during the first heating the sample from the test at 600°C at 4bar seems to be more active in low temperature range its $CH_4$ oxidation activity strongly shifts during cooling down (and also consecutive 2nd heating and cooling). This might be explained by a partial regeneration of the sample after 20h on stream in $SO_2$ containing atmosphere when the gas stream was switched to $N_2$ for cooling. Since the cooling could not be realized within seconds time scale, the sample was probably slightly regenerated at T > 450°C as already discussed in the previous section. Therefore, comparing the conversion profiles during 1st cooling (Figure 83, right) seems to be more suitable. It can clearly be seen that the samples deactivated at 450°C show the same light-out curve with a $T_{50}$ of 380 °C. With higher temperature the deactivation seems to more pronounced. Although potential sintering might have contributed to the deactivation, the poisoning effect of $SO_2$ seems to be stronger at higher temperature. At 600°C the conversion of $SO_2$ to $SO_3$ and then to $H_2SO_4$ is favored leading to a fast formation of alumina and palladium sulfates. However, at 600°C already partly decomposition of the sulfates can occur under atmospheric conditions with 10% oxygen [102, 104]. Taking into consideration, that at 4 bar the concentrations of $SO_2$ and $O_2$ are higher, the sulfates should be more stable and a continuous poisoning of the sample can be explained.

The formation of sulfur species on the catalyst during our tests is also proved by Temperature Programmed Desorption (TPD) experiments. In these tests the deactivated samples were heated with 10K/min in 5L/min $N_2$ up to 925°C while desorbing sulfur-species are monitored with a FT-IR ($SO_2$, $SO_3$, $H_2SO_4$ monitored).

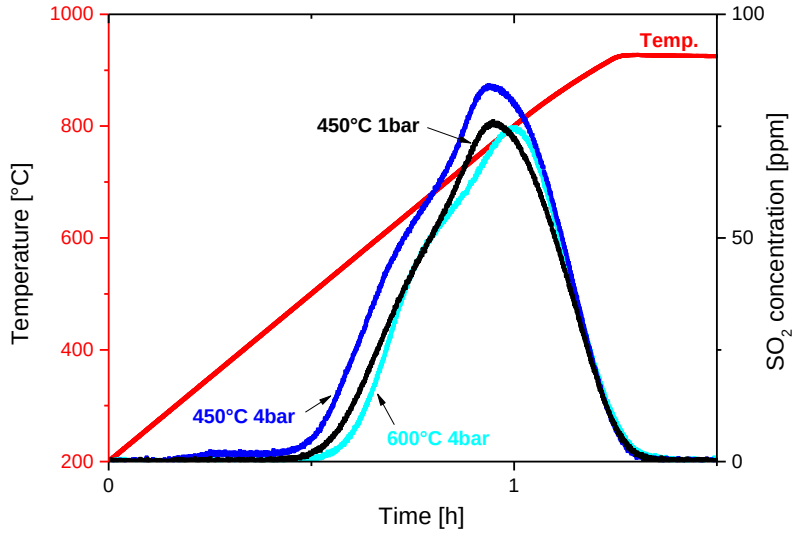


**Figure 84:** Sulfur-Temperature-Programmed-Desorption (S-TPD) of "JM catalyst"-samples treated with $SO_2$ containing atmosphere at 450°C and 600°C at 1bar and 4bar. Gas composition: 5L/min $N_2$. Sample size: 20mm length, 20mm diameter. Atmospheric pressure.

Figure 84 shows the result of the S-TPDs. It can be seen that $SO_2$ is released (no other sulfur-containing gaseous species observed) starting at 500°C from all samples. However, from the sample deactivated at 450°C at 4bar already at 300°C small amounts of $SO_2$ desorb (1-2ppm). This $SO_2$ could come from sulfur surface species that were stable under 4bar and now decompose at atmospheric pressure in $N_2$. Overall the sample treated at 450°C and 4bar stores the highest amount of sulfur-species. Again this could be explained by a higher pressure compared to the test performed at 450°C and 1bar leading to more stable species. However, the differences of stored sulfur amount are quite small and in all cases a high sulfur uptake can be confirmed.

## 9.2 PdPt/CZ

### 9.2.1 Deactivation with $SO_2$

The PdPt/CZ sample supported on a metal substrate was deactivated analogous to the procedure described in Figure 79 for 15h at 450°C. However, no regeneration was performed after 15h on stream but a consecutive light-off was done to compare the catalysts activity before and after aging.

Figure 85 shows the $CH_4$ conversion during time on stream and also the activity in fresh and deactivated state by means of light-off curves. During time on stream the $CH_4$ conversion drops within 15h from 80% to only 7%. The deactivation is faster and more pronounced than for the $Al_2O_3$ based Pd-Pt catalyst described in chapter 9.1. One reason for this is the lower loading of 100g/ft³ for the CZ sample and 120g/ft³ for the $Al_2O_3$ based sample. Furthermore, the different support materials play a major role in catalyst poisoning. Alumina is well known to form sulfates in presence of $SO_2/SO_3$, acting as a sulfur scavenger [26]. However, the $CeZrO_x$ support provides a lower specific surface area and is also more resistant to forming sulfates. This leads to a faster deactivation of the active noble metal sites. Additionally to a faster and more pronounced deactivation, the sample provides a very low $CH_4$ oxidation activity in a consecutive light-off (Figure 16, right). This indicates very pronounced poisoning of the noble metal sites by sulfates.

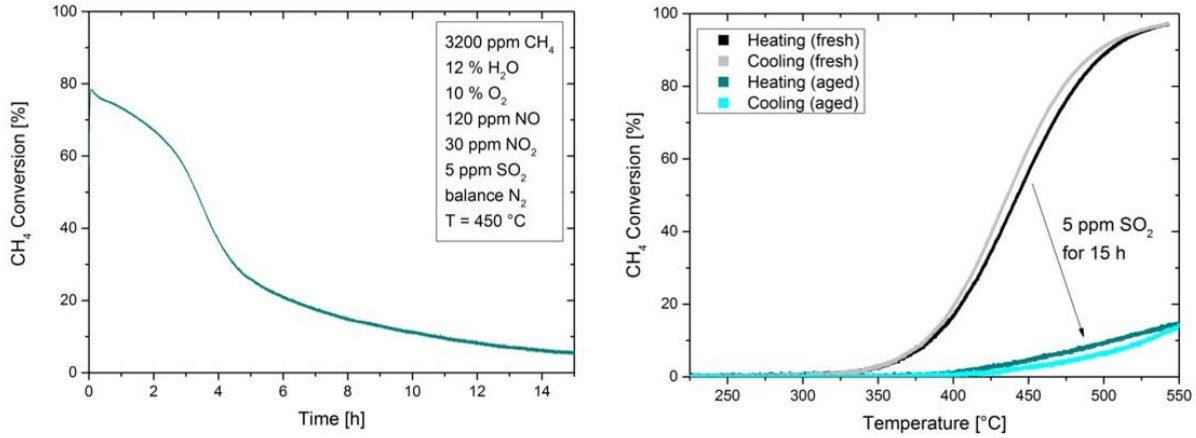


**Figure 85:** Left: $CH_4$ conversion over time for PdPt/CZ sample in 5ppm $SO_2$, 30ppm $NO_2$, 120ppm NO, 3200ppm $CH_4$, 10% $O_2$, 12% $H_2O$ in $N_2$. GHSV = 30000 $h^{-1}$. Right: $CH_4$ conversion during cooling and heating in fresh and deactivated state in 3200 ppm $CH_4$, 10 % $O_2$, 12 % $H_2O$ in $N_2$. GHSV = 30000$h^{-1}$.

### 9.2.2 Regeneration Tests

With the PdPt/CZ KIT powder catalyst regeneration experiments after sulfur deactivation were performed. The procedure is the same as for "JM catalyst" (Figure 79), but only the potent regeneration in rich mixture was applied. The only difference to the procedure shown in Figure 79 is that after 15h time on stream two consecutive light-off experiments were performed.

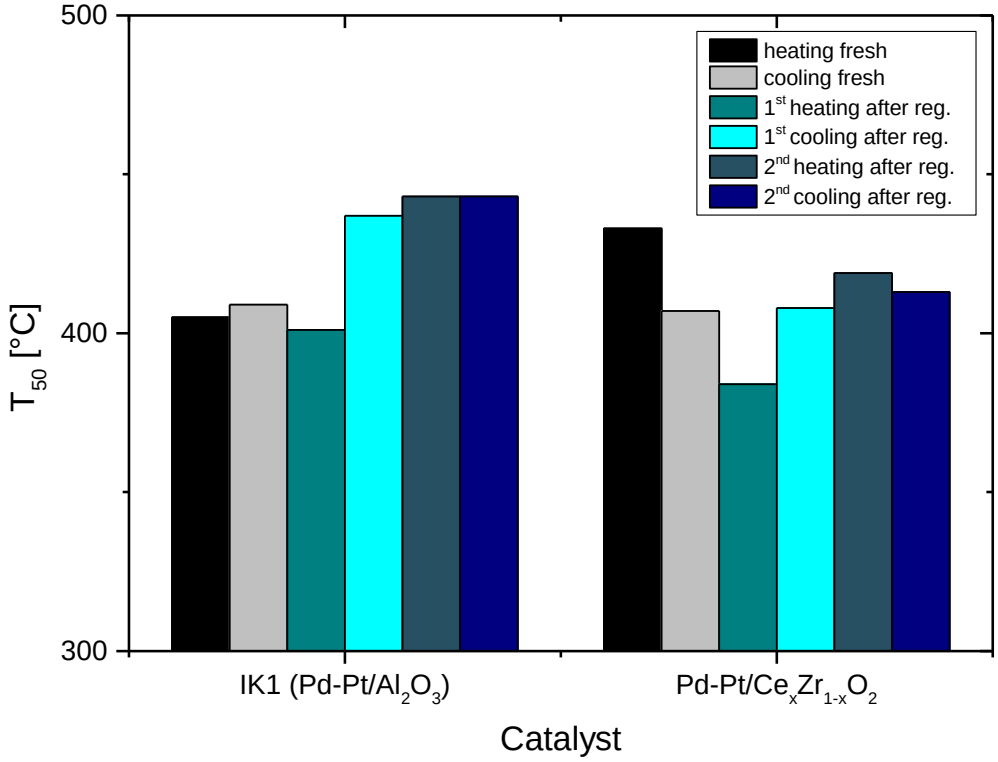


**Figure 86:** Temperature at which 50% methane conversion occurs ($T_{50}$) in fresh state and regenerated after 15h in $SO_2$ containing atmosphere by rich treatment during light-off experiments (heating and consecutive cooling) for "JM catalyst" and PdPt/CZ KIT.

Figure 86 summarizes the regeneration results for the PdPt/CZ KIT sample in comparison to the "JM catalyst". The deactivation for PdPt/CZ KIT is similar to the one shown in Figure 85. As already

shown in chapter 9.1.2, the rich treatment in 3200ppm $CH_4$, 12% $H_2O$ in $N_2$ led to a completely regenerated catalyst. The first light-off curve after regeneration is even shifted to lower temperature than in the fresh state. This is also emphasized by a $T_{50}$ which is about 50K lower than in the fresh state. One has to keep in mind that a light-off after 15h time on stream in $SO_2$ containing atmosphere only reached 17% conversion at 550°C. With respect to that, the regeneration procedure was found to be very successful on the $CeZrO_x$ based Pd-Pt catalyst. The $CeZrO_x$ is not able to store that much sulfates compared to $Al_2O_3$ [105]. Therefore, during regeneration only a smaller amount has to be decomposed and fewer sulfur-species migrate back to the noble metal sites (spill over). Higher activity in consecutive cooling/heating cycles confirms this assumption. $T_{50}$ during 2nd heating and cooling is in the same range as the 1st cooling in fresh state. The sample seems to be in a nearly fresh state during 2nd light-off after regeneration. Furthermore, on $ZrO_2$ only surface sulfates are formed and no bulk sulfation occurs according to *Luo et al.* [106].

To investigate the catalyst behavior under more engine relevant conditions, transient experiments in presence of $SO_2$ were performed on PdPt/CZ KIT. For this reason, an already used sample (15h in $SO_2$ containing atmosphere plus consecutive light off) was kept at 450°C with a gas composition of 3200ppm $CH_4$, 120ppm $NO_2$, 30ppm NO, 5ppm $SO_2$, 10% $O_2$, 12% $H_2O$ in $N_2$ while varying different parameters for short time (e.g. temperature or $O_2$ concentration).

Figure 87 shows the first part of this long-term experiment. As already shown before the activity rapidly decreases in presence of $SO_2$ leading to almost no activity after > 15 hours. At that point $SO_2$ dosage was stopped for one hour. However, under $SO_2$ free conditions at 450°C no regeneration of the catalyst was observed. Although no gaseous $SO_2$ was present, the poisoning sulfur species on the surface are too stable at this temperature in the presence of high $O_2$ content. After more time on stream the $O_2$ dosage was stopped for leading to net reducing conditions. Even though rich conditions were found to be markedly potent for regeneration, no increase in $CH_4$ activity was found at 450°C. Because of this, further tests were performed with this sample subsequent to the procedure shown in Figure 87.

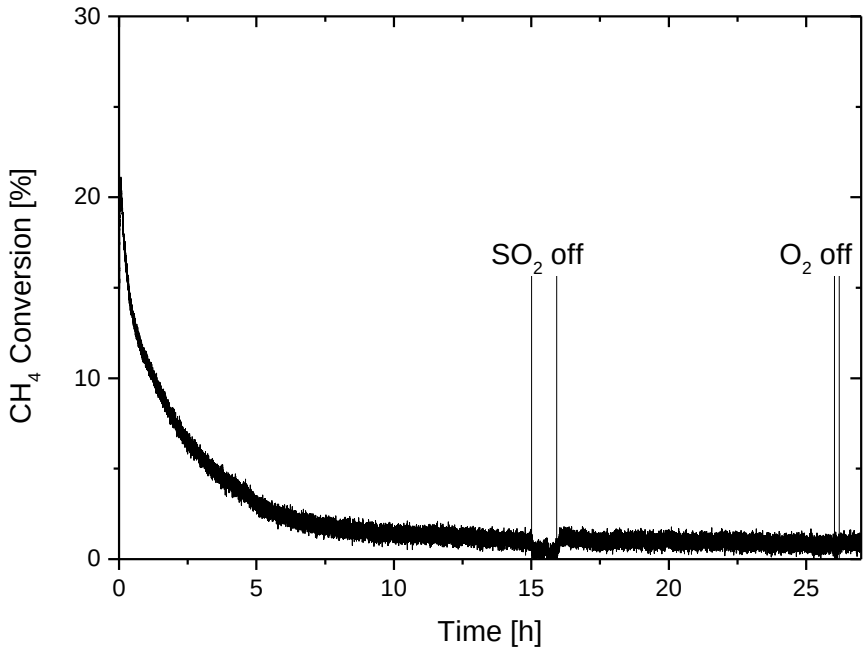


**Figure 87:** $CH_4$ conversion of PdPt/CZ KIT over time at 450°C. Gas composition 3200ppm $CH_4$, 120ppm $NO_2$, 30ppm NO, 5ppm $SO_2$, 10% $O_2$, 12% $H_2O$ in $N_2$. Flow: 1L/min. Changes in gas composition according to Figure. Overall flow always kept constant by balancing with $N_2$.

The effect of temperature on the $CH_4$ conversion in absence of $SO_2$ is demonstrated in Figure 88. Two changes in gas composition and temperature were induced: heating to 500°C in absence of $SO_2$ for 1 hour and after adequate time on stream at 450°C temperature was again increased in absence of $SO_2$ to 550°C for 1h. The change in temperature and gas composition was realized at the same time, i.e. as soon as $SO_2$ is shut down, temperature is increased. However, after 1h at

elevated temperature the gas was switched back on and is present during cooling. An increase in temperature leads to an increase of $CH_4$ conversion. However, only small changes can be observed when temperature is increased up to 550°C under oxidizing conditions when $SO_2$ is not present. Only during higher temperature periods, the catalyst is able to oxidize more $CH_4$ (17 % conversion at 550°C). However, no regeneration effect is observed, i.e. the $CH_4$ conversion goes back to the initial low level of 2-3% after temperature reaches 450°C again.

Under fuel rich conditions (no oxygen fed to the reactor, $SO_2$ still present) the same procedure was repeated. During these events, the catalyst was kept at 450°C for >10 hours in $SO_2$ containing atmosphere to secure a completely poisoned state. Even under reducing conditions at 500°C, no regeneration of the catalyst is observed. However, in the case temperature is increased up to 550°C a pronounced increase in activity is found. During heating to 550°C in the absence of $O_2$, the amount of $SO_2$ detected at the catalyst outlet is rising up to 50 ppm (compare Figure 107 in Appendix). After 1h at 550°C, 10% $O_2$ are added to the gas stream leading to a very high methane conversion of >70%. During cooling to 450°C, the activity decreases to ~25% and within the following 15 hours on stream to almost 0% conversion.

As already discussed before, rich conditions provide a promising strategy to regenerate sulfur poisoned catalyst. However, also the temperature is critical for that procedure. For the PdPt catalyst on ceria-zirkonia a suitable temperature of 550°C was found. Although $SO_2$ was still present during the regeneration at 550°C, an increase of 30 % conversion was achieved as can be seen in Figure 88.

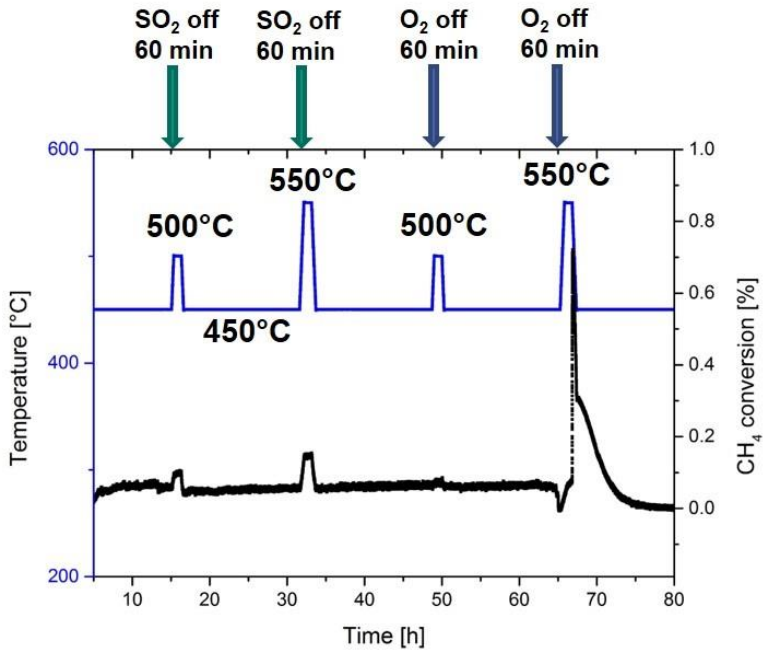


**Figure 88:** $CH_4$ conversion of PdPt/CZ KIT over time at 450°C subsequent to test shown in Figure 87. Gas composition 3200ppm $CH_4$, 120ppm $NO_2$, 30ppm NO, 5ppm $SO_2$, 10% $O_2$, 12% $H_2O$ in $N_2$. Flow: 1L/min. Changes in gas composition and temperature according to Figure. Overall flow always kept constant by balancing with $N_2$.

### 9.2.3 Summary $SO_2$ Tests

The effect of sulfur containing species was investigated by several experiments on Pd-Pt supported on $Al_2O_3$ and $CeZrO_x$. Both samples are highly affected by even very small amounts of $SO_2$, leading to a fast deactivation in exhaust-gas relevant temperatures between 400°C – 450°C. Blockage of the active sites by formation of sulfates and sulfites is responsible for the pronounced deactivation. Neither the $Al_2O_3$ based sample nor the Ceria-Zirkonia based sample were able to withstand the deactivation. However, the speed and extent of deactivation is slightly different. While $Al_2O_3$ is able

to form sulfates, it can act as a scavenger delaying the poisoning of the active sites. This positive property becomes disadvantageous during regeneration processes. A higher amount of sulfur species has to be decomposed from $Al_2O_3$ and a subsequent spill-over of surface sulfur-species from $Al_2O_3$ back to the active sites is more likely and pronounced. For both catalysts rich treatment leads to regeneration of the catalyst to some extent. However, a critical temperature is also needed to decompose the poisoning species from the catalyst surface. For the PdPt/CZ sample this temperature is >525°C under rich conditions. Under lean conditions with high oxygen excess, this temperature is much higher. Under reducing conditions almost complete regeneration is possible at temperatures above 550°C. This strategy was also found to be successful when $SO_2$ is still present. That would be the case when a catalyst is run in real application and the engine is switched to a fuel rich combustion mode ($\lambda<1$). To create the reducing environment for the catalyst also fuel injection after the engine might be an option.

Besides applying regeneration strategies another possibility would be to put the catalyst in front of the turbocharger. Therefore, the effect of $SO_2$ under pre-turbo conditions was investigated. Even at 600°C and 4bar, deactivation in presence of $SO_2$ was observed. However, the rate of deactivation is much slower than at 450°C. The effect of pressure was found to be quite small leading to slightly higher conversion due to increased residence time.

A combination of pre turbo positioning with periodic regenerations under rich conditions might be a promising way to provide high methane conversion over decent time scale. Concerning this strategy, optimization of the catalyst for these conditions might also contribute to a superior overall performance.

# 10 Engine Tests (HAN)

## 10.1 Objective

To create synergy between the projects, the outcome of the FVV project, a catalyst specimen, will be tested by HAN Automotive on a combustion engine. For the FVV members this gives insight on how the research result performs under real-world conditions. For VIV this cooperation gives information about how well catalytic methane conversion can be used in natural gas powered ships.

## 10.2 Engine choice

Various options arise for the test motor to use.

- VW TSi engine at HAN automotive testbed.
- 1 Megawatt engine at teststand from VIV member
- 1 Megawatt genset from VIV member
- Nonox engine at Nonox Hoensbroek
- Dual Fuel Caterpillar engine in Dutch development environment.

All engines are given a rating on a list of relevant aspects, and a final score is calculated. Most important in the rating is the achievable result of testing, but also broader aspects like availability and costs are taken into account. The results can be seen in Table 21.

From this table the HAN VW TSi engine has the highest score, so this engine is selected for the methane catalyst testing.

**Table 21:** Rating of engine choices

Rating

| ITEM | Weight | HAN VW TSI | VIV stationary engine | VIV genset | NoNox | D/F Cat3508 |
|---|---|---|---|---|---|---|
| Control of testbed | 2 | 5 | 2 | 1 | 5 | 4 |
| Required catalyst volume (cost) | 3 | 5 | 2 | 2 | 3 | 2 |
| Options for engine calibration | 4 | 3 | 1 | 1 | 5 | 4 |
| Fuel amount | 2 | 5 | 2 | 2 | 3 | 2 |
| Ease of test operation | 1 | 4 | 2 | 2 | 4 | 3 |
| Testbed costs | 4 | 5 | 5 | 5 | 1 | 3 |
| Measurement equipment | 4 | 4 | 1 | 1 | 5 | 2 |
| Endurance possible? | 2 | 3 | 4 | 4 | 2 | 2 |
| Exhaust gas composition | 5 | 5 | 2 | 2 | 2 | 2 |
| VIV relevance | 2 | 2 | 3 | 3 | 4 | 3 |
| FVV relevance | 3 | 2 | 3 | 3 | 3 | 1 |
| HAN relevance | 3 | 5 | 2 | 2 | 3 | 3 |
| Availability testbed | 4 | 5 | 3 | 3 | 3 | 1 |
| Preparation cost | 1 | 5 | 1 | 1 | 4 | 3 |
| Reliability testbed | 5 | 4 | 3 | 3 | 4 | 2 |

Score

| ITEM | HAN VW TSI | VIV stationairy engine | VIV genset | NoNox | D/F Cat3508 |
|---|---|---|---|---|---|
| Control of testbed | 10 | 4 | 2 | 10 | 8 |
| Required catalyst volume (cost) | 15 | 6 | 6 | 9 | 6 |
| Options for engine calibration | 12 | 4 | 4 | 20 | 16 |
| Fuel amount | 10 | 4 | 4 | 6 | 4 |
| Ease of test operation | 4 | 2 | 2 | 4 | 3 |
| Testbed costs | 20 | 20 | 20 | 4 | 12 |
| Measurement equipment | 16 | 4 | 4 | 20 | 8 |
| Endurance possible? | 6 | 8 | 8 | 4 | 4 |
| Exhaust gas composition | 25 | 10 | 10 | 10 | 10 |
| VIV relevance | 4 | 6 | 6 | 8 | 6 |
| FVV relevance | 6 | 9 | 9 | 9 | 3 |
| HAN relevance | 15 | 6 | 6 | 9 | 9 |
| Availability testbed | 20 | 12 | 12 | 12 | 4 |
| Preparation cost | 5 | 1 | 1 | 4 | 3 |
| Reliability testbed | 20 | 15 | 15 | 20 | 10 |
| Final score | 188 | 111 | 109 | 149 | 106 |

## 10.3 Engine specifications

Brand: Volkswagen
Type. 1.4 TSI
Engine code BLG

**Table 22:** Engine specifications

| | |
|---|---|
| Brand | Volkswagen |
| Type | 4 Cylinder TSI, Petrol |
| Engine code | BLG |
| Displacement | 1390cc |
| Compression ratio | 1:10 |
| Maximum power | 125 kW @ 6000 rpm |
| Maximum torque | 240 Nm @ 1750-4500 rpm |
| Exhaust gas treatment | Three way catalyst |
| EGR | No |
| Emission standard | EU4 |

**Figure 89:** VW 1.4 TSi engine.

## 10.4 CNG system

The engine is equipped with a secondary fuel system from Prins Autogas systems. It's a commercial available system, where HAN Automotive has the possibility to access calibration parameters. With this system CNG is indirectly injected into the engine, by means of Keihin gas injectors. The control system uses the injected petrol quantity to calculate the desired CNG amount. Although this initially results in the same lambda values as the petrol system, the CNG system also has an option to limit injected fuel amount. With this option it was shown a good lean-burn operation of the engine can be calibrated. Within the CNG control system there is also the possibility to offset the standard ignition timing, to take care of the extra ignition advance CNG usually needs, compared to petrol.

## 10.5 Operating point

The operating point of the engine will be chosen in such a way that the engine produces exhaust gasses which are comparable with the exhaust gas from a large lean burn industry engine. FVV desires the values shown in Table 23 originating from the Methane catalytic projects.

**Table 23:** Desired exhaust gas properties

| Parameter | Desired value | Unit |
|---|---|---|
| T_cat_in | 450 | [ $^0$C] |
| $CH_4$ | 3500 | [ppm] |
| CO | 500 | [ppm] |
| $CO_2$ | 6 | [%] |
| $O_2$ | 10 | [%] |
| HC | 200 | [ppm] |
| $H_2O$ | 12 | [%] |
| $SO_2$ | 2-5 | [ppm] |
| $NO_x$ | 150 | [ppm] |

From this table the temperature is most important, and it is necessary to have the engine in lean burn operation. This ensures exhaust gasses containing methane, oxygen and nitrous oxides.

After some iterations the following point was selected:

**Table 24:** operating point

| Parameter | | HAN | **MCI/II** |
|---|---|---|---|
| RPM | [rpm-1] | 1700 | |
| Torque | | 51 | |
| MAP | [mbar] | 1020 | |
| MAF | [kg/h] | 60 | |
| GHSV | [$h^{-1}$] | 80000 | |
| T_cat_in | [ °C] | 451 | **450°C** |
| T_cat_out | [ °C] | 319 | |
| P_cat_in | [mbar] | 68 | |
| P_cat_out | [mbar] | 10 | |
| $CH_4$ | [ppm] | 2680 | **3500** |
| CO | [pm | 660 | **500** |
| CO2 | [%] | 7,5 | **6** |
| O2 | [%] | 7,7 | **10** |
| HC | [ppm] | 169 | **200** |
| H2O | [%] | n.n. | **12** |
| SO2 | [ppm] | n.n. | **2-5** |
| NOx | [ppm] | n.n. | **150** |
| Lambda | [-] | 1,68 | |

## 10.6 Catalyst placement

There are several possibilities to place the catalyst. In the original engine configuration the catalyst is close coupled to the turbocharger. If it would be necessary to have it operating at lower temperatures it can be placed further away from the engine. Now that a good operating point is found, the original location of the catalyst can be used.

**Figure 90:** Original TWC.

With so-called V-band clamps the original catalyst was removed and replaced by the catalyst from the project partners.

**Figure 91:** Left: FVV/KIT sample. Right: Placement of sample at test-engine.

## 10.7 Test procedure

### 10.7.1 Duration

The tests were performed for two weeks. This consists of 2*5*8 = 80 hours of operation. The test is done keeping the engine operating steady state on the chosen setpoint. After proceeding the complete test program, in total 60 hours of catalyst testing were recorded.

### 10.7.2 Gas supply

CNG from the Dutch public gas is used for the testing. During testing the gas is supplied from two automotive gas tanks. These tanks are filled overnight by a Fuelmaker filling station.

The used gas is sampled and analyzed by certified institute Kiwa, results can be found in the appendix.

**Figure 92:** CNG tanks.

### 10.7.3 Data

The following signals are collected on the engine test bench during test:

- Engine speed
- Engine torque
- MAP
- MAF
- Intake temperature
- T_cat_in
- T_cat_out
- P_cat_in
- P_cat_out
- Lambda

- $CH_4$
- CO
- $CO_2$
- $O_2$
- HC
- $NO_x$

The following equipment will be used for that:

- National Instruments test bed control & measurement
- Siemens Ultramat 6 methane analyzer
- SUN DGA 1500 5 component exhaust gas analyzer.

### 10.7.4 Results Catalyst deactivation

Main result of the test is the conversion factor of methane, before and after catalyst. This can be seen in Figure 93.

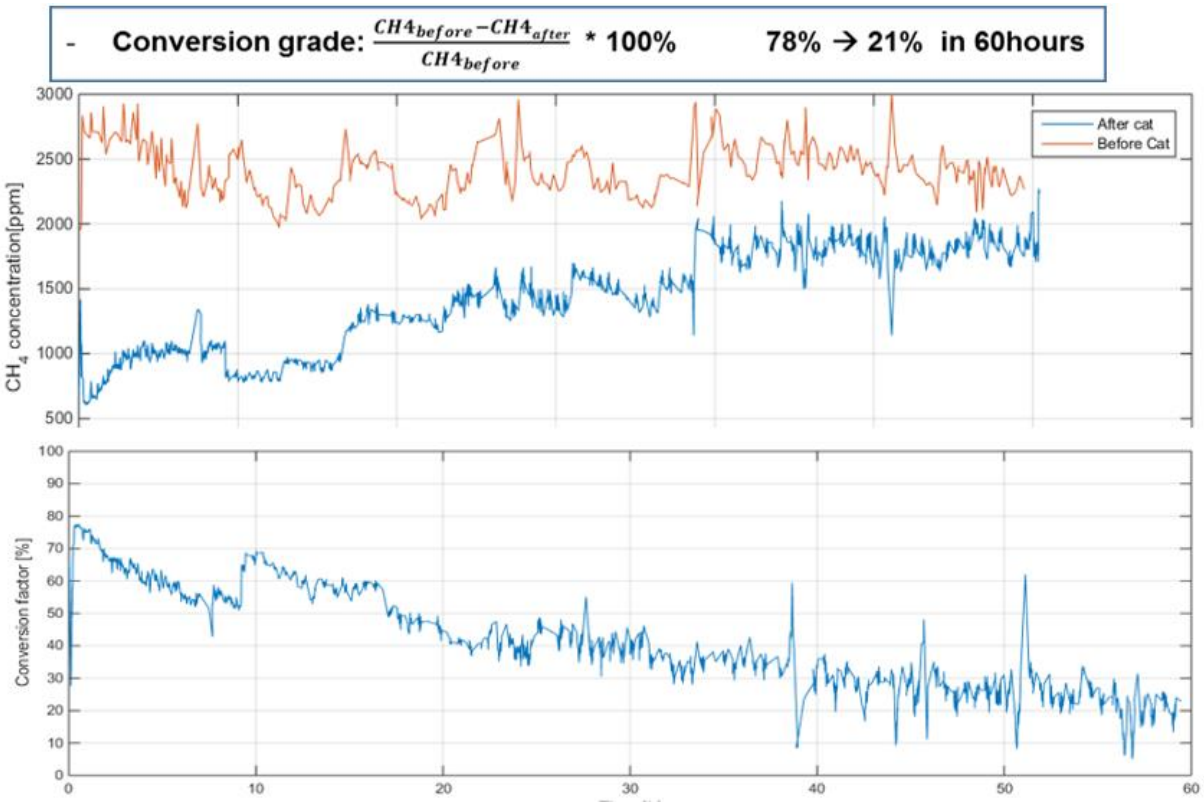


**Figure 93:** $CH_4$ Conversion factor during operation on engine.

### 10.7.5 Results Catalyst reactivation

In a second test series catalyst tests are performed including regeneration. Initially a steady state test is performed at the same operating point as the previous test, to create catalyst deterioration. After this, it is tried to regenerate the catalyst by running it under rich conditions. The engine controller is set at an increased fuel amount, to cross the lambda=1 limit. To keep exhaust gas temperature at the same level, the load was reduced. This also lowers the space velocity towards 50000 h-1. Exact values can be calculated from measurement-data.

A first experiment is done with a regeneration time of 30 minute. After a new degradation experiments with 1and 5 minutes rich operation can be performed. The resulting conversion factors can be seen in Figure 94.

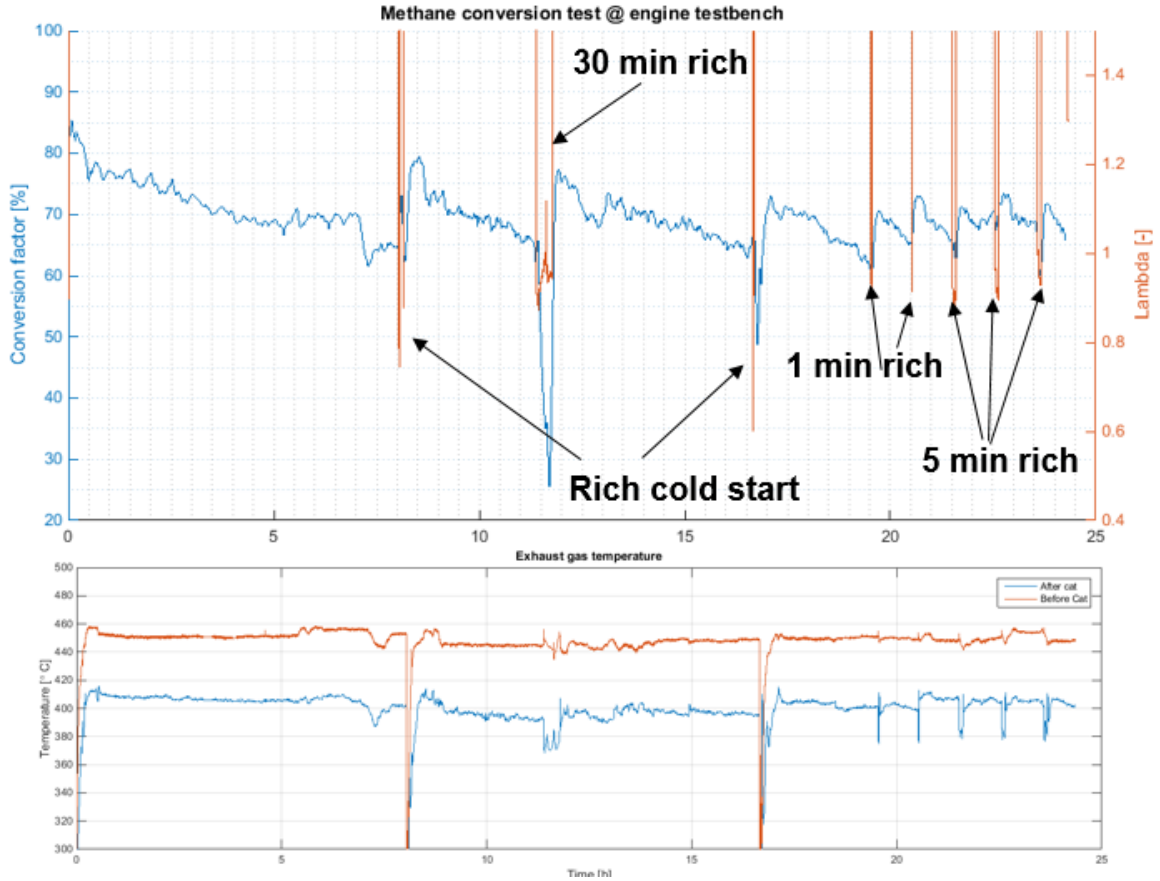


**Figure 94:** Regeneration testing.

# 11 Characterization of engine-aged samples (KIT)

## 11.1 Characteristics and Activity

The PdPt/CZ catalyst that was operating on a gas engine at HAN (chapter 10) was send back to KIT for further tests. As discussed before, the methane conversion of the catalyst during 60 hours in lean burn gas engine exhaust stream decreased from initially 78% to only 21%. The catalyst inlet temperature was kept constant at 450°C and the space velocity was 80000$h^{-1}$. To better understand what is happening under real engine operation conditions, the catalyst had to be characterized.

For further tests, the catalyst (130mm length, 120mm diameter) had to be cut in smaller pieces to fit to the lab test benches at KIT. Since the washcoat material is deposited on a metallic substrate provided by Emitec, drilling out of smaller cores had to be done by a company. By using a very thin diamond coated wire, DRAMET Draht und Metallbau GmbH was able to drill out cylinders with 25mm diameter and 42mm length.

**Figure 95:** Part of the Pd-Pt/CZ catalyst after operation at gas engine. Samples were drilled out with diameter of 25mm and length of 42mm.

To study the catalyst properties with spatial resolution, the 12 cm long catalyst was divided into 3 parts along the axial direction as shown in Figure 96. In radial direction, 3 cores were drilled out with uniform distance to the center. Overall, nine catalysts were obtained.

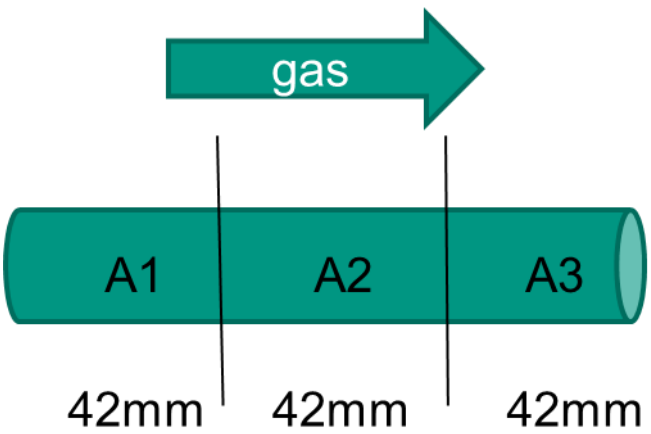


**Figure 96:** Schematic drawing of the distribution of catalyst cores.

The samples are labeled with Position 1, 2 and 3. Position 1 was drilled out from the part being located at catalyst inlet, position 2 from the middle and position 3 from the outlet of the catalyst.

To get a better insight into the process during engine operation, the drilled out cores were subjected to a TPD (Temperature Programmed Desorption). With this test the desorption of unstable species from the catalyst surface can be observed. The same procedure as described in chapter 9.1.3 was applied. Three samples (pos. 1, 2, 3) were heated up in 5L/min nitrogen up to 925°C. During this heating, gaseous species desorbing from the catalyst were monitored by a FT-IR spectrometer.

The results of the TPD are shown in Figure 97. Besides $SO_2$ no other species were observed although species like $SO_3$, $H_2SO_4$ could have been recorded. It can clearly be seen that sulfur species were formed on the catalyst during engine operation. A later performed analysis of the Dutch natural gas used as fuel for the engine test revealed the presence of 4.7ppm Tetrahydrothiphen (THT). This sulfur containing molecule is commonly used as ordorizer and can be determined as sulfur source leading to poisoning of the catalyst. During engine operation, THT gets mostly oxidized to $SO_2$ and can further be oxidized to $SO_3$/$H_2SO_4$ having the same effect as already discussed in chapter 9. Although the concentration of the odorizer is only ~5ppm in the fuel and arrives even more diluted on the catalyst due to lean operation of the engine, a pronounced poisoning effect with formation of sulfur species (most likely sulfates) can be observed. In Figure 97 it can be seen that the start of $SO_2$ release is at about 600°C for all three samples. However, at position 1 and 2 (inlet and middle part of big catalyst) a small band around 650°C occurs that is not present on position 3. The presence of 2 bands in the TPD is most probably due to 2 different sulfur species on the catalyst (e.g. Pd($SO_4$) and sulfates formed with the carrier). The reason for the absence on position 3 can be explained by two effects. Firstly, the amount of $SO_2$ in the exhaust stream and the time on stream during the experiment was rather short, which could have lead to complete deactivation in the exclusively in front of the catalyst serving as a $SO_2$ trap for the catalyst parts downstream. This is also an explanation for the higher amount of sulfur stored in the front of the big catalyst brick decreasing from position 1 to 2 to 3.

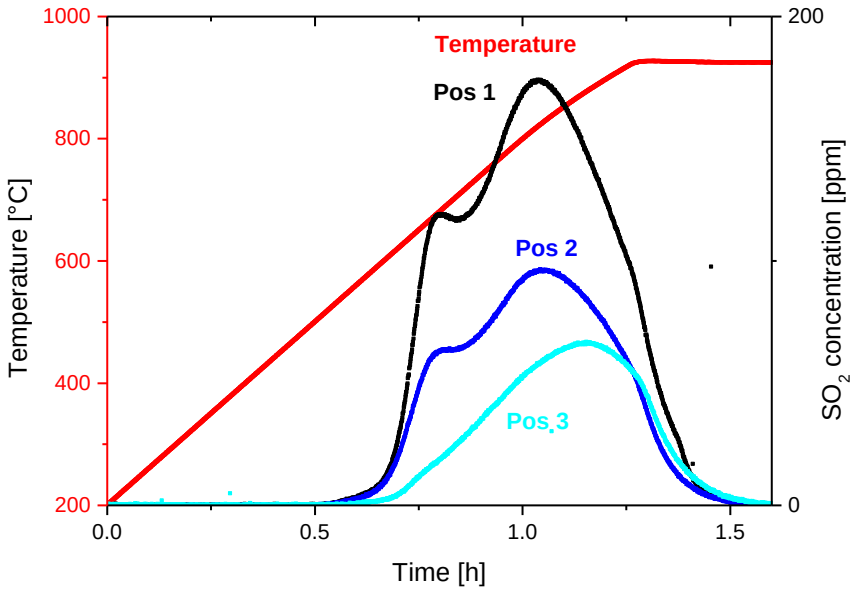


**Figure 97:** Sulfur-Temperature-Programmed-Desorption (S-TPD) of PdPt/CZ engine aged-samples. Gas composition: 5L/min $N_2$.

Secondly, the temperature along the catalyst during engine test was not uniform. While the inlet temperature was kept constant at 450°C, the outlet temperature was lower. As can be seen in Figure 93 the temperature difference is already about 50K at 60 to 80% methane conversion. With ongoing deactivation of the catalyst during the 60h engine test, this gap between inlet and outlet temperature should also have increased. As discussed in 9.1.1 the temperature during $SO_2$ poisoning also plays a role on the formation of sulfates and therefore on the deactivation. However, this effect is expected to play a minor role compared to the fact that the poisoning starts at the front of the catalyst and proceeds over time along the flow direction.

Besides the S-TPD the samples were also investigated by electron microscopy. No differences in washcoat corrosion or development of cracks was observed between the samples from position 1, 2 ,3 and the fresh samples. All samples showed a homogenously distributed washcoat structure. Figure 98 shows the structure of an engine aged catalyst part from position 2 with different magnification. In Figure 98 a) a coated channel with ~1500 µm width can be seen. With higher magnification, the porous structure of the washcoat becomes visible.

Detection of X-rays being emitted during electron microscopy gave information about the composition of the samples (EDX-analysis). Besides the metals present in the washcoat (Ce, Zr, La, Y) and the active metals (Pd and Pt) also S was observed on the deactivated sample. Analysis of the washcoat for a sample after S-TPD confirmed the release of sulfur from the catalyst.

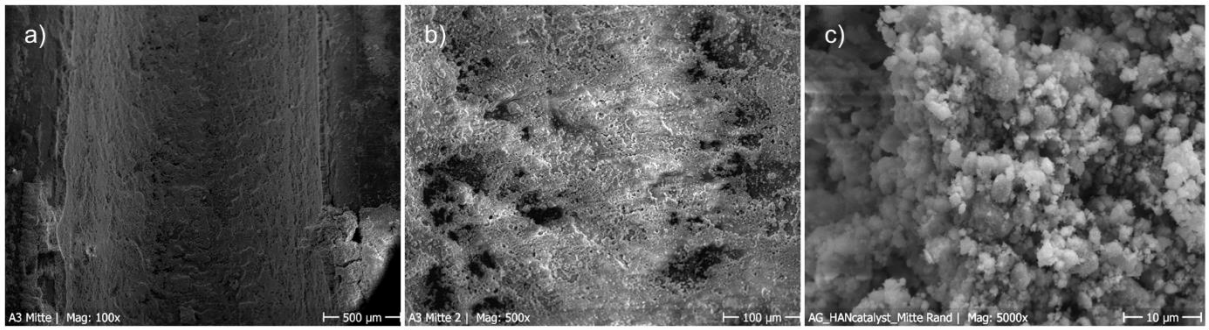


**Figure 98:** Images of engine used PdPt/CZ at position 2. a): image of a coated channel with 100x magnification. b): Image of washcoat with 500x magnification. c) Image washcoat structure with 5000x magnification.

The engine-aged catalyst samples were furthermore investigated by activity tests. Figure 99 a) shows the light-off curves for a sample at position 1 (inlet). For this, two consecutive heating/cooling cycles were performed in 3200ppm $CH_4$, 10% $O_2$ in $N_2$. Since the samples from different position show the same qualitative trend, only the conversion profiles of position 1 is shown here (Figure 99a)). In addition, a comparison between the fresh sample and three engine aged samples (pos. 1, 2 and 3) is shown. The $CH_4$ conversion during 1$^{st}$ cooling is plotted in Figure 99 b).

Surprisingly, during 1$^{st}$ heating the catalyst is more active than in the consecutive runs. A fast deactivation must have occurred at higher temperature during the first light-off experiment. This behavior was observed for all engine aged samples. A reason for this could be a regeneration during the end of the engine test when the catalyst was still warm leading to decomposition of $Pd(SO_4)$. During heating up, a spillover of sulfur species, as also observed in the tests in chapter 9.2.2, from support material to active sites might have occurred. Anyhow, the activity after 1$^{st}$ light-off is on a constant low level.

When comparing the fresh catalyst with the engine aged samples, a clear shift of the light-off curve to higher temperature can be observed. The most pronounced deactivation occurred at the catalyst inlet (pos. 1) and middle (pos. 2) and is in line with the high amount of sulfur in this area of the catalyst. At position 3 the activity is slightly higher but still shifted to higher temperature compared to the fresh state.

For the used samples the low conversion at high temperature might also be due to bypass of reactive gases. The drilled out metallic samples do not have a surrounding layer, which would provide a neat boundary. However, as can be seen in chapter 11.1.1, this bypass only accounts for max ~ 2%.

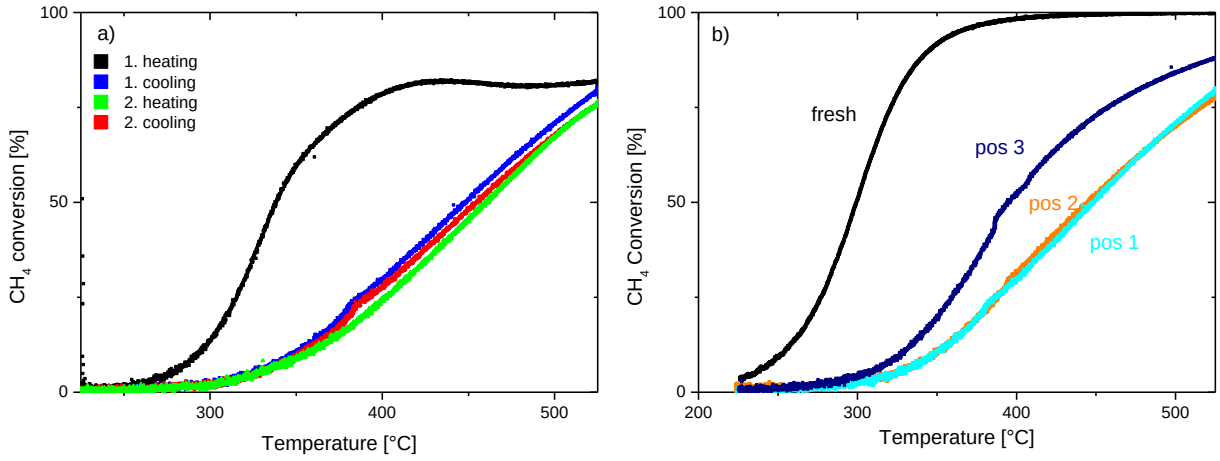


**Figure 99**: a): $CH_4$ conversion on engine deactivated PdPt/CZ (position 1) during two consecutive heating/cooling cycles between 225°C and 550°C. Gas composition: 3200ppm $CH_4$, 10% $O_2$ in $N_2$. Temperature ramp: 3K/min. GHSV = 30000 $h^{-1}$. b): $CH_4$ conversion during 1st cooling on fresh and engine aged PdPt/CZ samples. Gas composition: 3200ppm $CH_4$, 10% $O_2$ in $N_2$. Temperature ramp: 3K/min. GHSV = 30000 $h^{-1}$.

### 11.1.1 Regeneration

Since in chapter 11 sulfur poisoning was found to cause the constant deactivation of the catalyst during operation on an engine at HAN, an experiment was performed to compare the deactivated and sulfur-free state. For this, a light-off experiment was performed after S-TPD.

Figure 100 shows the result of this test. The 1st cooling curve before and after S-TPD is shown. A clear gain in activity can be observed after S-TPD. The high temperature treatment lead to the decomposition of poisoning sulfates and enabled the access to the active Pd-Pt sites. However, the activity after S-TPD is still lower than in the fresh state ($T_{50}$ fresh = 299°C; $T_{50}$ after S-TPD = 339°C). The high temperature during the TPD might have caused sintering of the noble metals leading to lower activity.

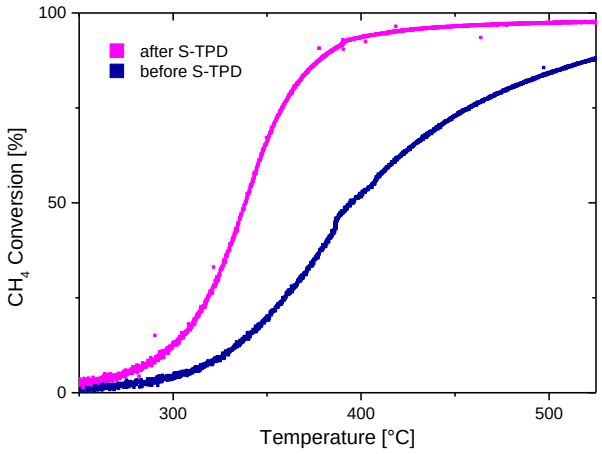


**Figure 100:** $CH_4$ conversion over time for Pd-Pt/CZ pos. 3 in deactivated state (after engine test) and regenerated state (after S-TPD, compare Figure 97) during cooling. Gas composition: 3200ppm $CH_4$, 10% $O_2$ in $N_2$. Temperature ramp: 3K/min. GHSV = 30000 $h^{-1}$.

## 11.2 Summary engine-aged samples

Chapters 10 and 11 nicely showed the benefits of combining research institutes with different focus in one project. Ideas from laboratory tests with catalysts at KIT lead to an advanced testing procedure on a real gas engine at HAN. The deactivation observed in former tests was also found during operation at 450°C under lean burn gas engine conditions. Analysis of the deactivated catalyst revealed that sulfur poisoning is responsible for the loss of activity. With spatial resolution along axial direction the sulfur content was analyzed. The closer to the catalyst inlet the higher the sulfur content was. This also correlates to the activity of the different aged samples. However, thermal treatment lead to partial regain of activity.

With the knowledge of the deactivation mechanism during engine operation, the results from engine regeneration tests (10.7.5) can be better understood. Since sulfur poisoning was found to be responsible for the loss of activity, reductive treatments are not very effective at 450°C. That is why the conversion does not increase very much after rich operation of the engine (Figure 94). As found in chapter 9.2.2 the rich operation has to be combined with a higher catalyst temperature.

# 12 Conclusion and Outlook

This project revealed many important aspects that are crucial for minimizing the methane emissions from lean burn gas engines. While processes like the design of the combustion chamber or valve timing can lead to lower methane emissions from the engine, optimization of the catalytic after-treatment systems offers a vast potential to achieve a cleaner exhaust-gas. Especially a rational coordination and interaction between engine and exhaust-gas after-treatment system is crucial for a successful future of the gas engine concerning emissions.

Under typical lean exhaust-gas conditions, palladium is essential for efficient conversion of methane. However, the factors influencing its low temperature activity and much more the long-term activity are numerous. As schematically illustrated in Figure 101, the interaction with water plays a critical role toward catalyst durability. Either produced by the catalytic reaction itself or much more coming from the engine, it leads to a blockage of active sites and hinders the methane adsorption and reaction to $H_2O$ and $CO_2$. Here, the alumina support seems to additionally contribute due to its rather high water storage capacity. Furthermore, the XAS study uncovered that completely oxidized PdO is necessary for high activity, as it is needed to activate the rather stable $CH_4$ molecule via the rate determining first $H_3C$-H bond dissociation. The stability and morphology of the highly active PdO depends on the carrier material. Ceria supports, which offer a high oxygen mobility, demonstrate promising properties under wet reaction conditions. Compared to common supports like alumina the methane oxidation activity remains high during long-term experiments (> 50 hours). The stabilizing effect of ceria seems also to be related to its lower water storage ability above 200°C.

This process is disturbed when $NO_x$ is present, which acts as promoter in presence of $H_2O$ but as an inhibitor in dry reaction conditions. As indicated by the operando DRIFTS measurements, the adsorption of $NO_x$ and formation of less stable nitrites/nitrates on catalyst surface prevents the long-term catalyst deactivation. Moreover, to restore the deactivation caused by water, reductive treatments were found to be very effective. They lead to formation of metallic $Pd^0$ which is accompanied by desorption of the inhibiting hydroxyls. However, the extent of regeneration also depends on temperature since complete oxidation of Pd to PdO under lean reaction conditions is needed to achieve the initial high conversion.

Considering that the gaseous fuel can also contain small amounts of sulfur, its impact was studied in this project. Although only present in the low ppm range, $SO_2$ strongly affects the catalyst behavior as very fast and severe poisoning occurs. The higher the sulfur content in the exhaust-gas stream, the faster the deactivation. $SO_2$ is able to form stable sulfates with the support material and especially with the critically needed PdO. The decomposition of the resulting sulfur-species can be achieved only at high temperature. As for the case of water deactivated samples, a reductive gas atmosphere lowers the temperature for regeneration. Under rich conditions decomposition of sulfur-species was achieved at temperatures above 525°C leading to active PdO again. The positive influence of rich pulses on a methane oxidation catalyst was also realized on a gas engine. Although the temperature of the catalyst was only at 450°C, switching to $\lambda < 1$ for short periods helped to regain activity of the catalyst.

As summarized in Figure 101, the interaction of PdO with $SO_2$ and water leads to a deactivated state. Regeneration at well-defined temperature and preferentially under reductive conditions leads in a first step to metallic Pd, which needs to be reoxidized to restore the active PdO sites. As demonstrated by the results of this study, a fundamental understanding of the individual steps showed in Figure 101 is essential for a rational control of catalyst long-term efficiency. By optimization of the support material and by the identification of an optimal time scale and temperature needed for the individual steps the overall performance and durability can be influenced. For example, due to the sulfur-storage ability of supports like $Al_2O_3$ a deceleration of the $SO_2$-poisoning effect can be obtained. However, this becomes disadvantageous during regeneration steps.

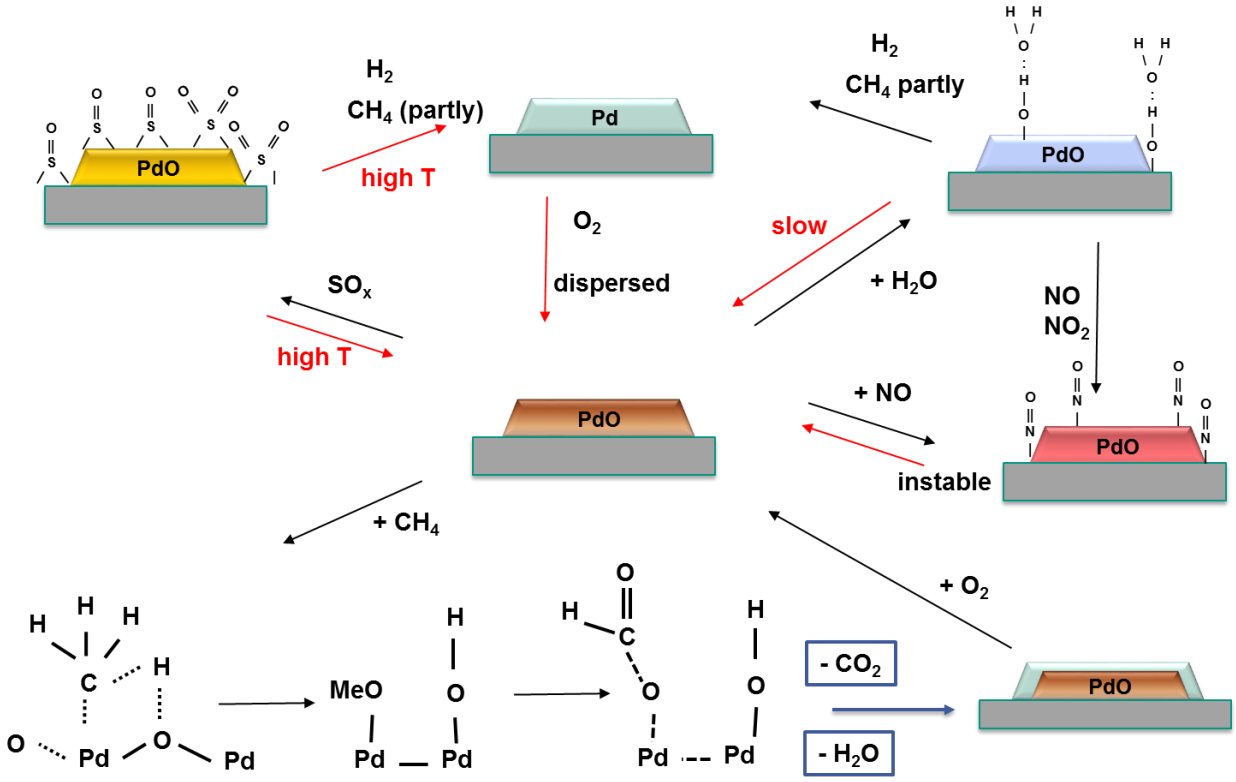


**Figure 101:** Schematic overview of the interactions of a Pd catalyst with external parameters and the way of $CH_4$ oxidation on active PdO derived from the project results.

Another possibility to influence the catalyst behavior is to locate it in front of the turbocharger. Higher temperature and higher pressure at this pre-turbo position enhance the catalyst activity. The impact of higher pressure was revealed by experiments combined with kinetic modeling. Besides an increase in residence time also the negative impact of varying concentrations with increasing pressure have to be considered. However, increasing temperature plays the major role when comparing pre-turbo with post-turbo positioning.

In the future, the complete system consisting of engine, catalyst and probably a regenerator has to be considered to guarantee ecological and economical operation of gas engines. The project showed that regeneration of today's catalytic converters is periodically needed to maintain high conversion. Important parameters for catalyst regeneration were evaluated during this project but further work hast to be done to optimize this procedure under more realistic conditions, e.g. presence of oxygen. Additionally, research on catalyst development and on related fundamental aspects needs to be continued as it offers the potential to obtain an improved generation of catalysts, which are more resistant towards water and sulfur deactivation.

# 13 Appendix

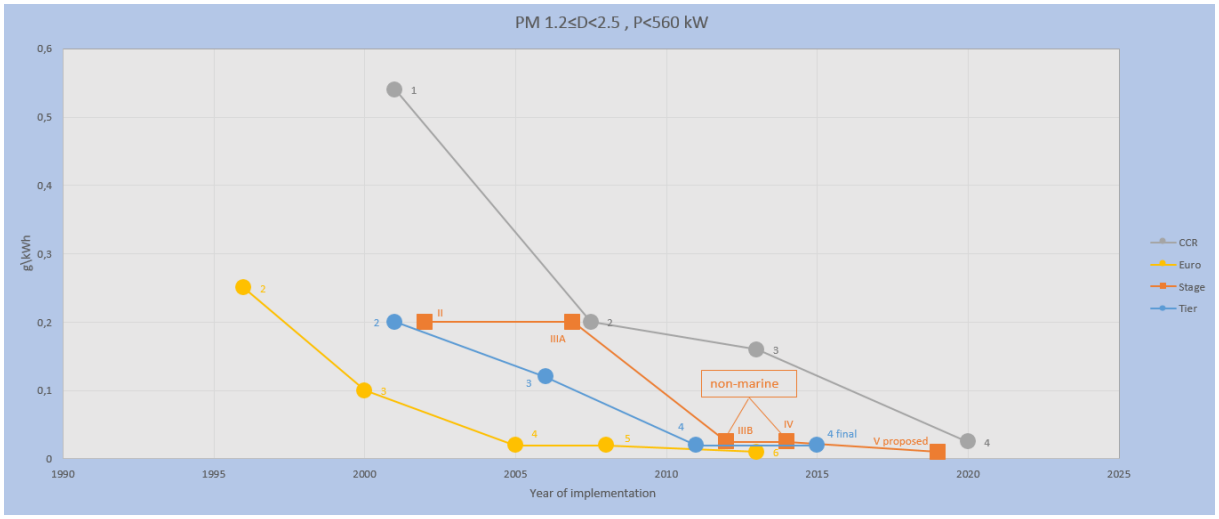


**Figure 102:** Particle matter limits, smaller engines (HAN).

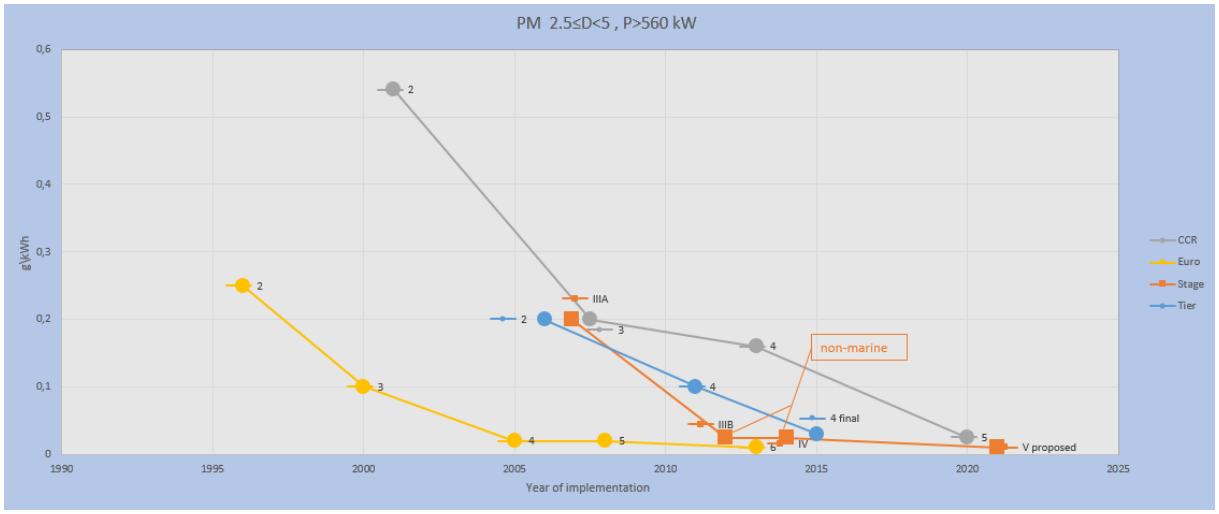


**Figure 103:** Particle matter limits, larger engines (HAN).

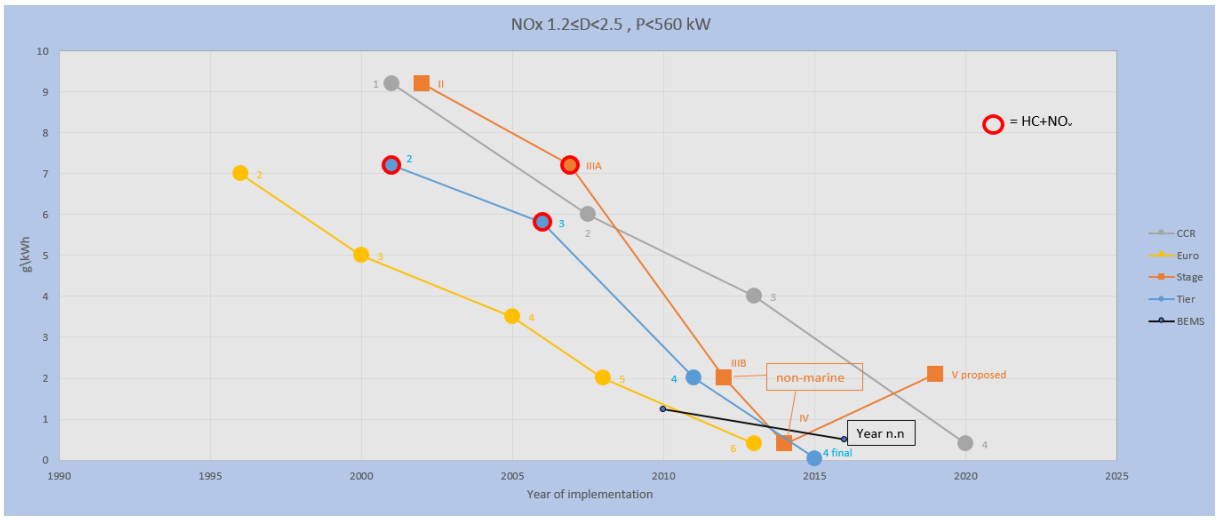


**Figure 104:** NOx limits, smaller engines (HAN).

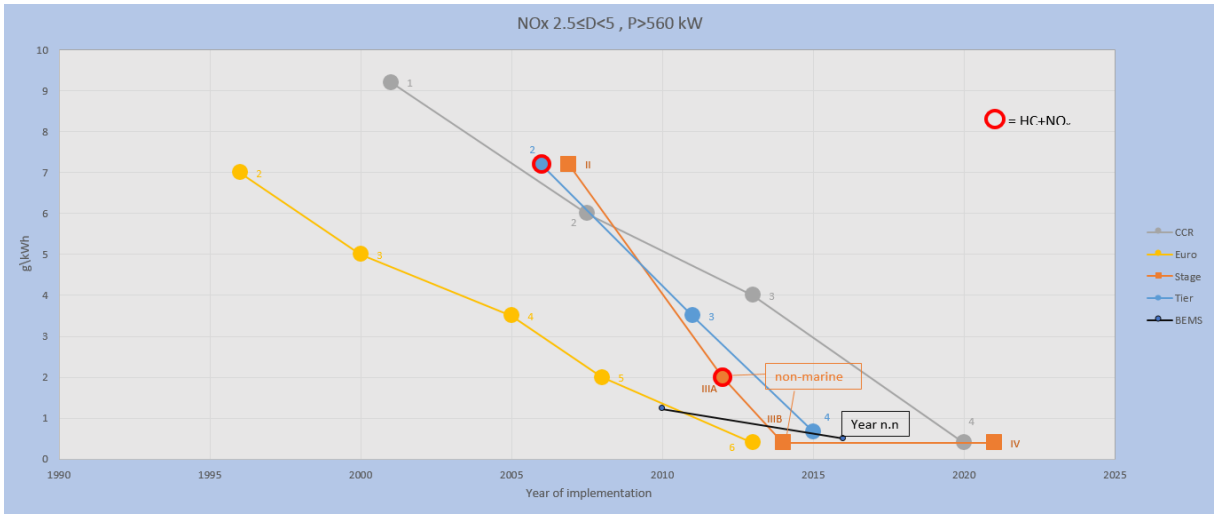


**Figure 105:** NOx limits, larger engines (HAN)

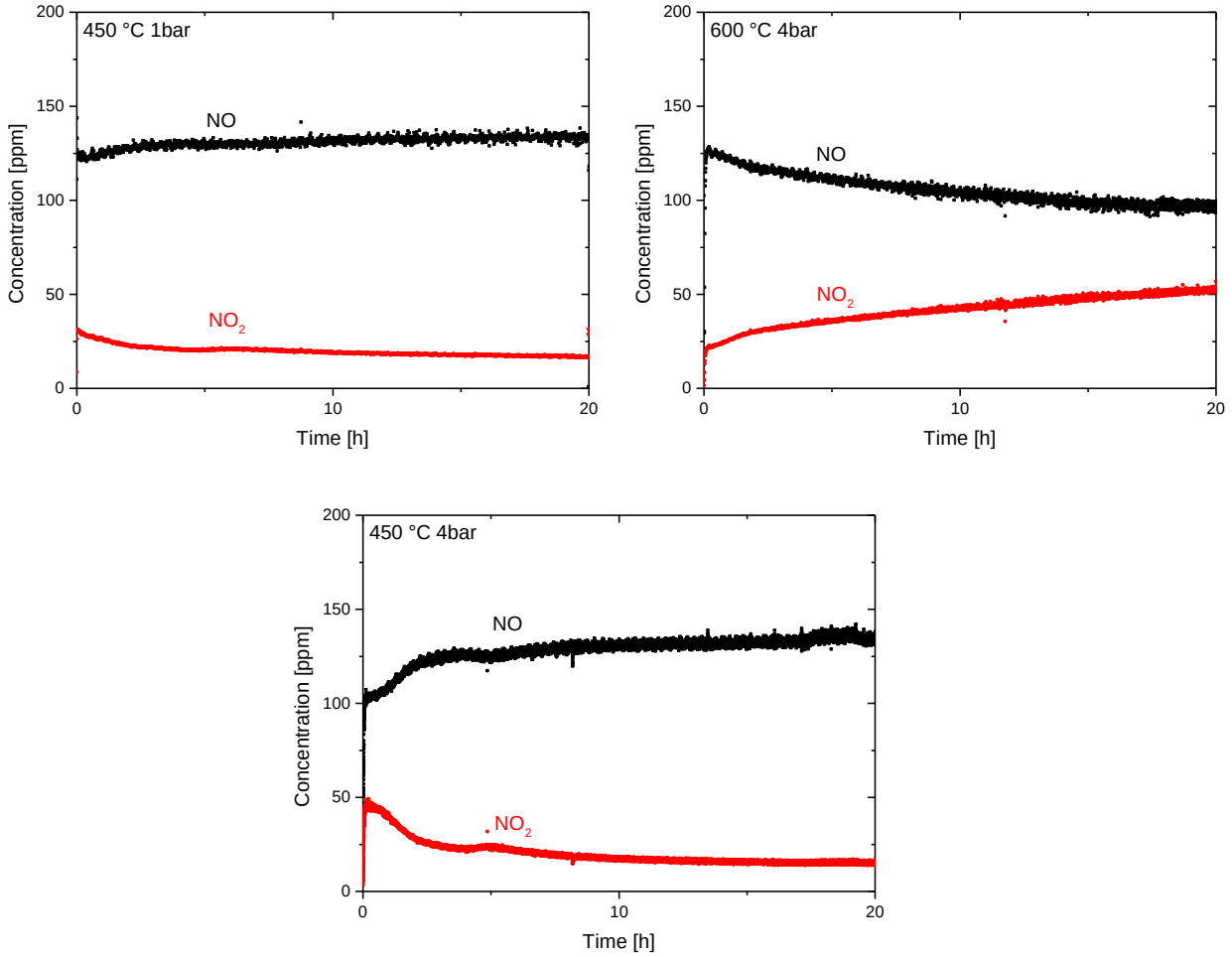


**Figure 106:** NO and $NO_2$ concentration during 20h long-term test of "JM catalyst" at different temperatures and pressures. Gas composition: 5ppm $SO_2$, 30ppm $NO_2$, 120ppm NO, 1000ppm $CH_4$, 10% $O_2$, 12% $H_2O$ in $N_2$. GHSV = 60000 $h^{-1}$.

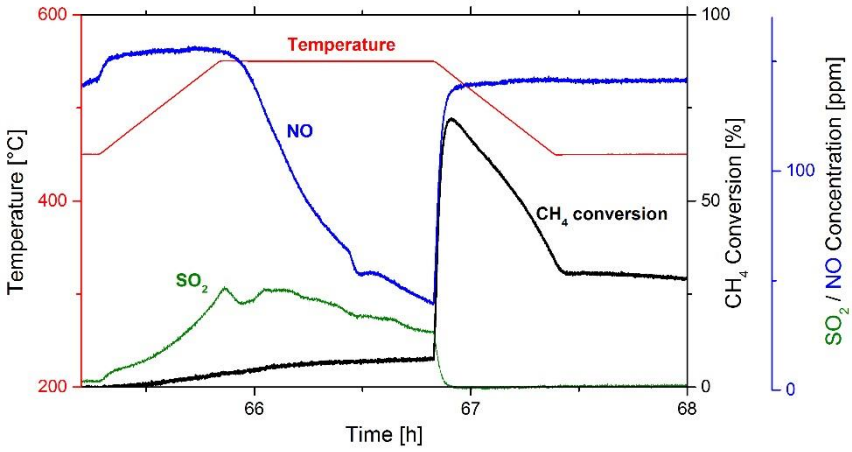


**Figure 107:** Devolution of $CH_4$ conversion, $SO_2$ and NO concentration and temperature over time during reactivation experiment. Gas composition until 66.8 h time on stream: 5ppm $SO_2$, 30ppm $NO_2$, 120ppm NO, 1000ppm $CH_4$, 12% $H_2O$ in $N_2$. 10% $O_2$ added starting from 66.8 h. GHSV = 30000 $h^{-1}$.

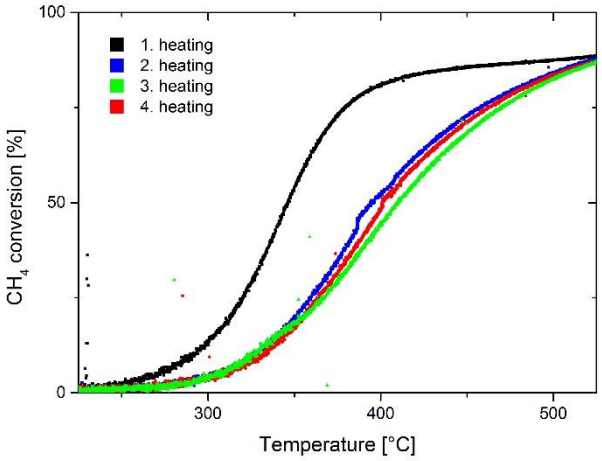


**Figure 108:** $CH_4$ conversion on engine deactivated PdPt/CZ (position 2) during two consecutive heating/cooling cycles between 225°C and 550°C. Gas composition: 3200ppm $CH_4$, 10% $O_2$ in $N_2$. Temperature ramp: 3K/min. GHSV = 30000 $h^{-1}$.

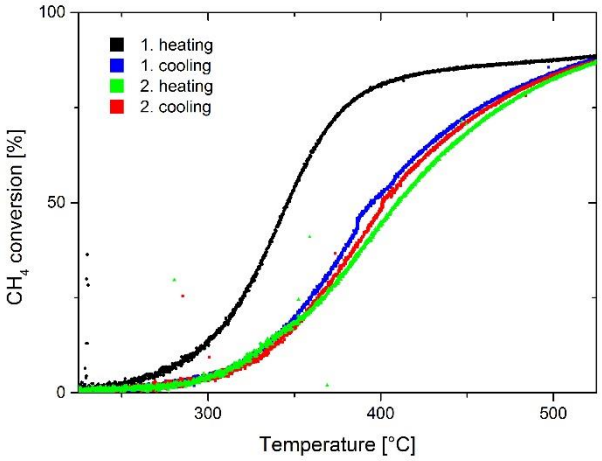


**Figure 109:** $CH_4$ conversion on engine deactivated PdPt/CZ (position 3) during two consecutive heating/cooling cycles between 225°C and 550°C. Gas composition: 3200ppm $CH_4$, 10% $O_2$ in $N_2$. Temperature ramp: 3K/min. GHSV = 30000 $h^{-1}$.

**ANALYSERAPPORT** Blad 1 van 2

Datum rapport : 11 oktober 2016
Projectnummer : 16-0479 HC

**Gegevens opdrachtgever**

Naam : HAN Automotive Research
Adres : Postbus 2217
Woonplaats : 6802 CE Arnhem
T.a.v. : Dhr. M. Merts

**Doel analyse**

Analyse van een gasmonster op hoofdcomponenten.

**Werkwijze**

De analyse is uitgevoerd op basis van ISO-6974 deel 1 t/m 3; "Natural gas - Determination of hydrogen , inert gases hydrocarbons up to C8 - Gas chromatografic method".
De berekeningen zijn uitgevoerd conform ISO-6976; "Natural gas - Calculation of calorific value , density and relative density".

**Omschrijving monster**

| Monsternr | Cilindernr | Datum | Tijd | Monsternaam |
|---|---|---|---|---|
| M50446 | 93037 | 04-10-2016 | 15:40 uur | Aardgas HAN Arnhem |

Monsternemer : J. Hendrikx

**Toegepast meetsysteem**

Fabrikant : Interscience Thermo Scientific
Type : Trace 1300 Gas Chromatograph
Serienummer : s/n 714530067
Bouwjaar : 2014

**Analyse gegevens**

Datum analyse : 07-10-2016
Analyse door : M. Veldkamp
Resultaat analyse : Zie blad 2
Paraaf analist :

Paraaf lab coördinator :
ing B.J. Gerritsen

**Figure 110:** Analysis of gaseous fuel used for engine tests at HAN Automotive.

**ANALYSERAPPORT** Blad 2 van 2

Naam monster : Aardgas HAN Arnhem, 04-10-2016 15:40 uur
Monsternummer : M50446
Projectnummer : 16-0479 HC

**Resultaat**

De analyseresultaten en de berekende fysische grootheden uit de samenstelling hebben de onderstaande waarden. De m³ wordt gedefinieerd bij 0°C (meetcondities) en 1013.25 mbar. De energie in MJ is herleid van de thermodynamische waarden van 25°C (verbrandingscondities) tot 0°C en bij 1013.25 mbar volgens ISO 6976.

| Component | Molprocenten | Onzekerheid (mol%) |
|---|---|---|
| Helium | 0.0454 | 0.0004 |
| Argon | 0.0124 | 0.0002 |
| Waterstof | 0.01 | 0.01 |
| Zuurstof | - | - |
| Stikstof | 12.98 | 0.06 |
| Kooldioxide | 1.251 | 0.006 |
| Koolmonoxide | - | - |
| Methaan | 81.43 | 0.07 |
| Ethaan | 3.38 | 0.01 |
| Propaan | 0.564 | 0.002 |
| Isobutaan | 0.0923 | 0.0004 |
| Butaan | 0.1096 | 0.0005 |
| neo-Pentaan | 0.00534 | 0.00003 |
| isoPentaan | 0.0288 | 0.0002 |
| n-Pentaan | 0.0274 | 0.0001 |
| cyclopentaan + 2,3-dimethylbutaan | 0.00240 | 0.00001 |
| 2,2-dimethylbutaan | 0.00453 | 0.00002 |
| 2-methylpentaan | 0.00607 | 0.00003 |
| 3-methylpentaan | 0.00342 | 0.00002 |
| n-Hexaan | 0.00887 | 0.00005 |
| C7-KWS | 0.01452 | 0.00007 |
| C8-KWS | 0.00621 | 0.00006 |
| Benzeen | 0.0176 | 0.0002 |
| Tolueen | 0.00257 | 0.00004 |

| Fysische grootheden: | | | |
|---|---|---|---|
| Calorische onderwaarde | 32.35 | 0.02 | MJ/m³ |
| Calorische bovenwaarde | 35.84 | 0.02 | MJ/m³ |
| Wobbe-index (inf.) | 40.18 | 0.03 | MJ/m³ |
| Wobbe-index (sup.) | 44.51 | 0.03 | MJ/m³ |
| Dichtheid t.o.v. lucht | 0.6483 | 0.0002 | - |
| Soortelijke massa | 0.8382 | 0.0003 | kg/m³ |

- < 0,001 mol%
De fysische grootheden hebben een onzekerheid van maximaal 0.2 % relatief (k=2).
Controle Kaarten volgens Kiwa Technology WI403.
Datum laatste kalibratie: maart 2016. Primair Referentie Materiaal: NPL2013100302-01/-09

**Figure 111:** Analysis of gaseous fuel used for engine tests at HAN Automotive.

**ANALYSERAPPORT** Blad 1 van 2

Datum rapport : 11 oktober 2016
Projectnummer : 16-0479 Zwa

**Gegevens opdrachtgever**

Naam : HAN Automotive Research
Adres : Postbus 2217
Woonplaats : 6802 CE Arnhem
T.a.v. : Dhr. M. Merts

**Doel analyse**

Het bepalen van het gehalte aan zwavelcomponenten in een monster bio- of aardgas.

**Werkwijze**

De analyses zijn gedaan met behulp van een temperatuurgeprogrammeerde gaschromatograaf met een capillaire kolom en een massaselectieve detector.
Middels selective ionmonitoring (SIM) is specifiek op zwavel geanalyseerd.

**Omschrijving monster**

| Monsternr | Cilindernr | Datum | Tijd | Monsternaam |
|---|---|---|---|---|
| M50447 | T06802 | 04-10-2016 | 15:45 uur | Aardgas HAN Arnhem |

Monsternemer : J. Hendrikx

**Toegepast meetsysteem**

| | GC | Massaspectrometer |
|---|---|---|
| Fabrikant | Interscience Thermo Scientific | Interscience Thermo Scientific |
| Type | Trace 1300 Gas Chromatograph | ISQ QD SQMS |
| Serienummer | s/n 714000002 | |
| Bouwjaar | 2014 | 2014 |

**Analyse gegevens**

Datum analyse : 05-10-2016
Analyse door : M. Veldkamp
Resultaat analyse : Zie blad 2
Paraaf analist :

Paraaf lab coördinator :
Ing B.J. Gerritsen

**Figure 112:** Analysis of gaseous fuel used for engine tests at HAN Automotive.

**ANALYSERAPPORT** Blad 2 van 2

Naam monster : Aardgas HAN Arnhem, 04-10-2016 15:45 uur
Monsternummer : M50447
Projectnummer : 16-0479 Zwa

**Resultaat analyses**

Het monster is onderzocht op aanwezigheid van de volgende zwavelverbindingen :

| Component | | Gehalte in mg/m³ | ppm |
|---|---|---|---|
| zwavelwaterstof | : | - | - |
| zwaveldioxide | : | - | - |
| methylmercaptaan | : | - | - |
| ethylmercaptaan | : | - | - |
| propylmercaptaan | : | - | - |
| isopropylmercaptaan | : | - | - |
| tert-butylmercaptaan | : | - | - |
| dimethylsulfide | : | - | - |
| carbonylsulfide | : | - | - |
| koolstofdisulfide | : | - | - |
| odorant ( T.H.T. ) | : | 18.7 | 4.7 |
| totale zwavelgehalte | : | 6.8 | |

- niet aangetroffen (<0.1 mg/m³)
De onderste detectiegrens bij deze analyse is 0.1 mg/m³
Voor componenten met een gehalte kleiner dan 1 mg/m³ is de nauwkeurigheid 0.1 mg/m³ absoluut.
Voor componenten met een gehalte groter dan 1 mg/m³ is de nauwkeurigheid 10% relatief.

De m³ is gebaseerd op 0°C en 101.325 kPa.

**Figure 113:** Analysis of gaseous fuel used for engine tests at HAN Automotive.

## 14 References

CIMAC. (2014). *Methane and formaldehyde emissions of gas engines.* CIMAC Position Paper.
*Dieselnet*. (sd). Opgehaald van Dieselnet: https://www.dieselnet.com/standards/eu/nonroad.php
Frederik Königsson, J. K.-E. (2013). *The Influence of Crevices on Hydrocarbon Emissions from a Diesel-Methane Dual Fuel Engine.* SAE.
Gasunie. (1988). *Physical properties of natural gases.* Groningen: N.V. Nederlandse Gasunie.
Hogg, R. (2014). Life Beyond Euro VI. *Automotive World*.
Horgen, O. M. (sd). Rolls Royce Marine - "The Environship Concept".
*Klimaatconferentie Parijs 2015 COP21*. (2015, 12). Opgeroepen op 01 20, 2016, van Europa Nu: http://www.europa-nu.nl/id/vjmhg41ub7pp/klimaatconferentie_parijs_2015_cop21
MAN. (2011). ME-GI Engine fuelled by LNG. Poland.
*Milieuzone vrachtauto's*. (2016). Opgeroepen op 01 20, 2016, van Gemeente Amsterdam: https://www.amsterdam.nl/veelgevraagd/?productid=%7B01301856-3A38-4B22-88BC-07D278CDBB9A%7D#case_%7b21636181-1595-4B5F-81F6-69EEA49853A6%7d
*The Blue World – Sustainable Inland Ships*. (2015). Opgeroepen op 01 20, 2016, van PPMC: http://ppmc-cop21.org/the-blue-world-sustainable-inland-ships/
TNO. (2013). *Current state and emission performance of CNG/LNG heavy-duty vehicles.* Delft.
Van der Burg, L. (2013). Samenwerken aan innovatie. Technologiecentrum Noord Nederland.
*Waarom zou ik investeren in een SCR-katalysator of roetfilter*. (2014, September 19). Opgeroepen op 01 19, 2016, van Groenervaren: http://www.groenervaren.nl/waarom-zou-ik-investeren-een-scr-katalysator-roetfilter

[1] P. Gélin and M. Primet, Applied Catalysis B: Environmental, 39 (2002) 1.
[2] T.V. Choudhary, S. Banerjee and V.R. Choudhary, Applied Catalysis A: General, 234 (2002) 1.
[3] A.C. Gluhoi and B.E. Nieutwenhuys, Catalysis Today, 119 (2007) 305.
[4] D. Ciuparu, M.R. Lyubovsky, E. Altman, L.D. Pfefferle and A. Datye, Catalysis Reviews-Science and Engineering, 44 (2002) 593.
[5] G. Centi, Journal of Molecular Catalysis A: Chemical, 173 (2001) 287.
[6] R.J. Farrauto, M.C. Hobson, T. Kennelly and E.M. Waterman, Applied Catalysis A: General, 81 (1992) 227.
[7] J.D. Grunwaldt, N. van Vegten and A. Baiker, Chemical Communications, (2007) 4635.
[8] A.K. Datye, J. Bravo, T.R. Nelson, P. Atanasova, M. Lyubovsky and L. Pfefferle, Applied Catalysis A: General, 198 (2000) 179.
[9] R.J. Farrauto, J.K. Lampert, M.C. Hobson and E.M. Waterman, Applied Catalysis B: Environmental, 6 (1995) 263.
[10] S. Colussi, A. Trovarelli, G. Groppi and J. Llorca, Catalysis Communications, 8 (2007) 1263.
[11] D. Ciuparu and L. Pfefferle, Applied Catalysis A: General, 218 (2001) 197.
[12] C.A. Müller, M. Maciejewski, R.A. Koeppel and A. Baiker, Catalysis Today, 47 (1999) 245.
[13] R. Burch and F.J. Urbano, Applied Catalysis A: General, 124 (1995) 121.
[14] P. Mars and D.W. van Krevelen, Chemical Engineering Science, 3, Supplement 1 (1954) 41.
[15] D. Ciuparu, E. Altman and L. Pfefferle, Journal of Catalysis, 203 (2001) 64.
[16] J. Au-Yeung, K. Chen, A.T. Bell and E. Iglesia, Journal of Catalysis, 188 (1999) 132.
[17] A.Y. Stakheev, A.M. Batkin, N.S. Teleguina, G.O. Bragina, V.I. Zaikovsky, I.P. Prosvirin, A.K. Khudorozhkov and V.I. Bukhtiyarov, Topics in Catalysis, 56 (2013) 306.
[18] P. Castellazzi, G. Groppi, P. Forzatti, A. Baylet, P. Marecot and D. Duprez, Catalysis Today, 155 (2010) 18.
[19] C.F. Cullis, T.G. Nevell and D.L. Trimm, Journal of the Chemical Society, Faraday Transactions 1: Physical Chemistry in Condensed Phases, 68 (1972) 1406.
[20] D. Ciuparu, E. Perkins and L. Pfefferle, Applied Catalysis A: General, 263 (2004) 145.
[21] W.R. Schwartz, D. Ciuparu and L.D. Pfefferle, The Journal of Physical Chemistry C, 116 (2012) 8587.
[22] L.S. Escandón, D. Niño, E. Díaz, S. Ordóñez and F.V. Díez, Catalysis Communications, 9 (2008) 2291.
[23] A.T. Gremminger, H.W. Pereira de Carvalho, R. Popescu, J.-D. Grunwaldt and O. Deutschmann, Catalysis Today, 258, Part 2 (2015) 470.

[24] N. Sadokhina, G. Smedler, U. Nylén, M. Olofsson and L. Olsson, Applied Catalysis B: Environmental, 200 (2017) 351.
[25] J.K. Lampert, M.S. Kazi and R.J. Farrauto, Applied Catalysis B: Environmental, 14 (1997) 211.
[26] D.L. Mowery, M.S. Graboski, T.R. Ohno and R.L. McCormick, Applied Catalysis B: Environmental, 21 (1999) 157.
[27] T.C. Yu and H. Shaw, Applied Catalysis B: Environmental, 18 (1998) 105.
[28] A. Guliaeff, K. Wanninger, F. Klose, G. Maletz and A. Tissler, SAE paper 2013-01-0531, (2013).
[29] M. Cargnello, J.J.D. Jaén, J.C.H. Garrido, K. Bakhmutsky, T. Montini, J.J.C. Gámez, R.J. Gorte and P. Fornasiero, Science, 337 (2012) 713.
[30] G. Lapisardi, L. Urfels, P. Gelin, M. Primet, A. Kaddouri, E. Garbowski, S. Toppi and E. Tena, Catalysis Today, 117 (2006) 564.
[31] K. Narui, H. Yata, K. Furuta, A. Nishida, Y. Kohtoku and T. Matsuzaki, Applied Catalysis A: General, 179 (1999) 165.
[32] R. Strobel, J.D. Grunwaldt, A. Camenzind, S.E. Pratsinis and A. Baiker, Catalysis Letters, 104 (2005) 9.
[33] A. Ersson, H. Kusar, R. Carroni, T. Griffin and S. Jaras, Catalysis Today, 83 (2003) 265.
[34] S. Brunauer, P.H. Emmett and E. Teller, Journal of the American Chemical Society, 60 (1938) 309.
[35] J.A. Anderson and M.F. Garcia, Supported metals in catalysis, Imperial College Press London, 2005.
[36] T. Takeguchi, S. Manabe, R. Kikuchi, K. Eguchi, T. Kanazawa, S. Matsumoto and W. Ueda, Applied Catalysis A: General, 293 (2005) 91.
[37] D. Chan, A. Gremminger and O. Deutschmann, Topics in Catalysis, 56 (2013) 293.
[38] S.D. Tischer, O., in H.G.C. Bock, T. ; Jaeger, W.; Koerkel, S. ; Rannacher, R.; Schloeder, J.P.; (Editor), Numerical simulation of catalytic reactors by molecular-based models, Springer, Heidelberg, 2013, p. pp.227.
[39] M.L. Rodríguez and L.E. Cadús, Chemical Engineering Science, 143 (2016) 305.
[40] Modeling and simulation of heterogeneous catalytic reactions : from the molecular process to the technical system, Wiley-VCH, Weinheim, 2012.
[41] L.L.K. Raja, R.J; Deutschmann, O; Warnatz, J; Schmidt, L.D;, Catal. Today, 59 (2000) 47.
[42] N. Mladenov, J. Koop, S. Tischer and O. Deutschmann, Chemical Engineering Science, 65 (2010) 812.
[43] O.T. Deutschmann, S; Kleditzsch, S.; Janardhanan, V.M; Correa, C; Chatterjee, D; Mladenov, N; Minh, H.D;, (2013).
[44] A. Konnov, Eurasian Chemico-Technological Journal, 2 (2000) 257.
[45] K.R. Fujimoto, F.H; Avalos-Borja, M.; Iglesia, E.;, Journal of Catalysis 179 (1998) 431.
[46] A. Trinchero, A. Hellman and H. Grönbeck, Surface Science, 616 (2013) 206.
[47] Y. Xin, H. Wang and C.K. Law, Combustion and Flame, 161 (2014) 1048.
[48] G.G. Bergeret, P.; , Handbook of Heterogeneous Catalysis, 2nd ed., Wiley-VCH Verlag GmbH & Co. KGaA, 2008, p. 738.
[49] P. Castellazzi, G. Groppi, P. Forzatti, A. Baylet, P. Marécot and D. Duprez, Catalysis Today, 155 (2010) 18.
[50] R. Gholami, M. Alyani and K. Smith, Catalysts, 5 (2015) 561.
[51] R.E.K. Hayes, S.T.; Li, P.K.C. ; Awdry, S.;, Chem. Eng. Sc., 56 (2001) 4815.
[52] S.T. Kolaczkowski, W.J. Thomas, J. Titiloye and D.J. Worth, Combustion Science and Technology, 118 (2007) 79.
[53] B.H. Liu, R. E.; Checkel, M. D.; Zheng, M.; & Mirosh, E. , Chemical Engineering Science, 56 (2001) 2641.
[54] C.F.N. Cullis, T.G.; Trimm, D.L. ;, Appl. Catal. A: Gen. , 263 (2004) 145.
[55] P. Hurtado, S. Ordonez, H. Sastre and F. Diez, Applied Catalysis B: Environmental, 47 (2004) 85.
[56] K.Y. Narui, H.; Furuta, K.; Nishida, A.; Kohtoku, Y.; T. Matsuzaki, Appl. Catal. A-Gen, 179 (1999) 165.
[57] D.H. Coller, B.C. Vicente and S.L. Scott, Chemical Engineering Journal, 303 (2016) 182.

[58] A. Gremminger, O. Deutschmann and J.-D. Grunwaldt, Abschlussbericht des Vorhabens Nr. 1134 der Forschungsvereinigung Verbrennungskraftmaschinen, Heft 1039-2014 (2014).
[59] C. Karakaya and O. Deutschmann, Applied Catalysis A: General, 445–446 (2012) 221.
[60] H. Yoshida, T. Nakajima, Y. Yazawa and T. Hattori, Applied Catalysis B: Environmental, 71 (2007) 70.
[61] D.N. Gao, C.X. Zhang, S. Wang, Z.S. Yuan and S.D. Wang, Catalysis Communications, 9 (2008) 2583.
[62] X. Fan, F. Wang, T.L. Zhu and H. He, Journal of Environmental Sciences-China, 24 (2012) 507.
[63] L. Spenadel and M. Boudart, The Journal of Physical Chemistry, 64 (1960) 204.
[64] C. Kind, R. Popescu, R. Schneider, E. Muller, D. Gerthsen and C. Feldmann, RSC Advances, 2 (2012) 9473.
[65] A. Boubnov, S. Dahl, E. Johnson, A.P. Molina, S.B. Simonsen, F.M. Cano, S. Helveg, L.J. Lemus-Yegres and J.-D. Grunwaldt, Applied Catalysis B: Environmental, 126 (2012) 315.
[66] R. Strobel, S.E. Pratsinis and A. Baiker, Journal of Materials Chemistry, 15 (2005) 605.
[67] M. Casapu, A. Fischer, A.M. Gänzler, R. Popescu, M. Crone, D. Gerthsen, M. Türk and J.-D. Grunwaldt, ACS Catalysis, 7 (2017) 343.
[68] J. Wan, R. Ran, X. Wu, Y. Cao, M. Li, D. Weng and K. Huang, Catalysis Today, 253 (2015) 51.
[69] S. Eriksson, M. Boutonnet and S. Jaras, Applied Catalysis a-General, 312 (2006) 95.
[70] R. Burch, F.J. Urbano and P.K. Loader, Applied Catalysis A: General, 123 (1995) 173.
[71] J. Stötzel, D. Lützenkirchen-Hecht, R. Frahm and J.D. Grunwaldt, Journal of Physics: Conference Series, 430 (2013) 012126.
[72] A. Urakawa, T. Bürgi and A. Baiker, Chemical Engineering Science, 63 (2008) 4902.
[73] D. Ferri, M.A. Newton and M. Nachtegaal, Topics in Catalysis, 54 (2011) 1070.
[74] J.-D. Grunwaldt and B. Clausen, Topics in Catalysis, 18 (2002) 37.
[75] A.M. Gänzler, M. Casapu, A. Boubnov, O. Müller, S. Conrad, H. Lichtenberg, R. Frahm and J.-D. Grunwaldt, Journal of Catalysis, 328 (2015) 216.
[76] J.D. Grunwaldt, M. Caravati, S. Hannemann and A. Baiker, Physical Chemistry Chemical Physics, 6 (2004) 3037.
[77] B. Ravel and M. Newville, Journal of Synchrotron Radiation, 12 (2005) 537.
[78] G.W. Smith and E.A. Carter, The Journal of Physical Chemistry, 95 (1991) 2327.
[79] C. Li, G. Li and Q. Xin, The Journal of Physical Chemistry, 98 (1994) 1933.
[80] P. Aghalayam, Y.K. Park, N. Fernandes, V. Papavassiliou, A.B. Mhadeshwar and D.G. Vlachos, Journal of Catalysis, 213 (2003) 23.
[81] H.-G. Cho and L. Andrews, The Journal of Physical Chemistry A, 116 (2012) 8500.
[82] V.J.F. Lapoutre, B. Redlich, A.F.G. van der Meer, J. Oomens, J.M. Bakker, A. Sweeney, A. Mookherjee and P.B. Armentrout, The Journal of Physical Chemistry A, 117 (2013) 4115.
[83] B.L. Mojet, S.D. Ebbesen and L. Lefferts, Chemical Society Reviews, 39 (2010) 4643.
[84] G. Busca and V. Lorenzelli, Journal of Catalysis, 72 (1981) 303.
[85] M. Öcal, R. Oukaci, G. Marcelin, B.W.L. Jang and J.J. Spivey, Catalysis Today, 59 (2000) 205.
[86] P. Hurtado, S. Ordonez, H. Sastre and F.V. Diez, Applied Catalysis B: Environmental, 47 (2004) 85.
[87] K. Otsuka, R. Takahashi, K. Amakawa and I. Yamanaka, Catalysis Today, 45 (1998) 23.
[88] K. Otsuka, R. Takahashi and I. Yamanaka, Journal of Catalysis, 185 (1999) 182.
[89] S. Eriksson, M. Boutonnet and S. Jaras, Applied Catalysis A: General, 312 (2006) 95.
[90] R.J.D.-L. Kee, G. ; Warnatz, J.; Coltrin, M.E.; Miller, J.A.;, Sandia National Laboratories, (1986).
[91] M.N. Subramaniam, C. Hayes, D. Tomazic, M. Downey and C. Bruestle, SAE International Journal of Engines, 4 (2011) 106.
[92] C. Hauck and T. Rammelt, Tagungsbandbericht des Vorhabens Nr. 1120 der Forschungsvereinigung Verbrennungskraftmaschinen, Heft R564 (2013).
[93] P. Gélin, L. Urfels, M. Primet and E. Tena, Catalysis Today, 83 (2003) 45.
[94] S. Colussi, F. Arosio, T. Montanari, G. Busca, G. Groppi and A. Trovarelli, Catalysis Today, 155 (2010) 59.

[95] X. Zi, L. Liu, B. Xue, H. Dai and H. He, Catalysis Today, 175 (2011) 223.
[96] S. Ordonez, P. Hurtado, H. Sastre and F.V. Diez, Applied Catalysis A: General, 259 (2004) 41.
[97] M. Honkanen, M. Kärkkäinen, T. Kolli, O. Heikkinen, V. Viitanen, L. Zeng, H. Jiang, K. Kallinen, M. Huuhtanen, R.L. Keiski, J. Lahtinen, E. Olsson and M. Vippola, Applied Catalysis B: Environmental, 182 (2016) 439.
[98] Y. Xi, N. Ottinger and Z.G. Liu, Effect of Reductive Regeneration Conditions on Reactivity and Stability of a Pd-Based Oxidation Catalyst for Lean-Burn Natural Gas Applications, SAE International, 2016.
[99] N. Ottinger, R. Veele, Y. Xi and Z.G. Liu, (2015).
[100] F. Arosio, S. Colussi, G. Groppi and A. Trovarelli, Catalysis Today, 117 (2006) 569.
[101] F. Arosio, S. Colussi, A. Trovarelli and G. Groppi, Applied Catalysis B: Environmental, 80 (2008) 335.
[102] J.-Y. Luo, D. Kisinger, A. Abedi and W.S. Epling, Applied Catalysis A: General, 383 (2010) 182.
[103] M. Monai, T. Montini, M. Melchionna, T. Duchoň, P. Kúš, C. Chen, N. Tsud, L. Nasi, K.C. Prince, K. Veltruská, V. Matolín, M.M. Khader, R.J. Gorte and P. Fornasiero, Applied Catalysis B: Environmental, 202 (2017) 72.
[104] O. Kröcher, M. Widmer, M. Elsener and D. Rothe, Industrial & Engineering Chemistry Research, 48 (2009) 9847.
[105] T. Kolli, M. Huuhtanen, A. Hallikainen, K. Kallinen and R.L. Keiski, Catalysis Letters, 127 (2009) 49.
[106] T. Luo and R.J. Gorte, Applied Catalysis B: Environmental, 53 (2004) 77.